Static and Dynamic Analyses of a Long-Span Cable-Stayed Bridge with Corroded Cables

By

Yang Xiang

Supervisor

Dr. Elena Dragomirescu

Co-supervisor

Dr. Beatriz Martin-Perez

Thesis submitted to the Faculty of Graduate and Postdoctoral Studies
in the partial fulfillment of the requirements for the degree of

Master of Applied Science

In

Department of Civil Engineering

University of Ottawa

uOttawa

Acknowledgments

I would like to express my sincere gratitude to my supervisors Dr. Elena Dragomirescu and Dr. Beatriz Martin-Perez. They helped me with my topic, gave me patient guidance, and enlighten me when I met difficulties. I deeply appreciate their encouragement and help.

I also want to thank my friends, Hui Jin, Jiaqi Xu and Shihan Xing who give me great help and support. I would like to thank the Civil Engineering Department of the University of Ottawa for offering me an opportunity to pursue my master's degree.

Most importantly, without the support and encouragement of my parents and my girlfriend, I couldn't have made it through all these years. I'm forever grateful to them.

Abstract

This study investigates the static behavior and dynamic behavior of the Stonecutters Cable-Stayed Bridge, which is the third longest cable-stayed bridge in the world, when a group of 8 cables is damaged by corrosion. In this thesis, the reduction in cable cross-section area is used to simulate the corrosion level. The corroded cables are divided into 2 groups of 4 cables, arranged in symmetric and asymmetric distributions on both decks. A finite element bridge model was employed to perform the analysis.

The validation of the model was established by comparing numerical results to the published results of the bridge. The model was then subjected to gravity load only to check the effects of corrosion level, the distance of the corroded cables and the distribution of the damaged cables on the decks' deflection and cable stresses change. In the dynamic analysis, the natural frequencies and mode shapes were compared with a reference case with no corrosion-damaged cables. A recorded wind load was applied on the deck to investigate the time-history response of the mid-span in the horizontal, vertical and torsional directions, and of the tower top in the horizontal direction. Moreover, frequency analysis was performed on the time-history response, and coupled motions at certain frequencies were observed. Numerical results as the ones presented in this thesis can complement information gathered from non-destructive testing technology in detecting corrosion-damaged stay-cables in cable-stayed bridges.

Contents

List of Figures

List of Tables

Notation

R_c	the corrosion ratio in the cable section
$d_{min,i}$	the minimum diameter of the wires in layer *i*
$d_{min,i+1}$	the minimum diameter of the wires in layer *i+1*
d_0	the diameter of the non-corroded wires
t	service life of wires, days
m, *n*	parameters that can be determined according to different corrosion data
a	thickness of zinc coating, μm
b	laboratory corrosion rate for zinc coating, μmd^{-1}
c	average corrosion depth of steel wire, μm
d	laboratory corrosion rate for steel wire, μmd^{-1}
R_i	radial corrosion ratio
C_1	the average corrosion depth of the first layer
C_i	the average corrosion depth of the i^{th} layer
$D(t)$	diameter loss due to corrosion, μm
C_1	section loss after 1 year of exposure, μm
β	exponent related to environmental exposure parameters
$\bar{S}$	mean stress level in the steel wire
$F(\bar{S},t)$	amplification coefficient of corrosion rate
t	time of exposure, years
CL	chloride concentration, mg/m^3
G, H	empirical coefficients
F_t and $F_{\bar{S}}$	are the independent effects of elapsed time, *t*, and the stress level, $\bar{S}$
$F_{\bar{s},t}$	the dual coupled effect
F	the constant number for all cases, (*F*=1.285)
$d_b(t)$	diameter of wire at time t, mm

i_{corr}	corrosion current density, μA/cm^2
f_n	the nth order frequency
L	the length of cable
S	the tensile force
μ	the linear density, mass per unit length
E_{eq}^{truss}	the equivalent truss element modulus of elasticity
E_{cable}	the actual cable modulus of elasticity
ρ	the cable material density
g	the acceleration due to gravity
L_x	the horizontal projected length of the cable
σ	the cable pre-stress
x(t)	the displacement of the structure at time t
$\dot{x}(t)$	the velocity of the structure
$\ddot{x}(t)$	the acceleration of the structure
m	the mass of the system
c	the damping coefficient
k	the stiffness of the structural system
$\{x(t)\}$	the displacement vector of the structure
$\{\dot{x}(t)\}$	the velocity vector of the structure
$\{\ddot{x}(t)\}$	the acceleration vector of the structure
[m]	the mass matrix of the structure
[c]	the damping coefficient matrix of the structure
[k]	the stiffness matrix of the structure
{f(t)}	the external force vector applied to the structure
ω	the circular frequency
i	the imaginary number
D_m, L_m and M_m	the drag load, lift load and torsional moment, respectively
ρ	the air density

$\overline{U}$	the mean wind velocity
B	the bridge deck width
L	the bridge length
α	the attack angle of wind
C_D, C_L, and C_M	the drag, lift and moment coefficients, respectively
Re	Reynolds number
B	the reference length for the deck width
ν	the air kinetic viscosity
S_{xx}	the power spectrum density
ω	the angular velocity
τ	the time increment
a	the corrosion level (%)
A	the total cross-sectional area
$\bar{A}$	the effective corroded cross-sectional area
S'	the stress after corrosion
S	the stress before corrosion

Chapter 1 - Introduction

1.1. Background on cable-stayed bridges

The first cable-stayed bridge was designed in the 18th century by C.T. Loescher as a draft when concrete and steel were not yet employed in the construction of bridge structures. Timber was the main construction material used for this bridge. The first modern cable-stayed bridge constructed was the Stromsund Bridge, which was built in Sweden in 1955 by using high-strength steel cables (Farquhar, 2008). The span length of the cable-stayed bridges at the time ranged from 80 to 100 m. However, with the choice of multi-stay suspension bridges with small cable spacings and with the development of construction materials in cables and girders, but also the advances in bridge deck shapes, nowadays the main span of a cable-stayed bridge can be extended to exceed 1,000 m. Today, the longest cable-stayed bridge is the Russky Bridge, which was built in Russia in 2012 with a span of 1,104 m (Virola and Ing-FEANI, 2011).

Cable-stayed bridges are popular among bridge structures, due to their economic efficiency, technical requirements and aesthetical appearance. They require fewer materials and no anchorages, which are significant economical advantages, and imply a shorter construction time, when compared with cable suspension bridges. The cable-stayed bridge consists of three main structural sub-systems: stiffening girder, tower, and inclined cables as shown in Figure 1.1 (Hua et al., 2009). The interaction of these components makes the structural behavior of cable-stayed bridges more efficient, considering the length of their span. The girder is subjected to bending and axial loading, and it can transmit the load to the tower(s) through the cables. The towers are the main structural components, which bear the load and transmit it to the foundation. Multiple cables which connect the decks and the towers are subjected to high stress. By comparing them to suspension bridges, in which the deck is hung below the main suspension cable by vertical hangers, cable-stayed bridges do not need firm anchorages

in each bank to resist the horizontal load of the main cables. The stiffness of cable-stayed bridges is greater, since the cables can handle higher stress, reducing the deformation of the decks under live load. Because no anchorages are employed, these bridges can be designed symmetrically. Therefore, it is challenging to design a long-span cable-stayed bridge considering the action of wind or seismic loads, which can threaten this slender and flexible structure. The static and dynamic characteristics of this type of bridge should be carefully considered in the design stage, especially when subjected to wind load.

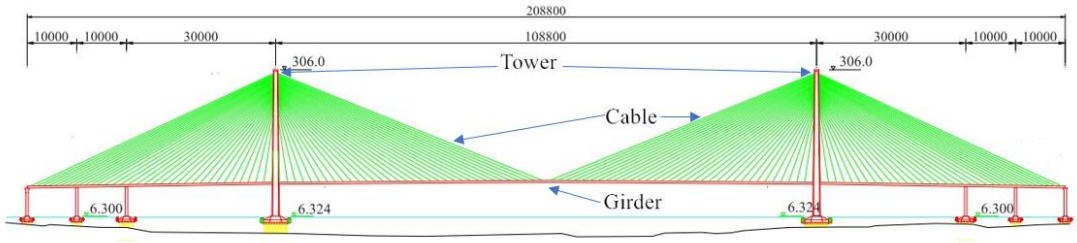

Fig. 1.1. Drawing of cable-stayed bridge (Hua et al., 2009)

In addition, cable-stayed bridges can be vulnerable to the actions of the exposure environment over their service life. Corrosion can be caused by the penetration of chloride ions into the steel wires inside the cables, through the sheath breakage which may be caused during the delivery or installation. This corrosion mechanism can be severe in the marine environment, where there is high chloride concentration in the air (Lu and He, 2016). Cable corrosion induced by an aggressive environment has a direct impact on the rupture of the steel wires and therefore on the bearing capacity of the cables (Pipinato et al., 2012). The maintenance of these stay-cables, after the bridge has been built is difficult to implement, especially for the prestressed cables. Because the cables are under tension and vulnerable to corrosion, due to the humid and salty environment above the sea, they are prone to be replaced within the service life of the bridge. It is thus important to make sure that the bridge can remain stable, even if several cables are in critical condition due to steel corrosion.

1.2. Cable corrosion

The stay cables are connected to the bridge tower at one end and are anchored to the bridge deck at the other end of the cable, transmitting the forces applied to the deck to the towers. Therefore, the stability of stay cables is vital to the integrity of cable-stayed bridges. For the early cable-stayed bridges, the cables were made by chains and bars, while for the modern bridges these are produced by high-strength steel wires, bundled together and protected by membranes which usually result in a cylindrical shape and a diameter of 3 to 7 mm. Thus, multiple steel wires are arranged in ropes and strands. For cable-stayed bridges, the strands can be formed from the helical winding of wires, while several strands are bundled together to form a cable (Caetano, 2016). The coatings are the main component of corrosion protection. In the early design, uncoated strands and cement grouts were used for stay-cables. However, with time it has been observed that the strands can be left unprotected by grouting and can corrode in just several months. Later on, a lubricant coating has been usually applied to the strands for corrosion protection. Nowadays, galvanizing is commonly used for coating the strands. The sheathings are the direct protection for the strands. The sheathing can be made of high-density polyethylene (HDPE), steel, stainless steel or aluminum. The HDPE with bright surface color is recently used as a better method to protect the strand (Tabatabai, 2005). The challenge in using this sheathing is that it can become brittle and can crack under ultraviolet radiation. The cables are the vulnerable components of the bridge system, due to their flexibility and the high tensile load they carry. Any damage to the cables will endanger the stability and safety of the entire bridge.

There are several ways that cables can be damaged, including physical methods and chemical methods. Chemical damage is always induced by the exposure environment. High amount of salt and humidity in the environment are the main factors to corrode the cables. Although the steel wires are manufactured with an anti-corrosion treatment and covered by a plastic sheathing, the breakage of the sheathing may result in moisture and other harmful substances penetrating the strands and the wires inside

the cable. The corrosion of wires consists of uniform corrosion, pitting corrosion, stress corrosion, fatigue corrosion and so on (Karanci, 2017). The most common types are the uniform corrosion, pitting corrosion and fatigue corrosion. Uniform corrosion is a type of corrosion that is uniformly distributed over the entire wire. This happens when the cable is exposed to an open atmosphere. Pitting corrosion refers to the corrosion that induces cavities on the surface of the wires, which can grow deeper, breaking the wire. Fatigue corrosion is the type of corrosion due to the coupling effect of a corrosive environment and cyclic load. The fatigue corrosion caused by cyclic load will accelerate the electrochemical corrosion, weakening the characteristics of the wires (Yang, 2013).

A corroding cable can put the entire bridge system in serious danger. When cable corrosion occurs, the effective cross-sectional area of the cable is reduced, thus the stiffness of the cable as well as its capacity will decrease. Severe corrosion can result in a sudden breakage of the cable. Different approaches for performing cables inspection consist of visual, magnetic, ultrasonic, radiographic and X-ray methods (Tabatabai, 2005). However, they are all time-consuming and expensive to implement on site.

1.3. Wind effects on bridges

The wind effect on structures is a complex aerodynamic phenomenon. When the random variation of the wind acts on a bridge and on its components, which have already small vibrations, the wind-induced pressure on the bridge surface forms a specific distribution, which is also continuously changing. The effect of the wind-induced pressure distribution can be regarded as lifting load, drag load and torsional moment on the bridge deck. Therefore, to simplify the phenomenon, random wind flow effect can be divided into these three different forces, when acting on a structure. Under the effect of wind-induced load, the response of the entire bridge can be regarded as a result of mean wind load and fluctuating wind load.

Wind load can be very damaging to bridges if design engineers do not pay enough attention to the bridge aerodynamics. The Tacoma Narrows Bridge located in Washington dramatically collapsed just a few months after it opened to traffic in 1940. The bridge was discovered to sway and buckle dangerously under a mild wind condition. The Tacoma Narrows Bridge had a vertical vibration mode, which led to one-half of the main span to rise while the other span lowered. The mass of the bridge could sufficiently control this kind of vibration, under standard wind conditions. However, a twisting mode suddenly occurred under mild wind conditions, thus the left side of the road raised, and the other side of the road lowered, with the centerline of the road remaining still. The entire bridge oscillated, and it finally collapsed due to cables rupture under the effect of such severe vibration mode. Furthermore, flutter was instated as the terminology used for such wind-induced vibration (Billah and Scanlan, 1991). Although there were no casualties but only money loss in this unexpected accident, the event made engineers realize the importance of bridge aerodynamics.

1.4. Research objectives

As more cable-stayed bridges are set into use, the potential threat that cables corrosion poses for the entire bridge has arisen increasing attention of structural engineers. The cables, which can support most of the weight of a bridge deck and most of the loads induced by vehicles, pedestrians and wind, are vital for the structural integrity of the whole bridge system. The corrosion of cables has a major effect on the strength, funtionality and life of stay-cable bridges. Therefore, the inspection of a bridge, especially the inspection of cables, after its completion, is critical to locate unreliable components and to ensure restoring its stability. The common methods to evaluate the condition of cables include visual inspection, vibration-based cable force measurement, laser-based force measurement, ultrasonic assessment, etc. These methods have the advantage of detecting rupture, corrosion or force loosening of cables. However, it is time-consuming and expensive to perform the inspection for all the cables of a bridge.

Inspections can also produce traffic disruption. Therefore, it is difficult to perform frequent inspections on a bridge, especially for the aging strucutres which need to be regularly examined and monitored. The corrosion level of corroded cables is also hard to know once the corrosion is detected.

The main target of this thesis is to find an analysis method to estimate the effect of the corroded cables and their corrosion level on the structural response of a long-span cable-stayed bridge model. To achieve this goal, first different combinations of corroded cables of a cable-stayed bridge must be investigated in this research. The different layouts of the affected cables can lead to various responses of the bridge, thus identifying the significant response for a certain corroded cables combination becomes a second objective of the current research. The structural responses to be analyzed in this research include the static and wind-induced dynamic behaviors, focusing on the deflection of the main deck and the variation of cable stresses for the static response. Natural frequencies and the deck and towers responses under wind loading condition are analyzed for the dynamic response. Each case with a different cable corrosion condition can reflect the location and the degree of corroded cables, as well as the consequent behaviour of the bridge.

In this research, the Stonecutters Cable-stayed Bridge was used as a case study to perform both static and dynamic analyses. The Stonecutters Bridge was chosen not only because it can represent the world super-long main span bridge with a length of 1,018 m, but also because its twin decks are only supported by cables. The response for this kind of long-span bridge is worth studying. The completed cable-stayed bridge model was built by Sabri (2012), and Feng (2015) performed a modification on the model for investigating the flutter analysis. After validation, the model is chosen as a starting point in the current research to apply different corrosion levels for the stay cables and to perform the static and dynamic analysis with the corroded cables.

A series of comparisons between a healthy bridge and a damaged bridge with corroded cables is made in this research. In the static analysis, the cable stresses and

deflection of the main span are carefully investigated for different scenarios, which can demonstrate the effect of corroded cables and their position along the deck on the overall structural response of the bridge. As for dynamic analysis, the natural frequency of each scenario is checked, and each frequency with its corresponding mode shape is studied. Finally, wind load during a period of time, calculated according to recorded wind data, is applied to the model. The time-domain responses of cable stresses, mid-span and tower tops in each scenario are studied and compared to each other. The data processing from time-domain to frequency-domain is needed and done with the help of MATLAB.

1.5. Analysis methodology

The model of the Stonecutters Bridge investigated was developed using the finite element method as a primary method for structure analysis. The finite element method (FEM) employed through the commercial software ABAQUS is an efficient tool to conduct a structural analysis of such complex structures. In the current thesis, several modelling assumptions were considered for better simulating the interaction between the cables and the bridge deck for different levels of cable corrosion. The option of the implicit and explicit integration schemes can handle complex contacts and load conditions (ABAQUS Inc., 2012).

1.6. Thesis layout

Chapter 1 provides a brief introduction which includes the main objective, the current problem about cable-stayed bridges, the method applied in the study and the importance of this research. Chapter 2 contains the literature review for previous studies on cable-stayed bridge design, corrosion model details and the structural analysis of cable-stayed bridges with problems in stay cables. Chapter 3 mainly describes the details of the numerical model created in ABAQUS and the validation of the model through the comparison between natural frequency and the mode shape of this model and the reference model published in the available literature. In Chapter 4, the static results are

compared within different corrosion levels and cases. The deflection of decks and stress variance of each cables due to gravity load only are discussed. Chapter 5 discusses the dynamic results in terms of natural frequencies, mode shapes and response of deck and tower when wind load is applied. The Power Spectra Density (PSD) is used as a tool to display the frequency domain of the responses. Chapter 6 concludes all the results obtained and proposes recommendations for future work.

Chapter 2 - Literature review

2.1. Overview of cable-stayed bridges

2.1.1 Structural load system of the cable-stayed bridge

The design of cable-stayed bridges has been developing since the 18th century. Cable-stayed bridges benefit from the stability of triangular shapes, and the load transfer pattern is also a simple force system as shown in Figure 2.1 (Olamigoke, 2017). The inclined elastic cables support the gravity load of the deck, allowing the bridge to have a longer span. The loads applied on the deck are transferred to the pylons through the cables, thus forming a complex structural system.

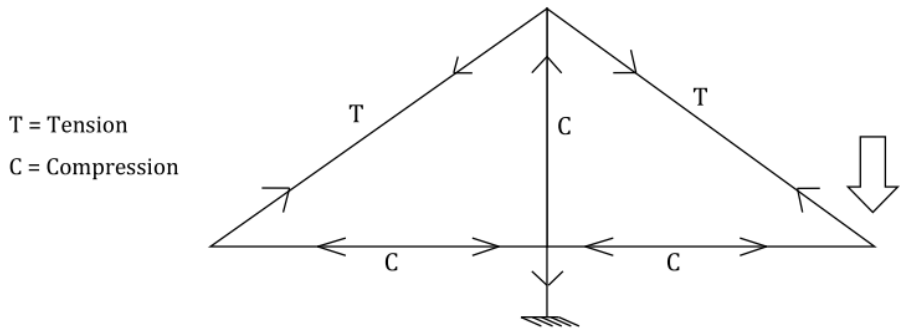

Fig. 2.1. Force system of a cable-stayed bridge (Olamigoke 2017)

However, the cables cannot provide rigid supports as they are elastic components designed to resist only tension. The cable sag due to its own weight accounts for the difficulty to determine the internal forces and reactions using the static equilibrium equations. Moreover, the compression in the deck induced by the axial force of the cables subjects it to bending moment, the deck behaving like a beam-column causing second-order behavior. The pylons, which are slender elements, take not only the compression from the cables, but also bend due to the transverse loads induced by wind or earthquake loads, or due the unsymmetrical load distribution from the cables. Therefore, the deck experiences more deflection, which makes the structure become statically indeterminate (Olamigoke, 2017).

2.1.2. Components of a cable-stayed bridge

The stay cables play an important role in the stability of cable-stayed bridges, therefore special attention is always paid for their design. The wires are arranged in strands which can be bundled as parallel or helical shapes. As shown in Figure 2.2 (Kivi, 2009), the parallel strand is formed by a group of parallel wires. The 7-wire strand, which is the simplest and most common strand, is made by 6 wires spirally twining around one core wire. A bundle of such strands can form a whole stay cable. The helical strand earns its name from helical winding of multilayer wires around a core wire. The locked coil strand is made from the assembly of wires with different shapes, consisting of a core helical strand, one or more layers of wedge-shaped wires and helically arranged z-shape wires in the outer layers (Caetano, 2016). The steel used for stay cables is stronger than regular steel, due to the higher carbon percentage in the composition. The cables strength for a long span bridge can reach 1,860 MPa to1,960 MPa (Hauge and Andersun, 2011). However, the ductility of high-strength steel is relatively lower than that of a normal steel cable. According to Gimsing and Georgakis (2011), the moduli of elasticity for simple helical, spiral and locked coil strands are 190 GPa, 170 GPa and 180 GPa, respectively.

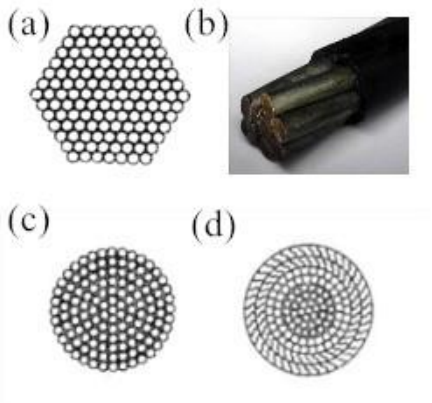

Fig. 2.2. Types of strands: (a) parallel strand, (b) 7-wire strand, (c) helical strand, (d) locked coil strand (Kivi, 2009).

The decks of cable-stayed bridges are designed to carry various loads, including

dead load, traffic load, wind load, etc. In order to resist and transfer the bending moment, torsional moment, shear force and axial force, the cross-section of the deck needs to be designed carefully. Usually, the I-girder, box girder and truss girder are adopted in the bridge deck design. The I-girders were usually used to support the concrete deck placed on top of them in the early designs, because these are easy to design and construct. However, the open system of the I-girders is not efficient in resisting torsional moments. The truss girders consist of open truss girders, which are similar to the I-girders but with the deck spanning between the two edge trusses, and with closed truss girders, which have lower bracing at the bottom chords of the truss. The open truss girders have the advantage of being light, but they still lack torsional stiffness. The closed truss girders are improved to resist the wind load. The box girders, which are adopted with a closed shape to provide enough stiffness for torsional forces, are suitable for the long-span cable-stayed bridge. The shape of a box girder can be rectangular or of inverted trapezoidal shape, and the sizes of the cross-section need to take the aerodynamic stability into account (Olamigoke, 2017).

The pylons are the main component to bear the entire load transferred from other components. This slender structure should be designed to resist the vertical compression and the transverse bending moment. Therefore, the various configurations such as A-frame, H-frame and inverted Y-frame, diamond-shaped towers, etc., are adopted for tower's design (Gimsing and Georgakis, 2011). The tower can be made of concrete, steel or combination of concrete and steel. The concrete tower has a good behavior in compression, and the steel one is easy to fabricate and assemble.

2.1.3. Stay cables arrangements

The stay cables arrangements can be classified according to the number of planes in the vertical direction, including single-plane bridge, double-plane bridge, inclined-plane bridge and multiple-plane bridge, which are all shown in Figures 2.3 (a)-(d). The cables are connected to the center axis of the longitudinal direction for the single-plane bridge (Figure 2.3 (a)) and are anchored beneath the deck to stabilize the connection. This type

of bridge requires a main span with high torsional stiffness. However, this type of bridge has span and width limitations due to the restriction of capacity in the cable system and towers.

The double-plane bridge is the type of bridge for which two planes of cables are located on the two sides of the span (Figure 2.3 (b)). The cables are connected to the edges of the deck, and the towers have stiff connections with the deck. A beam between the two pylons is required to resist transverse moments applied on the towers. The inclined-plane bridge is another kind of double-plane bridge with the two towers connected at the top to increase the lateral stiffness (Figure 2.3 (c)). The cables are also anchored at the top of the towers.

The multiple-plane bridge has more than two planes of cables in the center and two edges of the deck to carry more than one span (Figure 2.3 (d)). The benefits of this bridge are the high capacity to traffic flow and high lateral stiffness provided by the two decks.

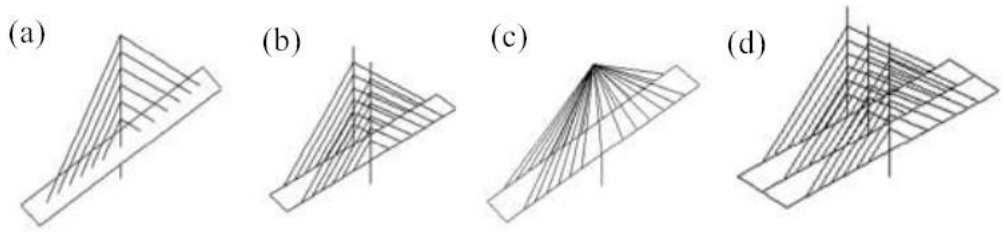

Fig. 2.3. Different types of bridges: (a) single-plane bridge, (b) double-plane bridge, (c) inclined-planed bridge, (d) multiple-plane bridge (Olamigoke, 2017)

The tower's shape, supporting method, span length, load distribution, etc., are factors that determine the cables arrangement. The common arrangements are fan arrangement, semi-fan arrangement, harp arrangement and asymmetric arrangement (Figure 2.4, Olamigoke, 2017). Figure 2.4 (a) shows the fan arrangement in which all the cables are connected to the top of the tower. This arrangement has spread anchors on the main deck, and the cables, which mainly take the vertical component of live load and dead load, can reduce the longitudinal response of the main deck and moment on the tower. However, the narrow connections observed on the towers require a complex

design and lead to stress concentrations on the top of the tower. The harp arrangement is illustrated in Figure 2.4 (b) with parallel cables at different heights connecting the deck and tower. This arrangement helps to stiffen the decks and avoids stress concentrations on the tower, but it increases the horizontal component of the cable stresses. The semi-fan arrangement, which is seen in Figure 2.4 (c), is regarded as an ideal design of cable arrangement, combining both advantages of the fan and harp arrangements. The asymmetric arrangement is shown in Figure 2.4 (d) with an unbalanced distribution of cables with respect to the tower. This type of bridge is designed to fulfill requirements of aesthetic design or clearance requirements.

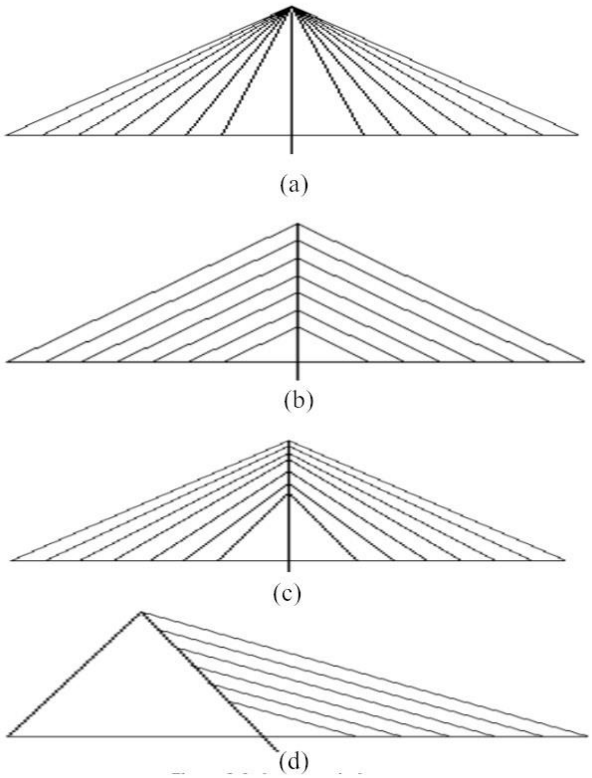

Fig. 2.4. Different types of cable arrangement: (a) fan arrangement, (b) harp arrangement, (c) semi-fan arrangement, (d) asymmetric arrangement (Olamigoke, 2017)

2.2.Corrosion on stay cables

The cable-stayed bridge is vulnerable to the damaging effect due to fatigue. Material deterioration is a certain threat to the existing cable-stayed bridge. Corrosion of wires

is a main cause of deterioration and is more common in cable-stayed bridges (Karanci, 2017). The General Rafael Urdaneta Bridge in Venezuela opened in 1962 had four cables rupturing due to deterioration in 1980. After the entire cable system was replaced with a new cable system in 1999, corrosion was still found in cables and sockets, which caused up to 30% tension loss in the cables (Sarcos-Portillo et al., 2003). The St. Nazaire Bridge in France built in 1974 also experienced severe corrosion of cables after several years of service, and a similar cable corrosion was reported for the Köhlbrand bridge located in Germany (Bao, 2014). The Morandi Bridge located in Genoa, Italy, has recently collapsed in the summer of 2018, with the suspicion of cable corrosion being the cause of the bridge failure (Pollock, 2018). The corrosion of bridge wires concerns bridge designers and owners, and it draws extended financial investment in maintenance and replacement of affected cables.

2.2.1. Corrosion process

Cable corrosion has a major impact on the stay cable system. Bao (2014) found that cable corrosion has three steps. The moisture gas with chloride and sulfate passing through the high-density polyethylene (HDPE) sheathing is the first step. The permeability of any material cannot be zero in order to allow the gases to diffuse through them. The molecules of gases try to arrange themselves to reach an equal distribution on both sides of HDPE sheath. Another direct mechanism which allows the corrosive gases to get in contact with the wires is the damage of the HDPE sheath (Salter, 2006). The damage of the HDPE sheath can occur during transportation and installation, thus accelerating the aging of the material and making it fragile. The zinc coating corrosion happens in the second step, since the HDPE fails to protect it from exposure to air. The consuming of zinc coating starts from oxidizing zinc to zinc oxide (ZnO), which is a white powder that is unable to dissolve in water. The ZnO then turns into zinc carbonate ($ZnCO_3$), zinc hydroxide ($Zn(OH)_3$) and zinc sulfate ($ZnSO_4$) when reacting with carbon dioxide and sulfur dioxide dissolved in moisture air. The $ZnCO_3$ layer, which is a dominant compound, is found to form a compact layer which is hard

to dissolve, mitigating the corrosion effect on steel wires. However, the $ZnSO_4$ is easy to be dissolved and erodes from the metal surface, accelerating the loss of zinc coating (Karanci, 2017).When the zinc coating is fully consumed, the steel wires start to be corroded as the last step. The factors contributing to the corrosion rate include the wetness, wind, temperature, pH and air pollutants (Stahl and Gagnon, 1996). Two main types of corrosion are observed in the steel wires: uniform corrosion and localized corrosion. Uniform corrosion results in the major loss of volume in the wires due to oxidizing reaction between metal surface and the corrosive environment. The main product of wire surface is hydrous ferrous oxide (Fe_2O_2), which is also known as rust. The wetting and drying cycles induced by the temperature changes throughout the year, accelerating the corrosion rate for the wires directly exposed to the environment. Pitting corrosion is one of the most common localized corrosion mechanisms. The corrosion rate in the localized region is greater than that in other regions, resulting in pits on the surface. Pitting corrosion happens when the localized damage occurs on the surface of protective coating, creating a region exposed to the corrosive environment (Karanci, 2017). The deep pits can be isolated or a group of them can form a large region of damage. The stress concentration also occurs under tensile force within these pits.

Stress corrosion and corrosion fatigue lead to wire failures when combining the corrosion and mechanical loading. Stress corrosion happens when the steel is subjected simultaneously to a corrosive environment and stress due to tensile forces. The metal with multiple chemical components such as carbon (C), Manganese (Mn), Sulphur (S) and silicon (Si) also makes itself sensitive to stress corrosion. The ruptured cross-section is normally displayed as brittle rupture without necking (Liang, 2008; Karanci, 2017). Corrosion fatigue occurs when the metal is subjected to an aggressive environment and repeated loads, such as traffic load and wind load. Then the wire fractures permanently under the condition of simultaneous corrosion and repeated cyclic loading at lower stress or fewer cycles than that is required in only fatigue occurs (Coca et al., 2011).

2.2.2. Distribution of cable corrosion

The extent of corrosion in the cable section varies from wire to wire, and it is mainly examined by visual inspection. Elachachi et al. (2006) assumed that the wire corrosion is related to the distance between the wire and the sheath, and the time it takes to erode is in proportion to this distance. Xu and Chen (2006) also found that the corrosion was severe for the most outside layer and mitigated along the radial direction in a real cable corrosion section, as shown in Figure 2.5. Corrosion can vary along the cable with a higher risk at anchorage locations. Furthermore, the length of the cable is also a factor accounting for the possibility of corrosion. The longer the cable is, the more likely it is to corrode, because of a higher risk of damaging the protective sheath. Xu and Chen (2013) and Chen and Yang (2014) studied the corrosion of wires in stay cables and found the corrosion extent was related to the distance from the sheath breakage instead of the distance from the cable centerline, as shown in Figure 2.6. This distribution appears because the wires are tightly wrapped with the sheath, making it hard for rainfall to penetrate through the gaps between wires.

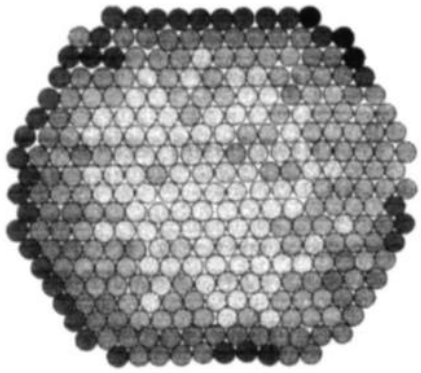

Fig. 2.5. Observation of corrosion distribution, where the darker the wire, the higher the corrosion incidence (Xu and Chen, 2006)

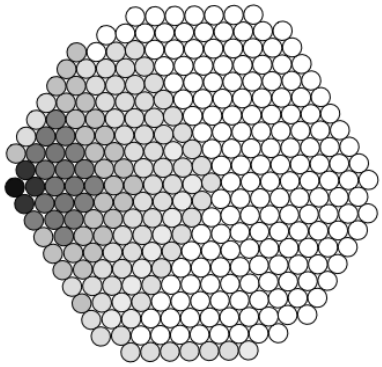

Fig. 2.6. Corrosion distribution in the cable section (Chen and Yang, 2014)

2.2.3. Cable corrosion models

The modeling of the corrosion process in a stay cable can help to predict the ensuing damage and to assess the overall performance of the cable-stayed bridge in terms of the time-dependent vulnerability.

The corrosion rate is essential to estimate the metal loss within a period of time. The corrosion condition of the wire cross-section can then be determined through the known corrosion rate. Liang (2008) proposed a corrosion predicting model that can estimate the corrosion condition of each layer of wires and the safety of the cable. The author performed an accelerated corrosion experiment to investigate the relationship between the different stresses and corrosion rates for steel and zinc coating, respectively. The experiment was performed to simulate the local environment conditions in the lab, which include acid rain. He found the corrosion rate was positively related to the subjected stress for both steel and zinc coating, as shown in Figures 2.7 and 2.8. Equation (2.1) (Liang, 2008) was established for estimating the time when the wire reached a certain corrosion level. In Eq. (2.1), the unknown factors m and n were determined by the known values of t, a, c and their corresponding stress from two known corroded cables. As for the distribution in the cross-section, the corrosion levels of each layer were assumed to be related to the distance from the center point. The corrosion depth followed Eq. (2.2) (Liang, 2008). Through this model, if the corrosion depth of the wires in the outermost layer is known, the corrosion depth of other layers of wires and corresponding time can be estimated.

$$m\frac{a}{b} + n\frac{c}{d} = t \tag{2.1}$$

where: t: service life of wires, days

m, n: parameters that can be determined according to different corrosion data

a: thickness of zinc coating, μm

b: laboratory corrosion rate for zinc coating, μmd^{-1}

c: average corrosion depth of steel wire, μm

d: laboratory corrosion rate for steel wire, μmd^{-1}

$$C_i = R_i \times C_1 \tag{2.2}$$

where: R_i: radial corrosion ratio, $R_i = i^{-0.232}$ in this case.

C_1: the average corrosion depth of the first layer

C_i: the average corrosion depth of the i^{th} layer

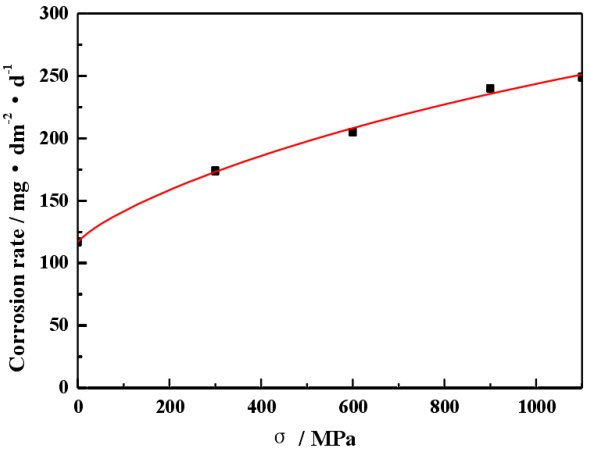

Fig. 2.7. Corrosion rate of steel wire under different stresses (Liang, 2008)

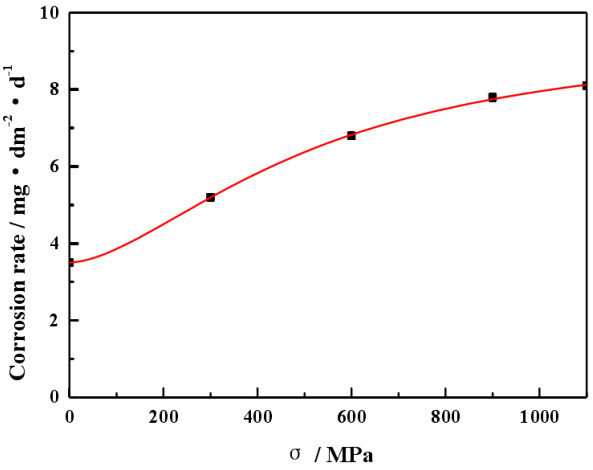

Fig. 2.8. Corrosion rate of zinc coating under different stresses (Liang, 2008)

However, the drawback of Liang's model (2008) is that it ignores the stress changes due to reduction of cross-sectional area of the wires, and thus the corrosion rate may vary while the stress changes. Therefore, the cable corrosion rate needs to be determined for different exposure environments.

Lu and He (2016) also studied stay cable corrosion under a marine environment, and they defined a relationship between the corrosive parameters and the service life period. The distribution of corrosion along a cross-section was considered to be evenly distributed. Two main factors, which are the chloride concentration and the service stress level in the corroded outer steel wires, were considered in the model.

In the corrosion model for the wires, the corrosion loss is also related to the diameter reduction in the radial direction and the chloride concentration. The expression is given by Eq. (2.3) (Lu and He, 2016). The amplification coefficient $F(\bar{S},t)$ was introduced for describing the effect of the stress level on accelerating the corrosion process, and it is expressed as per Eq. (2.4) (Lu and He, 2016). The uncertain parameters in Eq. (2.3), which are C_1, β, *G, H, CL* and $F(\bar{S},t)$, are assumed through existing reports and papers by Morcillo et al. (2013), Klinesmith et al. (2007) and Li et al. (2007) in this research. These factors vary depending on the location where the bridge is located.

$$D(t) = \left\{\left[C_1 F(\bar{S},t)t^{\beta}\right] - \left[C_1 \int_0^t t^{\beta} \frac{\partial F(\bar{S},t)}{\partial t} dt\right]\right\}(1+\frac{CL}{G})^H \qquad (2.3)$$

where: $D(t)$: diameter loss due to corrosion, μm;

C_1: section loss after 1 year of exposure, μm;

β: exponent related to environmental exposure parameters;

$\bar{S}$: mean stress level in the steel wire;

$F(\bar{S}, t)$: amplification coefficient of corrosion rate;

t: time of exposure, years;

CL: chloride concentration, mg/m^3;

G, H: empirical coefficients.

$$F(\bar{S}, t) = F_t + F_{\bar{S}} + F_{\bar{s},t} + F \tag{2.4}$$

where: F_t and $F_{\bar{S}}$: are the independent effects of elapsed time, *t*, and the stress level, $\bar{S}$.

$F_{\bar{s},t}$ is the dual coupled effect

F is the constant number for all cases, (*F*=1.285)

The in-service stress, distribution of corrosion in a cross-section as well as the spatial distribution of chloride penetration along the bridge span were considered in the model. However, the internal movement between wires, fatigue, and other factors that affect the stress state were neglected.

The corrosion models proposed by Liang (2008) and Lu and He (2016) reflect the corrosion condition through the reduction in cross-sectional area. However, the uncertain factors, which are determined through the experiments in the lab for Liang's model and through assumptions and measurements of the local environment for Lu and He's model, make corrosion prediction in stay cables of the Stonecutters Cable-stayed Bridge difficult due to lack of information. Corrosion is an electrochemistry process governed by the kinetics of the cathodic and anodic reactions, and it can be expressed in terms of the corrosion current through Faraday's law. By applying this law to a corroding steel wire, a general expression for the remaining diameter is introduced in Eq. (2.5) (Andrade et al., 1993). The corrosion period can then be estimated only when

the corrosion current density i_{corr} is known. Xie et al. (2015) found that the corrosion current density is related to the stress as shown in Figure 2.9. In this thesis, to account for the corrosion level in the cables, the effective cross-sectional area after corrosion has taken place is adopted (Lonetti et al., 2011; Vikas et al., 2013). A uniform corrosion distribution in the cross-sectional area of the cable is assumed for simplification. Equation (2.5) provides a simple expression to predict the service life of the cable given the corrosion rate i_{corr} and a percentage of corrosion-induced diameter loss.

$$d_b(\mathrm{t}) = d_b - 0.0232 \cdot i_{corr} \cdot t \tag{2.5}$$

where: $d_b(t)$: diameter of wire at time t, mm;

i_{corr}: corrosion current density, μA/cm^2;

t: time of service, year;

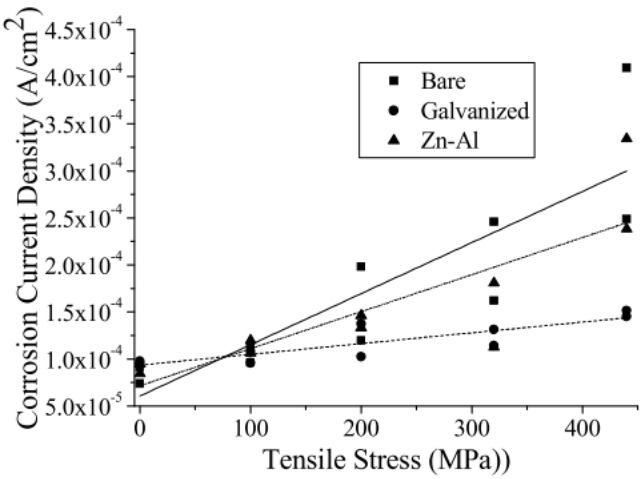

Fig. 2.9. Corrosion current densities of cable wires with different stresses (Xie et al., 2015)

2.2.4 Mechanical properties of corroded cables

Corrosion changes some of the mechanical properties of the cables. The ultimate stress of wires has found to decrease due to corrosion (Barton et al., 2000; Li et al., 2012). Barton et al. (2000) investigated the ultimate load in galvanized wires, ungalvanized wires, and stripped-galvanized wires by applying an accelerated corrosion approach. Their experiments indicated that the cracking or pitting effects on the surface may

influence the decay rate of the ultimate load. Besides, the ultimate load showed little sensitivity to the preload level in the wire. Nakamura et al. (2004) performed several experiments to investigate the tensile strength, elongation and fatigue strength of corroded galvanized and bare wires. They found that the true tensile strength, the breaking force divided by the reduced cross-sectional area due to corrosion, did not decrease as the corrosion level increased, as shown in Figure 2.10; however, the nominal or engineering tensile strength, the rupture force divided by the original cross-sectional area, was observed to decrease with increasing mass loss (Figure 2.11). The material itself is not sensitive to the corrosion. The elongation of the corroded wires decreased linearly for bare steel and galvanized wires, after consuming the galvanized surface as shown in Figure 2.12. Figure 2.13 introduced by Li et al. (2012) shows the relationship between the stress and the strain of corroded and uncorroded wires. As shown in Figure 2.13, their study proved that the elongation and nominal ultimate strength of corroded wires were decreased and showed high sensitivity to wire corrosion. Furthermore, the elastic modulus of the corroded and non-corroded wires remained the same.

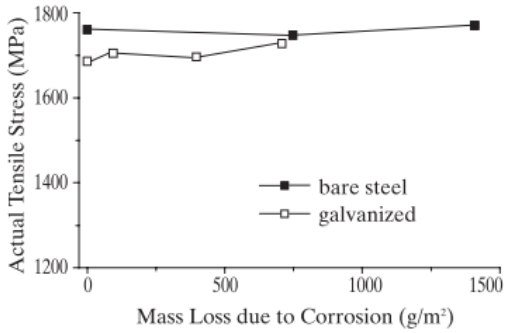

Fig. 2.10. True tensile strength of corroded wires (Nakamura et al., 2004)

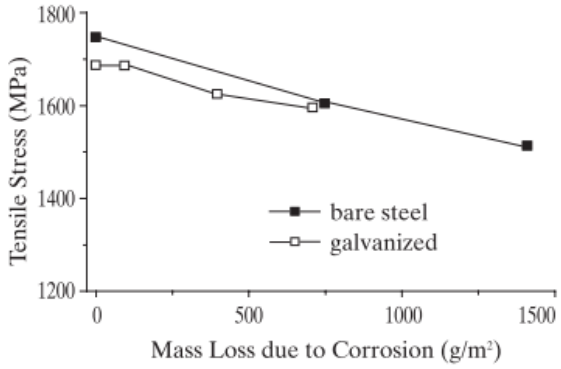

Fig. 2.11. Nominal tensile strength of corroded wires (Nakamura et al., 2004)

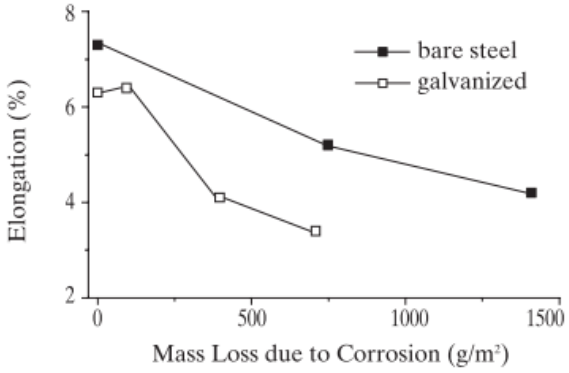

Fig. 2.12. Elongation of corroded wires (Nakamura et al., 2004)

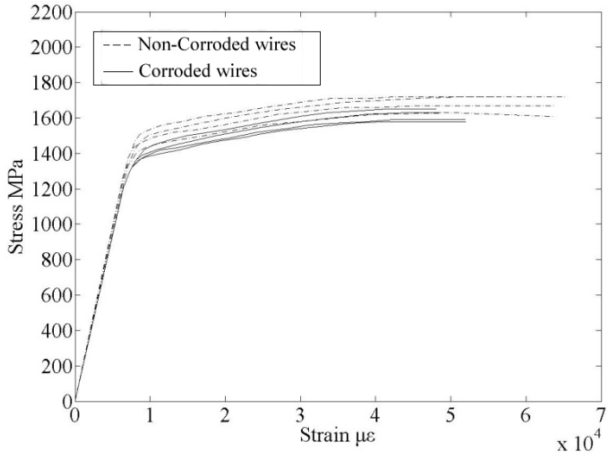

Fig. 2.13. The relationship between stress and strain of wires (Li et al., 2012)

Xu and Chen (2013) conducted a series of tensile tests for corroded cables, revealing the relationship between the diameter loss and the mechanical properties of the cable, as shown in Figure 2.14. The yield load, ultimate load, and ultimate strain decreased as the corrosion level increased (i.e., for lower diameters), but the change in the yield strain was not significant.

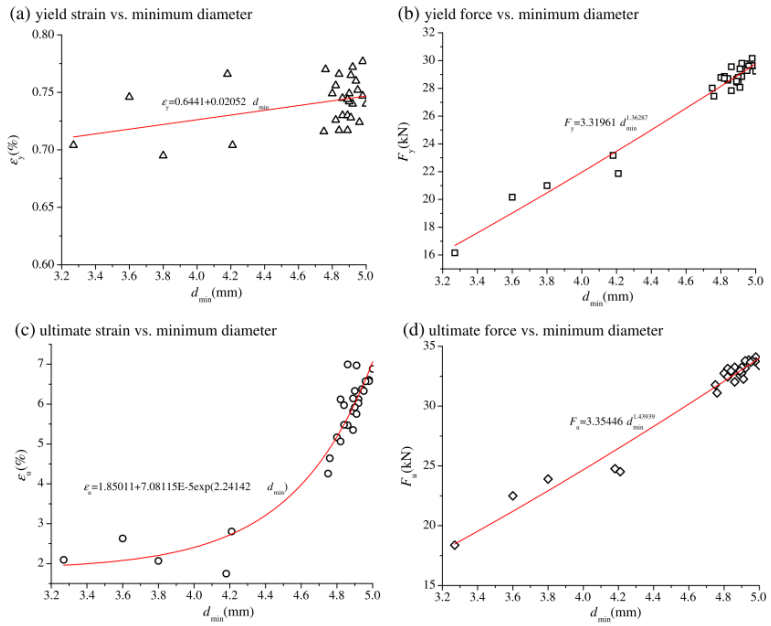

Fig. 2.14. The relationship between mechanical parameters and diameter loss (Xu and Chen, 2013)

2.2.5. Corrosion control and detection methods

The direct corrosion control techniques for stay cables are a galvanized surface and sheath wrapping around the wires. The sheath is applied on the cable to provide a barrier against rainfall and acid gas from polluted air, such as SO_2 and CO_2, into the cable. The galvanized surface can not only protect the steel wire from exposing it to moisture, but it also acts as a protection because the zinc is more reactive than iron and oxidizes in preference to iron, producing an impact byproduct to slow down the corrosion rate. In the 1980s, the carbon fiber composite cable (CFCC) consisting of carbon fiber-reinforced polymer (CFRP) parallel wire bundles were proposed to replace the high strength steel cables considering its corrosion and fatigue resistance. The CFCC is found to be lightweight, to have a higher strength and stiffness and to resist crack propagation which may cause failure of the structure, making it very reliable to be applied in cable-stayed bridges (Meier, 2012). Furthermore, the CFCC cable was numerically modelled in a long-span cable stayed bridge for out-of-plane instability under wind load, and was found to have smaller horizontal and torsional deck response

when compared to the steel cable (Kao et al., 2006).

The most common way to inspect stay cables is by visual inspection. During a visual inspection, the crack and aging of the sheath and the degradation condition of wires under the sheath are the main parts to inspect. For some inside wires, for which is hard to perform a visual inspection, the acoustic emission (AE) method allows the engineers to detect and locate the area of corrosion and fatigue of the wires, by using elastic energy wave created by internal defects of the steel wires (Guo, 2014). Another method applied to detect the corrosion condition is called Magnetostrictive sensor (MS), which uses the phenomenon known as the deformation creating a change in magnetization. Any change in strain or deformation can create a pulse of elastic wave to change the magnetic induction of a material, which can be detected and processed by MS (Betti et al., 2014). The AE and MS technologies are usually combined to detect the damaged wires. Other nondestructive methods to detect the defects of cables consist of magnetic leakage detection and vibration monitoring (Guo, 2014). The magnetic leakage method is an indirect method to determine the size of a defect through measuring the leaking magnetic field of a cable surface. The magnetic force gathered will happen when the defects exist inside or outside the wires. The vibration monitoring system can detect the damage by determining the internal forces. The frequency of cable gathered by the sensors mounted on the cables can determine the static internal forces with the preconditions, which are the cable length, linear density and boundary conditions. The relationship between frequency and internal forces is shown in Eq. (2.6). The changes in internal forces can reflect the damaged condition of the cables.

$$f_n = \frac{n}{2L}\sqrt{\frac{S}{\mu}} \tag{2.6}$$

where: f_n: the nth order frequency

L: the length of cable

S: the tensile force

μ: the linear density, mass per unit length

In this research, the possibility of detecting the cable damage level and location is investigated through numerical analysis of a bridge. This could be combined with non-destructive technology in order to optimize the monitoring of damage in a real bridge.

2.3. Structural analysis of cable-stayed bridges

2.3.1. Development of finite element model

With the development of technology, computers become an efficient tool for analyzing complex structures stability. Compared to physical experiments, numerical methods have the advantages of saving time and money, not being limited by space and equipment, and collecting data easily. The finite element method is widely used in analyzing complicated structural problems. By using finite element software, each component of a bridge can be simplified as beam or truss elements, while the characteristic of each material and connections can be defined through the software as well. After applying different loads, the model can provide the potential bridge responses corresponding to various scenarios.

The difficulty of finite element modeling of cable-stayed bridges is to determine the type of element used to represent the cables. Stay cables are tension members that can only bear axial tensile forces but have no resistance to bending moments. The 2-node truss element, which has the same behavior, is widely used in finite element models. However, the effect of cable sag induced by its self-weight induces geometric nonlinearity in the bridge structure and needs to be considered in the numerical analysis. To idealize the cable behavior with truss elements, the equivalent Young's modulus introduced by Ernst (1965) is widely used, and it is shown in Eq. (2.7):

$$E_{eq}^{truss} = \frac{E^{cable}}{1+\frac{(\rho g L_x)^2}{12\sigma^3}E^{cable}} \tag{2.7}$$

where: E_{eq}^{truss} is the equivalent truss element modulus of elasticity,

E_{cable} is the actual cable modulus of elasticity,

ρ is the cable material density,

g is the acceleration due to gravity,

L_x is the horizontal projected length of the cable,

σ is the cable pre-stress.

The one-element cable has satisfied results in the static or quasi-static analysis of cable-stayed bridges (Cheng and Lau, 2002). However, this kind of cable cannot simulate the transverse vibration in dynamic analysis. Cheng and Lau (2002) investigated the effect of using three-node cables and multi-link cables instead of a single truss cable on the dynamic behavior of the bridge, with the intention of accounting for the nonlinearity of the cable. The results showed that the multi-link cable model reflects better the transverse motion of cables due to vibrations than the single truss cable. The coupled movement of stay cables and deck could be identified. Also the first few frequencies of the bridge model with multi-link cables were similar to the analytical frequencies obtained by Eq. (2.6), indicating that the cable vibration model has little effects on other parts of the bridge. Sabri (2012) used a similar multiple-element cable model in the dynamic analysis of the Stonecutters Cable-stayed Bridge Model, showing the same benefit of modeling the coupled motion between the cables and the deck.

In this thesis, investigating the effects of cables vibration is not the main objective, and for the purpose of simplification, a single truss element is used for each cable; however, the equivalent cable stiffness which is shown in Eq. (2.7) is adopted to conduct the bridge analysis.

2.3.2. Dynamic analysis and natural frequencies of bridge models

The dynamic motion of the bridge is described by the equation of motion, which uses the theory of a system vibration. Craig and Kurdila (2006) mentioned that the mass, stiffness and damping properties are the three main structural characteristics of the structure to determine its dynamic response. The inertia force F_t, the damping force F_d

and the spring force F_s are described by Eqs. (2.8), (2.9) and (2.10), respectively:

$$F_t = -m\ddot{x}(t) \tag{2.8}$$

$$F_d = c\dot{x}(t) \tag{2.9}$$

$$F_s = kx(t) \tag{2.10}$$

where x(t): the displacement of the structure at time t,

$\dot{x}(t)$: the velocity of the structure,

$\ddot{x}(t)$: the acceleration of the structure,

m: the mass of the system,

c: the damping coefficient,

k: the stiffness of the structural system.

The equation of motion results from applying the equilibrium condition by combining all of the three internal forces and the excitation force f(t) in Eq. (2.11):

$$[\mathrm{m}]\{\ddot{x}(t)\} + [\mathrm{c}]\{\dot{x}(t)\} + [\mathrm{k}]\{x(t)\} = \{\mathrm{f(t)}\} \tag{2.11}$$

where $\{x(t)\}$: the displacement vector of the structure,

$\{\dot{x}(t)\}$: the velocity vector of the structure,

$\{\ddot{x}(t)\}$: the acceleration vector of the structure,

[m]: the mass matrix of the structure,

[c]: the damping coefficient matrix of the structure,

[k]: the stiffness matrix of the structure, and

{f(t)}: the external force vector applied to the structure.

The dynamic response of the structure can be described in terms of vibration frequency. The excitation function f(t) and response function x(t) can be written in complex form, as shown in Eqs. (2.12) and (2.13), respectively, and the equation of undamped motion as given in Eq. (2.14) is used to solve the eigenvalue of the structure (Ewins 2003):

$$f(t) = \int_{-\infty}^{+\infty} F(\omega)\, e^{i\omega t} d\omega \tag{2.12}$$

$$x(t) = \int_{-\infty}^{+\infty} X(\omega)\, e^{i\omega t} d\omega \tag{2.13}$$

$$\{[K] - [\omega^2][M]\}\{[x(t)]\} = \{[f(t)]\} \tag{2.14}$$

where ω: the circular frequency,

i: the imaginary number.

The solution to Eq. (2.14) gives the eigenvalues, which are the frequencies of the structure, and its corresponding eigenvectors of the system. The eigenvalues are also the square of the natural frequency, which only depend on the structure's stiffness and mass, and they can reflect the frequency at which the system is likely to vibrate freely without any damping forces. The eigenvectors represent the mode shapes of the structure for certain frequencies. In the dynamic analysis of the bridge model, the applied dynamic load needs to be compared with the natural frequency of the structure to avoid resonance when they both reach the same value. Otherwise, resonance will lead to an amplification of the dynamic response until the bridge fails.

2.3.3. Wind load simulation

As slender structures, long-span bridges are vulnerable to aerodynamic instabilities due to wind action, which has been studied for several decades since the failure of the Tacoma Narrows bridge in 1940 (Billah and Scanlan, 1991). The aerodynamic response of the bridge is caused by the interaction between the wind load and the structure, and it is the combination of the mean wind load and dynamic wind load. The mean wind load can be divided into three components, which are the lift force, the drag force and the torsional moment according to the effect of pressure distribution (Chen, 2005), as shown in Figure 2.15. Scanlan (1996) derived the mean wind load equations for the three components in Eqs. (2.15), (2.16) and (2.17), respectively:

$$D_m = \frac{1}{2}\rho\bar{U}^2 C_D BL(\alpha) \tag{2.15}$$

$$L_m = \frac{1}{2}\rho\bar{U}^2 C_L BL(\alpha) \tag{2.16}$$

$$M_m = \frac{1}{2}\rho\bar{U}^2 C_M B^2 L(\alpha) \tag{2.17}$$

where D_m, L_m and M_m: the drag load, lift load and torsional moment, respectively,

ρ: the air density,

$\bar{U}$: the mean wind velocity,

B: the bridge deck width,

L: the bridge length,

α: the attack angle of wind,

C_D, C_L, and C_M: the drag, lift and moment coefficients, respectively.

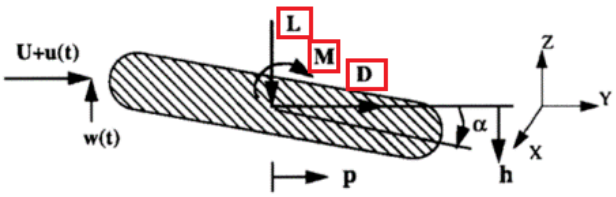

Fig. 2.15. Three components of wind load on the deck (Chen et al., 2000)

The wind force coefficients C_D, C_L, and C_M are dimensionless and are determined by wind tunnel experiments. In a wind tunnel experiment, the dimension of the model, air density, attack angle of wind and wind velocity are all under control. All the known values are substituted into Eqs. (2.15), (2.16) and (2.17) to derive the unknown coefficients. From the data acquired in the experiments, Chen (2005) found that all the coefficients vary as the attack angle of wind changes. Besides, the drag load coefficient is affected by the cross-section of the deck and Reynolds number (Re), which is related to the wind velocity and deck width as shown in Eq. (2.18):

$$Re = \frac{V \cdot B}{\nu} \tag{2.18}$$

where V: the wind velocity,

B: the reference length for the deck width,

ν: the air kinetic viscosity.

Diana et al. (2013) performed wind tunnel experiments to investigate the wind force coefficients on the Messina bridge model. Figure 2.16 demonstrates the static aerodynamic coefficients of the bridge deck for different Reynold numbers corresponding to smooth and rough surfaces. The authors found that the values obtained for a smooth deck vary with the wind attack angles, and the wind velocity hardly changes the coefficients values. The roughness can impact the lift and moment coefficients when changing wind velocities compared to those of a smooth surface. Furthermore, the values of the three coefficients corresponding to a smooth surface are close to those obtained by assuming a rough surface at low wind speeds.

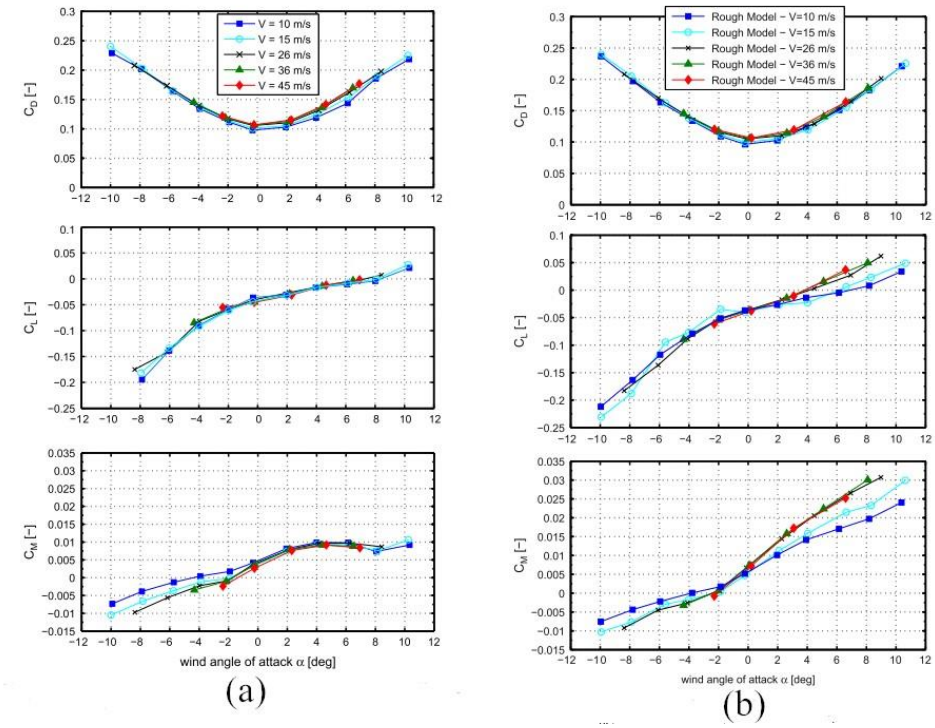

Fig. 2.16. Wind load coefficients as a function of wind attack angles and wind velocities (a) in the smooth surface; (b) in the rough surface (Diana et al., 2013).

Larsen et al. (2012) did a similar study for the Stonecutters Cable-stayed Bridge to

obtain the three important wind load coefficients. Figure 2.17 provides the details for the experimental results.

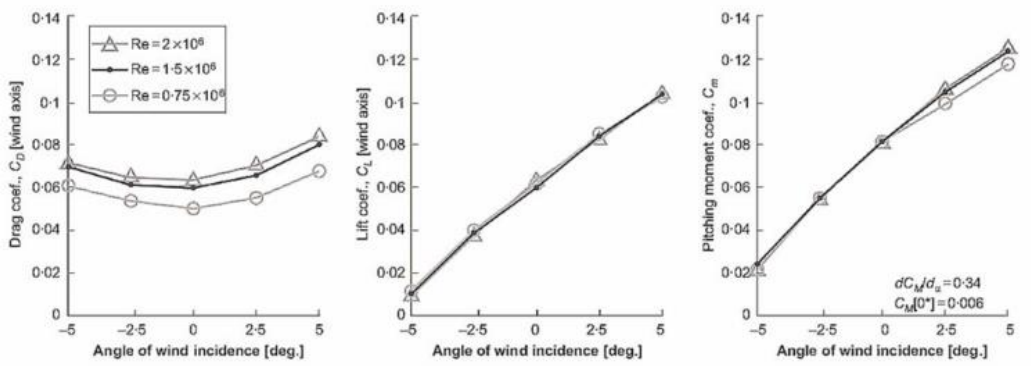

Fig. 2.17. The wind load coefficients obtained for Stonecutters cable-stayed bridge model (Larsen et al., 2012)

When comparing Figures 2.16 and 2.17, the variation of the three coefficients with the angle of attack is found to be similar. For both bridge experiments, the wind attack angles have more influence on the values of the coefficients than Reynold's number. Diana et al. (2013) also mentioned that the higher Re corresponding to a rough surface was closer to real conditions. There is a large overlap between the wind load coefficients for v = 36 m/s in Figure 2.16 (b) and those in Figure 2.17; very little difference can also be observed between Re = 1.5 x 10^6 and Re = 2.0 x 10^6 in Figures 2.16 (b) and 2.17, respectively. The wind load coefficients can therefore be assumed to be the same for specific wind attack angle regardless of Reynold's number. Feng (2015) summarized the wind tunnel experiment of the Stonecutters Bridge performed by Hui (2013) and listed the steady wind load coefficients in Table 2.1.

Table 2.1. Static wind load coefficients for the Stonecutters bridge and for different wind attack angles (Feng, 2015)

Angle(Deg.)	C_D	C_L	C_M
-5	0.083	-0.29	-0.049
-3	0.074	-0.212	-0.029
0	0.07	-0.155	-0.018
3	0.073	0.021	0.029
5	0.079	0.079	0.048

2.3.4. Fourier analysis

In dynamic analysis, Fourier analysis aims at transforming the time-domain response into a frequency-domain response. Fourier series is used to describe the dynamic response through dividing it into frequency components, which have distinct frequencies with their own phases and amplitudes. Then, the Fourier series approach can be extended to a Fourier Transform in terms of the signals with an infinite period (Heerah, 2009). Newland (2012) explained that to make sure the periodic signal $x(t)$ could be transformed using Fourier transform, the single $x(t)$ should satisfy the condition expressed in Eq. (2.19):

$$\int_{-\infty}^{\infty}|x(t)|dt < \infty \tag{2.19}$$

The Fourier transform X(ω) can be presented in terms of $x(t)$ in Eq. (2.20):

$$\mathrm{X}(\omega) = \frac{1}{2\pi}\int_{-\infty}^{\infty} x(t)e^{-i\omega t}\,dt \tag{2.20}$$

In practice, the response signal $x(t)$ is recorded as a finite time duration with discrete points according to the sampling scheme. The Discrete Fourier Transform (DFT), which is the Fourier transform with N discrete points in a finite series, was introduced by Newland (2012). The formal definition of the DFT for the series $\{x_r\}$, r=0, 1, 2, ..., (N-1) is given in Eq. (2.21):

$$X_k = \frac{1}{N}\sum_{r=0}^{N-1} x_k e^{-i(\frac{2\pi kr}{N})} \tag{2.21}$$

where k = 0, 1, 2, ..., (N-1).

The Fast Fourier transform (FFT), which is a computer algorithm for calculating DFT or inverse discrete Fourier transform, was also introduced by Newland (2012). The FFT is more efficient and requires the N to be an integral power of 2, thereby reducing the processing time to calculate the DFT of the response time history (Heerah, 2009).

When performing the FFT, the time history signal can be transformed into the frequency domain with a variation of amplitude. For the random signal, the signal function is assumed to be white noise, which contains all the frequencies within the

frequency spectrum. The random responses cannot be calculated by valid Fourier transform, because they do not satisfy Eq. (2.19). The Power Spectrum Density (PSD) was introduced to present the frequency domain results (Heerah 2009). The PSD as written in Eq. (2.22) is the Fourier transform of the autocorrelation function $R_{xx}(\tau)$ of the random response $x(t)$ (Newland, 2012). Around 1960's, the Welch's method improved the PSD by considering overlapping segments in the time history and computing the power spectrum for each segment (Trauth et al., 2006). The Welch's PSD has the advantage of increasing the signal to noise ratio of the power spectrum without losing frequency resolution (Heerah, 2009).

$$S_{xx}(\omega) = \frac{1}{2\pi}\int_{-\infty}^{+\infty} R_{xx}(\tau)e^{-i\omega t}d\tau \tag{2.22}$$

Where: S_{xx}: the power spectrum density

ω: the angular velocity,

τ: the time increment.

2.4. Structural behavior of bridge with damaged cables

The structural behavior of cable-stayed bridges has been increasingly studied with the use of finite element models. Unless some parameters have to be obtained from physical experiments, other analysis can be performed with the help of numerical models. The model results can be a powerful prediction to the real response.

It is worth studying if damages in the stay cables could lead to safety vulnerability in these slender bridges. Kao and Kou (2010) investigated the effects of ruptured cables on the structural behavior of stayed-cable bridges. The authors conducted a numerical study on a three-span cable-stayed bridge, with the main span of 600 m, and removed cables one by one in the analysis to investigate the ensuing remaining cable forces, the horizontal displacement of the tower, and the sagging of the center of the main span. The authors noted that the cables adjacent to ruptured cables experienced an increase in cable forces. When the outermost cable ruptured, both the tower and the center of the

main span underwent a significant increase in displacement (Tables 2.2 and 2.3). It was also observed that cable ruptures lead to uplifts in other locations of the deck.

Table 2.2. Deviation of top-of-tower displacement from broken cable at different locations (Kao and Kou, 2010)

Side span			Center span		
No. of broken cable	Top-of-tower Displacement (after breakage, m)	Influence of top-of-tower displacement (%)	No. of broken cable	Top-of-tower Displacement (after breakage, m)	Influence of top-of-tower displacement (%)
1	2.4551	196.94	15	0.3949	-52.24
2	1.0580	27.96	16	0.7586	-8.25
3	1.0423	26.06	17	0.7826	-5.35
4	0.9240	11.75	18	0.8225	-0.52
5	0.8552	3.43	19	0.8414	1.77
6	0.8156	-1.35	20	0.8463	2.36
7	0.8004	-3.20	21	0.8431	1.97
8	0.8005	-3.18	22	0.8352	1.01
9	0.8090	-2.16	23	0.8287	0.23
10	0.8186	-0.99	24	0.8242	-0.32
11	0.8250	-0.22	25	0.8228	-0.49
12	0.8275	0.08	26	0.8244	-0.30
13	0.8272	0.05	27	0.8283	0.18
14	0.8263	-0.06	28	0.8291	0.27
		Top-of-tower displacement (m) with no broken cable		0.8268	

Table 2.3. Deviation of main span deflection resulting from broken cable at different locations (Kao and Kou, 2010)

Side span			Center span		
No. of broken cable	Displacement, center of girder of center span(m)	Deviation of the displacement (%)	No. of broken cable	Displacement, center of girder of center span(m)	Deviation of the displacement (%)
1	5.8266	62.43	15	5.1222	42.79
2	3.9085	8.96	16	3.8991	8.69
3	3.8909	8.46	17	3.9523	10.18
4	3.7270	3.90	18	3.8004	5.94
5	3.6296	1.18	19	3.6998	3.14
6	3.5742	-0.36	20	3.6227	0.99
7	3.5516	-0.99	21	3.5770	-0.28
8	3.5481	-1.09	22	3.5516	-0.99
9	3.5592	-0.78	23	3.5521	-0.98
10	3.5722	-0.42	24	3.5594	-0.78
11	3.5803	-0.19	25	3.5686	-0.54
12	3.5858	-0.04	26	3.5757	-0.32
13	3.5931	0.16	27	3.5860	-0.03
14	3.5869	-0.01	28	3.5858	-0.04
		Displacement, center of girder of Center-span with no broken cable(m)		3.5872	

Vikas et al. (2013) studied the effects of cable degradation on the structural behavior of cable-stayed bridges by conducting a numerical analysis of a bridge with the main deck of 220 m, as shown in Figure 2.18. The authors modeled the corroded cables by applying the reduction of the modulus of elasticity and cross-sectional area as a function of corrosion level. In their model, the modulus of elasticity and cross-sectional area are inversely proportional to the corrosion level. The authors performed static and dynamic analyses on the bridge model with one cable reaching the ultimate

strength and failing. The cable that failed was the second cable on the left side close to the mid-span.

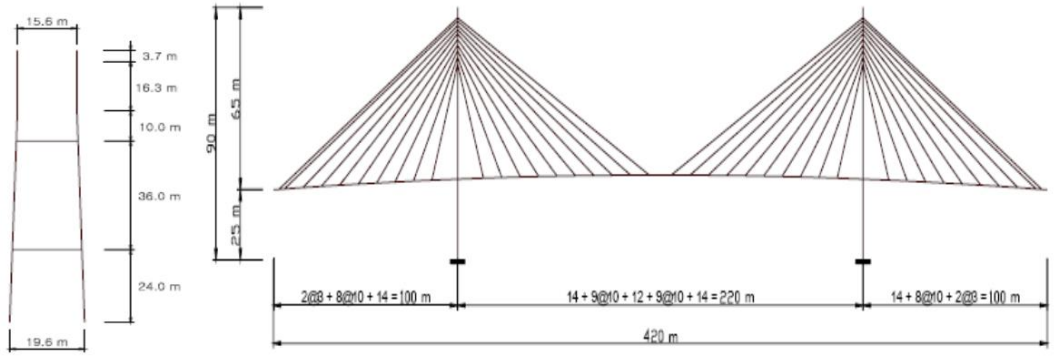

Fig. 2.18. The layout of the bridge and tower (Vikas et al., 2013)

The authors found that the internal forces of cables around the ruptured cable were increased and that those of cables away from the ruptured cable were reduced. The deflection of half deck, illustrated in Figure 2.19, shows an increase of 6.9% around the location where the cable failed. A gradual decrease in natural frequency as the corrosion level increased was observed in the dynamic analysis, as illustrated in Figure 2.20.

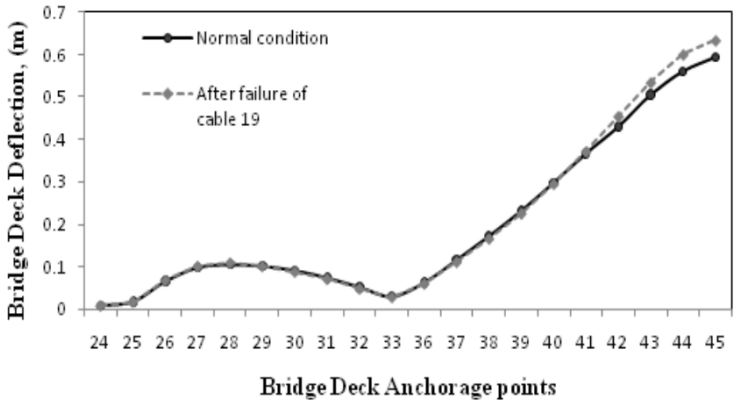

Fig. 2.19. Comparison of deflection in deck before and after cable failure (Vikas et al., 2013)

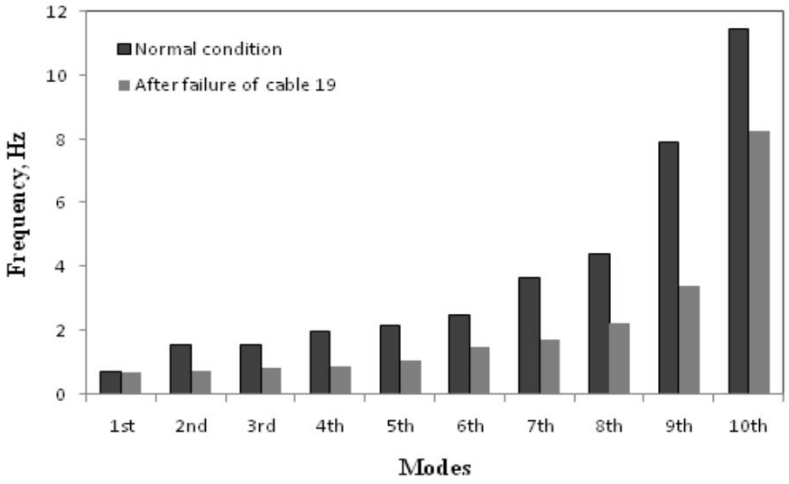

Fig. 2.20. Comparison of natural frequencies before and after cable failure (Vikas et al., 2013)

Das et al. (2016) proposed a progressive collapse analysis for a cable-stayed bridge with a 457.2-m main span and cable failures in the side span. The authors used a nonlinear dynamic procedure to extract the response in the key locations including the center of the span, the top of the pylon and the end cables. More than one cable failures were considered in this study. Through the results, the authors stated that the end cables of either side of the bridge were the most vulnerable, increasing probability of a failure throughout the whole structure. The extra deflection on the pylon top and deck were observed due to the failure of the cables. Olamigoke (2017) studied the sudden cable loss in a three-plane cable-stayed bridge and also observed the load redistribution along the span, as shown in Figure 2.21. It is interesting to find that the cable loss in one plane can result in stress increase in another plane.

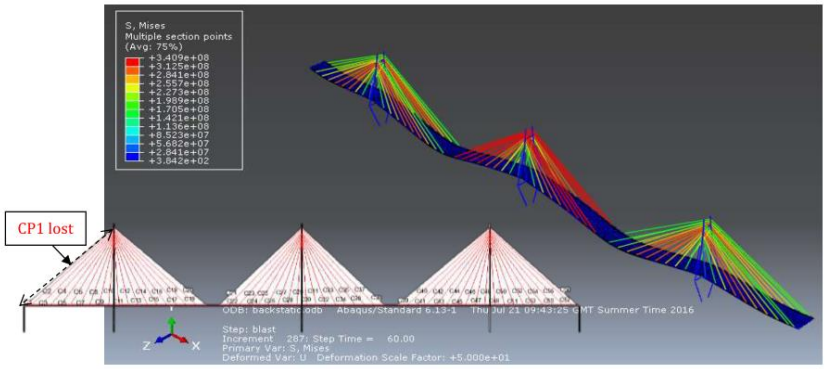

(a)

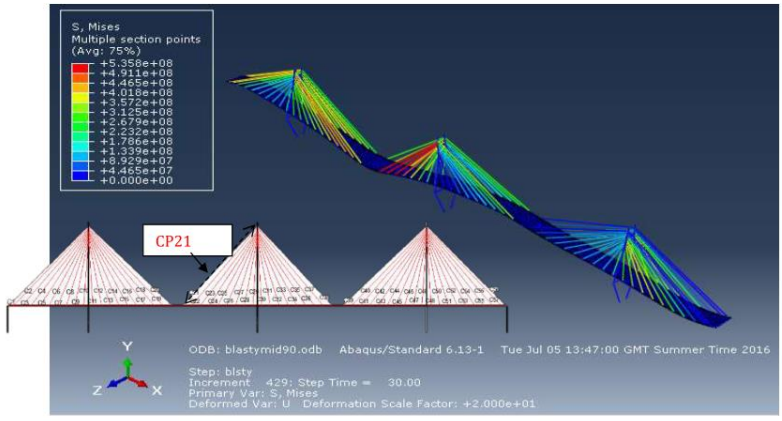

(b)

Fig. 2.21. Load distribution along the span with one cable lost (a) case of CP1 lost, (b) case of CP21 lost (Olamigoke, 2017)

The previous studies focused on the effect of ruptured cables caused by either corrosion or sudden events on the structural behavior of cable-stayed bridges. Few studies have investigated the structural behavior of a cable-stayed bridge with gradual corrosion. Zhang (2015) investigated the effect of damaged cables for a cable-stayed bridge with a 220-m main span (Figure 2.22). The reduction in Young's modulus and cross-sectional area were also used to simulate different damage levels. The author obtained the results of deck deflection, internal forces and natural frequency when the cables were damaged from 10% to 100% degree on the side span and on the main span, as shown in Figures 2.23, 2.24 and 2.25. From Figure 2.23 it is observed that the deflection increased as the corrosion level increased, and the middle point and location near the towers have the largest change. The increase in the internal forces of the

damaged cables and of adjacent ones due to the increased corrosion condition can be observed in Figure 2.24. As for the dynamic response, most of the natural frequencies decreased as the corrosion level increased, except for some that increased and corresponded to higher vibration modes, as shown in Figures 2.25 (b) and (d). The static and dynamic responses from the numerical model reflect the changes caused at different corrosion levels and corrosion cable locations for the short span cable-stayed bridge. However, there are missing studies on the effect of corroded cables on long span cable-stayed bridges. The current study only concentrates on the deterioration of both cables at the same location, and the effect of different location on both sides needs to be further investigated. Furthermore, the response of a long-span cable-stayed bridge with corroded cables subjected to real wind conditions has not been looked into yet. This research will focus on this gap on the state-of-the-art through numerical analysis of a long-span cable-stayed bridge.

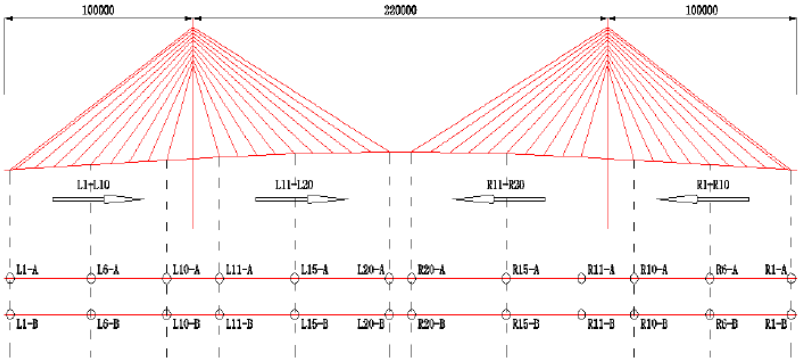

Fig. 2.22. Configuration of the bridge (Zhang, 2015)

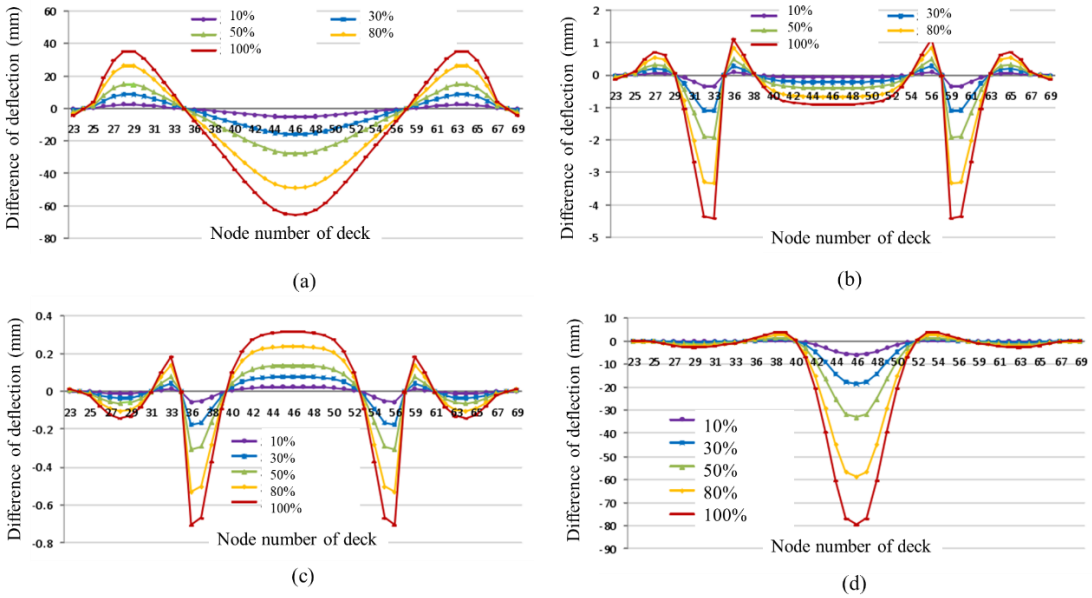

Fig. 2.23. The deck deflection change at different corrosion levels, and the corrosion cable located at (a) L1 and R1 cables, (b) L10 and R10 cables, (c) L11 and R11 cables, (d) L20 and R20 cables (Zhang, 2015)

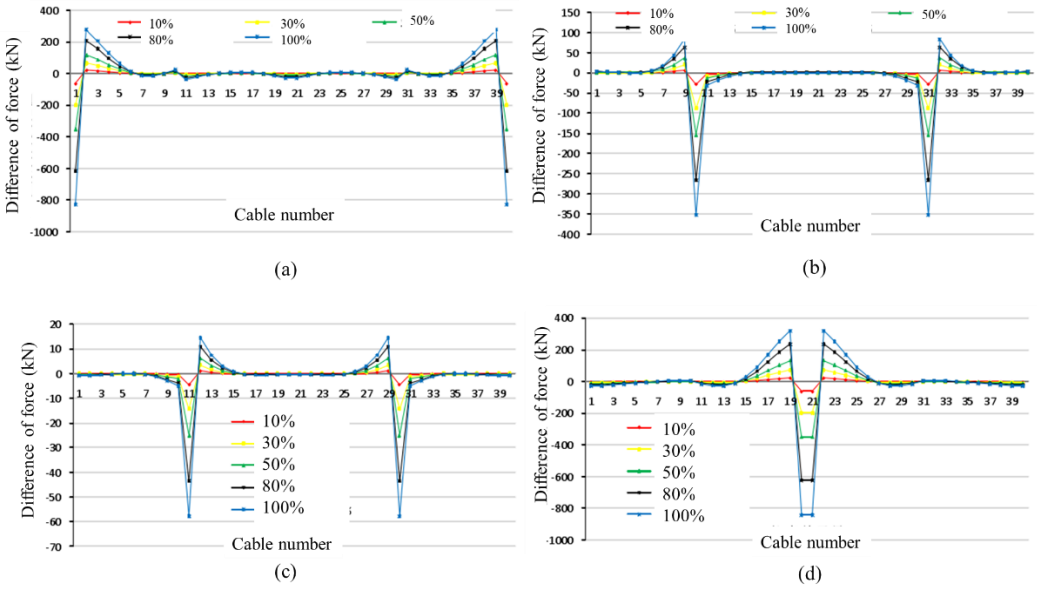

Fig. 2.24. The cable forces at different corrosion levels, and the corrosion cable located at (a) L1 and R1 cables, (b) L10 and R10 cables, (c) L11 and R11 cables, (d) L20 and R20 cables (Zhang, 2015)

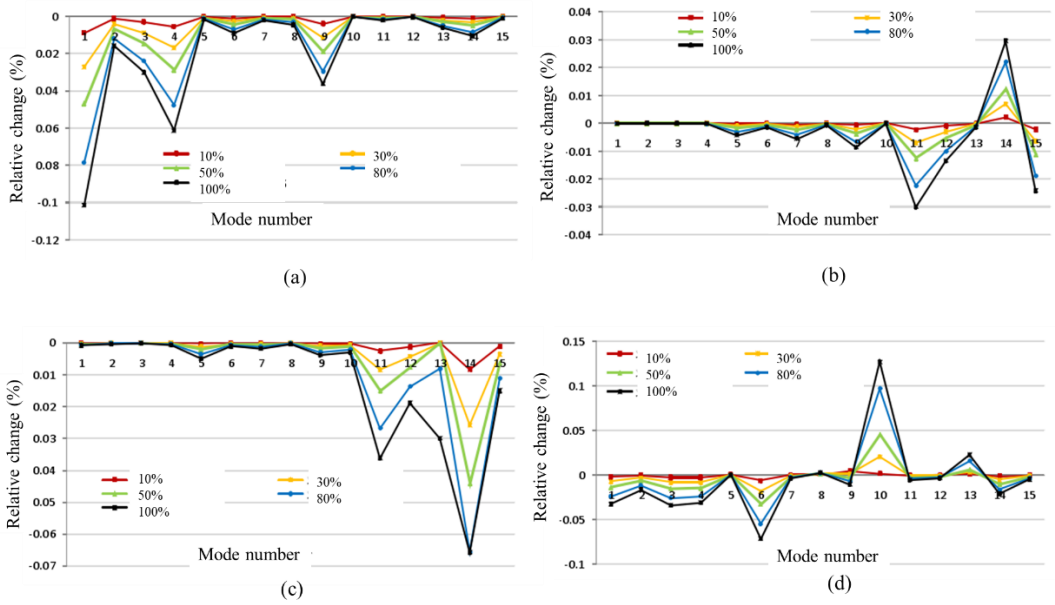

Fig. 2.25. The frequency relative change at different corrosion levels, and the corrosion cable located at (a) L1 and R1 cables, (b) L10 and R10 cables, (c) L11 and R11 cables, (d) L20 and R20 cables (Zhang, 2015)

2.5. Conclusion

This chapter has reviewed corrosion in stay cables of cable-stayed bridges. In particular, it has presented how corrosion affects the safety of the cable-stayed bridge, corrosion models proposed to predict the cable's corrosion morphology and corresponding time to achieve a certain damage, the methods to detect corrosion and previous studies that have investigated the influence of corrosion-induced cable damage on different bridges. Although two different corrosion distributions on the cable cross-sectional area are reported in the literature, uniform corrosion is normally chosen as a simplification for modelling purposes. Due to a lack of sufficient information to characterize the exposure environment of different cable-stayed bridges, published corrosion models which rely on specific lab experiments and measurements of a local environment cannot be applied to the service life prediction of damaged stay cables of any cable-stayed bridge. It is thus simpler to measure the corrosion rate and apply Faraday's law to predict the induced damage. When considering the wind load, the wind load coefficients in three directions are found to be the same for specific wind attack angles, regardless of the

Reynolds number. Previous studies on corrosion-induced damaged stay cables have focused on the structural behavior of the cable-stayed bridge in terms of deck deflection, cable stresses and natural frequencies when one or more cables rupture. In a study on the structural behavior of a medium-span cable-stayed bridge, the analysis focused on the effect of cables that were gradually corroded at different locations along the deck. However, lower number of studies focused on the static and dynamic responses of a long-span cable-stayed bridge due to corroded stay cables. The objective of this thesis research is to fill this gap by conducting numerical analysis, with the goal of detecting cable damage, which could be combined with non-destructive testing to address the mentioned shortcomings.

Chapter 3 - Modeling and validation

3.1. Introduction to Stonecutters Bridge

The Stonecutters Bridge was built to connect Nam Wan Kok and Tsing Yi Islands, spanning the Rambler Channel in Hong Kong. The construction of the Stonecutters Bridge began in 2004 and was completed in 2009, being the third longest cable-stayed bridge in the world, with a length of 1,596 m and a main span of 1,018 m. The geometrical details of the bridge are presented in Figure 3.1. The bridge has a unique slender twin-box deck, which is 53 m wide connected by cross girders that are spaced longitudinally 18 m center to center. The cross-section of the bridge deck is shown in Figure 3.2. The main span, which is made of steel, is entirely supported by cables, while the connections to the towers depend only on damping devices. The back spans, which have the same cross-section, are made of concrete and are supported by cables and end piers. An aerodynamics investigation and a wind tunnel test for the twin-box girder were carried out to ensure the aerodynamic stability of the deck (Kaji et al., 2010).

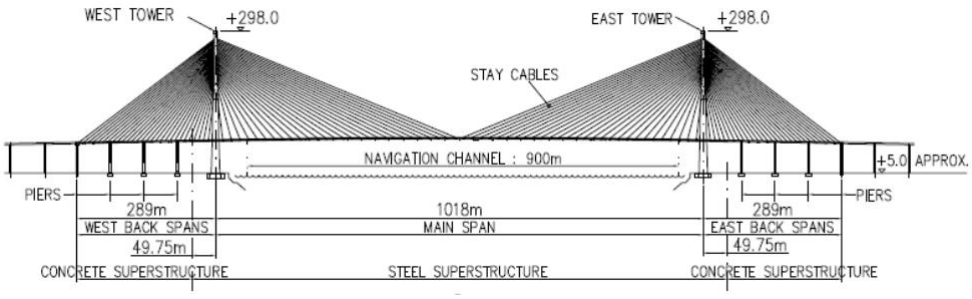

Fig. 3.1. Side view of Stonecutters cable-stayed bridge (Kaji et al., 2010).

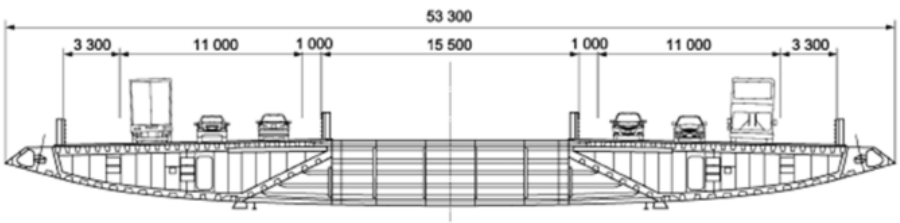

Fig. 3.2. Cross-section of the bridge deck (Kaji et al., 2010)

The independent towers are made of concrete, up to level +175 m, and a composition of concrete and steel from level +175 m to level +293 m. The towers begin as an oval section with 24 m across at the base, and end up as a circular cross section with 7 m in diameter at level +175 m. The upper towers were designed to have a steel outer skin and inner steel anchor boxes for the stay cables. The four end piers at one side consist of three single column piers and one twin-column portal structure. The piers and bearings on the tower work together to restrain the deck from moving laterally (Falbe-Hansen et al., 2017). Figure 3.3 shows the cross-section details of the Stonecutters Bridge towers and end piers.

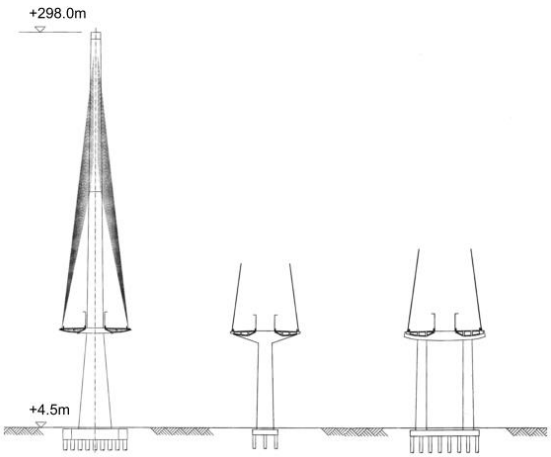

Fig. 3.3. Tower and end piers (Falbe-Hansen et al., 2017)

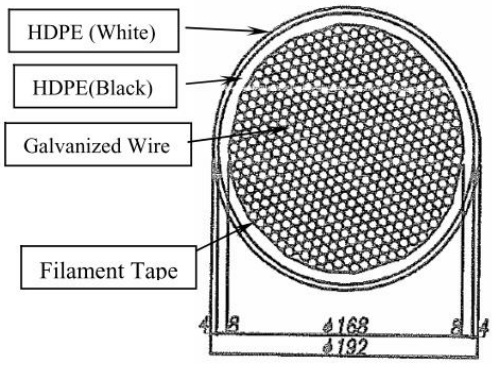

Fig. 3.4. Cross section of stay cable (Kaji et al., 2010)

The stay cables are arranged as a semi-fan configuration, with a total of 224 parallel stay cables supporting the deck at an interval of 18 m, 112 cables on each East and West

side of the deck. The stay cables are prefabricated parallel wire strands and designed as a compact form, which can reduce the area exposed to wind. The cross-section of the stay cables, which is shown in Figure 3.4, is comprised of 7-mm galvanized wires with a tensile strength of 1,770 MPa. The wires in the cables were prestressed in the factory and wrapped with filament tape. Then, the entire cable was covered with 10-mm thick HDPE coating (Kaji et al., 2010). The dimples on the HDPE coating of the cable can break the water flow caused by rain (rivulet) to keep the cable thinner and to counteract the rain-wind induced vibrations.

3.2. Modeling method

The finite element method (FEM) is widely used in the civil engineering field as an efficient method to solve complex structural systems. The FEM is applied in stress analysis, vibration analysis, displacement analysis and impact analysis, etc. It can provide a simplified way to simulate the structure through different types of elements. The FEM can also perform dynamics analysis, to estimate the structural responses caused by dynamic loads such as earthquakes and wind loadings, to analyze the dynamic characteristics of a structure. The results estimated by FEM can be very close to the real responses of the structure when using the appropriate elements, boundary conditions, loading conditions, material models and other structural factors for simulating the real conditions the structure is subjected to.

The finite element analysis software ABAQUS was used in this research to analyze the Stonecutters Cable-stayed Bridge. ABAQUS software is a powerful finite element program, suited for structural analysis, fluid dynamics analysis, and electromagnetic analysis. This software specializes in solving complicated solid mechanics, structural mechanics systems, simulating huge and complex models and dealing with non-linear problems. ABAQUS has a rich source of elements and material model libraries, which can simulate a variety of complicated geometrical shapes and most engineering

materials, such as different metals, reinforced concrete, and other geotechnical materials. It is also easy to build a structural model by defining the geometry of the parts, boundary conditions, material properties, loading conditions, etc. ABAQUS/CAE enables visualization when building the structural models and when meshing the structure. The analisys steps which contain two different major procedure types with several substeps in ABAQUS, are related to outputs regarding different loading and boundary conditions. When the job is finished and submitted, all the processed data and results are written into .dat file and .obd file, from which the response data can be extracted.

3.3. Scope of work

The primary target of using ABAQUS in this research is to build a 3D finite element model of the Stonecutters Cable-stayed Bridge to conduct static and dynamic analyses and study the effect of corrosion in the stay cables on the calculated response. The one-element cable method (OEC) is used in the cable model. When the bridge is built, the deflection and cables stresses are calculated when only gravity load is applied. Using the frequency step, the natural frequencies and the corresponding mode shapes can be determined. Next, the bridge's vibration response under a period of recorded wind load is simulated. Since there are different levels of corrosion and combination of corroded cables, the static load and dynamic load need to be applied to each scenario to determine the results.

3.4. Finite element model

3.4.1. The geometric properties of the bridge

Figure 3.5 shows different views of the finite element discretization of the Stonecutters Cable-stayed Bridge. The model created in ABAQUS is a fish-bone model, with its structure being very similar to the bone of a fish. This kind of model simplifies the structure and replaces each structural element with a one-dimensional finite element. The locations of the lumped masses are derived from the geometry of the gravity centers

and shear centers of the real structure.

The geometric details of the bridge are extracted from the available scientific literature by Kaji and Grady (2010), Falbe-hansen et al. (2004) and Falbe-hansen et al. (2017). Every part of the bridge model has the same dimensions as the real bridge. The total length of the bridge is 1,596 m, which consists of a main span of length of 1,018 m and two back spans of length of 289 m each. The intervals between the piers are 79.75 m, 70 m, 70 m and 69.25 m from the tower to the end pier, respectively. The cross girder connecting the twin deck has a length of 15.3 m. The elevation of the tower top and the centerline of the road are 298 m and 78.3 m, respectively. The spacing between the cable anchors of the main span is 18 m and for those of the side spans is 10 m.

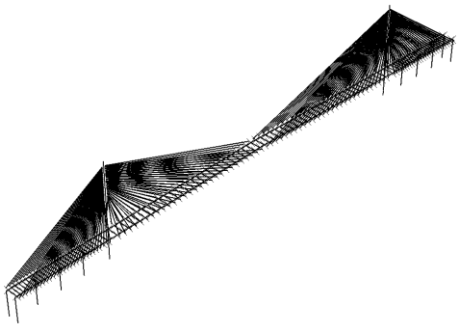

(a)

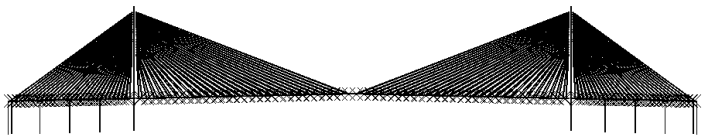

(b)

Fig. 3.5. ABAQUS model of Stonecutters cable-stayed bridge: (a) general view, (b) side view

Although the overall geometric dimensions of the bridge can be easily obtained from public resources, some detailed properties still need to be determined and assumed. Because the cross-sectional shape of the steel deck and concrete deck is irregular, some

geometric properties, tabulated in Table 3.1, were extracted with the help of the STAAD section analysis (Sabri, 2012). The warping constants for both decks were not used in the modelling, because the closed cross-section is considered stiff enough. The shear center and mass center, which are presented in Figure 3.6. (a) and (b), lie in different locations due to deck's unique shape.

Table 3.1. Geometric properties of the deck (Sabri, 2012)

		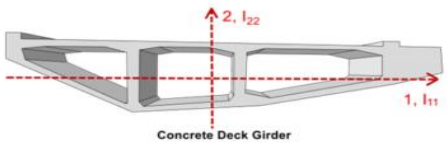	
Area (m^2)	1.05	Area (m^2)	19.27
I_{11} (m^4)	1.42	I_{11} (m^4)	20.68
I_{22} (m^4)	31.32	I_{22} (m^4)	609.64
J (m^4)	3.96	J (m^4)	60.69
Warping Constant (m^6)	15.78	Warping Constant (m^6)	N/A
I_{11}= Moment inertia about 1 axis, I_{22}= Moment of inertia about 2 axis J= Torsional moment of inertia,			

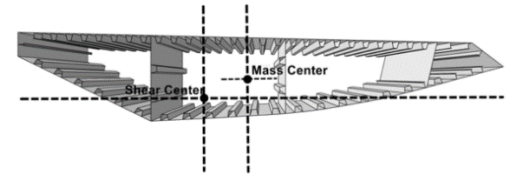

(a)

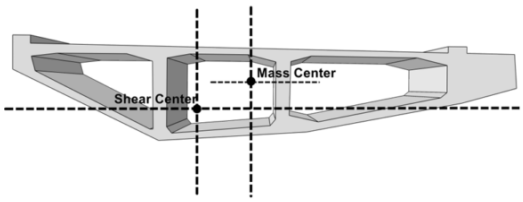

(b)

Fig. 3.6. Cross-section of the deck: (a) Steel deck, (b) Concrete deck (Sabri, 2012)

The stay cables are composed of 7-mm galvanized wires with the largest cable having a total of 451 wires (Kaji et al., 2010). However, the dimensions of the cables

are not the same throughout the bridge owing to diverse forms of load distribution among the cables. In order to easily identify the cables, they are named and numbered by specifying their location in the bridge. The x-direction and z-direction in ABAQUS represent the South and West directions in global coordinates, respectively (Figure 3.5(a)). The numbering and notation convention for each cable can be found in Figure 3.7. The point of origin is set at the mid-span. The west-side of the north and south decks are named as WN and WS, respectively. In the east side, the north deck and south deck are referred to as EN and ES, respectively. Cables are numbered sequentially from the first cable near the mid-span to the last cable on the back span. For instance, cable ES1 represents the first cable near the mid-span on the east side of the south deck. Table 3.2 provides the details of the 224 stay cables of the bridge.

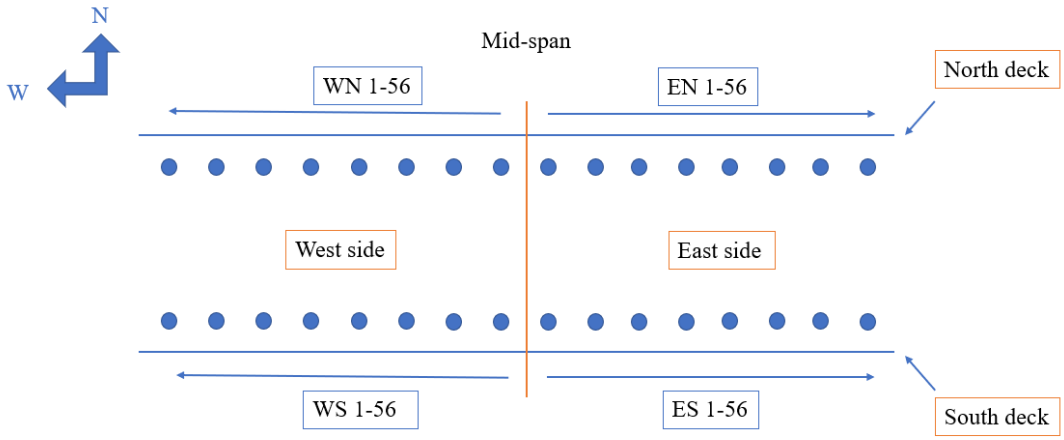

Fig. 3.7. Numbering and notation convention of cables in the plan view

Table 3.2. Dimensions of stay cables (Sabri, 2012)

Cable No.				Length of cable (m)	Horizontal length (m)	Angle of inclination rad	Angle of Inclination degrees	Diameter (m)	Area (m^2)
ES1	EN1	WN1	WS1	533	509	0.30	17.26	0.192	0.029
ES2	EN2	WN2	WS2	515.18	491.7	0.30	17.36	0.192	0.029
ES3	EN3	WN3	WS3	497.37	473.7	0.31	17.75	0.192	0.029
ES4	EN4	WN4	WS4	479.45	455.7	0.32	18.11	0.192	0.029
ES5	EN5	WN5	WS5	461.7	437.7	0.32	18.56	0.182	0.026
ES6	EN6	WN6	WS6	444	419.7	0.33	19.04	0.182	0.026
ES7	EN7	WN7	WS7	426.2	401.7	0.34	19.52	0.182	0.026
ES8	EN8	WN8	WS8	408.6	383.7	0.35	20.11	0.182	0.026
ES9	EN9	WN9	WS9	391.1	365.7	0.36	20.76	0.175	0.024
ES10	EN10	WN10	WS10	373.44	347.7	0.37	21.40	0.175	0.024
ES11	EN11	WN11	WS11	356	329.7	0.39	22.16	0.175	0.024
ES12	EN12	WN12	WS12	338.74	311.7	0.40	23.05	0.175	0.024
ES13	EN13	WN13	WS13	321.39	293.7	0.42	23.96	0.170	0.023
ES14	EN14	WN14	WS14	304.3	275.7	0.44	25.04	0.170	0.023
ES15	EN15	WN15	WS15	287.37	257.7	0.46	26.27	0.170	0.023
ES16	EN16	WN16	WS16	270.48	239.7	0.48	27.60	0.170	0.023
ES17	EN17	WN17	WS17	253.92	221.7	0.51	29.18	0.160	0.020
ES18	EN18	WN18	WS18	237.6	203.7	0.54	30.98	0.160	0.020
ES19	EN19	WN19	WS19	221.49	185.7	0.58	33.03	0.160	0.020
ES20	EN20	WN20	WS20	205.85	167.7	0.62	35.45	0.160	0.020
ES21	EN21	WN21	WS21	190.7	149.7	0.67	38.28	0.144	0.016
ES22	EN22	WN22	WS22	176	131.7	0.73	41.56	0.144	0.016
ES23	EN23	WN23	WS23	162.2	113.7	0.79	45.49	0.144	0.016
ES24	EN24	WN24	WS24	149.3	95.7	0.88	50.13	0.144	0.016
ES25	EN25	WN25	WS25	137.7	77.7	0.97	55.65	0.113	0.010
ES26	EN26	WN26	WS26	124.34	59.7	1.07	61.31	0.113	0.010
ES27	EN27	WN27	WS27	114.4	41.7	1.20	68.62	0.113	0.010
ES28	EN28	WN28	WS28	106.8	23.7	1.35	77.18	0.113	0.010
ES29	EN29	WN29	WS29	107.4	19.7	1.39	79.43	0.113	0.010
ES30	EN30	WN30	WS30	113.8	29.7	1.31	74.87	0.113	0.010
ES31	EN31	WN31	WS31	121	39.7	1.24	70.85	0.113	0.010
ES32	EN32	WN32	WS32	130.5	49.75	1.18	67.59	0.113	0.010
ES33	EN33	WN33	WS33	137	59.75	1.12	64.14	0.144	0.016
ES34	EN34	WN34	WS34	144.3	69.75	1.07	61.09	0.144	0.016
ES35	EN35	WN35	WS35	151.8	79.75	1.02	58.31	0.144	0.016
ES36	EN36	WN36	WS36	159.8	89.75	0.97	55.83	0.144	0.016
ES37	EN37	WN37	WS37	168	99.75	0.94	53.58	0.160	0.020
ES38	EN38	WN38	WS38	176.4	109.75	0.90	51.53	0.160	0.020
ES39	EN39	WN39	WS39	185	119.75	0.87	49.66	0.160	0.020
ES40	EN40	WN40	WS40	194	129.75	0.84	48.02	0.160	0.020
ES41	EN41	WN41	WS41	203.1	139.75	0.81	46.52	0.170	0.023
ES42	EN42	WN42	WS42	212.4	149.75	0.79	45.17	0.170	0.023
ES43	EN43	WN43	WS43	221.7	159.75	0.77	43.90	0.170	0.023
ES44	EN44	WN44	WS44	231.2	169.75	0.75	42.76	0.170	0.023
ES45	EN45	WN45	WS45	240.8	179.75	0.73	41.71	0.175	0.024
ES46	EN46	WN46	WS46	250.45	189.75	0.71	40.74	0.175	0.024
ES47	EN47	WN47	WS47	260.2	199.75	0.70	39.85	0.175	0.024
ES48	EN48	WN48	WS48	270	209.75	0.68	39.03	0.175	0.024
ES49	EN49	WN49	WS49	279.88	219.75	0.67	38.26	0.182	0.026
ES50	EN50	WN50	WS50	289.8	229.75	0.66	37.55	0.182	0.026
ES51	EN51	WN51	WS51	299.84	239.75	0.64	36.91	0.182	0.026
ES52	EN52	WN52	WS52	309.83	249.75	0.63	36.28	0.182	0.026
ES53	EN53	WN53	WS53	319.86	259.75	0.62	35.70	0.192	0.029
ES54	EN54	WN54	WS54	330.1	269.75	0.61	35.20	0.192	0.029
ES55	EN55	WN55	WS55	340.2	279.75	0.61	34.68	0.192	0.029
ES56	EN56	WN56	WS56	350.3	289.75	0.60	34.19	0.192	0.029

3.4.2. Element types

ABAQUS provides a variety of elements to simulate various parts in a real structure. These elements are defined according to their degrees of freedom, numbers of nodes and behavior during loading. In this bridge model, B31, T3D3, RB3D2, and MPC

elements were utilized to assemble the fish-bone model of the bridge.

The B31 element is a 3-D elastic beam element with two nodes and 6 degrees of freedom at each end. ABAQUS assumes the transverse shear behavior of the B31 element as linear elastic with a fixed modulus, and therefore independent of the response of the beam section to axial and bending deformation. The B31 elements are used for the twin decks, the cross girders connecting the decks, the towers and the piers.

Normally, ABAQUS can use the defined profile properties and defined section material to calculate the stiffness properties for the section of the element. It is easy to define the height, depth or thickness of hollow sections for normal shapes. However, the sectional properties of the deck section cannot be defined precisely in the program due to its irregular shape, thereby it is necessary to define a "generalized" profile to calculate them. ABAQUS uses the set of geometric properties listed in Table 3.1, as created in a "generalized" profile, to define the cross section of the twin decks. Although the "generalized" profile does not represent the real cross section, it allows for linear and nonlinear responses (Feng, 2015). In addition, the defined hollow circle section was assigned to represent the section of the towers, and the rectangular hollow section was associated to piers at the back spans.

The T3D3 element with 3 nodes and 3 degrees of freedom per node is suitable to simulate slender structures, which can only transfer axial loads and do not have bending and shear stiffness. Therefore, the T3D3 element is a good tool to simulate stay cables. This 3-node element is usually used for modelling curved prestressed cables in structures or pipelines in the offshore industry. In this model, the T3D3 element was defined as a tension-only member through its material properties and was assigned a pre-tension load according to calculations, to meet the requirements of real tendons and avoid numerical singularities and convergence problems when the elements are subjected to large-displacement analysis. The applied pre-tension loads help to develop some transverse stiffness to the cables. Details of the pre-tension loads applied to the cables can be found in Appendix A.

The RB3D2 element is a 2-node rigid beam element which serves as a stiff connection to the bridge. The rigid element can link two bodies and make them move together. Due to the advantage of no calculation for the element itself, the element's motion is determined only by the 6 degrees of freedom of the reference points (ABAQUS Inc. 2012). In this model, the deck section is an irregular section as seen in Section 3.4.2., and the shear center and mass center are not in the same location, as illustrated in Figure 3.6 (a) and (b). Hence, the RB3D2 element is used as a rigid connector for the mass and shear centers of the deck. The detailed arrangement of the RB3D2 element between the shear center and mass center is shown in Figure 3.8.

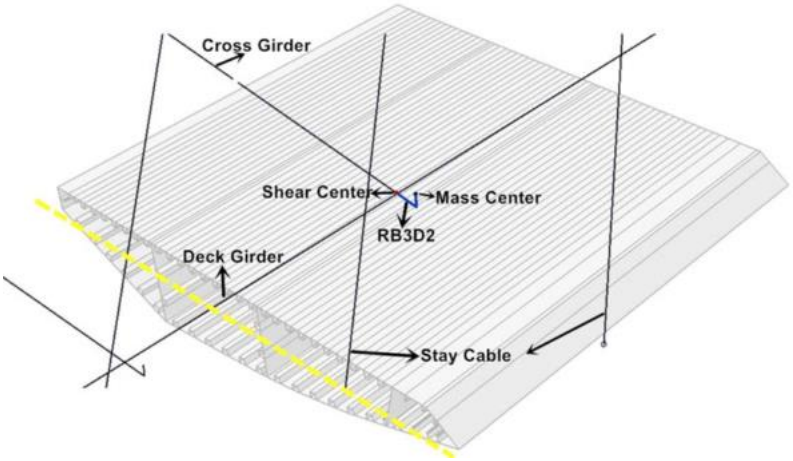

Fig. 3.8. L-shape arrangement of RB3D2 element (Feng, 2015)

The multi-point constraints (MPC) beams in ABAQUS are used to constrain the displacement and rotation of a first node to that of a second node, to ensure that the deck elements can move as an ensemble. The first node, also known as the slave node, follows the movement of the degrees of freedom of the master node, which is the second node. In the bridge model, the MPC beam constraints are widely used as anchor boxes on the upper towers and the edge of the decks. The MPC beam constraints can connect the nodes of stay cables and tower center as shown in Figure 3.9 (a). Stay cables on each side of the tower have two separate MPC constraints that connect them to the towers. The MPC beam is shown as the red component in Figure 3.9 (a). There is a total of 4 cables, 2 on each side, connecting to the same elevation point on the tower. In

addition, the cables are connected by MPC beam constraints to the edge of the deck, as demonstrated in Figure 3.9 (b). The MPC beam traverses the longitudinal deck element from the cross-girder element to the cable anchor location, as shown by the red dashed line in Figure 3.9 (b). The length of the MPC beam is the same as the width of the deck.

Under this circumstance, the stay cables can have an accurate response when coupled with the towers and decks, especially when performing dynamic analysis to investigate vibration mode shapes. The pre-tension loads that are defined in the stay cables can be directly transferred to the towers and decks.

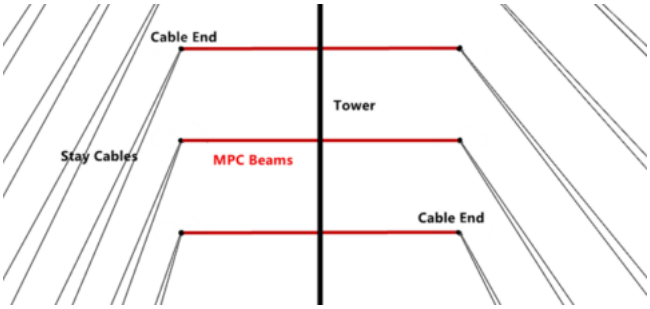

(a)

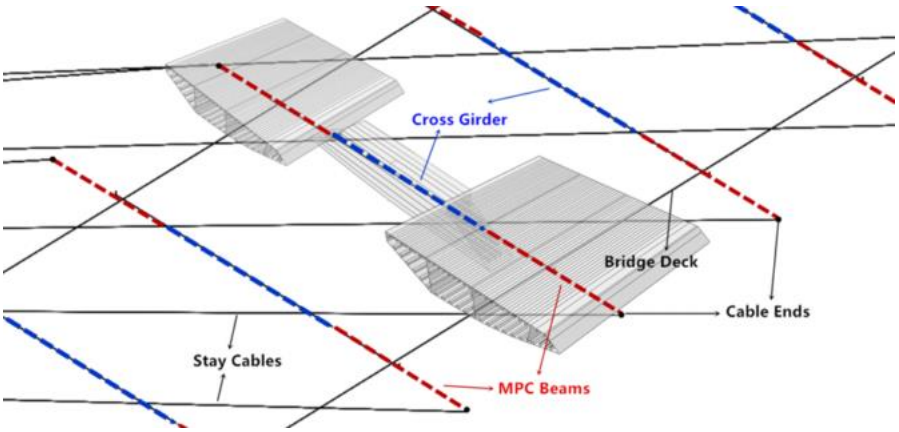

(b)

Fig. 3.9. Arrangement of MPC: (a) on the towers, (b) on the deck (Feng, 2015)

3.4.3. Material properties

In this bridge model, the main materials used for the Stonecutters Cable-stayed Bridge are reinforced concrete for the back spans, towers, piers and side cross girders, steel for the main span and high-strength steel for the stay cables. The material properties are

defined in the material section in ABAQUS and listed in Table 3.3.

Table 3.3. Material properties in the bridge model (Feng, 2015)

Material	Structural Members	Mass Density (kg/m^3)	Young's Modulus (GPa)	Poisson's Ratio
Reinforced concrete	Towers, Piers, Back-span, Side Cross girders	2400	60	0.2
Steel/S420M	Centre Deck, Cross Girders	7850	205	0.3
Cable steel	Stay Cables	7800	200	0.28

The actual cables are not trusses as defined in this model, and the cable sag is associated with cable nonlinearities. The most common approach to idealize the cable behavior by truss elements is to modify the modulus of elasticity, which can resist the deflection against the cable force and support conditions. The idealized modulus of elasticity, E_{eq}^{truss} of the cable is calculated from the Ernst equation (Ernst, 1965) mentioned in section 2.3.1. For the convenience of the reader it is rewritten in Eq. (3.1):

$$E_{eq}^{truss} = \frac{E^{cable}}{1+\frac{(\rho g L_x)^2}{12\sigma^3}E^{cable}} \tag{3.1}$$

where: E_{eq}^{truss} is the equivalent truss element modulus of elasticity,

E_{cable} is the actual cable modulus of elasticity,

ρ is the cable material density,

g is the acceleration due to gravity

L_x is the horizontal projected length of the cable

σ is the cable pre-stress

The mass properties for the deck section are obtained with the help of STAAD's section wizard, and they are listed in Table 3.4 (a) and (b) for the steel and concrete decks, respectively.

Table 3.4. Mass properties of deck cross-section: (a) Steel deck, (b) Concrete deck (Feng, 2015)

Moment of inertia about the mass center for steel deck (kg*m2)	
I_{xx}	5.81E+06
I_{yy}	1.16E+07
I_{zz}	6.32E+06
I_{xy}	3.59E+04
I_{yz}	-0.114
I_{zx}	1.51
Total mass (kg)	204883.28

(a)

Moment of inertia about the mass center for concrete deck (kg*m2)	
I_{xx}	3.89E+06
I_{yy}	1.16E+07
I_{zz}	1.36E+06
I_{xy}	-1.46E+04
I_{yz}	0
I_{zx}	-7.45E-09
Total mass (kg)	412241.13

(b)

3.4.4. Boundary conditions

Boundary conditions (BC) are constraints that are necessary for solutions of a boundary value problem. In an FEM model, the BC consist of fixed ends, hinges or rollers and are determined by restraining certain degrees of freedom to simulate the real constraint conditions for the structure.

In the bridge model, the back spans, piers and towers are assumed to be fixed in the model. As seen in Figure 3.10, the tower, three-side piers and two-end piers are fixed to the ground. Besides, the piers and back spans are fixed according to the following considerations. In the bridge design, the back spans are located at the ground and supported by several firm piers. The spacings of cable anchorages and cross girders

are smaller than those of the steel span. In addition, the reinforced concrete deck of the back spans can provide stiffer properties and acts as a stiff anchor balancing the weight and load of the main span. It is for these reasons that the back span can be assumed to be fixed in this study.

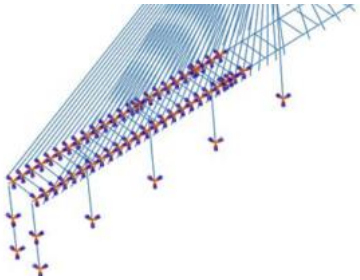

Fig. 3.10. The boundary conditions of the back span

3.5. Analysis steps

3.5.1. Static response

When conducting the analysis in ABAQUS, the first step is to determine the static response of this model when only gravity load is applied. ABAQUS can provide various types of calculation steps depending on the results needed. For the static results, the 'static general' type was created. The results come from the output request section. In this thesis, the deflection of the main span and the stress of each cable are the main indicators to reflect the influence of corroded cables. Therefore, the element set of decks corresponding with vertical displacement output and cables corresponding with stress and strain components were selected in the static step.

3.5.2. Dynamic response

The dynamic response of the bridge consists of the natural frequency investigation and the wind load-induced response. The natural frequencies can reflect the vulnerable frequencies of the structure, especially when the applied dynamic load has the same frequency. The wind load-induced response mainly presents the time-history displacement of the mid-span and towers.

The ‘frequency’ step was created to calculate the first 30 natural frequencies and their corresponding mode shapes. The subspace iteration method was chosen for this. This method has the advantage of achieving rapid convergence to eigenvectors in full space. The mode shapes can be viewed in the *.obd* file after finishing the calculation. The first ten vibration modes are the most important for dynamic analysis, which include lateral, vertical, torsional or coupled vibration modes of the decks or towers.

In order to investigate the structure under real load conditions, wind-induced loading was considered in this study. The wind load was calculated from a period of recorded wind data, which was collected through an anemometer installed by the SUNLab team at the solar panels research site located on the flat roof of the Mann Parking Building at the University of Ottawa. The solar panel is shown in Figure 3.11. The wind speed and wind direction can be recorded through the sensors installed in the solar panel.

Fig. 3.11. The solar panel and sensors (Mehranfar, 2014)

The sensors can record wind speeds and incidence angle in a period of time. Data corresponding to 500 seconds, which was collected in February 2014, are shown in Figure 3.12. In this study, the angle of wind incidence has been neglected as a simplification. The wind was assumed to have 0 degrees of incidence to the deck. The maximum velocity among the 500 seconds wind data is 8.20 m/s, and the mean velocity is 4.15 m/s (Figures 3.12 (a) and (b)), which are mild values for the Hong Kong area where the Stonecutters Bridge is. The bridge is located in an open channel and exposed

to high wind velocity. Therefore, the measured wind data was increased five times, among which the maximum wind speed becomes 41 m/s and mean wind speed becomes 20.75 m/s (Figure 3.12 (c)), to simulate the critical wind speed at the bridge site. The modified maximum wind speed is close to the natural wind environment for an extreme wind storm (Feng, 2015).

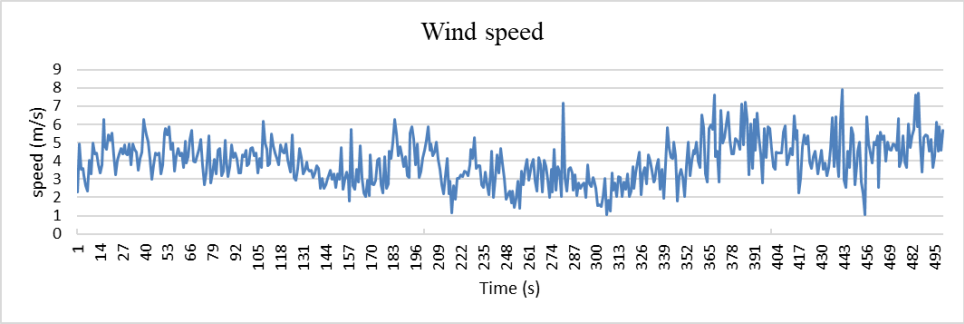

(a)

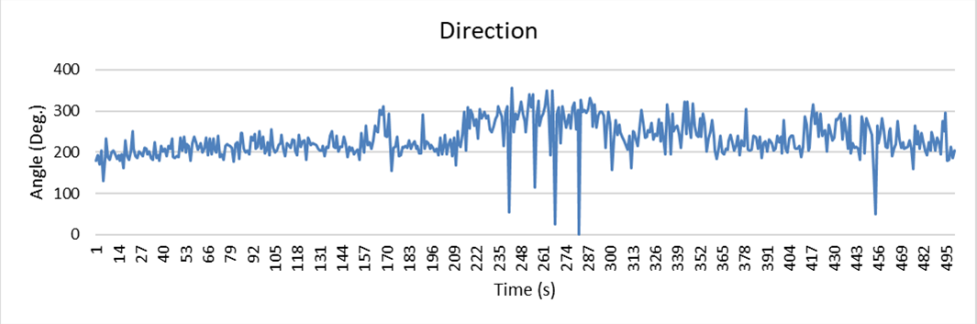

(b)

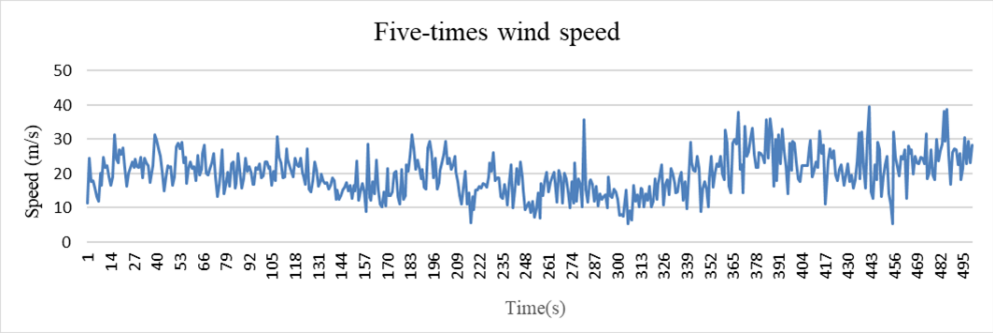

(c)

Fig. 3.12. Wind velocity and direction record: (a) record of wind speed, (b) record of wind direction, (c) record of five-times wind speed (Mehranfar, 2014)

To calculate the wind load, the quasi-steady mean wind load equations proposed

by Scanlan (1996) were used to determine the 500 s time-history wind load. The equations are listed below from Eqs. (3.2) to (3.4). The wind load can be divided into three equivalent components: the drag load D_m, the lift load L_m and the moment M_m.

$$D_m = \frac{1}{2}\rho\overline{U}^2 C_D BL(\alpha) \tag{3.2}$$

$$L_m = \frac{1}{2}\rho\overline{U}^2 C_L BL(\alpha) \tag{3.3}$$

$$M_m = \frac{1}{2}\rho\overline{U}^2 C_M B^2 L(\alpha) \tag{3.4}$$

where: ρ is the density of air, 1.225 kg/m^3

$\overline{U}$ is the mean wind velocity (in this study, the collected wind speed was used as $\overline{U}$ as a simplification).

C_D, C_L, C_M are drag, lift and moment coefficients, respectively.

B, L are the bridge deck width and bridge length, respectively

α is the attack angle of the wind (here it is assumed to be 0 degrees)

In this analysis step, the three components of wind load are applied along both bridge decks. In this step, a 'model dynamic' type was created with a 500-seconds time period. The displacement of the decks and the stress components of the cables were defined in the field output. Then, the time-history response of the mid-span and cables was extracted.

After extracting the time domain data, the Fast Fourier Transform (FFT) method was used to transform the time-domain data to frequency-domain data. The power distribution of the discrete frequency components is generated by means of the Power Spectrum Density (PSD) method. It is clear to observe the power variance with respect to the frequency, and the structure will have largest response at the frequency with the highest power density.

The time domain of the displacement of the mid-span and both towers was regarded as a signal that contains dynamic characteristics. In order to investigate the frequency characteristics, PSD in Matlab was used as a tool to process the signals. The code can be found in the Appendix C. The frequency domain diagram can present the critical

frequency of vertical, lateral and torsional responses of the deck and horizontal displacement of tower under the wind load.

3.6. Bridge model validation

3.6.1. Overview

The bridge model validation is an important step, before proceeding with further analysis. Only if the finite element model of the bridge has a similar response to the real structure, the model can be considered as valid, and the results from the model are acceptable. The differences are either from the modeling errors resulting from simplified assumptions, or from the parameter errors owing to the uncertainties in material and geometric properties.

The validation of the finite element model of a bridge is usually performed by comparing the measured data, which is usually obtained from a structural monitoring system, with the model's results. The measured natural frequency of the Stonecutters cable-stayed bridge has not been released by the Highways Department of Hong Kong until present. Therefore, the natural frequencies of the bridge, which were obtained from another finite element model built by the engineer of the Hong Kong Highways Department, Michael C. H. Hui, are used as a reference case (Hui et al., 2006). In this research, the published data by Hui et al. (2006) is used as a reference model to perform the validation.

3.6.2. The natural frequency of the structure

The dynamic response of the structure is determined by the equation of motion for the system (see Eq. (3.5)). The main structural characteristics of a vibrating system are the mass, stiffness and damping properties, which determine the stiffness, inertia and damping forces of the system by solving the equation of motion described in Eq. (3.5). The solution of the equation is a series of eigenvalues. The eigenvalues are the square of the angular frequencies with the units of radian per time. The natural frequencies are the angular frequencies when there is no damping and no external force in the system.

The natural frequency is the frequency when the structure oscillates for a certain period without any driving or damping force. The corresponding vibrations are called natural vibration modes.

$$[M]\{\ddot{x}\} + [C]\{\dot{x}\} + [K]\{x\} = \{f(x)\} \quad (3.5)$$

where: [M] is the mass matrix of the structure

[C] is the damping ratio matrix of the structure

[K] is the stiffness matrix of the structure

x is the displacement of the structure

f(x) is the external force in terms of displacement x

A series of natural frequencies are arranged from low to high. The lowest frequency means a long period, low acceleration and low energy. It is easy to excite the system with low energy, therefore the structure easily vibrates at a certain mode of low frequency. The first ten natural frequencies are the primary values the analysis is focusing on.

3.6.3. The comparison of published data and model results

With the frequency step in ABAQUS, the natural frequency of the bridge can be determined. The 3D finite element model can provide a complete representation of the vibration modes. The first ten vibration modes and the corresponding natural frequencies of the FEM of the Stonecutters Cable-stayed Bridge are illustrated in Figures 3.13-3.22.

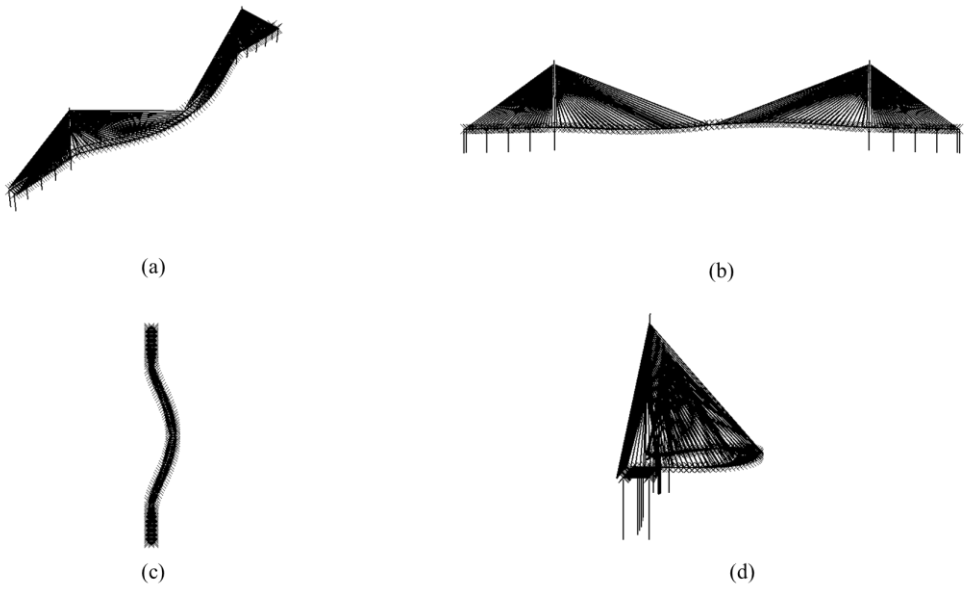

Fig. 3.13. 1st mode shape, f=0.14491 Hz, (a) general view, (b) front view, (c) plan view, (d) side view

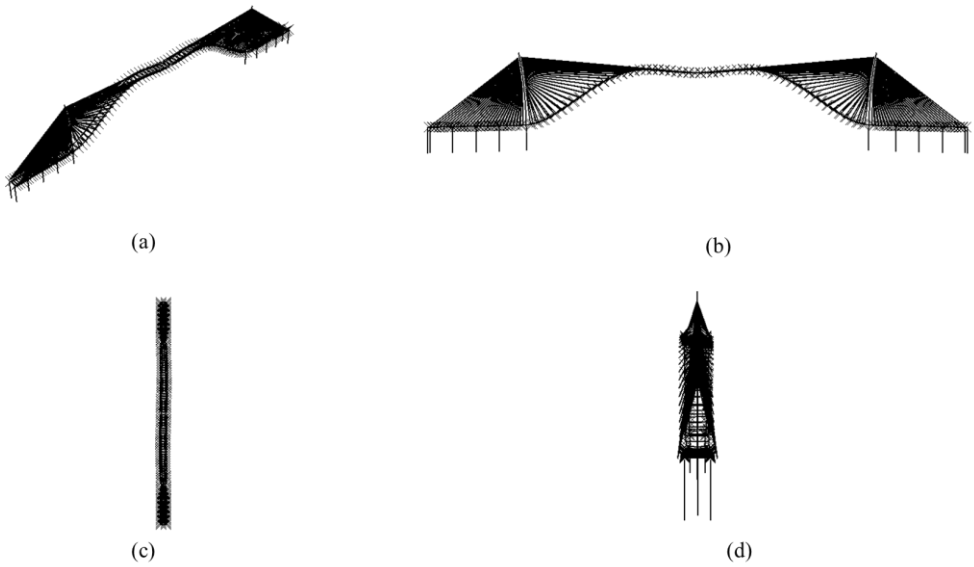

Fig. 3.14. 2nd mode shape, f=0.17225 Hz, (a) general view, (b) front view, (c) plan view, (d) side view

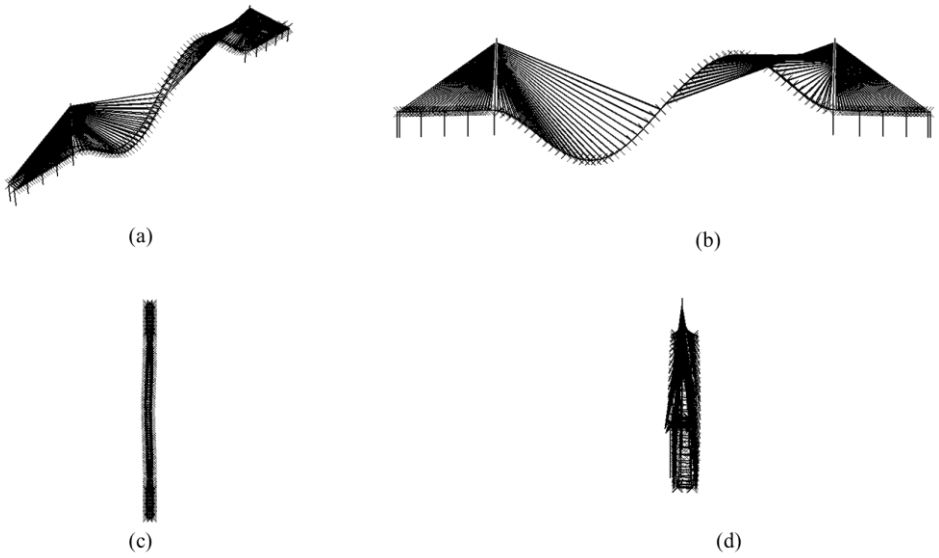

Fig. 3.15. 3rd mode shape, f=0.19197 Hz, (a) general view, (b) front view, (c) plan view, (d) side view

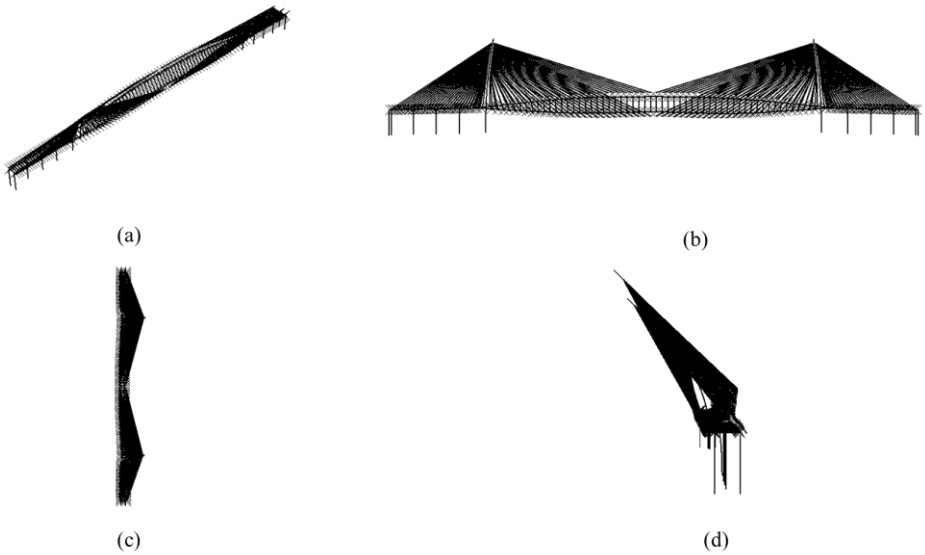

Fig. 3.16. 4th mode shape, f=0.25343 Hz, (a) general view, (b) front view, (c) plan view, (d) side view

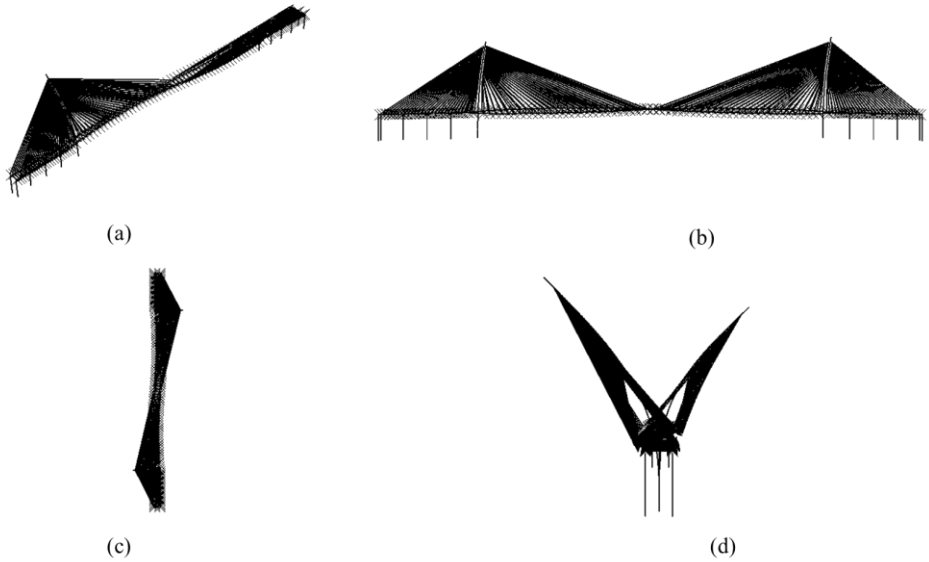

Fig. 3.17. 5th mode shape, f=0.25621 Hz, (a) general view, (b) front view, (c) plan view, (d) side view

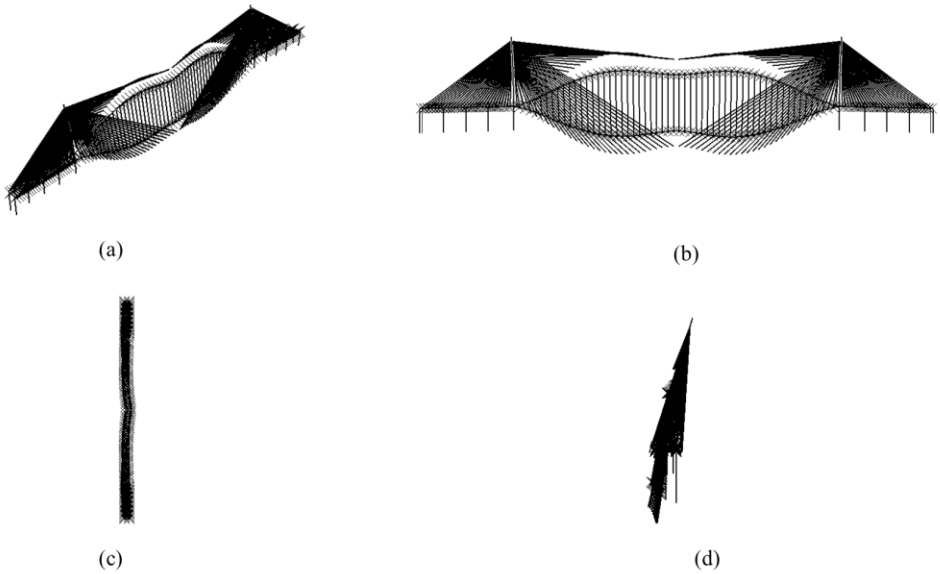

Fig. 3.18. 6th mode shape, f=0.32384 Hz, (a) general view, (b) front view, (c) plan view, (d) side view

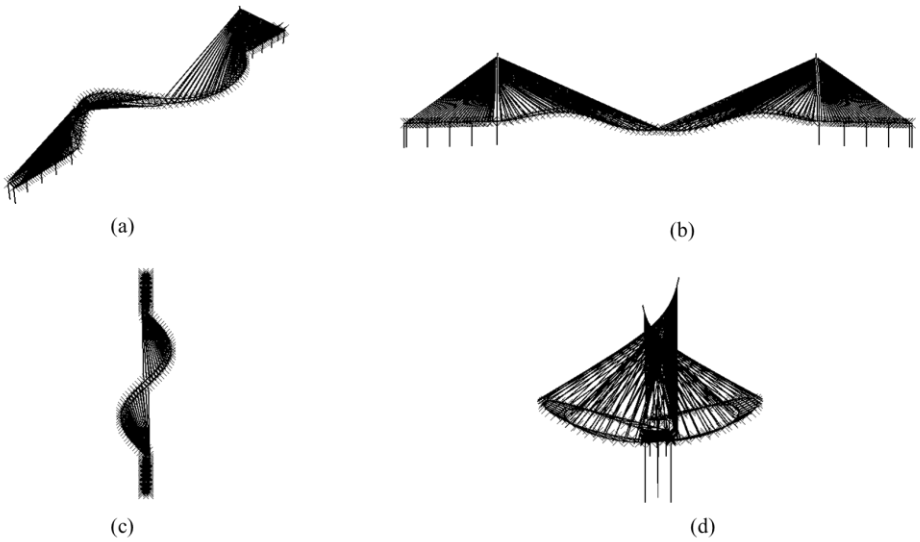

Fig. 3.19. 7th mode shape, f=0.3583 Hz, (a) general view, (b) front view, (c) plan view, (d) side view

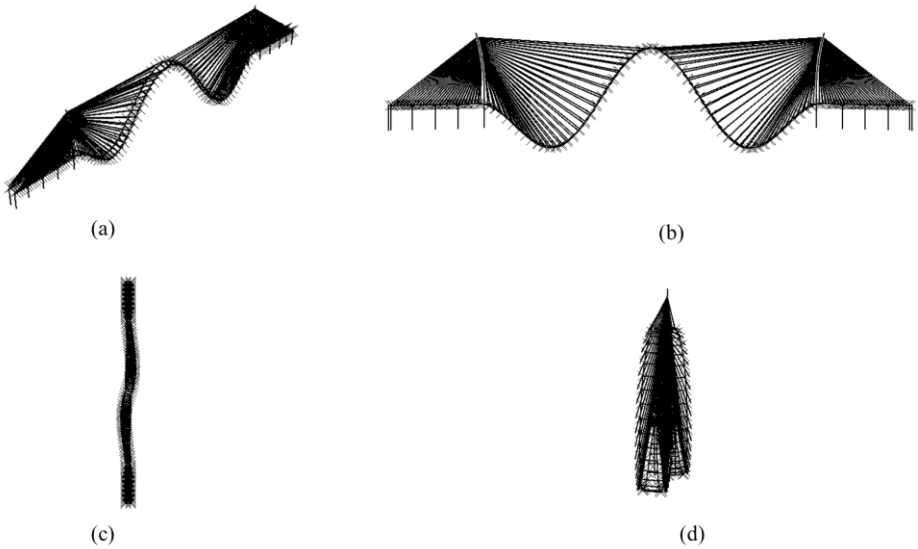

Fig. 3.20. 8th mode shape, f=0.38733 Hz, (a) general view, (b) front view, (c) plan view, (d) side view

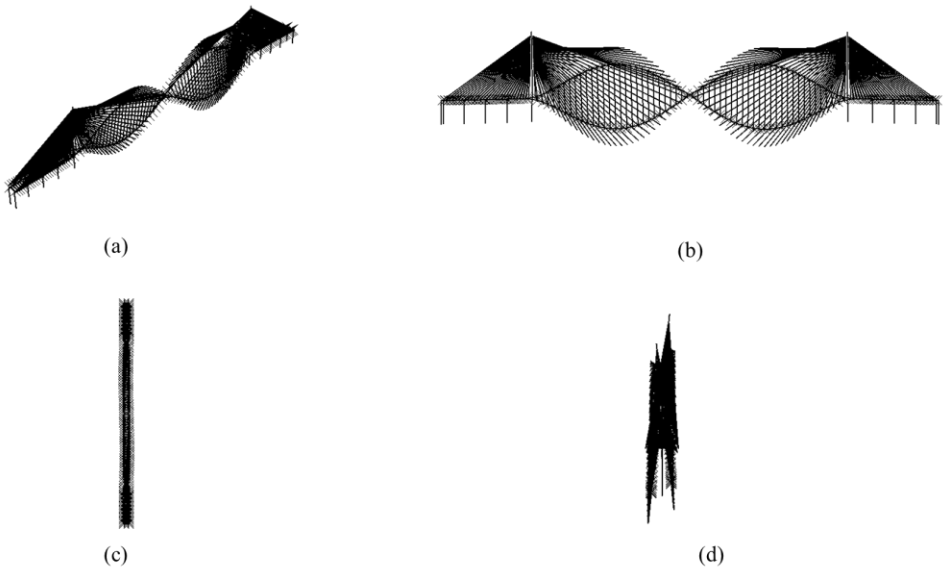

Fig. 3.21. 9th mode shape, f=0.42366 Hz, (a) general view, (b) front view, (c) plan view, (d) side view

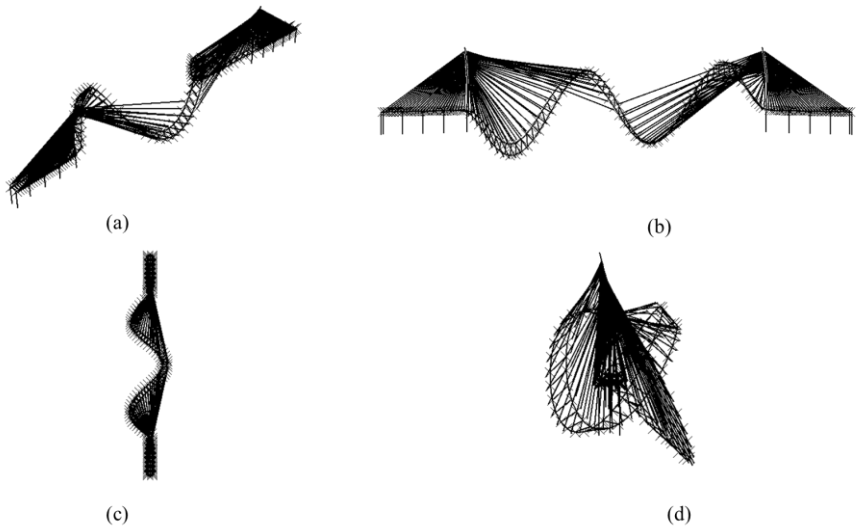

Fig. 3.22. 10th mode shape, f=0.5811 Hz, (a) general view, (b) front view, (c) plan view, (d) side view

Figures 3.13 to 3.22 present the four views of each vibration mode (general, front, plan and side views). The natural frequencies vary from 0.145 Hz to 0.581 Hz. Among the ten mode shapes, the decks vibrate prior to the towers, and the decks' movement starts from only horizontal or vertical or twist movement to coupled twist and horizontal movements. The lowest natural frequency of 0.145 Hz corresponding to the first mode being the first horizontal bending motion of the bridge deck (Figure 3.13) which is almost symmetric. The second horizontal bending motion of the bridge deck,

corresponding to the 7th mode shape as illustrated in Figure 3.19, which is an asymmetric mode at a natural frequency of 0.358 Hz. The first two natural frequencies for the lateral bending modes of the bridge deck are well separated. The first vertical motion of the bridge deck is symmetric at a natural frequency of 0.172 Hz (2nd mode shape in Figure 3.14), and the second one is asymmetric at a frequency of 0.192 Hz (3rd mode shape in Figure 3.15). Unlike the horizontal vibration motion, the first two frequencies for the vertical motion of the bridge deck are quite close. The lateral motion dominates the vibration of the towers. The first lateral motion for the towers is symmetric at a natural frequency of 0.253 Hz (4th mode shape in Figure 3.16). The towers move in opposite direction at a frequency of 0.256 Hz (5th mode in Figure 3.17). The early occurrence of tower vibration modes may imply that the towers used in the bridge are relatively slender (Zhu, 2014). The first torsional mode dominates the deck in symmetric motion at a natural frequency of 0.324 Hz (6th mode shape in Figure 3.18). The second one is an asymmetric vibration mode of the main deck at a frequency of 0.424 Hz (9th mode shape in Figure 3.21). The first two torsional modes of the bridge deck are not so close.

The widely accepted natural frequency data published by Hui et al. (2006) is compared with the results from this study in Tables 3.5-3.6.

Table 3.5. Comparison of natural frequencies and mode shapes

Published natural frequency by Hui, et al.			Natural Frequency from finite element model		
Mode No.	Natural Frequency (Hz)	Mode shape	Mode No.	Natural Frequency (Hz)	Mode shape
1	0.145	S-H-deck	1	0.145	S-H-deck
2	0.19	A-H-towers	2	0.172	S-V-deck
3	0.197	S-H-towers	3	0.192	A-V-deck
4	0.201	S-V-deck	4	0.253	S-H-tower
5	0.246	A-V-deck	5	0.256	A-H-tower
6	0.302	A-V-deck	6	0.324	S-T-deck
7	0.311	S-V-deck	7	0.358	A-H-deck
8	0.361	A-H-deck	8	0.387	S-V-deck
9	0.376	A-V-deck	9	0.424	A-T-deck
10	0.422	S-V-deck	10	0.581	A-T-V-deck

S : symmetry, A : asymmetry, H : horizontal, V : vertical, T : torsion

According to the data published by Hui et al. (2006), the mode shapes are different from the results of this finite element model, except the first mode shape, in which both sets of results have the same dominant mode shape with symmetric horizontal deck motion. The second horizontal motion of vibration of the bridge deck happens at the 8th mode at a natural frequency of 0.361 Hz. The first two natural frequencies in horizontal motion of the decks are relatively separate. In the investigation of Hui et al. (2006), the towers have bending movement at a lower frequency compared to this finite element model. However, the two lateral modes dominating the towers' movement at natural frequencies of 0.19 Hz and 0.197 Hz, respectively, are close and have an early occurrence as the results of the current FE model. The first two vertical modes dominate the main deck movement at natural frequencies of 0.201 Hz and 0.246 Hz, respectively. The first two natural frequencies in the vertical modes of vibration are quite close, which is also the same as the result from the current FE bridge model. However, the torsional motion of vibration is not observed within the first ten mode shapes in the results reported by Hui et al. (2006).

Table 3.6. Difference between published data and current bridge finite element model

	Published natural frequency by Hui, et al. (2015)	Natural Frequency from finite element model	
Mode No.	Natural Frequency (Hz)	Natural Frequency (Hz)	Difference
1	0.145	0.145	0.06%
2	0.19	0.172	9.34%
3	0.197	0.192	2.55%
4	0.201	0.253	-26.08%
5	0.246	0.256	-4.15%
6	0.302	0.324	-7.23%
7	0.311	0.358	-15.21%
8	0.361	0.387	-7.29%
9	0.376	0.424	-12.68%
10	0.422	0.581	-37.70%

Table 3.6 tabulates the natural frequencies for the first ten mode shapes resulting

from Hui et al. (2006) and the current investigation, as well as the difference between both sets of numerical data. From the results presented in Table 3.6, it is noted that the natural frequencies associated with the first ten modes are not so different from both sets of results (within 15% difference), except for the fourth and tenth modes, wherein the frequencies obtained by the current model are slightly higher. Overall, the differences in natural frequencies range from 0.06% to 37.7%. The first mode has the closest frequency to the published one, which means that the most fundamental frequency is the same for both models. The fourth and tenth modes have frequency differences of 26.8% and 37.7%, respectively. The higher differences may be caused by the different element properties or constrains adopted by each model. The remaining frequency differences are acceptable, within a 15% range. Although the difference in frequencies from both sets of models tends to increase for higher mode shapes, the first ten modes are very important because these are the most likely to occur for the bridge, within tolerant differences.

In addition to Hui et al.'s work (2006), Larsen and Larose (2015) also mentioned in their study the frequency results of the Stonecutters Bridge. The basic eigenmodes of the Stonecutters Cable-stayed Bridge are shown in Figure 3.23, separating the vertical, lateral and torsion movements. It can be seen that the lateral movement of the deck also occurs in the first mode shape at 0.145 Hz. Each movement is well separated in these eight mode shapes and no coupled modes appear. The lateral and vertical movements are observed in the lower frequencies, which range from 0.145 Hz to 0.361 Hz, and the deck starts to twist at a frequency of 0.428 Hz.

The results from the FEM model of the Stonecutters Bridge by Larsen and Larose (2015) are compared with Hui et al. (2015) results and the FEM of the bridge used in the current study, as presented in Table. 3.7. The FE bridge model in the current study shows similar eigenmodes as the frequencies corresponding to lateral and vertical modes obtained in the current study are close to both sets of published results, while those corresponding to the torsional modes are slightly lower.

Table 3.7. Comparison of frequencies by different models

Eigenmode	Natural Frequency (Hz) of the Stonecutters Cable-stayed Bridge		
	FEM by Larsen and Larose (2015)	FEM by Hui et al. (2015)	FEM in this study
1st vertical (sym)	0.191	0.201	0.172
2nd vertical (asym)	0.233	0.246	0.192
1st lateral (sym)	0.145	0.145	0.145
2nd lateral (asym)	0.361	0.361	0.358
1st torsion (sym)	0.428	0.425	0.324
2nd torsion (asym)	0.592	x	0.424
x: the value is not listed in the reference			

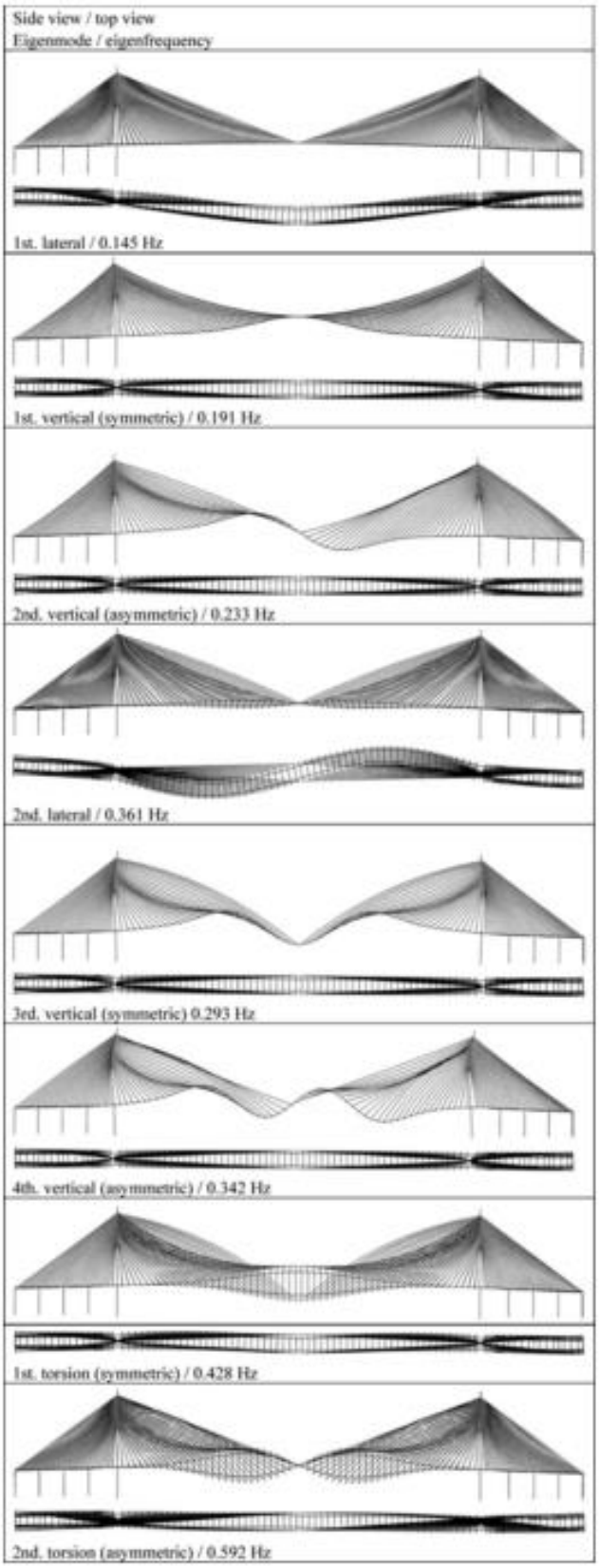

Fig. 3.23. Side view and top view of basic eigenmodes in the Stonecutters Bridge (Larsen and Larose, 2015)

In general, the results reported herein are in line with Larsen and Hui's outcomes.

The fundamental frequency and corresponding mode shapes of current FE model in this study are same as that of reference models, while the most frequencies of the first 10 modes show close values to published results. Therefore, the finite element model in this research is considered to be valid to proceed with the static and dynamic analyses.

Chapter 4 - Static behavior

In this chapter, the finite element model is statically analyzed under the effect of gravity load only. First, the response of the bridge to service loads is checked against design serviceability state criteria. Then, different corrosion scenarios are introduced to study the behavior of the bridge with affected stay cables. With only gravity load applied, the chapter presents the changes in deflection of the main span and the relative change ratios of cable stresses for different corrosion levels, locations and distributions. Comparisons are made against the reference case where no stay cable is affected by corrosion.

4.1. Serviceability limit state check

The behavior of the finite element model of the Stonecutters Bridge under service loads was checked against serviceability requirements specified in design standards. In particular, the serviceability limit state (SLS) is that associated to the bridge deck deformation under service loads. The Stonecutters Cable-stayed Bridge was designed based on the Hong Kong Structures Design Manual for Highways and Railways (SDM) and supplemented by British Standard BS5400 and other codes (Falbe-hansen et al., 2004). Due to lack of access to the design code from Hong Kong, the Canadian highway bridge design code CSA-S6-06 was used as a reference.

Table 4.1 presents the different load factors and load combinations specified in CSA-S6-06. The SLS combination 1 which contains both dead and live loads in the table was chosen to check for the serviceability limit state of the bridge. Due to the lack of design information, the calculation was simplified by applying the dead and live loads on the decks. The load factors for the dead and live loads are 1.00 and 0.90, respectively. The dead load of each component can be automatically applied, when defining the material density of the materials used in ABAQUS. Under transitory loads, clause 3.8.3 of CSA-S6-06 specifies the live load. The CL-625 truck, which has a gross

weight of 625 kN, was used to determine the live load due to its widespread use as a lower limit in designing interprovincial transportation roads and bridges. The truck load and lane load are shown in Figure 4.1. As explained in clause 3.8.3.3, the lane load reduces each axle load to 80% and superimposes a uniformly distributed load of 9 kN/m. Then, the axle loads and the uniform distributed loads are applied to the bridge model with the factor of 0.90. When the axle loads move at the center point of the main span, the critical deflection can be observed as shown in Figure 4.2.

Table 4.1. Load factors and load combinations (CSA-S6-06)

	Permanent loads			Transitory loads					Exceptional loads			
Loads	*D*	*E*	*P*	*L**	*K*	*W*	*V*	*S*	*EQ*	*F*	*A*	*H*
Fatigue limit state												
FLS Combination 1	1.00	1.00	1.00	1.00	0	0	0	0	0	0	0	0
Serviceability limit states												
SLS Combination 1	1.00	1.00	1.00	0.90	0.80	0	0	1.00	0	0	0	0
SLS Combination 2†	0	0	0	0.90	0	0	0	0	0	0	0	0
Ultimate limit states‡												
ULS Combination 1	α_D	α_E	α_P	1.70	0	0	0	0	0	0	0	0
ULS Combination 2	α_D	α_E	α_P	1.60	1.15	0	0	0	0	0	0	0
ULS Combination 3	α_D	α_E	α_P	1.40	1.00	0.50§	0.50	0	0	0	0	0
ULS Combination 4	α_D	α_E	α_P	0	1.25	1.65§	0	0	0	0	0	0
ULS Combination 5	α_D	α_E	α_P	0	0	0	0	0	1.00	0	0	0
ULS Combination 6**	α_D	α_E	α_P	0	0	0	0	0	0	1.30	0	0
ULS Combination 7	α_D	α_E	α_P	0	0	0.90§	0	0	0	0	1.30	0
ULS Combination 8	α_D	α_E	α_P	0	0	0	0	0	0	0	0	1.00
ULS Combination 9	1.35	α_E	α_P	0	0	0	0	0	0	0	0	0

**For the construction live load factor, see Clause 3.16.3.*
†For superstructure vibration only.
‡For ultimate limit states, the maximum or minimum values of α_D, α_E, and α_P specified in Table 3.2 shall be used.
§For wind loads determined from wind tunnel tests, the load factors shall be as specified in Clause 3.10.5.2.
***For long spans, it is possible that a combination of ice load F and wind load W will require investigation.*

Legend:
A = ice accretion load
D = dead load
E = loads due to earth pressure and hydrostatic pressure, including surcharges but excluding dead load
EQ = earthquake load
F = loads due to stream pressure and ice forces or to debris torrents
H = collision load arising from highway vehicles or vessels
K = all strains, deformations, and displacements and their effects, including the effects of their restraint and the effects of friction or stiffness in bearings. Strains and deformations include strains and deformations due to temperature change and temperature differential, concrete shrinkage, differential shrinkage, and creep, but not elastic strains
L = live load (including the dynamic load allowance, when applicable)
P = secondary prestress effects
S = load due to differential settlement and/or movement of the foundation
V = wind load on traffic
W = wind load on structure

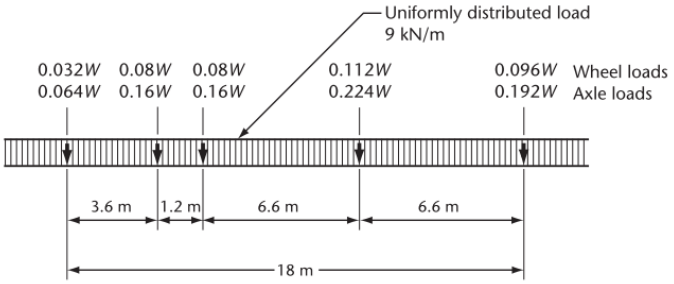

Fig. 4.1. Lane load definition (CSA-S6-06)

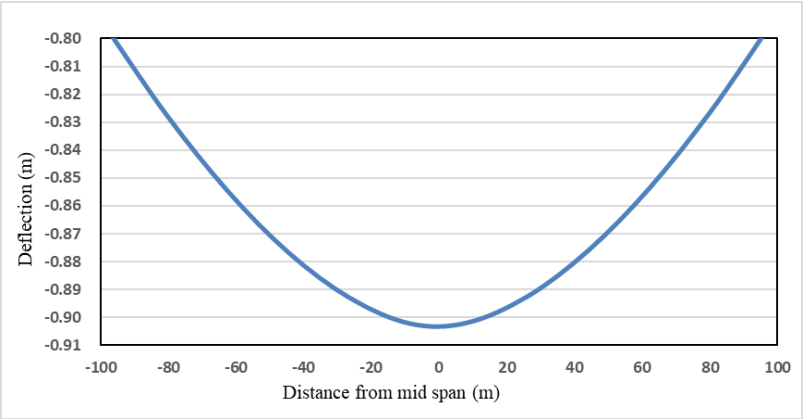

Fig. 4.2. The deck deflection in SLS

The result in Figure 4.2 shows the maximum deflection is -9.02×10^{-1}m at the center point of the main span. In the design code CSA-S6-06, the deflection limit of a long-span cable-stayed bridge is not clearly defined. In other references, the deflection limit for cable suspended bridges is L/300 (Vickneswaran and Eyre, 2013), where L is the main span length, and the allowable deflection due to live load for a long-span cable-stayed bridge is defined as L/400 (Thu and Khaing, 2014). In this research, the finite element model represents a long-span cable-stayed bridge, which should meet the deflection requirement of L/400. The allowable deflection for this model is 2.55 m, which is larger than the maximum deflection of 9.02×10^{-1}m under SLS, ensuring the finite element model meets SLS requirements. In the following analyses, the live load is ignored, and only the dead load was applied for the static analysis.

4.2. Distribution of corroded cables

The static analysis was conducted for different case scenarios in which cables are damaged to various levels of corrosion and positioned at different locations over the length of the twin decks of Stonecutters Bridge model. To simulate the cable corrosion cases, which consider both symmetric and asymmetric distributions, and to identify the critical case, the corroded cables are placed in symmetric and asymmetric positions with respect to the middle point of the deck. The design of this bridge is conservative in terms of strength and number of cables. Losing one single cable due to corrosion might not have significant effect on the overall response of the bridge. However, no

research is available for groups of several corroded cables, which could have a significant impact on the structural response of the bridge. In this research, a group of eight cables were selected for corrosion simulation, and these were classified into four major configurations which are shown in Figure 4.3.(a) to (d). Note that corroded cables are denoted as orange in Figure 4.3.

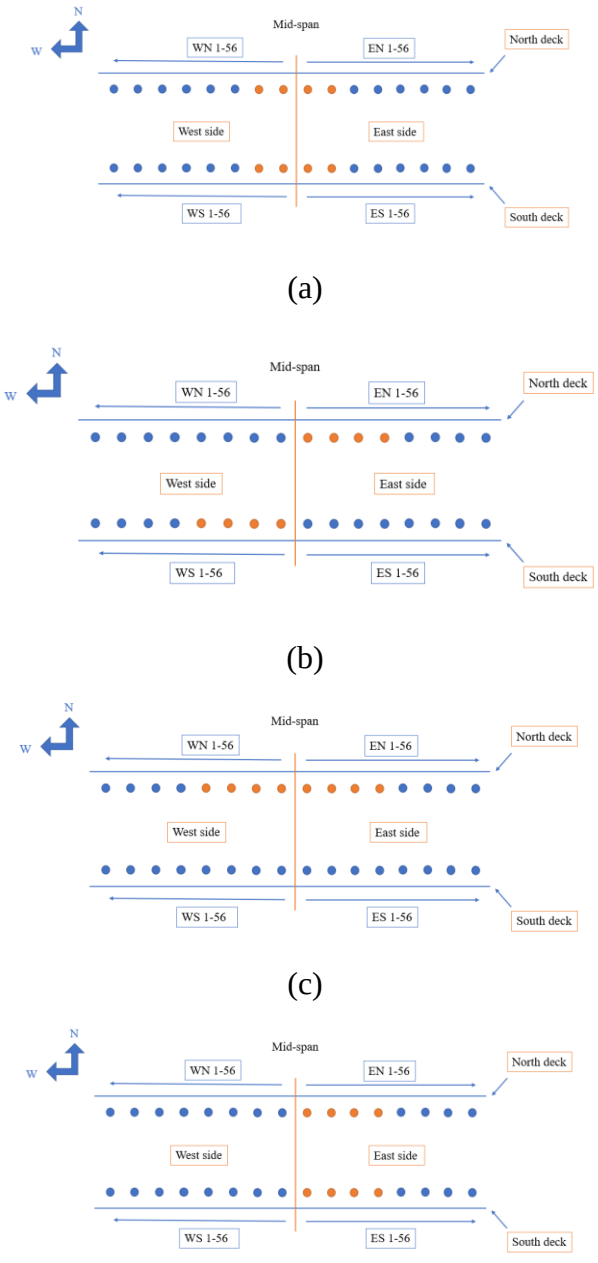

(a)

(b)

(c)

(d)

Fig. 4.3. Four major corroded configurations with respect to middle point of the span: (a) major case 1, (b) major case 2, (c) major case 3, and (d) major case 4

In these four major cases, each dot represents one cable, and the middle line represents the midpoint of the bridge deck. The 32 stay cables in the vicinity of the middle of the span are represented by 32 dots for simplification. The cables affected by corrosion in the bridge model are colored orange, and the rest of the unaltered cables are colored blue. Each cables corrosion case is meant to excite certain types of motion of the deck and to engage certain types of mode shapes. The purpose of selecting cables corrosion case 1 (Figure 4.3 (a)), where cables from every side of the bridge are corroded, is to affect the vertical vibration modes of the deck. Cables corrosion cases 2 and 3 (Figures 4.3 (b) and (c)), in which the corroded cables are asymmetrically distributed relative to the longitudinal axis, are meant to provide more flexibility to the dynamic loadings exciting the torsional vibration modes. Cables corrosion case 4 (Figure 4.3 (d)), in which all the affected cables lie on the east side of span, is meant to facilitate the excitation of the vertical and torsional vibration modes. However, case 4 also has the purpose of making these mode shapes asymmetric.

Within each major cable corrosion case presented above, several subcases were also simulated, in order to investigate the response affected by the distance of the corroded cables from the middle point of the span. Subcase examples for major case 3 are shown in Figure 4.4, while the rest of the subcases are presented in Appendix D. Each corrosion subcase affects the cables at different locations along the deck. For example, for the cables corrosion case 3, the subcase 3-1 affects the cables closest to the middle point of the span, whereas subcases 3-2 and 3-3 affect cables slightly away from the middle of the deck, as it can be seen in Figure 4.4(a) to (c). Finally, within each subcase, different levels of corrosion were investigated: 25% corrosion level, 50% corrosion level, and 75% corrosion level. The percentage corrosion level denotes the percentage loss of cross-sectional area of the cable. The three different corrosion damage levels consider slight corrosion, medium corrosion and severe corrosion, respectively. It is unlikely that a 75%-corrosion damage would be found on an in-service bridge; however, the most severe corrosion case closely represents when a cable

has ruptured.

(a)

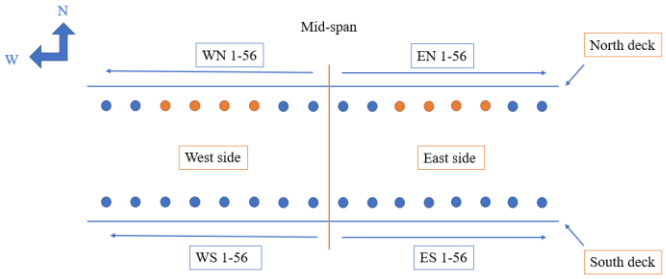

(b)

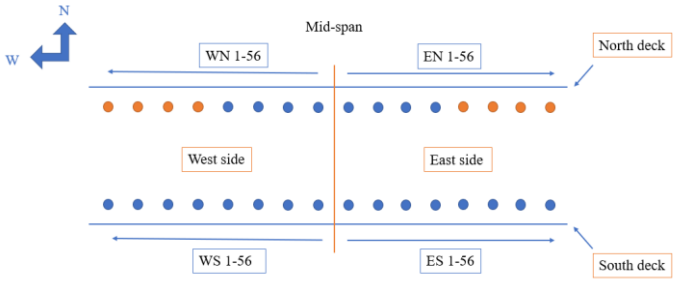

(c)

Fig. 4.4. Subcases of major case 3: (a) subcase 3-1, (b) subcase 3-2, (c) subcase 3-3.

The nomenclature used herein to distinguish the subcases is "*m*-*n*-*a*," where *m* is the major case number, *n* is the subcase number, and *a* is the corrosion level represented by the percentage in area reduction in the affected cables. For example, case 3-1-50 represents the major cables corrosion case 3 (both sides of the bridge along with a single deck affected), subcase 1 (cables closest to the mid-span affected), with a corrosion level of 50% in the affected cables.

In the current study, the corroded cables were simulated by reducing the effective

area of the cable cross section. The corrosion level employed for each affected cable does not change the elastic modulus of the cables; however, it changes the ultimate strength and yield strength of the cable. This assumption was also employed by other studies (Li et al., 2012), where a couple of corroded wires from a replaced cable were tested from Figure 2.13. The current model didn't change the ultimate strength, yield strength and the elastic modules because the maximum cable stress for the SLS case in the static condition was 110 MPa (Figure D10 in Appendix D) which is below the yield strength. Changing the effective cross-sectional area can properly simulate the corrosion condition of the cables, because corrosion leads to loss of steel. Three different degrees of corrosion were selected as 25%, 50% and 75%. Each corrosion level is defined by the Eq. 4.1

$$\mathrm{a} = \left(1 - \frac{\bar{A}}{A}\right) \times 100 \tag{4.1}$$

where: a is the corrosion level (%)

A is the total cross-sectional area

$\bar{A}$ is the effective corroded cross-sectional area

The design life for the Stonecutters Bridge is 120 years (Kite et al., 2007). According to Eq. (2.5) and Figure 2.9 in Chapter 2, the time to reach a certain corrosion-induced damage in the cable can be approximated. For this bridge model, the corrosion current density was assumed to be 125 μA/cm^2, a value taken from Figure 2.9, for galvanized wires sustaining a tensile stress of 110 MPa. The 1st to 8th cables on WN, EN, WS and ES sides were corroded for the numerical analyses. Due to the different diameters along the cables, the smallest diameter which needs less time to reach the effective cross-sectional area was 182 mm among the affected cables. When substituted into Eq. (2.5), the estimated time for a 25%, 50% and 75% corrosion level is 15.7, 31.4 and 47.1 years, respectively, assuming a constant corrosion rate over that period. The

real time may be slightly longer due to protection provided by the outer sheath, but still within the service life of the bridge. Therefore, the assumed corrosion levels in the analyses could happen during the bridge's service life.

4.3. Deck deflection comparison

4.3.1. Effect of corrosion level

The Stonecutters Bridge is a cable-stayed bridge with twin decks which has the cables connected to the lateral edges of each deck, thus resulting in four fans of bridge stay cables. The deflections of both sides of the decks under the effect of the gravity load are analyzed in the current section, and the deflections of the main span are represented in Figure 4.5(a) to (h) for different cables corrosion subcases.

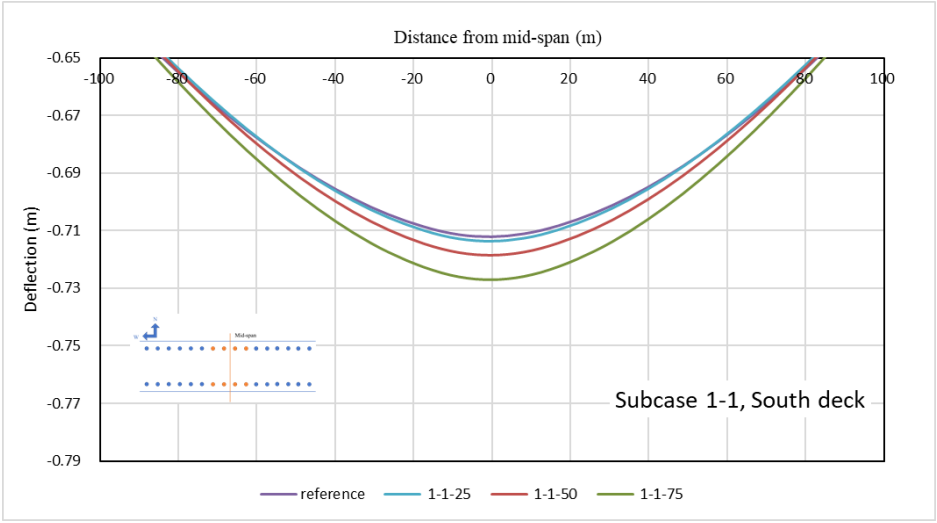

(a)

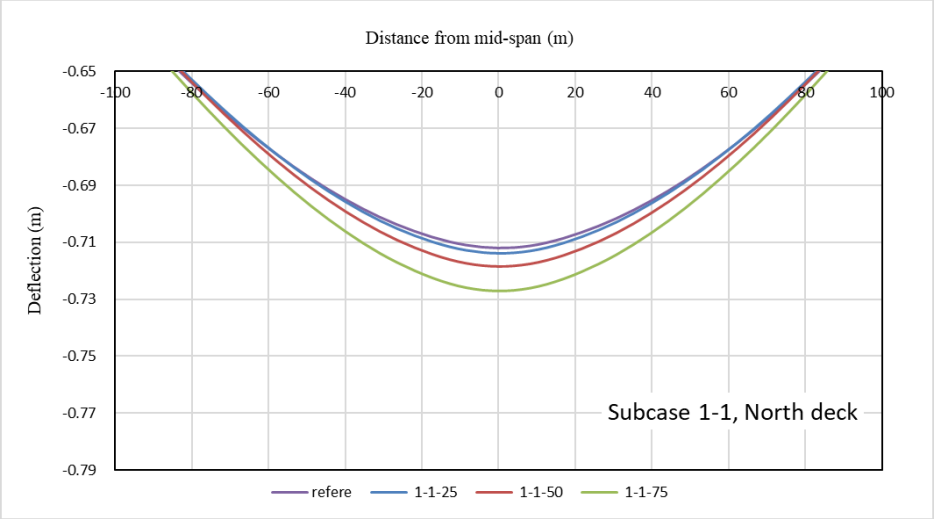
Distance from mid-span (m)
Deflection (m)
-0.65
-0.67
-0.69
-0.71
-0.73
-0.75
-0.77
-0.79
-100
-80
-60
-40
-20
0
20
40
60
80
100
Subcase 1-1, North deck
refere
1-1-25
1-1-50
1-1-75

(b)

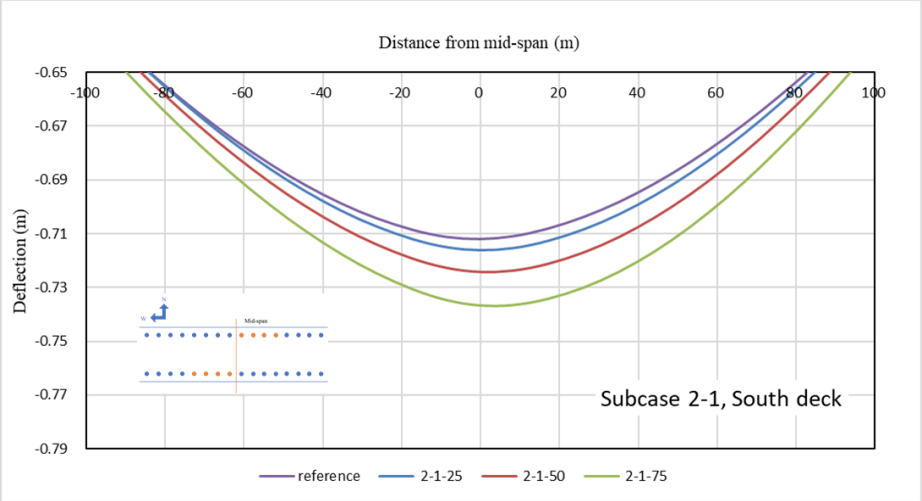
Distance from mid-span (m)
Deflection (m)
-0.65
-0.67
-0.69
-0.71
-0.73
-0.75
-0.77
-0.79
-100
-80
-60
-40
-20
0
20
40
60
80
100
Subcase 2-1, South deck
reference
2-1-25
2-1-50
2-1-75

(c)

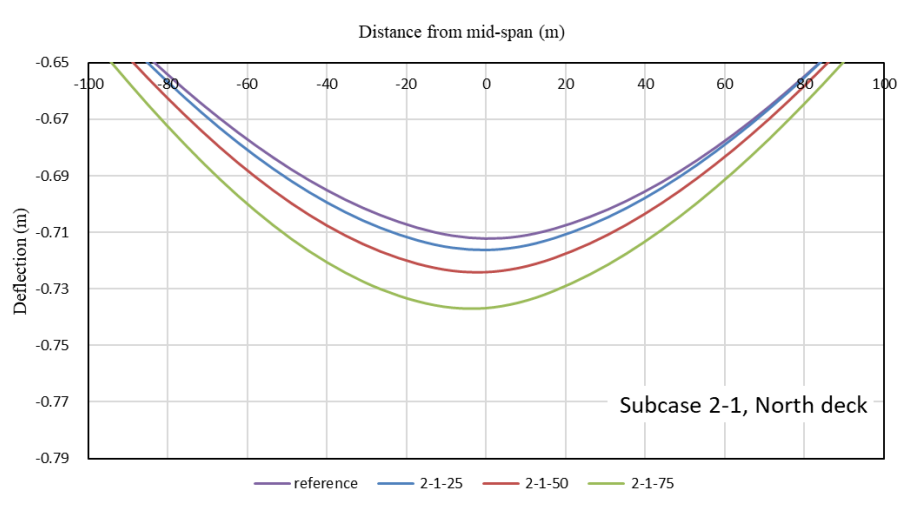
Distance from mid-span (m)
Deflection (m)
-0.65
-0.67
-0.69
-0.71
-0.73
-0.75
-0.77
-0.79
-100
-80
-60
-40
-20
0
20
40
60
80
100
Subcase 2-1, North deck
reference
2-1-25
2-1-50
2-1-75

(d)

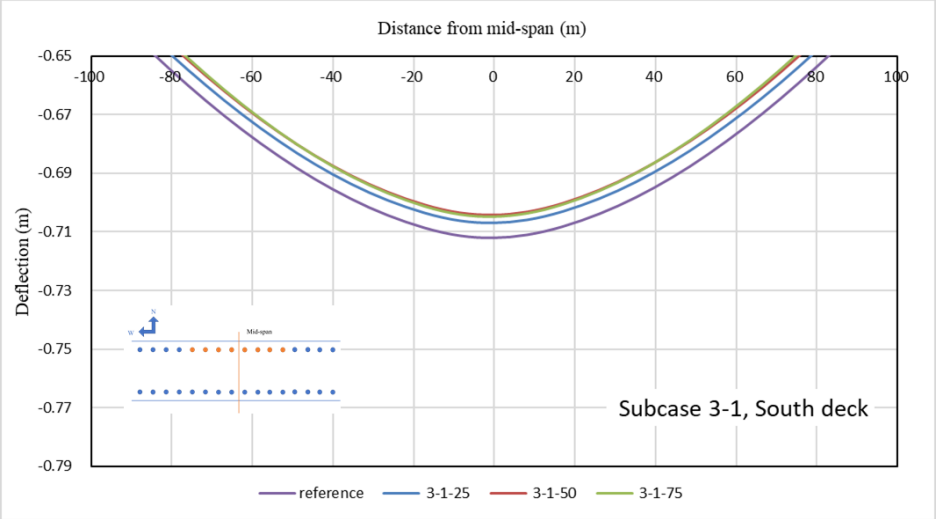
Distance from mid-span (m)
-0.65
-0.67
-0.69
-0.71
-0.73
-0.75
-0.77
-0.79
Deflection (m)
-100
-80
-60
-40
-20
0
20
40
60
80
100
Subcase 3-1, South deck
reference
3-1-25
3-1-50
3-1-75

(e)

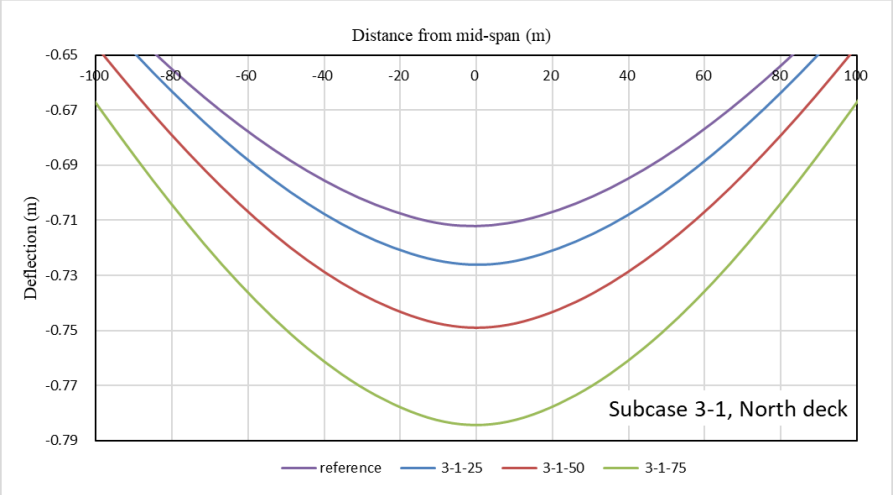
Distance from mid-span (m)
-0.65
-0.67
-0.69
-0.71
-0.73
-0.75
-0.77
-0.79
Deflection (m)
-100
-80
-60
-40
-20
0
20
40
60
80
100
Subcase 3-1, North deck
reference
3-1-25
3-1-50
3-1-75

(f)

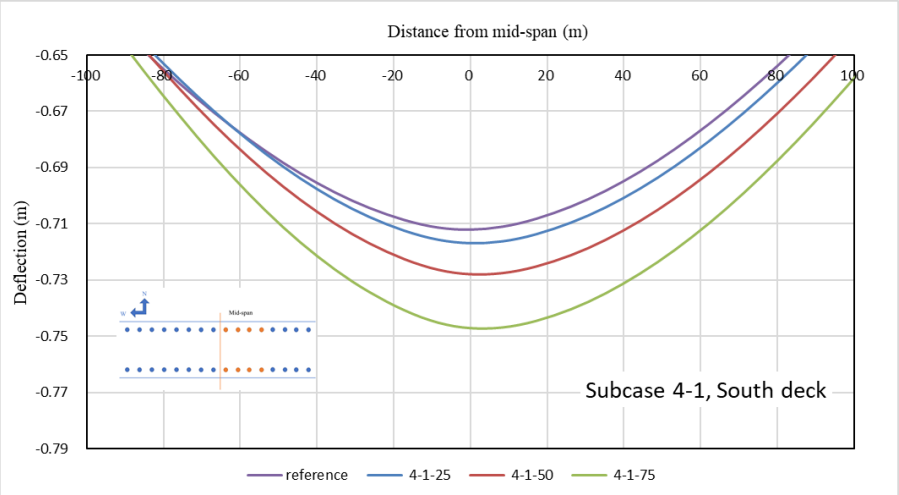
Distance from mid-span (m)
-0.65
-0.67
-0.69
-0.71
-0.73
-0.75
-0.77
-0.79
Deflection (m)
-100
-80
-60
-40
-20
0
20
40
60
80
100
Subcase 4-1, South deck
reference
4-1-25
4-1-50
4-1-75

(g)

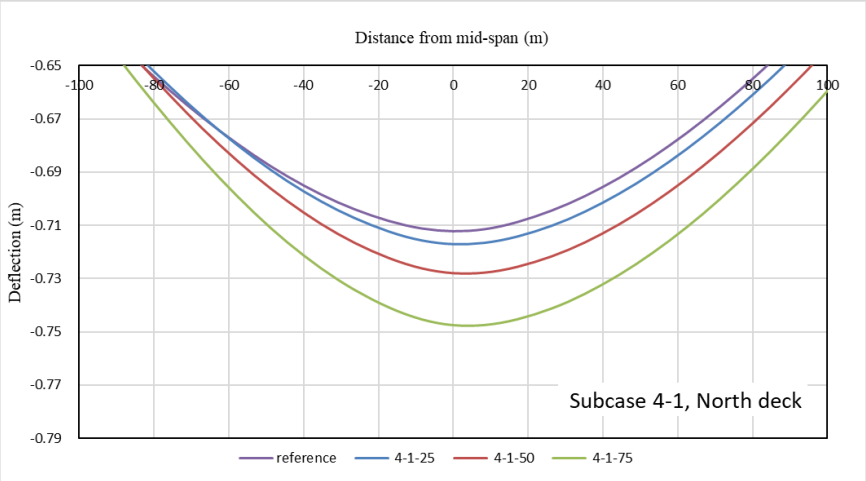

(h)

Fig. 4.5. Deflections of both decks with different degrees of corroded cables. (a): South deck for subcase 1-1; (b) North deck for subcase 1-1; (c) South deck for subcase 2-1; (d) North deck for subcase 2-1; (e) South deck for subcase 3-1; (f) North deck for subcase 3-1; (g) South deck for subcase 4-1; (h) North deck for subcase 4-1.

Figure 4.5(a) to (h) plot the deflection of the decks for each scenario, with respect to the reference case. Note that the 'reference' case represents a bridge model without corroded cables. The positive coordinates represent the west side of the deck, with respect to middle point of the span, and the negtive ones correspond to the east side of the deck.

Figure 4.5(a) and (b) show the deflections of both decks for subcase 1-1 with different corrosion levels. The maximum deflections are -7.14×10^{-1} m, -7.18×10^{-1} m and -7.27×10^{-1} m for subcases 1-1-25, 1-1-50 and 1-1-75, respectively. The deck deformed symetrically, and the maximum deflection happened in the middle of the deck. Subcase 1-1 with 25% corrosion damage registered a deflection close to the reference case, which had no corroded cables and a deflection of -7.12×10^{-1} m. The deflections of both decks for subcase 2-1 are shown in Figures 4.5(c) and (d). The maximum deflections for subcases 2-1-25, 2-1-50 and 2-1-75 are -7.16×10^{-1} m, -7.24×10^{-1} m and -7.37×10^{-1} m, respectively. However, the deformation of both decks are asymmetrical, and the maximum deflection happened at 0.7 m, 2.3 m

and 3.91 m from the middle in the west side for the south deck, and at -0.7 m, -2.3 m and -3.91 m from the middle in the east side for north deck. Figure 4.5(e) and (f) present the deflection of both decks for subcase 3-1. Owing to the presence of the corroded cables only on the north deck, the maximum deflections for the north deck are -7.26×10^{-1} m, -7.49×10^{-1} m and -7.84×10^{-1} m for subcases 3-1-25, 3-1-50 and 3-1-75, respectively. On the south deck, the maximum deflections are -7.07×10^{-1} m, -7.04×10^{-1} m and -7.04×10^{-1} m for the three different corrosion levels. The deflections on the south deck are also slightly lower than those of the reference case, which is -7.12×10^{-1} m. Both maximum deflections occured in the middle of the span. Figure 4.5(g) and (h) demonstrate the deflections of both decks for subcase 4-1. The largest deflection observed in subcases 4-1-25, 4-1-50 and 4-1-75 are -7.17×10^{-1} m, -7.28×10^{-1} m and -7.48×10^{-1} m, respectively. Both decks have an asymmetric deformation, and the largest deflection occurs in the west side. The maximum deflection and corresponding location for each case are presented in Figure B4 of Appendix B.

The maximum deck deflection was encountered when the cables have the worst corrosion condition, namely 75% corrosion level. As a consequence, both decks had the largest vertical deflection for the subcases with less effective cable cross-sectional area. Because the design for the bridge is conservative, the 25% corrosion level does not result in much higher deflection than the reference case. Since the deck is still supported by the other heathy cables, the deflection of the deck caused by 50% and 75% corrosion levels is not double that of 25% corrosion level. For the symmetric cases such as major case 1, the increasing vertical deflection due to an increase in the degree of cable corrosion occurs on both decks. As for major case 3, in which the corroded cables are located on the north deck only, similar changes are observed on the north deck deflection; however, the south deck is slightly lifted with increasing corrosion level to counterbalance the deformation in the north deck. Moreover, the maximum deflection occurs at the mid-span due to their symmetric distribution. As for major cases 2 and 4,

which have asymmetric distributions with respect to the centerline at mid-span, the largest deflection does not happen at the middle point of the span. Due to the imbalanced distribution of corroded cables in subcase 2-1, the largest deflection happens close to the corroded cables location. As for subcase 4-1, in which all the corroded cables are located on the east side, the slope of the east side is larger than that of the west side, resulting in the largest deflection encountering on the west side of the deck.

4.3.2. Effect of distance from mid-span

The different cable corrosion subcases illustrated in Figure 4.4(a) to (c) show that the distance between the location of the corroded cables and the mid-span influence the maximum deflection of the decks and their corresponding point along the deck where this is registered. In this section, the location of the corroded cables along the deck is investigated for the four major cases for 75% corrosion level in the cables, since this can cause the most critical deflection condition for the bridge deck.

Figure 4.6(a)-(h) illustrate the deflected shape of the south and north decks for major cases 1 to 4, and their corresponding subcases with a corrosion damage in the cables of 75%. It can be noticed that when the corrosion level is the same for each affected cable, the location of the corroded cables with respect to the mid-span makes the main span behave differently under the effect of the gravity load.

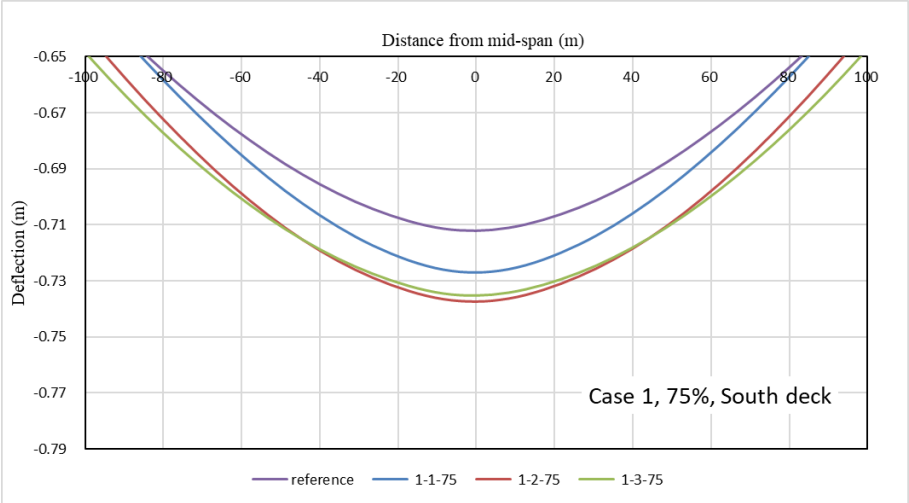

(a)

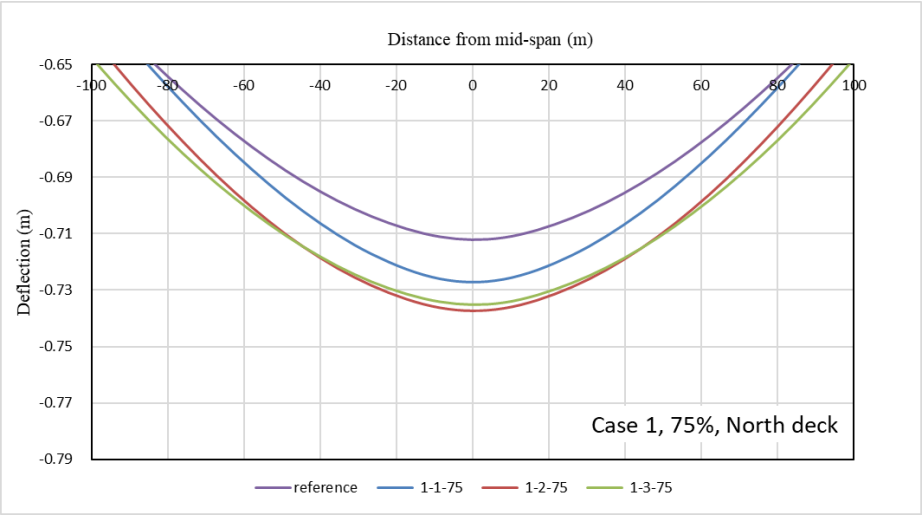
Distance from mid-span (m)
-0.65
-0.67
-0.69
-0.71
-0.73
-0.75
-0.77
-0.79
Deflection (m)
-100
-80
-60
-40
-20
0
20
40
60
80
100
Case 1, 75%, North deck
reference
1-1-75
1-2-75
1-3-75

(b)

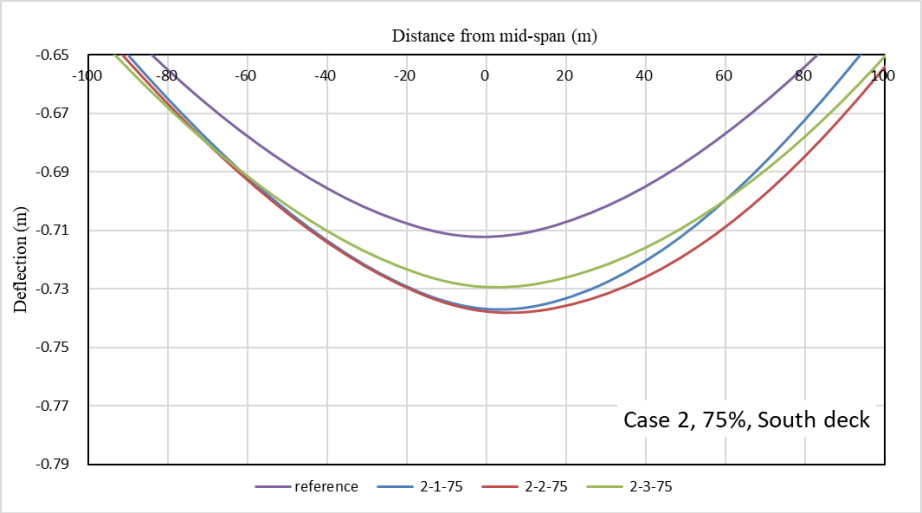
Distance from mid-span (m)
-0.65
-0.67
-0.69
-0.71
-0.73
-0.75
-0.77
-0.79
Deflection (m)
-100
-80
-60
-40
-20
0
20
40
60
80
100
Case 2, 75%, South deck
reference
2-1-75
2-2-75
2-3-75

(c)

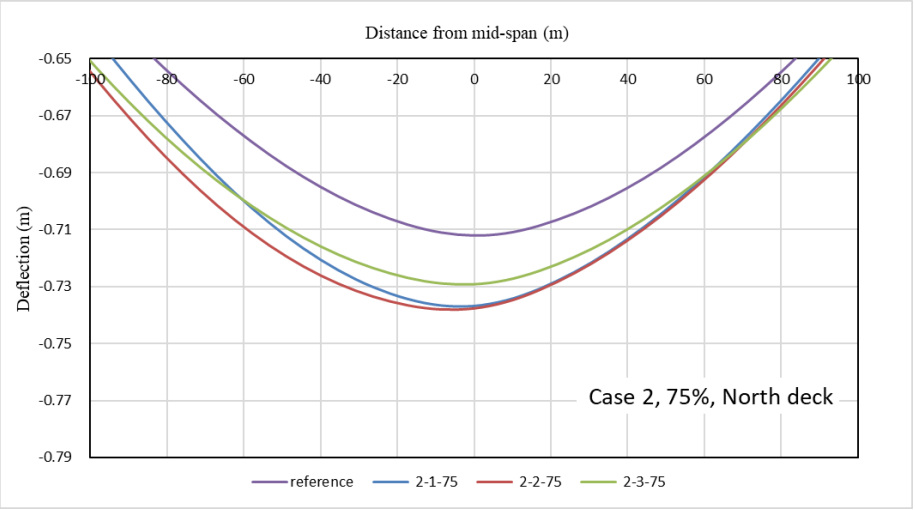
Distance from mid-span (m)
-0.65
-0.67
-0.69
-0.71
-0.73
-0.75
-0.77
-0.79
Deflection (m)
-100
-80
-60
-40
-20
0
20
40
60
80
100
Case 2, 75%, North deck
reference
2-1-75
2-2-75
2-3-75

(d)

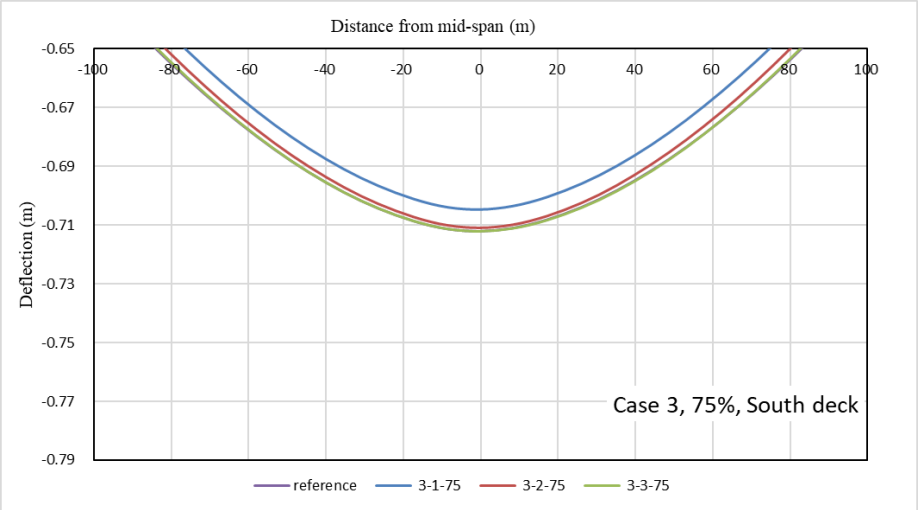
Distance from mid-span (m)
-0.65
-0.67
-0.69
-0.71
-0.73
-0.75
-0.77
-0.79
Deflection (m)
-100
-80
-60
-40
-20
0
20
40
60
80
100
Case 3, 75%, South deck
reference
3-1-75
3-2-75
3-3-75

(e)

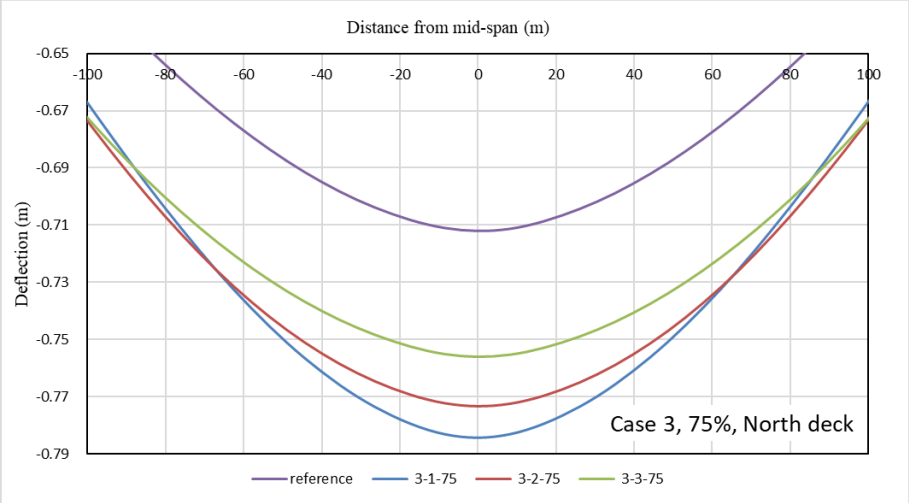
Distance from mid-span (m)
-0.65
-0.67
-0.69
-0.71
-0.73
-0.75
-0.77
-0.79
Deflection (m)
-100
-80
-60
-40
-20
0
20
40
60
80
100
Case 3, 75%, North deck
reference
3-1-75
3-2-75
3-3-75

(f)

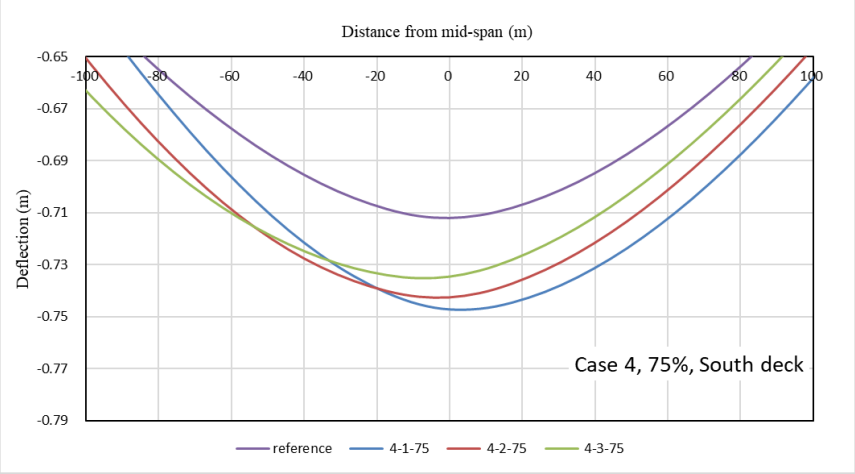
Distance from mid-span (m)
-0.65
-0.67
-0.69
-0.71
-0.73
-0.75
-0.77
-0.79
Deflection (m)
-100
-80
-60
-40
-20
0
20
40
60
80
100
Case 4, 75%, South deck
reference
4-1-75
4-2-75
4-3-75

(g)

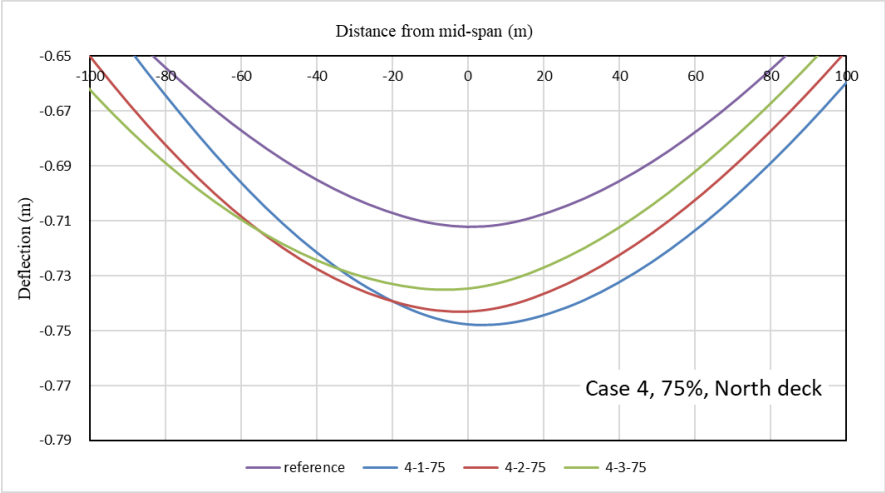

(h)

Fig. 4.6. Vertical deflection of the main span for different subcases with 75% corrosion level, (a) South deck for major case 1; (b) North deck for major case 1; (c) South deck for major case 2; (d) North deck for major case 2; (e) South deck for major case 3; (f) North deck for major case 3; (g) South deck for major case 4; (h) North deck for major case 4.

For the major case 1, it was noticed that the deck deflection increased as the corroded cables were located away from mid-span, and it registered values in the range of-7.27×10^{-1} m to -7.37×10^{-1} m, as it can be noticed in Figure 4.6(a) and (b). The smaller deflection, represented by the purple line in these graphs corresponds to the reference case, where no corrosion was applied to the cables, which had a maximum deflection of -7.12×10^{-1} m. The subcase 1-1-75 registered a small deflection for the bridge deck, closer to the reference case; however, for the subcases 1-2-75 and 1-3-75, the deflections of the deck registered higher values of -7.37×10^{-1} m and -7.35×10^{-1} m, respectively. Also, for these two subcases, the deck deflection had similar distribution along the span, because the arrangement of the corroded cables was symmetric with respect to the mid-span. As for the major case 2 shown in Figure 4.6(c) and (d), the vertical deflection also increased for each subcase. The subcases 2-1-75, 2-2-75 and 2-3-75 registered maximum deflections of -7.37×10^{-1} m, -7.38×10^{-1} m and -7.29×10^{-1} m, respectively. The deflection for subcase 2-3-75 is closer to

the reference case. Subcases 2-1-75 and 2-2-75 have a similar deflection at 3.91 m and 6.11 m from the mid-span on the east side of north deck and west sides of the south deck. However, the location corresponding to the maximum deflection registered for subcase 2-3-75 is at 2.91 m, which is closer to the middle point of deck than the other two subcases. The maximum deflection occurred at the corresponding location of corroded cables. For the major case 3 in Figure 4.6(e) and (f), the deck deflection was observed in the range of -7.04×10^{-1} m to -7.12×10^{-1} m for the south deck and -7.56×10^{-1} m to -7.84×10^{-1} m on the north deck. The subcase 3-1-75 registered a larger deflection of -7.84×10^{-1} m for the north deck and a smaller one of -7.04×10^{-1} m on the south deck. On the contrary, the subcases 3-3-75 registered a larger deflection of -7.56×10^{-1} m on the north deck and a smaller deflection of -7.12×10^{-1} m of the south deck. The deck deflections for these three subcases were similar, for which the maximum deflection was registered at the middle point of deck, due to their symmetric corroded cables arrangement with respect to the mid-span. Figure 4.6(g) and (h) presented the deflection of major case 4. The increased deflection was spotted with respect to the reference case, and the values for subcases 4-1-75, 4-2-75 and 4-3-75 were registered, which are -7.48×10^{-1} m, -7.43×10^{-1} m and -7.35×10^{-1} m, respectively. The subcase 4-1-75 determined a higher deflection at 3.51 m on west side, while the subcases 4-2-75 and 4-3-75 had smaller deflections at -3.11 m and -7.11 m, respectively.

Major cases 1 and 2 show similar deck deflection trends for the corresponding subcases, with increasing vertical deflection when the corroded cables are located further away from the mid-span. On both decks, the maximum deflection of subcase 2 is larger than that of subcases 1 and 3 in major cases 1 and 2. For major case 1, when there are only two corroded cables on each side, the 3rd and 4th cables from the middle point take more load to support the deck, with the largest deflection due to cable corrosion occurring at mid-span. When the corroded cables are the first 4 cables from the middle point as subcase 1-3-75, the deflection of the decks is not increased at mid-

span but is slightly higher at the ends of the span. For major case 2, in which the first four cable from mid-span are corroded on two different sides of each deck, the deflection pattern is similar for subcases 2-1-75 and 2-2-75, with the largest deflection for subcase 2-2-75. Moreover, the largest deflection occurs on the side where corroded cables are located along each deck. However, the corresponding location of maximum deflection for subcase 2-3-75 is closer to the mid-span due to the asymmetric arrangement. This unbalanced deflection between the two decks would create a twist of both decks as subcase 2-3-75 has less deflection than the other two subcases shown in Figure 4.6(c) and (d).

The subcases 3-1 and 4-1 are the most critical cases for both major cases 3 and 4, proving the importance of the 1st to 4th cables on all sides with respect to the middle point. The south deck deflection slightly increased comparing to the reference case deflection as shown in Figure 4.6(e) to counterbalance the north deck where the cables were damaged. On the north deck, however, the highest deflection occurred at mid-span, and the corroded cables, which cover the 1st to 4th cables from the mid-span in subcase 3-1, lead to the largest deflection compared to the other subcases, in which the healthy cables located within the four cables supported the mid-span and prevented the deck from deflecting more. For the major case 4, both decks have the same deflection. The subcase 4-1, in which four corroded cables were located on both decks of the east side, registered the largest deflection due to the same reason as subcase 3-1. Because of asymmetry in the distribution of corroded cables relative to the mid-span, the location of the largest deflection was spotted from the west side to the east side, as the location of corroded cables was shifted away from the mid-span.

4.3.3. Effect of corroded cables distribution

The impact on the bridge deck deflection created by the distribution of the corroded cables has been investigated by comparing the same subcases of the four major cases investigated, namely: 1-1, 2-1, 3-1 and 4-1, 1-2, 2-2, 3-2 and 4-2, 1-3, 2-3, 3-3 and 4-3. The deck deflection comparisons are presented in Figures 4.7(a) to (f) for the most

advanced corrosion damage of 75% cross-section loss.

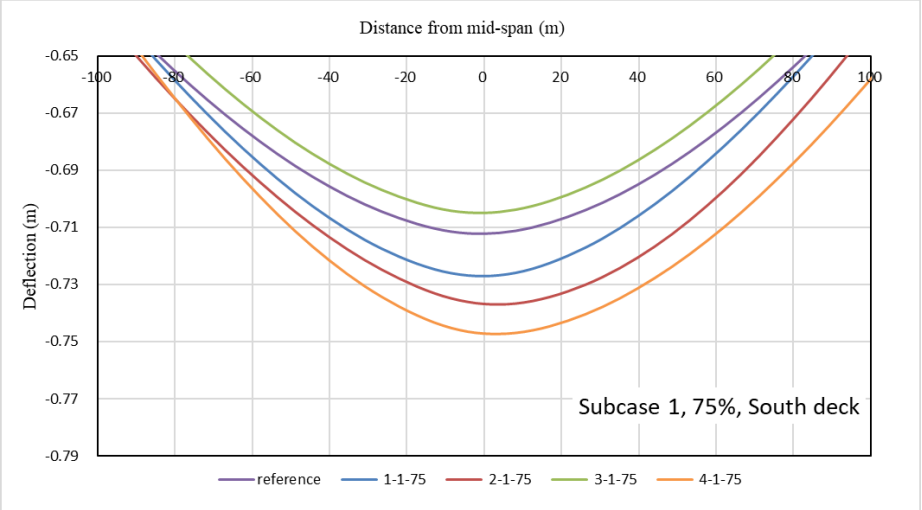

(a)

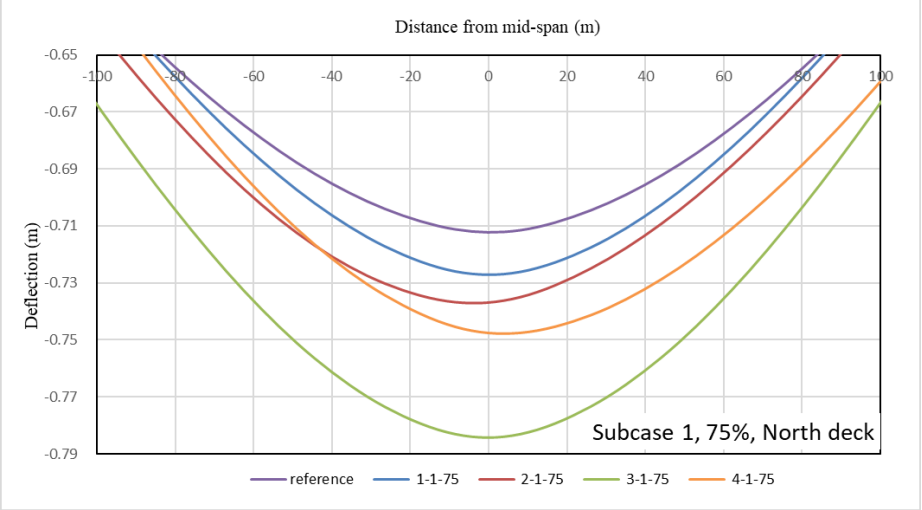

(b)

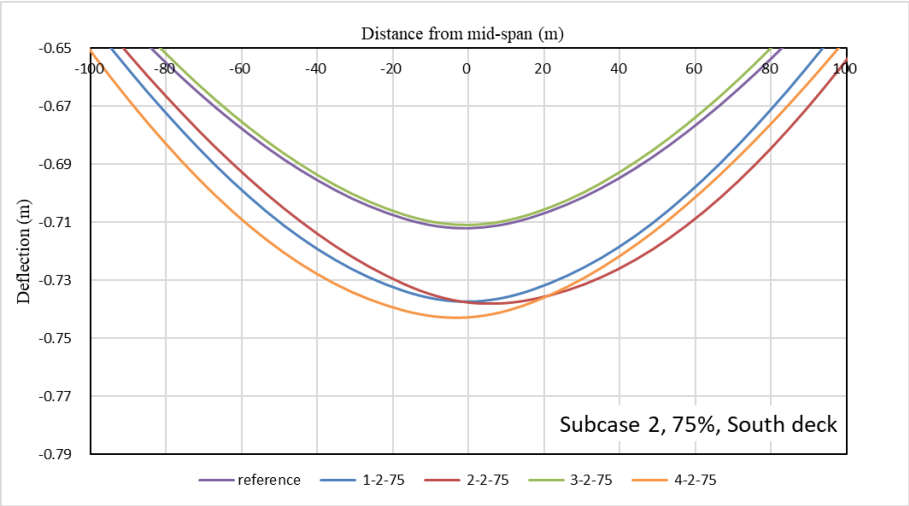
Distance from mid-span (m)
-0.65
-0.67
-0.69
-0.71
-0.73
-0.75
-0.77
-0.79
Deflection (m)
-100
-80
-60
-40
-20
0
20
40
60
80
100
Subcase 2, 75%, South deck
reference
1-2-75
2-2-75
3-2-75
4-2-75

(c)

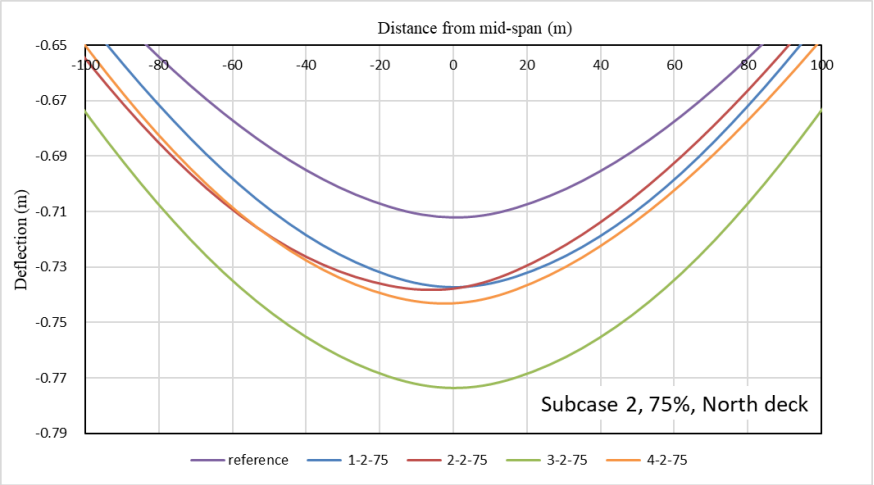
Distance from mid-span (m)
-0.65
-0.67
-0.69
-0.71
-0.73
-0.75
-0.77
-0.79
Deflection (m)
-100
-80
-60
-40
-20
0
20
40
60
80
100
Subcase 2, 75%, North deck
reference
1-2-75
2-2-75
3-2-75
4-2-75

(d)

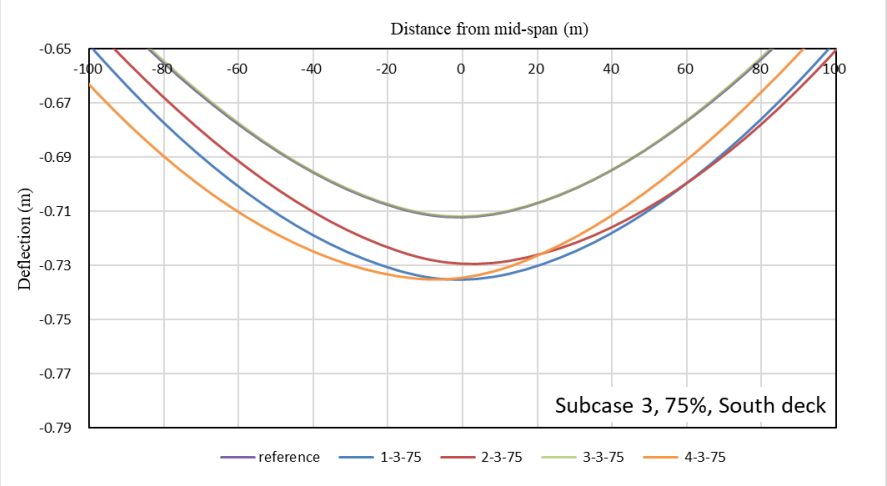
Distance from mid-span (m)
-0.65
-0.67
-0.69
-0.71
-0.73
-0.75
-0.77
-0.79
Deflection (m)
-100
-80
-60
-40
-20
0
20
40
60
80
100
Subcase 3, 75%, South deck
reference
1-3-75
2-3-75
3-3-75
4-3-75

(e)

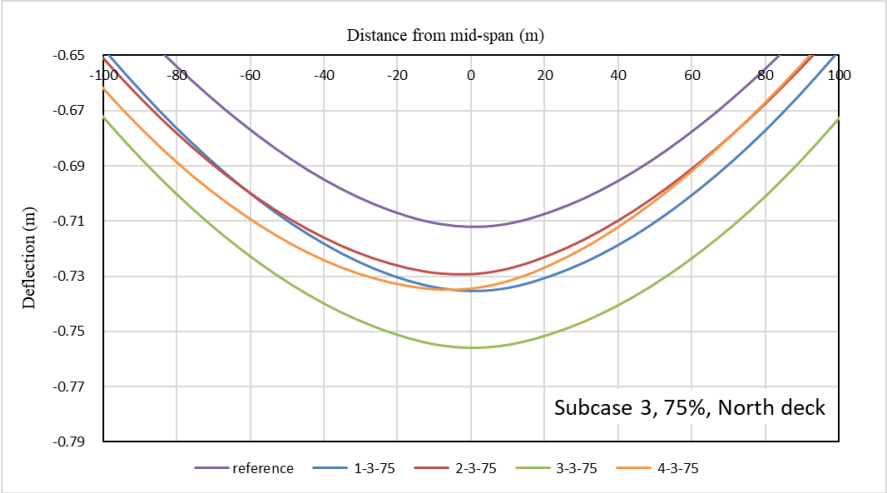

(f)

Fig. 4.7. Vertical deflection of the main span for different major cases with 75% corrosion level: (a) South deck for subcase 1; (b) North deck for subcase 1; (c) South deck for subcase 2; (d) North deck for subcase 2; (e) South deck for subcase 3; (f) North deck for subcase 3.

Figures 4.7(a) and (b) present the deflection changes in terms of subcase 1 on both decks. The subcase 1-1-75, 2-1-75, 3-1-75 and 4-1-75 registered deck deflections of -7.27×10^{-1} m, -7.37×10^{-1} m, -7.04×10^{-1} m and -7.48×10^{-1} m, respectively, of the south deck and -7.27×10^{-1} m, -7.37×10^{-1} m, -7.84×10^{-1} m and -7.48×10^{-1} m, respectively, of the north deck. The subcase 4-1-75 and 3-1-75 registered a larger deflection of the south deck and north deck, respectively. For the deck deflection compared in Figure 4.7(c) and (d), it was noticed that the maximum deflection among the four cases is in the range of -7.11×10^{-1} m to -7.43×10^{-1} m on the south deck (Figure 4.7(c)), and -7.37×10^{-1} m to -7.73×10^{-1} m on the north deck (Figure 4.7(d)). The deflection registered for the subcase 3-2-75 was closer to the reference case; however, the subcase 4-2-75 deck deflection was close to the deflections reported for subcases 1-2-75 and 2-2-75 and registered the maximum value of the south deck. The subcase 3-2-75 showed the largest deflection among the other subcases in the north deck. Figures 4.7(e) and (f) indicated the different major cases deflections compared for subcase 3. The largest deflection ranged from -7.12×10^{-1} m to -7.35×10^{-1} m of the south deck and -7.29×10^{-1} m to -7.56×10^{-1} m in

the north deck. The subcase 3-3-75 showed a close deflection to the reference case, while the subcase 1-3-75 and subcase 4-3-75 had the same maximum value of deflection of -7.35×10^{-1} m, but corresponding to different locations of the south deck (Figure 4.7(e)). The higher deflection value was registered for the subcase 3-3-75 on the north deck (Figure 4.7(f)).

Among all the cables corrosion cases investigated, the major case 3 resulted in the largest deflection for the north deck, because the affected cables were only located on this deck. Also a largest deflection value was noticed for the major case 4 of the south deck for all the subcases, because all four corroded cables were located on one side of both decks and symmetric with regard to the longitudinal line.

4.3.4. Summary

In order to easily compare the effect of the cable corrosion cases on the deck response, Table 4.2 shows the maximum deflection and the corresponding location registered for each case discussed above and for the increased corrosion percentage with regard to the reference case, where no corrosion was applied to the cables. The maximum vertical deflections range from -7.04×10^{-1} m to -7.48×10^{-1} m for the south deck and -7.27×10^{-1} m to -7.84×10^{-1} m for the north decks. Although the eight corroded cables are included in all cases, the maximum deflection is different for each case. The importance of the 1st to 4th cables around the mid-span is also pointed out by this comparison. When the corroded cables are located at the same location on both decks (major cases 1 and 4), the same deflection occurred for both sides of the deck. The symmetric distribution of affected cables can result in symmetric deck deflection. The deflections for major case 3 were relatively high values for the north deck and low values for the south deck. Both decks deflected asymmetrically when the corrosion cables arrangement corresponded to major case 2. From Table 4.2, it can be noticed that the main span has the largest deflection for major case 4 of the south deck and for major case 3 of the north deck compared to the other major cases for the north and south decks. The location of the largest deflection is not always on the side of the deck where the

corroded cables are, as seen in subcase 4-1-75, for which corroded cables were located on the east side and the maximum deflection point was on the west side of the same deck.

Table 4.2. Maximum deflection summary for all cases on both decks

South	Max Deflection(m)	Percentage	Location (m)	North	Max Deflection(m)	Percentage	Location (m)
Reference	-0.712	0.00%	0.00	Reference	-0.712	0.00%	0.00
1-1-75	-0.727	2.11%	0.00	1-1-75	-0.727	2.11%	0.00
1-2-75	-0.737	3.44%	0.00	1-2-75	-0.737	3.44%	0.00
1-3-75	-0.735	3.16%	0.00	1-3-75	-0.735	3.16%	0.00
2-1-75	-0.737	3.47%	3.91	2-1-75	-0.737	3.47%	-3.91
2-2-75	-0.738	3.66%	6.11	2-2-75	-0.738	3.66%	-6.11
2-3-75	-0.729	2.38%	2.91	2-3-75	-0.729	2.38%	-2.91
3-1-75	-0.704	-1.11%	0.00	3-1-75	-0.784	10.11%	0.00
3-2-75	-0.711	-0.14%	0.00	3-2-75	-0.773	8.51%	0.00
3-3-75	-0.712	0.00%	0.00	3-3-75	-0.756	6.18%	0.00
4-1-75	-0.748	5.00%	3.51	4-1-75	-0.748	5.00%	3.51
4-2-75	-0.743	4.28%	-3.11	4-2-75	-0.743	4.28%	-3.11
4-3-75	-0.735	3.22%	-7.11	4-3-75	-0.735	3.22%	-7.11

m-n-a : *m* means the major case, *n* means the subcase, *a* means the percentage of corrosion

Location: positive means on west side, negtive means on east side

4.4. Effect of cable corrosion level on cable stresses

The cables work together in the bridge system and are sensitive to the loading conditions. The corrosion in the stay cable reduces the cross-sectional area, resulting in load redistribution among the rest of the cables. To investigate the changes in cable stress due to the cable corrosion levels, the following section shows the stress comparison for the different cases considered.

Each cable stress relative change percentage, which reflects the change of stress compared to the stress obtained for the reference case, was calculated to determine how cable stresses vary, as different corrosion cases and subcases are applied to the stay cables. The relative change percentage of the cable stress is defined by Eq. 4.2. The positive values of the cable stress relative change percentage indicate an increase in the stress, whereas the negative values point to a decrease in the stress, with respect to the reference case stress. It can be noticed that the maximum cable stress for the reference

case due to gravity load only is 96 MPa, which is much lower than the tensile strength of the cable as shown in Figure 4.8. From the analysis, it is concluded that the stresses in the corroded cables did not exceed the yield strength of the high-strength steel.

$$\text{Stress relative change percentage} = \frac{S' - S}{S} \times 100\% \quad (4.2)$$

where: S': the stress after corrosion;

S: the stress before corrosion.

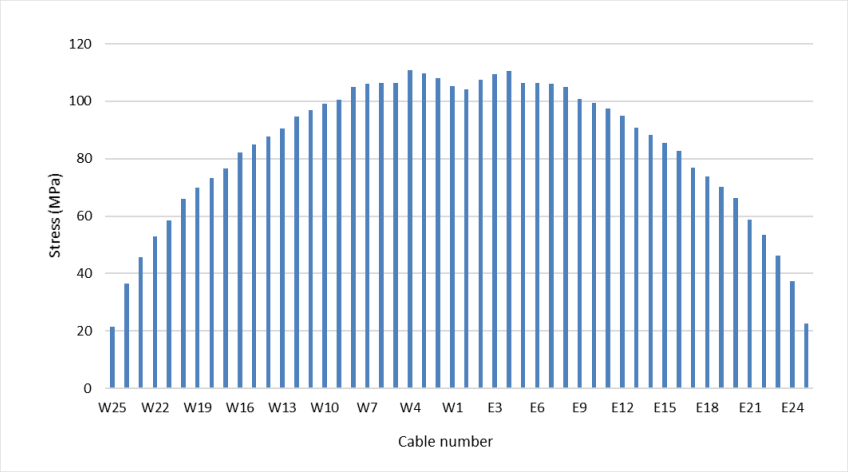

Fig. 4.8. Cable stress in reference case

4.4.1. Effect of cable corrosion levels

The stress relative change percentages for the cables located along the main span, obtained under the gravity load, are depicted in Figures 4.9(a) to (h). A total number of 50 cables on the main deck were selected to represent the stress relative change percentage. The *x* axis in Figure 4.9 represents the cable identifying number located on the main span; W and E signify the west and east sides of the deck in regard to the mid-span, respectively. The stress relative change percentage, as defined by Eq. 4.2, is represented on the vertical *y* axis of Figures 4.9(a) to (h).

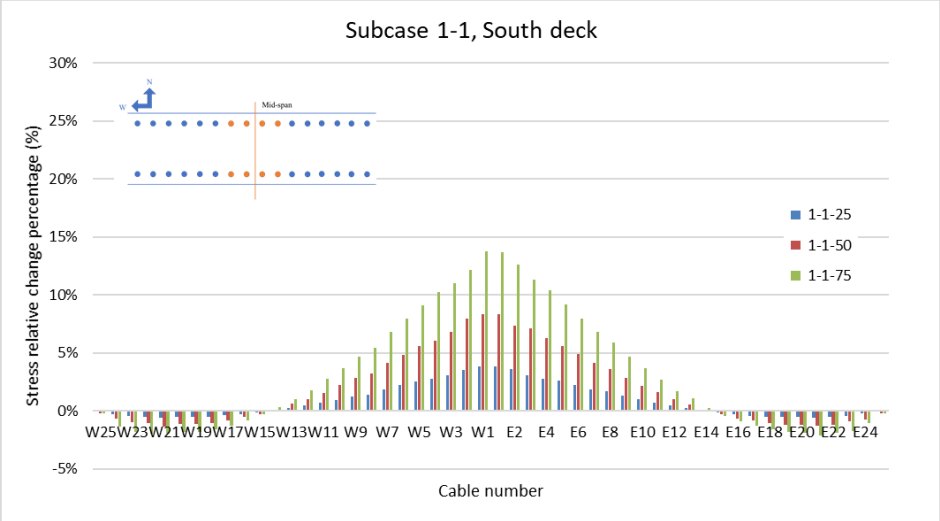
Subcase 1-1, South deck
Stress relative change percentage (%)
30%
25%
20%
15%
10%
5%
0%
-5%
Mid-span
1-1-25
1-1-50
1-1-75
W25 W23 W21 W19 W17 W15 W13 W11 W9 W7 W5 W3 W1 E2 E4 E6 E8 E10 E12 E14 E16 E18 E20 E22 E24
Cable number

(a)

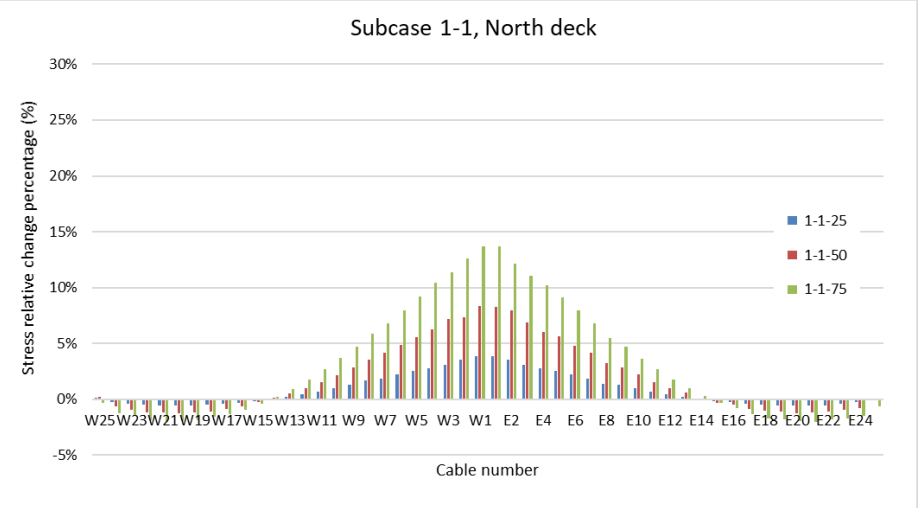
Subcase 1-1, North deck
Stress relative change percentage (%)
30%
25%
20%
15%
10%
5%
0%
-5%
1-1-25
1-1-50
1-1-75
W25 W23 W21 W19 W17 W15 W13 W11 W9 W7 W5 W3 W1 E2 E4 E6 E8 E10 E12 E14 E16 E18 E20 E22 E24
Cable number

(b)

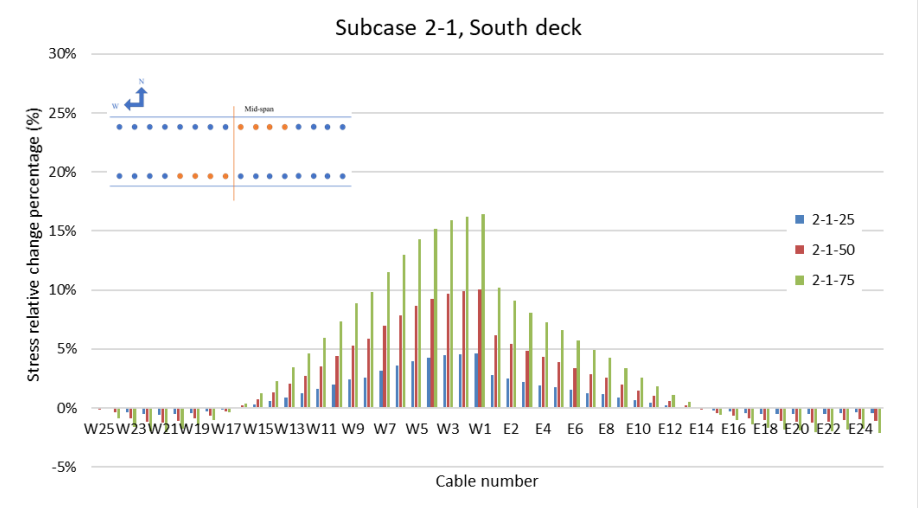
Subcase 2-1, South deck
Stress relative change percentage (%)
30%
25%
20%
15%
10%
5%
0%
-5%
Mid-span
2-1-25
2-1-50
2-1-75
W25 W23 W21 W19 W17 W15 W13 W11 W9 W7 W5 W3 W1 E2 E4 E6 E8 E10 E12 E14 E16 E18 E20 E22 E24
Cable number

(c)

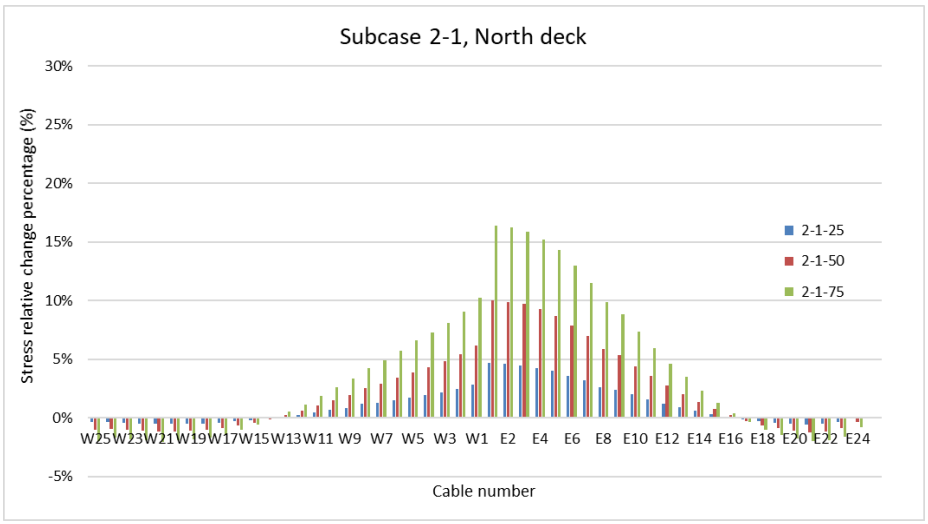
Subcase 2-1, North deck
Stress relative change percentage (%)
30%
25%
20%
15%
10%
5%
0%
-5%
W25 W23 W21 W19 W17 W15 W13 W11 W9 W7 W5 W3 W1 E2 E4 E6 E8 E10 E12 E14 E16 E18 E20 E22 E24
Cable number
2-1-25
2-1-50
2-1-75

(d)

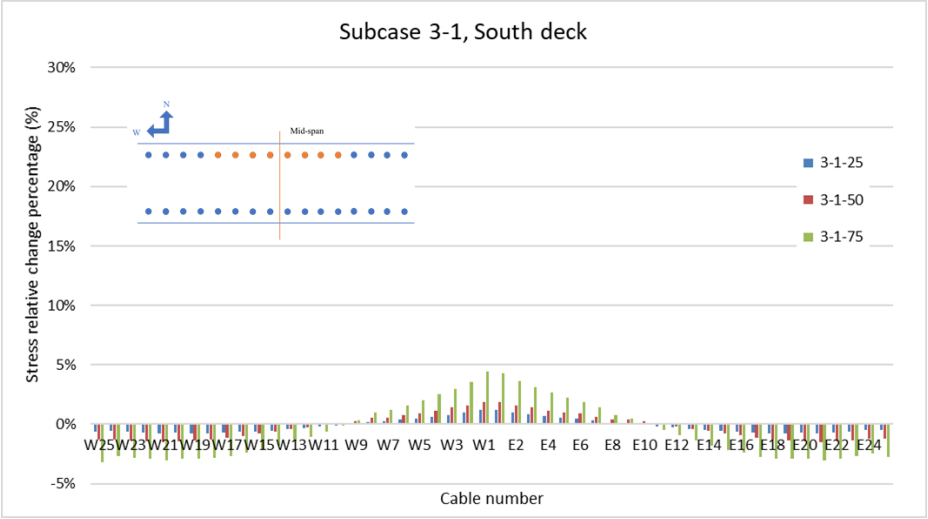
Subcase 3-1, South deck
Stress relative change percentage (%)
30%
25%
20%
15%
10%
5%
0%
-5%
N
W
Mid-span
W25 W23 W21 W19 W17 W15 W13 W11 W9 W7 W5 W3 W1 E2 E4 E6 E8 E10 E12 E14 E16 E18 E20 E22 E24
Cable number
3-1-25
3-1-50
3-1-75

(e)

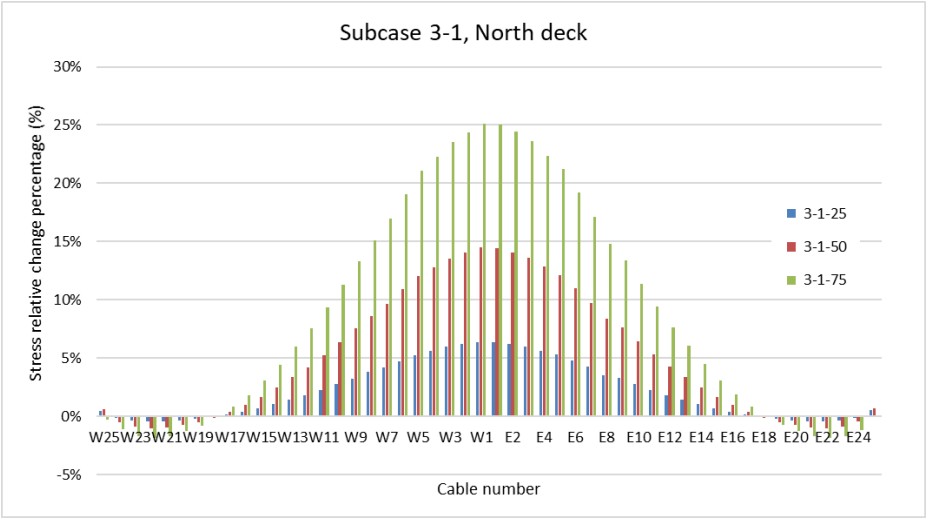
Subcase 3-1, North deck
Stress relative change percentage (%)
30%
25%
20%
15%
10%
5%
0%
-5%
W25 W23 W21 W19 W17 W15 W13 W11 W9 W7 W5 W3 W1 E2 E4 E6 E8 E10 E12 E14 E16 E18 E20 E22 E24
Cable number
3-1-25
3-1-50
3-1-75

(f)

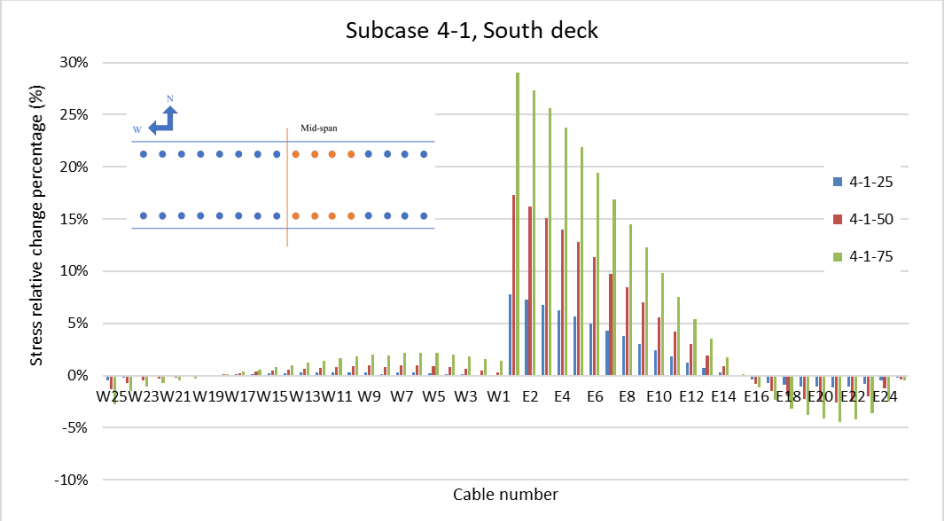

(g)

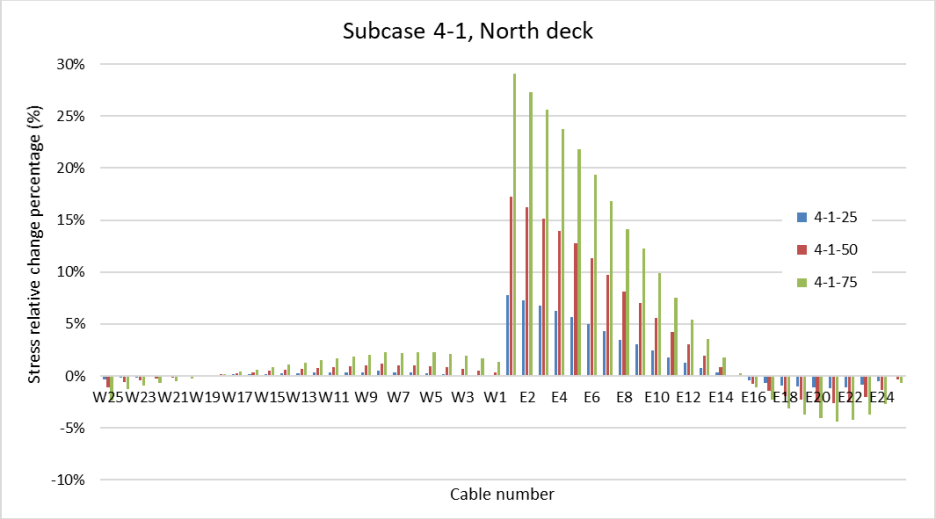

(h)

Fig. 4.9. Distribution of cable stress relative change percentages for different levels of cable corrosion: (a) South deck for subcase 1-1; (b) North deck for subcase 1-1; (c) South deck for subcase 2-1; (d) North deck for subcase 2-1; (e) South deck for subcase 3-1; (f) North deck for subcase 3-1; (g) South deck for subcase 4-1; (h) North deck for subcase 4-1.

For subcase 1-1 (Figures 4.9(a) and (b)), where cables W2, W1, E1 and E2 on both sides of the deck are corroded, the stress relative change percentage is symmetric with respect to the mid-span and it is identical on both south and north decks. The highest stress percent change amplitudes are recorded in the middle of the deck, and they are

3.87%, 8.33% and 13.73% for 25%, 50% and 75% corrosion levels, respectively. The largest reduction in stress percent change is noticed on cables E21 and W21, registering stress ratios of -0.57%, -1.32% and -2.13% reduction for 25%, 50% and 75% corrosion levels, respectively. The stress reduction is comparatively smaller than the stress augmentation. In the subcase 2-1, which is shown in Figures 4.9(c) and (d) for the south and north decks, respectively, cables E1 to E4 on the north deck and W1 to W4 of the south deck are altered. The largest relative change percentage occurs on cable W1 on the south deck and cable E1 on the north deck with a 4.65%, 10.04% and 16.40% increase for corrosion levels of 25%, 50% and 75%, respectively. The stress relative change percentage increases more on the west side of the south deck and the east side of the north deck due to the corroded cables located on the corresponding deck sides. The cables near the two towers bear less stress on both decks, with a reduction ratio of less than -2.05%. For subcase 3-1 presented in Figures 4.9(e) and (f), the corroded cables are all located on the north deck, with cables E1 to E4 and W1 to W4 being affected. The stress relative change percentage increases on the north deck are higher than those on the south deck, with 6.4%, 14.51% and 25.13% for cables W1 and E1 on the north deck, with corrosion levels of 25%, 50% and 75%, respectively, and 1.23%, 2.68% and 4.43% for cables W1 and E1 on the south deck. However, the stress losses are higher on the south side (Figure 4.9(e)). The largest negative stress relative change percentages registered values of -0.75%, -1.73% and -3.20% for cables W21 and E21 on the south deck and -0.43%, -1.01% and -1.82% for cables W21 and E21 on the north deck, with 25%, 50% and 75% corrosion levels, respectively. For subcase 4-1 (Figures 4.9(g) and (h)), the stress relative change percentages are higher on the east sides of both decks. The cables on the west side barely experience a change in the stress values compared to the reference case. For the corroded cables located on the east side, the highest relative change percentages are 7.81%, 17.30% and 29.07% for the three different corrosion levels, respectively, affecting cable E1 on both decks. The stress decrease registered a ratio of -1.16%, -2.6% and -4.44% in cable W21 on both decks

for the three corrosion levels 25%, 50% and 75%, respectively.

For all the cases considered, cable corrosion increases the stresses of the corroded and adjacent cables, allowing only for small differences of stress relative change percentage for the rest of the cables. Because the cables that are more damaged have less cross-sectional area and take more load, a higher level of corrosion results in a larger increase in the cable stress percent change. Since corroded cables take more load, the largest increases of stress occur where the corroded cables are located. The stress relative change percentages in the adjacent cables are less influenced than the stress increased due to the corroded cables, because the cross-sectional area does not change for healthy cables. The stress reduces in cables which are located away from the corroded cables due to the load redistribution. As for the cables W21 to W25 and E21 to E25 close to the towers, their internal stresses decrease with the higher corrosion level, causing the larger stress loss among these cables.

4.4.2. Effect of distance from mid-span

When the corroded cables are located further from the middle point of the deck, the largest percent difference happened in different cables. Comparing the stress relative change percentage for different subcases can help discover some trends when damaged cables shift position. The same cables on both north and south decks, as used in the previous section, were investigated with 75% corrosion level (Figures 4.10(a) to (h)).

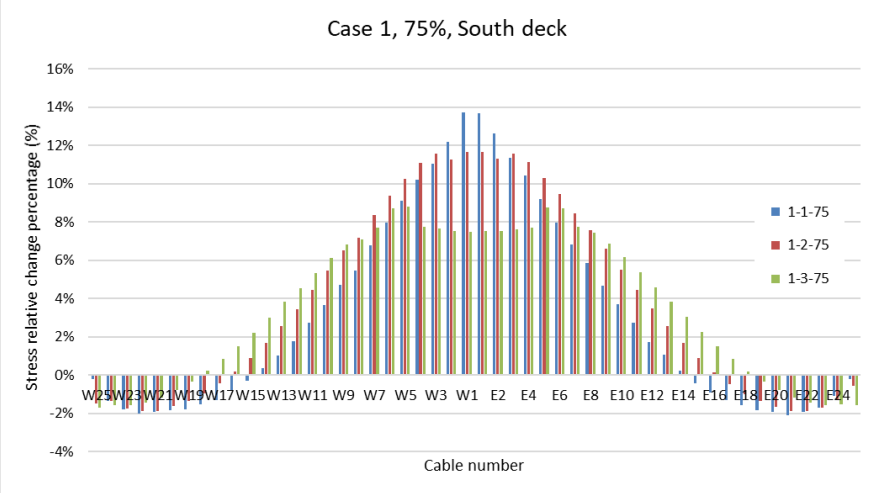

(a)

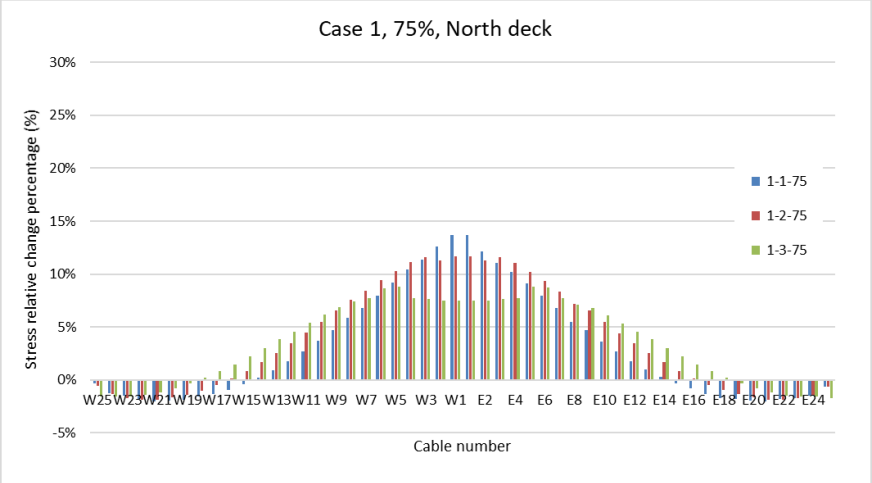
Case 1, 75%, North deck
Stress relative change percentage (%)
30%
25%
20%
15%
10%
5%
0%
-5%
W25 W23 W21 W19 W17 W15 W13 W11 W9 W7 W5 W3 W1 E2 E4 E6 E8 E10 E12 E14 E16 E18 E20 E22 E24
Cable number
1-1-75
1-2-75
1-3-75

(b)

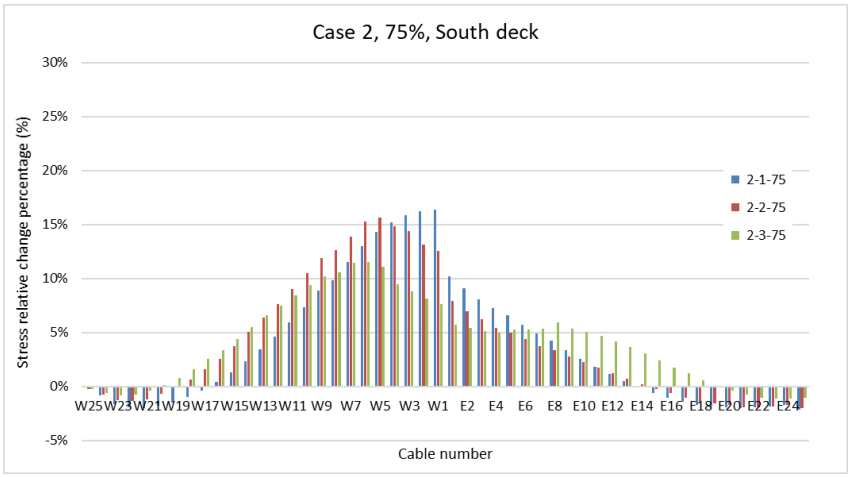
Case 2, 75%, South deck
Stress relative change percentage (%)
30%
25%
20%
15%
10%
5%
0%
-5%
W25 W23 W21 W19 W17 W15 W13 W11 W9 W7 W5 W3 W1 E2 E4 E6 E8 E10 E12 E14 E16 E18 E20 E22 E24
Cable number
2-1-75
2-2-75
2-3-75

(c)

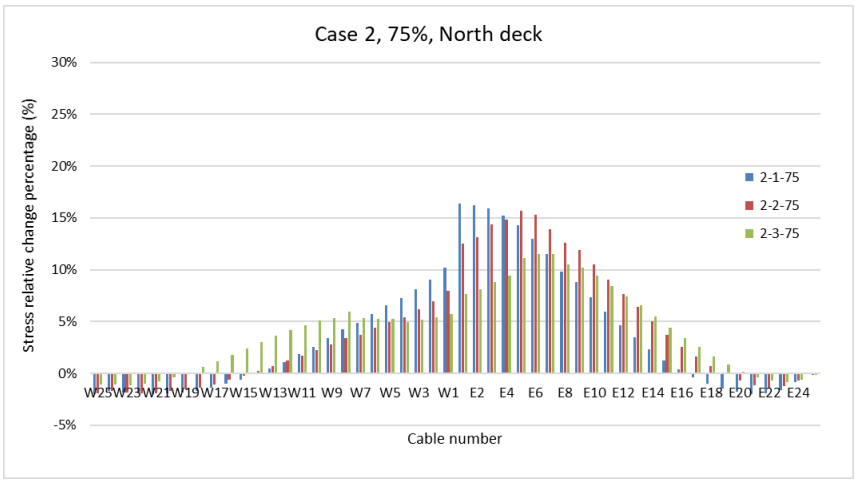
Case 2, 75%, North deck
Stress relative change percentage (%)
30%
25%
20%
15%
10%
5%
0%
-5%
W25 W23 W21 W19 W17 W15 W13 W11 W9 W7 W5 W3 W1 E2 E4 E6 E8 E10 E12 E14 E16 E18 E20 E22 E24
Cable number
2-1-75
2-2-75
2-3-75

(d)

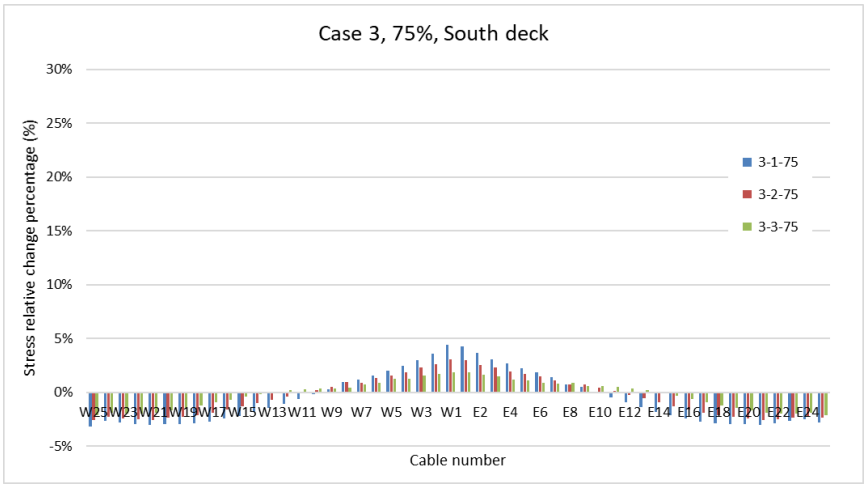
Case 3, 75%, South deck
Stress relative change percentage (%)
30%
25%
20%
15%
10%
5%
0%
-5%
W25 W23 W21 W19 W17 W15 W13 W11 W9 W7 W5 W3 W1 E2 E4 E6 E8 E10 E12 E14 E16 E18 E20 E22 E24
Cable number
3-1-75
3-2-75
3-3-75

(e)

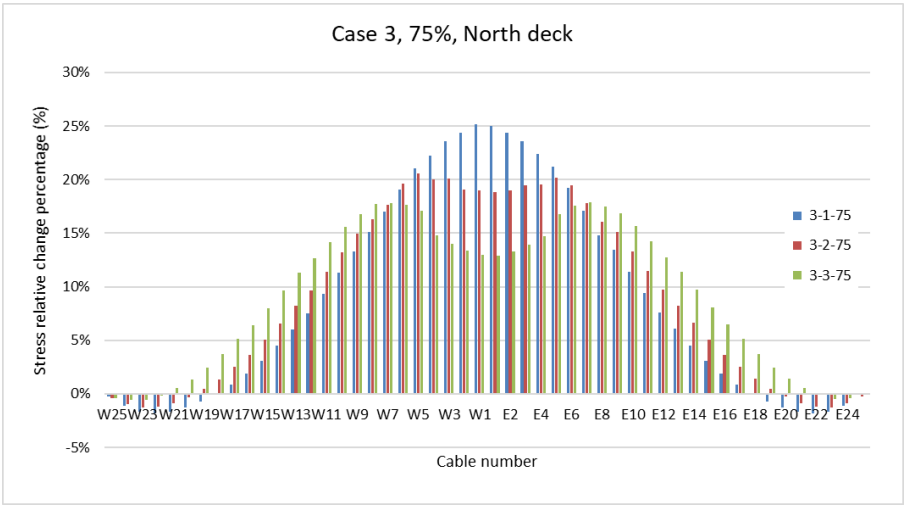
Case 3, 75%, North deck
Stress relative change percentage (%)
30%
25%
20%
15%
10%
5%
0%
-5%
W25 W23 W21 W19 W17 W15 W13 W11 W9 W7 W5 W3 W1 E2 E4 E6 E8 E10 E12 E14 E16 E18 E20 E22 E24
Cable number
3-1-75
3-2-75
3-3-75

(f)

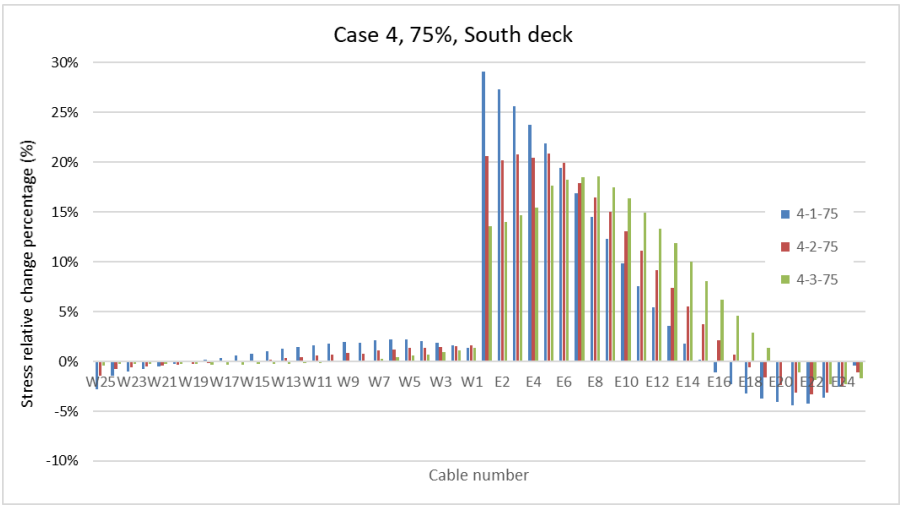
Case 4, 75%, South deck
Stress relative change percentage (%)
30%
25%
20%
15%
10%
5%
0%
-5%
-10%
W25 W23 W21 W19 W17 W15 W13 W11 W9 W7 W5 W3 W1 E2 E4 E6 E8 E10 E12 E14 E16 E18 E20 E22 E24
Cable number
4-1-75
4-2-75
4-3-75

(g)

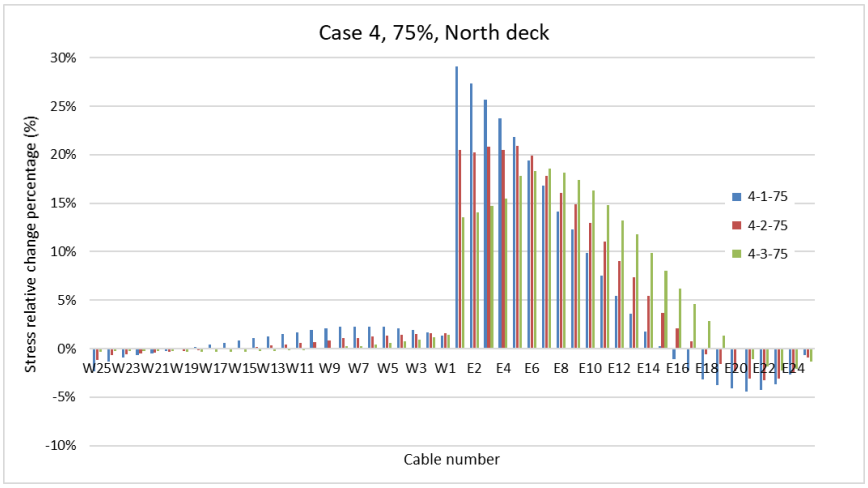

(h)

Fig. 4.10. Stress relative change percentage comparison for different subcases with 75% corrosion level: (a) South deck for subcase 1-1; (b) North deck for subcase 1-1; (c) South deck for subcase 2-1; (d) North deck for subcase 2-1; (e) South deck for subcase 3-1; (f) North deck for subcase 3-1; (g) South deck for subcase 4-1; (h) North deck for subcase 4-1.

For major case 1 (Figures 4.10(a) and (b)), the highest percent changes are 13.73% on cables W1 and E1, 11.68% on cables W1 and E1 and 8.81% on cables W5 and E5 for subcases 1-1, 1- 2 and 1-3, respectively. The highest stress reduction is -2.13% on E21 and W21, -1.90% on E21 to E22 and W21 to W22, and -1.72% on E25 and W25 for the three subcases, respectively. For major case 2 shown in Figures 4.10(c) and (d), the highest relative stress change percentage is 16.4% for cable W1, 15.65% for cable W5 and 11.51% for cable W6 for the south deck for subcases 2-1, 2-2 and 2-3, respectively. Cables E1, E5 and E6 located on the north deck for subcases 2-1, 2-2 and 2-3 registered the same reduction ratios as the south deck. The largest reductions of stress change percentage are -2.13%, -2.03% and -1.14% for cables E25, E25 and E23 on the south deck and W25, W25 and W23 on the north deck. The reductions are relatively small compared to the stress increase. Figures 4.10(e) and (f) showed the comparison for major case 3. The largest stress relative change percentage is 25.13% for cables W1 and E1, 20.55% for cables W5 and E5, and 17.89% for cables W7 and

E7 of the north deck for subcases 3-1, 3-2 and 3-3, respectively. The reductions in stress for cables on the north deck are small and can be ignored. The increase in the relative change percentages was not obvious on the south deck. The highest increase in the relative change percentages is 4.43%, 3.07% and 1.87% for cables W1 and E1 on the south deck for the subcases 3-1, 3-2 and 3-3, respectively. The lowest percent change is on the south deck with -3.20%, -2.57% and -2.14% for cables W25 and E25 for subcases 3-1, 3-2 and 3-3, respectively. As for the major case 4 (Figures 4.10(g) and (h)), the highest stress increase ratio is 29.07% on cable E1, 20.88% on cable E5 and 18.55% on cable E7 for both decks and for subcases 4-1, 4-2 and 4-3, respectively. The largest stress drop is -4.44% on cable E21, -3.31% on cable E22, and -2.31% on cable E23 for both decks and for subcases 4-1, 4-2 and 4-3, respectively. The stress changes are not significant on the west side of the decks for the case 4.

In all the investigated cases, the largest relative change percentage is registered for subcase 1 for each of the major cases 1 to 4, which corresponds to the case where the corroded cables are located in the vicinity of the mid-span. When the distance between the corroded cables and the middle point of the decks increases, the highest relative change percentage exists in the damaged cables which are located at a further position. The cable loads in the corroded cables located further from the mid-span increase less than in subcase 1, thus the largest relative change percentage decreases as the distance increases. The changes of the stress in the affected cables are larger than the ones registered for the other cables.

4.4.3. Effect of corroded cables distribution

The changes in stresses caused by different distributions of the corroded cables are discussed in Figures 4.11(a) to (f), where the same subcases for each major case are compared for the same corrosion level of 75%.

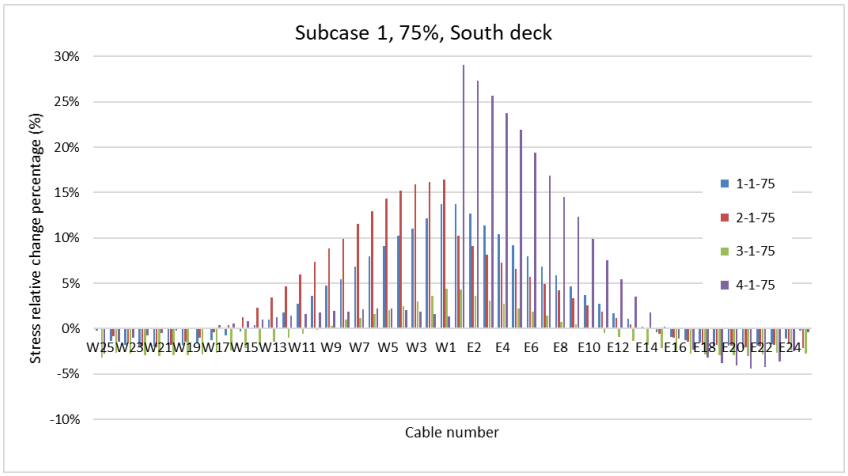
Subcase 1, 75%, South deck
Stress relative change percentage (%)
30%
25%
20%
15%
10%
5%
0%
-5%
-10%
W25 W23 W21 W19 W17 W15 W13 W11 W9 W7 W5 W3 W1 E2 E4 E6 E8 E10 E12 E14 E16 E18 E20 E22 E24
Cable number
1-1-75
2-1-75
3-1-75
4-1-75

(a)

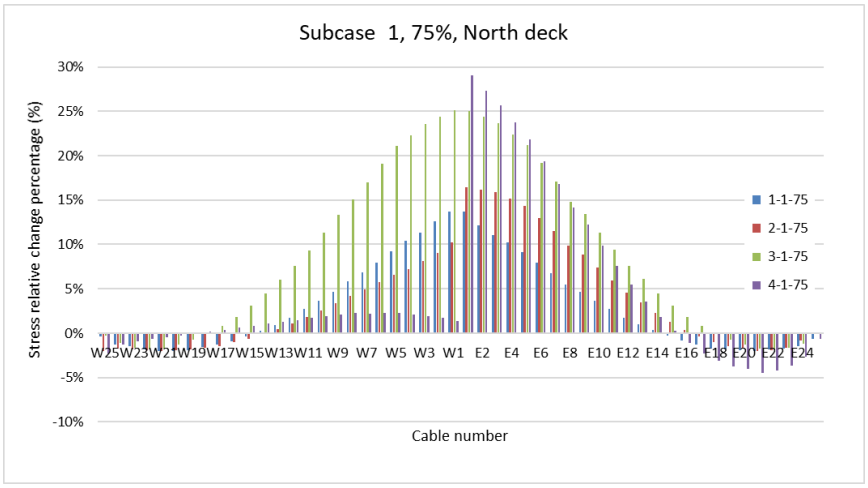
Subcase 1, 75%, North deck
Stress relative change percentage (%)
30%
25%
20%
15%
10%
5%
0%
-5%
-10%
W25 W23 W21 W19 W17 W15 W13 W11 W9 W7 W5 W3 W1 E2 E4 E6 E8 E10 E12 E14 E16 E18 E20 E22 E24
Cable number
1-1-75
2-1-75
3-1-75
4-1-75

(b)

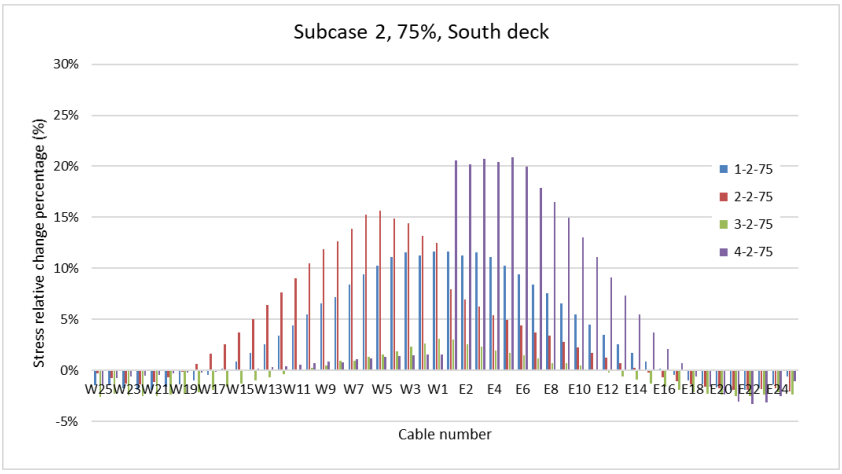
Subcase 2, 75%, South deck
Stress relative change percentage (%)
30%
25%
20%
15%
10%
5%
0%
-5%
W25 W23 W21 W19 W17 W15 W13 W11 W9 W7 W5 W3 W1 E2 E4 E6 E8 E10 E12 E14 E16 E18 E20 E22 E24
Cable number
1-2-75
2-2-75
3-2-75
4-2-75

(c)

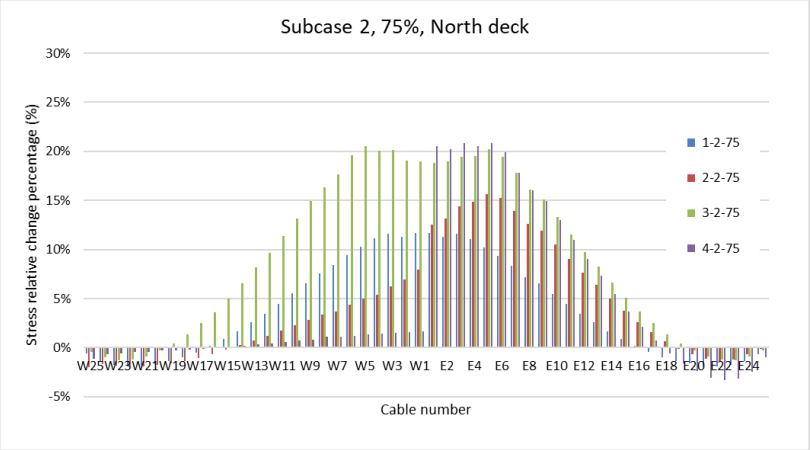

(d)

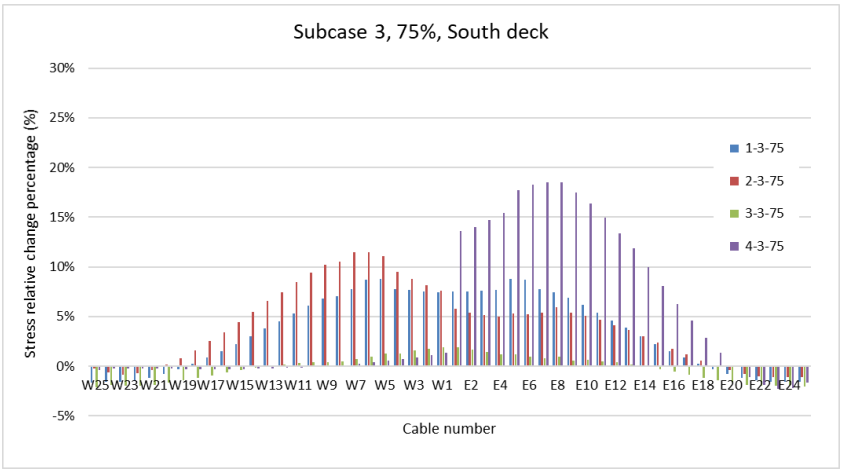

(e)

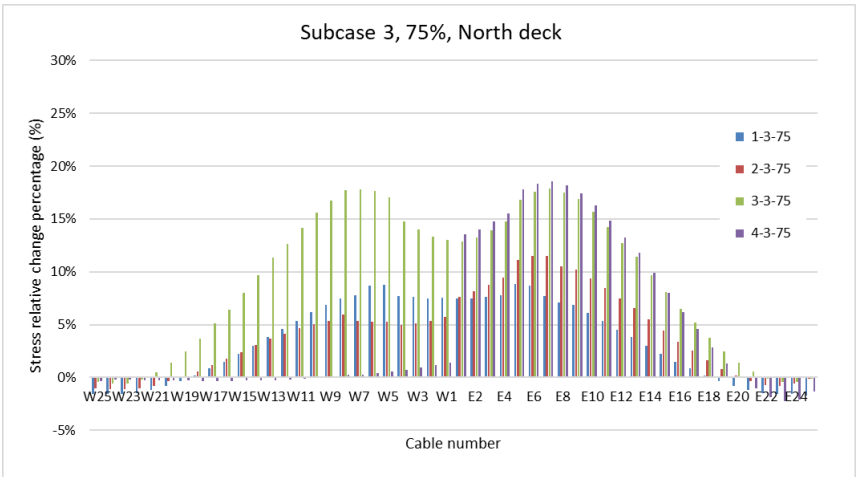

(f)

Fig. 4.11. Stress relative change percentage comparison for different major cases with 75% corrosion level: (a) South deck for subcase 1; (b) North deck for subcase 1; (c) South deck for subcase 2; (d) North deck for subcase 2; (e) South deck for subcase 3; (f) North deck for subcase 3.

Figures 4.11(a) and (b) illustrate the stress percentage differences for the four cases investigated for the same subcase 1, for 75% corrosion level, when the affected cables are closest to the mid-span of the bridge. The highest increase of relative change percentage can be observed in subcase 4-1-75, registering the stress increase of 29.07% for cable E1 on both decks. For the subcase 2 shown in Figures 4.11(c) and (d), the subcase 4-2-75 also resulted in the larger stress increase, in the range of 19.9% to 20.88% for cables E1 to E6 on both decks; however, the subcase 3-2-75 showed an increase stress percentage in the range of 18.84% to 20.55%, which is close to that in subcase 4-2-75, for cables E1 to E6 and W1 to W6 on the north deck. The stress relative change registered for the four major cases in subcase 3 shown in Figures 4.11(e) and (f) have a similar trend. The subcase 4-3-75 caused the largest increase in stress in the range of 17.68% to 18.55% in cables E5 to E8 on both decks. The subcase 3-3-75 resulted in an 'M' shape in the stress relative change percentage distribution, with a close percentage change to that of subcase 4-3-75 on the north deck.

From all the investigated cases and subcases, the major case 4 is considered critical, as the largest stress increase was noticed for both decks, due to the fact that all the corroded cables are located on one side only. Major case 3, which also has all corroded cables on one deck, results in stress relative change percentages close to major case 4. The reduction of cable stress can also be observed in the cables with large numbers, i.e., those located the furthest from mid-span, as seen in Figures 4.11(a) to (f).

4.4.4. Summary

The results presented in this section show how the distribution of the corroded cables and different levels of corrosion impact the stresses in the cables. When the cables are affected by corrosion, a redistribution of stresses occurs. The corroded cables show a comparative increase in stresses, while the adjacent cables also get affected by increasing their stresses. The cables near the towers bear less stress than the stresses of the cables used for the reference case, where no corrosion is applied. The higher the

level of corrosion of the cables is, the higher the stresses they withstand. When the corrosion is simulated on the cables located in the middle of the span, these cables are more stressed than the cables from other locations along the deck. The same phenomena also happen when all the cables on one side or one deck are affected. In practice, smart sensors installed at the bridge site could be used to detect these relative stress change percentages as a result of cable damage due to corrosion.

Chapter 5 - Dynamic response of the bridge model

In this chapter, the dynamic response of the Stonecutters Bridge model, especially for the middle span and towers, is discussed for the different corrosion scenarios introduced in Chapter 4. The natural frequencies of the first 30 vibration modes are presented to show the changes in frequency due to stay cables corrosion. The time history responses and their corresponding power spectrum density (PSD) are also examined, denoting the possible coupled motions of the deck and the corresponding vibration frequencies.

5.1. Parametric study of natural frequency

As discussed in Chapter 3, the eigenvalues and eigenvectors, which result from solving the eigenvalue equations of the structure, can be interpreted as the frequencies and corresponding mode shapes of the structure free vibrations. The natural frequency and mode shapes can effectively analyze the dynamic characteristics of the bridge. The first natural frequencies are the dominant modes for the structural behavior at which the structure will vibrate. Cable-stayed bridges are complicated structures which consist of various structural components with different stiffness and damping characteristics. They are more flexible than the girder bridges, and the precise structural analysis of natural frequencies and natural mode shapes is essential (Vikas et al., 2013).

For the Stonecutters Bridge model, the natural frequency analysis was conducted obtaining the first 30 modes of vibration, which contains the low and high orders of vibration modes and out of which the first 10 modes are actually the most important and are extracted from the finite element model. The parametric study focuses on changing the corrosion level in the stay cables, as per the static analysis performed in Chapter 4. Then, it considers translating the position of the corroded cables along the bridge deck, and finally, it compares different corroded cables and level of corrosion arrangements. To further analyze the impact of corrosion damage on the stay cables,

the frequency relative change with respect to a healthy bridge without cable corrosion is computed according to Equation 5.1:

$$\text{Frequency relative change} = \frac{\text{frequency after corrosion} - \text{frequency before corrosion}}{\text{frequency before corrosion}} \quad (5.1)$$

5.1.1. Effect of corrosion level

The percentage (%) change in vibration frequencies for major cases 1, 2, 3 and 4 and different levels of corrosion damage is illustrated in Figures 5.1, 5.2, 5.3 and 5.4, respectively. For each major case, the stay cables near the mid-span of the bridge were corroded (subcase 1).

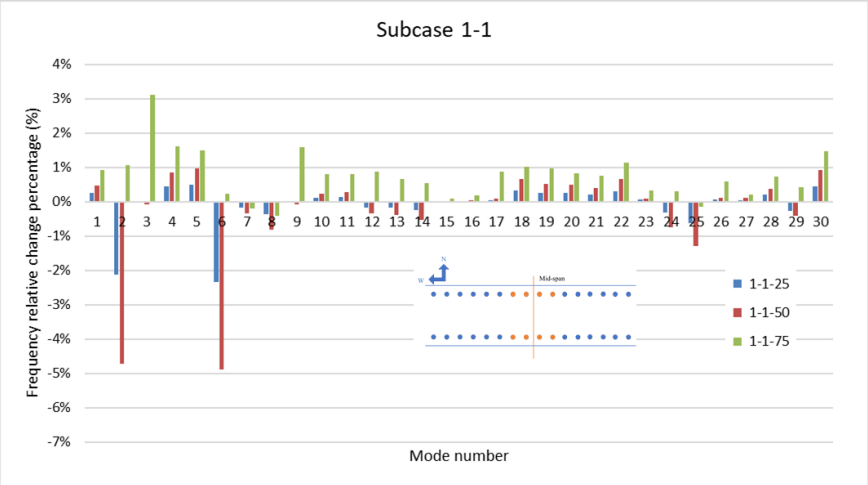

Fig. 5.1. Frequency relative change percentage for subcase 1-1

For case 1-1, as illustrated in Figure 5.1, the corrosion level induces a change of the frequency value and affects certain vibration modes more than others. The first 10 vibration modes have a larger influence on the structural behavior of the bridge than the higher modes. For the case with 25% corrosion level, 1-1-25, the natural frequencies for the 1st, 4th, 5th, 10th, 11th, 18th to 22nd 28th and 30th vibration modes increased in respect to the undamaged cables (reference case). However, the increased ratios for these modes are less than 0.5%. The frequencies corresponding to the rest of the

vibration modes decreased or did not change in respect to the undamaged (reference) case; for the 2nd and 6th vibration modes the frequency relative change decreased the most, reaching values of -2.12% and -2.33%, respectively. Similar observations are noted for the case with 50% corrosion level (subcase 1-1-50); however, the frequency relative change increase (especially 0.85%, 0.97% and 0.93% for the 4th, 5th and 30th modes, respectively) and the decrease (especially -4.71% and -4.89% for the 2nd and 6th modes, respectively) are larger than those observed for the 25% corrosion case. For the case with 75% corrosion damage (subcase 1-1-75), the frequencies decreased by less than -0.5%, only the 7th, 8th, and the rest of the modes, the frequencies have increased showing larger ratios than for the other two cases. The 3rd vibration mode registered the largest increase frequency ratio, with a value of 3.1% above that of the undamaged (reference) case.

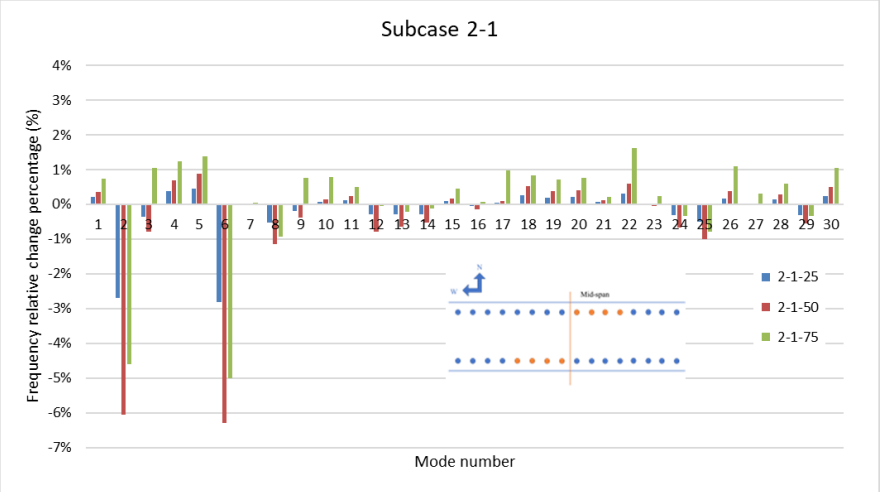

Fig. 5.2. Frequency relative change percentage for subcase 2-1

For the subcase 2-1 (Figure 5.2), the increasing level of corrosion in the stay cables led to an increase in the frequencies compared to the reference case, for most of the vibration modes, and only for some of the modes the relative frequency change ratio decreased (2nd and 6th modes in Figure 5.2). For the case with 25% corrosion level, subcase 2-1-25, the natural frequencies for the 2nd, 3rd, 6th, 8th, 12th to 14th, 24th, 25th and

29th modes decreased with respect to undamaged case; among these modes, the 2nd and 6th modes registered relatively large decreases of frequency relative ratios, of -2.69% and -2.82%, respectively. The rest of the modes showed only small increase ratios for the natural frequencies, which were less than 0.5%. The frequencies observed for the case with 50% corrosion level was similar to that of 25% corrosion damage. The natural frequencies had the similar variation trends for the vibration modes, but registered larger increments. The increase ratios are less than 1%, while the decrease ratios for the 2nd and 6th modes are -6.06% and -6.3%, respectively; these are the largest decreases compared to the other two corrosion conditions. For the case with 75% corrosion damage (subcase 2-1-75), for most of the modes the frequencies increased, except for the 2nd, 6th, 8th, 12th to 14th, 24th, 25th and 29th modes which decreased in frequencies, with respect to the reference case. The 3rd, 4th, 5th registered increase ratios of 1.05%, 1.24%, 1.37%, respectively. The 2nd and 6th modes registered relatively higher decrease ratios of -4.61% and -5.01%, respectively.

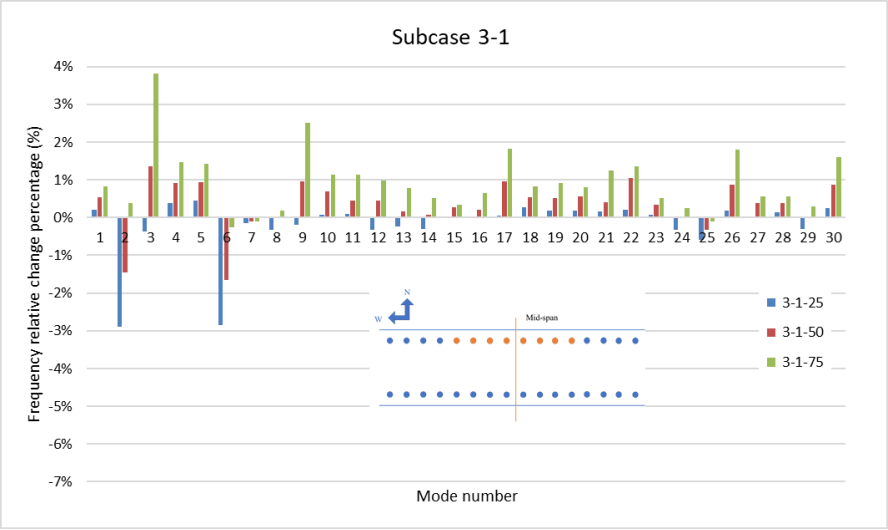

Fig. 5.3. Frequency relative change percentage for subcase 3-1

The results for subcase 3-1, where the corroded cables were placed at the north deck only, are shown in Figure 5.3. For the case with 25% corrosion level, subcase 3-1-25, the natural frequencies for the 2nd, 3rd, 6th to 9th, 12th to 14th, 24th, 25th and 29th decreased

with respect to the undamaged case; moreover, the 2nd and 6th modes registered the largest decreases of -2.9% and -2.85%, respectively. Small increase ratios in natural frequencies can be observed for the remaining modes as well. For the case with 50% corrosion level (subcase 3-1-50), only the 2nd, 6th, 7th and 25th vibration modes registered a decrease in natural frequencies with respect to the undamaged case. The 2nd and 6th modes have relatively large decrease in relative change ratios with values of -1.45% and -1.66%, respectively. The increased relative change percentages for the 3rd and 22nd are respectively 1.36% and 1.05%. For the case with 75% corrosion damage (subcase 3-1-75), most of the vibration modes have larger increases than the subcases 3-1-25 and 3-1-50, except for modes 6th, 7th and 25th, which have small decreases in frequencies. The 3rd, 9th, 17th, 26th and 30th registered relatively high increased relative change ratios of 3.82%, 2.5%, 1.82%, 1.81% and 1.6%, respectively.

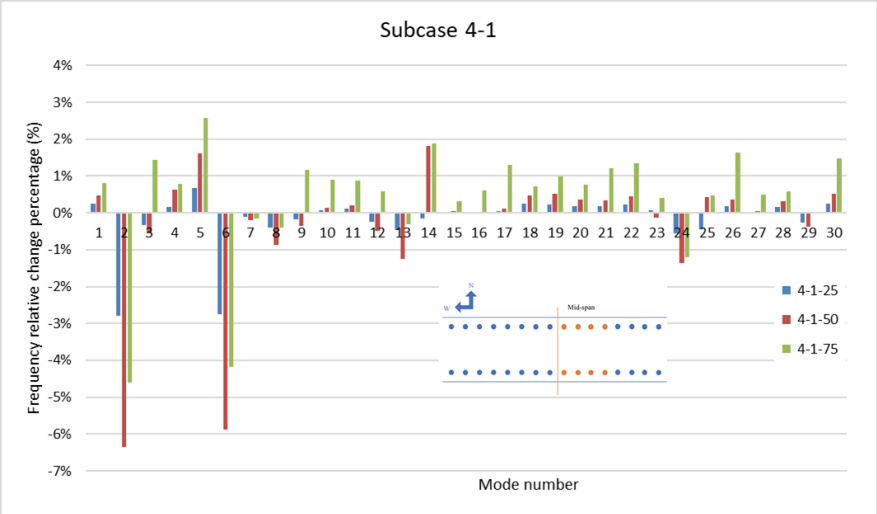

Fig. 5.4. Frequency relative change percentage for subcase 4-1

As for subcase 4-1 (see Figure 5.4), the corroded cables are placed on both decks but on the east side with respect to the middle point. For the case with 25% corrosion level, subcase 4-1-25, the natural frequencies for the 2nd, 3rd, 6th to 9th, 12th to 14th, 24th, 25th and 29th decreased with respect to the undamaged case, among which the 2nd and 6th modes registered relatively large decreases of -2.8% and -2.74%, respectively. The

rest of the modes showed little increases in natural frequencies. The frequencies observation for the case with 50% corrosion level (subcase 4-1-50) is similar to that of 25% corrosion level. The natural frequencies have similar increasing and decreasing trends, but with larger increments, except for the 14th, 23rd and 25th modes; for these vibration modes, the subcase 4-1-50 resulted in opposite trend of relative frequency change. The increases for the 5th and 14th were 1.62% and 1.8%, respectively; the decreases for the 2nd and 6th modes are -6.36% and -5.88%, respectively, which are the largest decreases among the vibration modes. For the case with 75% corrosion damage (subcase 4-1-75), the 2nd, 6th to 8th, 13th and 24th modes have decreases in frequencies, and the rest of the modes have increased frequencies, compared to the other two cases. The 3rd, 5th, 9th, 14th, 21st, 22nd, 26th and 30th modes registered increases of 1.43%, 2.58%, 1.16%, 1.88%, 1.22%, 1.35%, 1.65% and 1.48%, respectively. The 2nd and 6th modes registered relatively higher decreases of -4.6% and -4.18%, respectively.

5.1.2. Effects of distance from mid-span

The impact of a case with 75% corrosion level was investigated for cables located at different positions along the span of the bridge (subcases 1 to 3); the differences were recorded in terms of increasing the distance between two groups of four corroded cables along the West and East sides of both decks. The results for the four major cases are presented in Figures 5.5 to 5.8, respectively.

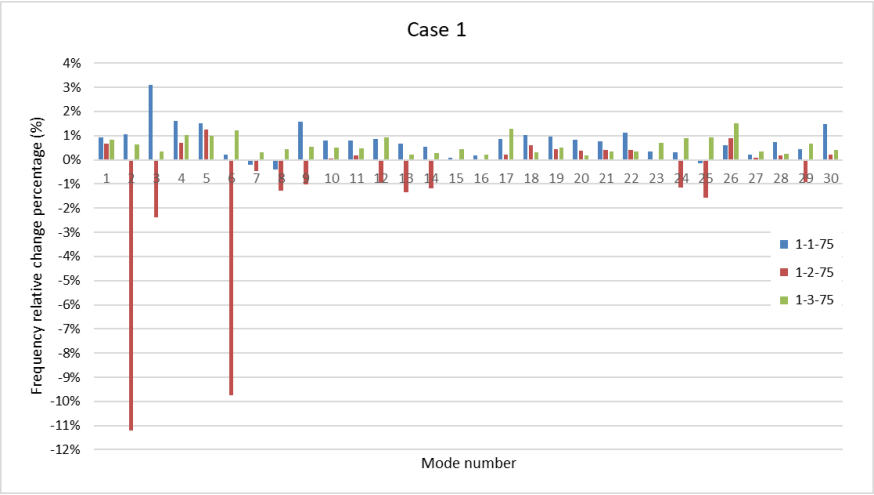

Fig. 5.5. Frequency relative change percentage for different subcases of case 1

Figure 5.5 represents the change of frequencies for the major case 1, considering the 75% corrosion level. For the subcase 1-1-75, most of the modes registered an increase in the natural frequencies with respect to the non-corroded case, except for the 7th, 8th and 25th modes. The 3rd, 4th, 5th, 9th and 30th modes registered relatively high increase relative change ratios of 3.1%, 1.61%, 1.51%, 1.59% and 1.48%, respectively. For the case in which the corroded cables were located from the 3rd cable in respect with the middle point of the deck (subcase 1-2-75), the 2nd, 3rd, 6th to 9th, 12th to 14th, 16th, 24th, 25th and 29th modes experienced a decrease in frequencies with respect to the undamaged case; the 2nd, 3th and 6th modes registered a relatively large decrease of -11.22%, -2.37% and -9.73%, respectively. The increased relative change percentages for the other modes are not obvious. For the case in which the corroded cables were located from the 5th cable from the mid-span (subcase 1-3-75), all the frequencies increased with respect to the reference case. The increased frequencies percentages were small for all the modes and also these were lower than the frequency changes registered for the subcase 1-1-75 in the first 10 modes.

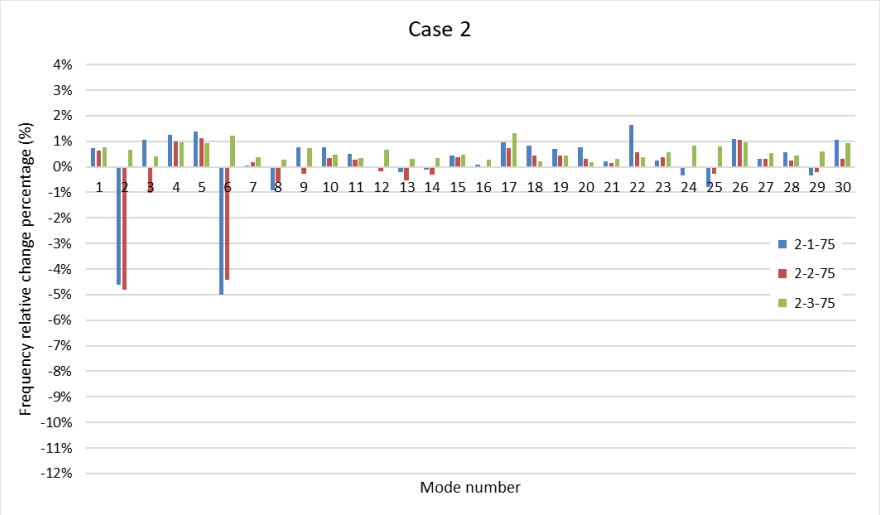

Fig. 5.6. Frequency relative change percentage for different subcases of case 2

Figure 5.6 presents the results for several subcases of the major case 2, in which

the damaged cables are located on the east side of the north deck and the west side of the south deck. For the subcase 2-1-75, most of the modes registered a slight increase in the natural frequencies with respect to the non-corroded case, except for the 2nd, 6th, 8th, 11th to 14th, 24th, 25th and 29th modes. The 2nd and 6th modes registered relatively large decreases of -4.61% and -5.01%, respectively. The relatively large ratios were 1.05%, 1.24%, 1.37% and 1.63% for the 3rd, 4th, 5th and 22nd modes, respectively. For the case in which the corroded cables were located from the 3rd cable from the middle point (subcase 2-2-75), the 2nd, 3rd, 6th, 8th, 9th, 12th to 14th, 25th and 29th modes experienced a decrease in frequencies with respect to the undamaged case, among which the 2nd and 6th modes registered a relatively large decrease of -4.82% and -4.41%, respectively. The increase ratios for the other modes were insignificant. For the case in which the corroded cables were located from the 5th cable from the mid-span (subcase 2-3-75), all the modes' frequencies increased with respect to the reference case. An increase in the frequency ratios was also observed for the 2nd and 6th modes.

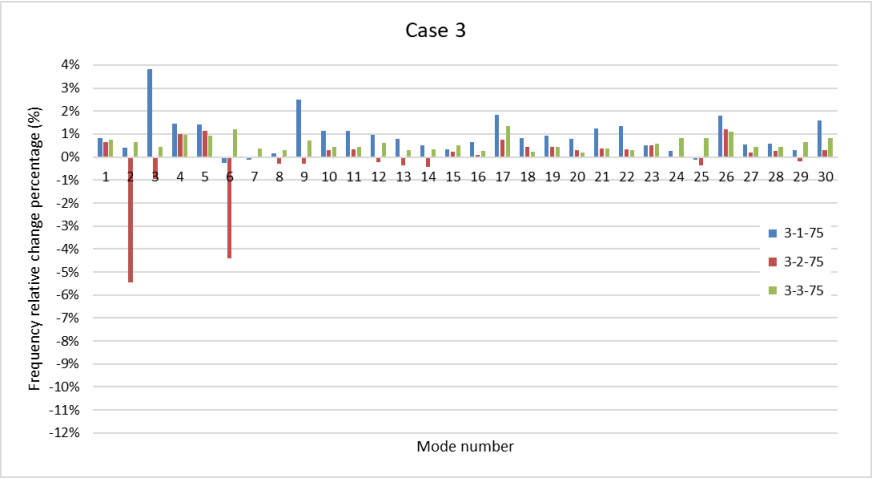

Fig. 5.7. Frequency relative change percentage for different subcases of case 3

For the major case 3, as illustrated in Figure 5.7, all the cables are corroded on the north deck. Thus, for the subcase 3-1-75, for which all the corrosion affected cables are near the middle of the deck, low decrease ratios were observed only for the 6th and 7th modes with -0.25% and -0.11% decreases, respectively. The increase ratios with respect

to the undamaged case were relatively high for most of the remaining modes compared to the other cases. Significant increases of 3.82% and 2.5% for 3rd and 9th modes can be noted in Figure 5.7. For the subcase 3-2-75, with the corroded cables located from the 3rd cable from the middle point, the 2nd, 3rd, 6th to 9th, 12th to 14th, 24th, 25th and 29th modes experienced a decreased frequency with respect to the reference case. Significant drops in the frequencies can be observed for the 2nd and 6th modes, up to -5.45% and -4.43%, respectively. The rest of the modes had slight increases in the natural frequencies. For the case in which the corroded cables were located from the 5th cable from the mid-span (subcase 3-3-75), the natural frequencies were increased for all the modes, although the increase was not pronounced.

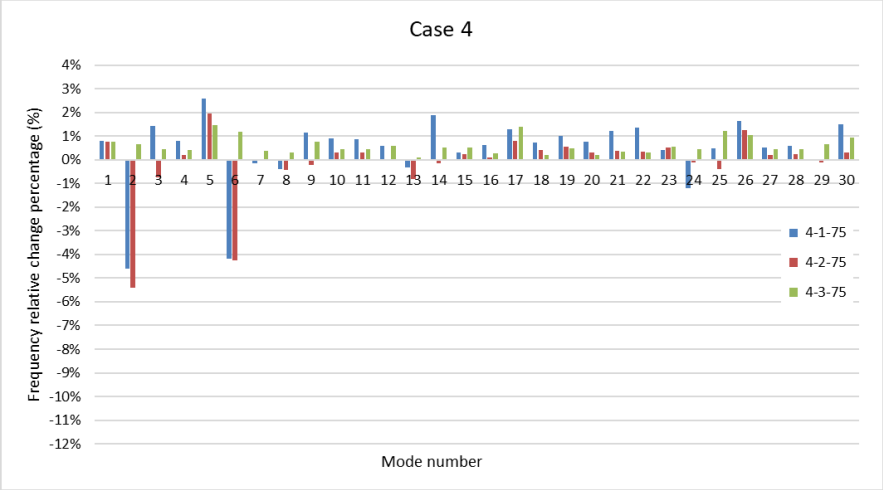

Fig. 5.8. Frequency relative change percentage for different subcases of case 4

Figure 5.8 presents the results for several corrosion subcases of major case 4, in which the corroded cables are located on the east side of both decks. For the subcase 4-1-75, for which the corroded cables were on both sides of the middle point, only the 2nd, 6th to 8th, 13th, 24th and 29th modes registered decreased frequency ratios, whereas the rest have increased frequencies. The 2nd and 6th modes had significant decreased relative frequency change ratios of -4.6% and -4.18%, respectively. The increased frequency ratios of 1.43%, 2.58%, 1.88% and 1.65% for the 3rd, 5th, 14th and 26th modes were

relatively high. For the subcase 4-2-75, similar observations were noted in that the 2nd, 3rd, 6th, 8th, 9th, 12th to 14th, 24th, 25th and 29th modes experience decreases in natural frequencies. Significant drops of -5.4% and -4.25% for the 2nd and 6th modes, respectively, are observed in Figure 5.8. The increased ratios for the other modes were less than that for subcase 4-1-75. For the subcase 4-3-75, all the modes registered increased frequencies ratios, although these increases were limited. The increased ratios for the 2nd and 6th modes can be observed only for the case 4-3-75.

5.1.3. Effect of corroded cables distribution

In order to investigate the effects brought by different arrangements of corroded cables along the deck, the same subcases and same 75% level of corrosion for the four major cases are compared in Figures 5.9 to 5.11.

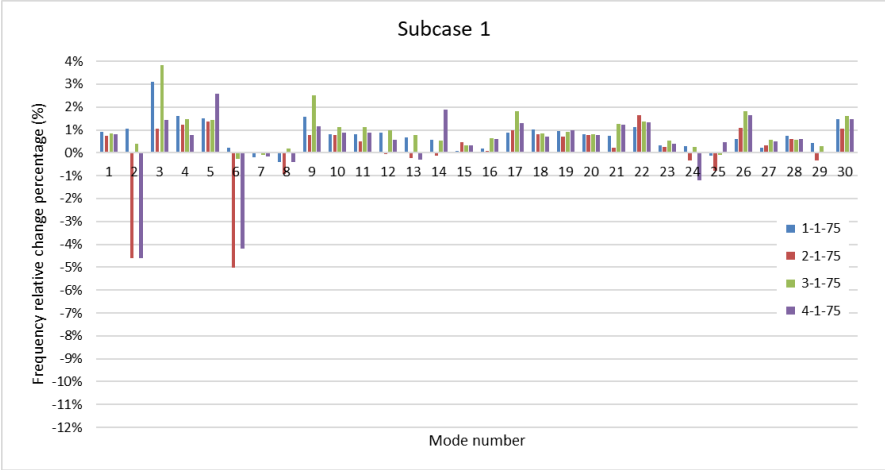

Fig. 5.9. Frequency relative change percentage of different major cases for subcase 1

For the subcases 1-1, 2-1, 3-1 and 4-1 (Figure 5.9), when all the affected cables are around the middle of the deck, the frequencies change ratio increased for almost all the modes, except for the lower modes 2, 6 to 8 and higher modes 13, 14, 24, 25 and 29. The major corrosion cases 2 and 4 result in the largest decrease of the frequency change for the 2nd (-4.61% for subcase 2-1-75 and -4.6% for subcase 4-1-75) and 6th (-5.01% for subcase 2-1-75 and -4.18% for subcase 4-1-75) modes, and the major case 1 and 3

cause a relatively large increase in frequency change for the 3rd (3.1% for subcase 1-1-75 and 3.82% for subcase 3-1-75) and 9th (1.59% for subcase 1-1-75 and 2.5% for subcase 3-1-75) modes. For the major case 4, where corroded cables are all on one side of the deck, the 5th and 14th vibration modes result in the highest frequency change with a value of 2.58% and 1.88%, respectively, compared to other modes.

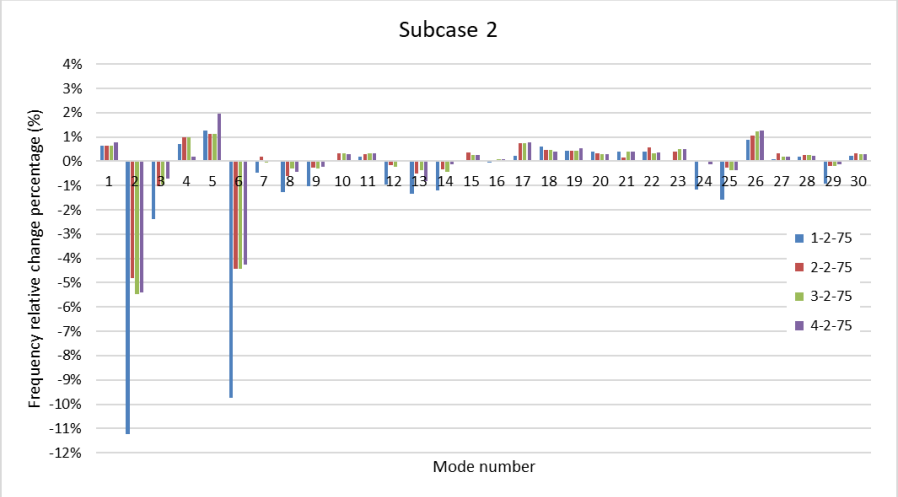

Fig. 5.10. Frequency relative change percentage of different major cases for subcase 2

As the corroded cables are located from the 3rd cable from the middle of the deck, as in subcase 2 illustrated in Figure 5.10, similar observations can be noted for each mode. It can be observed that the 2nd and the 6th modes have a distinct larger decrease in frequency, especially for the subcase 1-2-75 in which a decrease in frequency of 11.22% and 9.73%, respectively, is observed compared to the undamaged case. The subcase 4-2-75 resulted in the largest increase of frequency change (1.95%) for the 5th mode. The other modes registered relatively low frequency changes for the four cases.

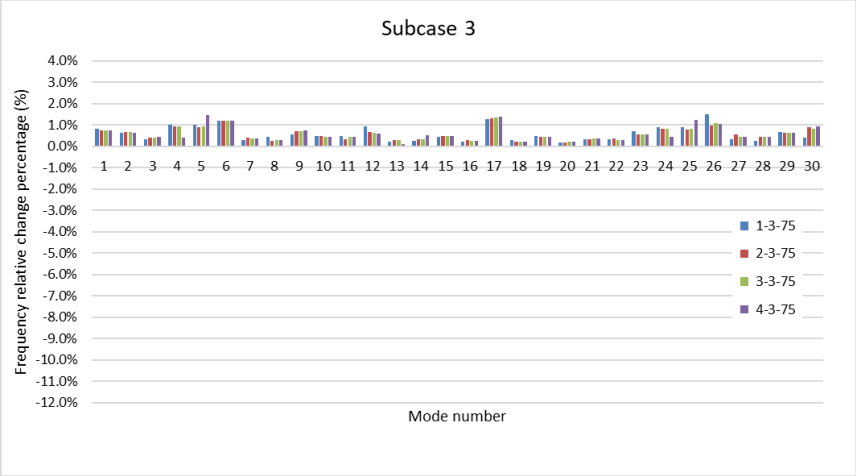

Fig. 5.11. Frequency relative change percentage of different major cases for subcase 3

When the corroded cables are located from the 5th cable from the middle of the deck (subcase 3 in Figure 5.11), it is observed that the frequency ratios for all 30 vibration modes increased, regardless of the major case; however, the increase percentage was always within 1.5%. The subcase 4-3-75 registered the highest increase in frequency change with values of 1.47%, 1.39% and 1.23% for the 5th, 17th and 25th modes, respectively.

5.1.4. Effects on the mode shapes

The eigenvalues and eigenvectors of the structure can be determined through the equation of motion as discussed in Chapter 3. The eigenvalues characterize the frequency of the structure, and the eigenvectors reflect the relative positioning of coordinates, also known as the mode shapes. Each frequency corresponds to a certain mode shape, and the fundamental vibration mode is related to the lowest natural frequency solved by the equation of motion.

It can be noticed that the first 10 vibration mode shapes for each case were affected by the cable corrosion level, the corroded stay cables distribution on both decks and the distance from the center to the corroded cables. The vibration mode shapes were identified by visualizing the coupled movement of decks, towers and cables. The detailed mode shapes can be referred to in Figures 3.13 to 3.22. Some differences are

observed in the mode shapes due to different distributions of the corroded cables for the major cases 3 and 4. Figures 5.12 and 5.13 show an example of such vibration modes alteration caused by the corrosion subcases 3-1-75 and 4-1-75, respectively.

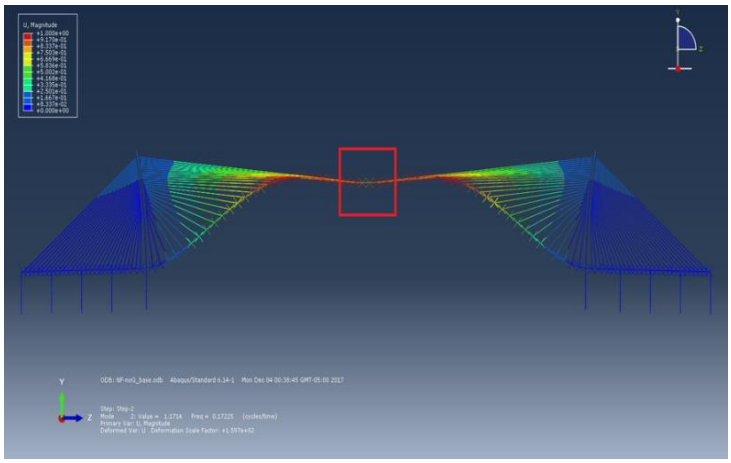

(a)

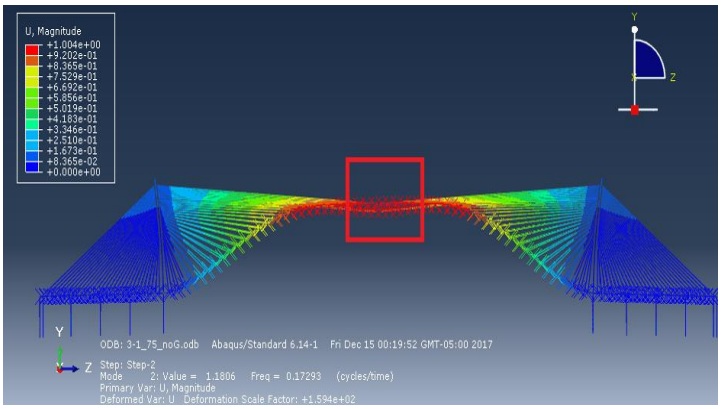

(b)

Fig. 5.12. The 2nd mode shape of (a) reference case, (b) subcase 3-1-75

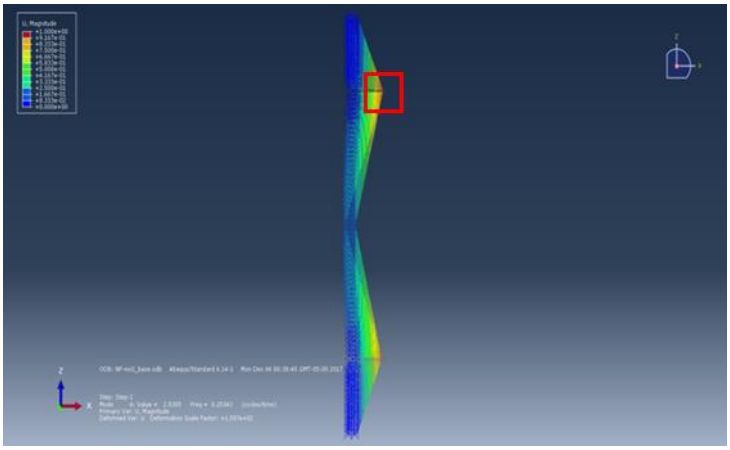

(a)

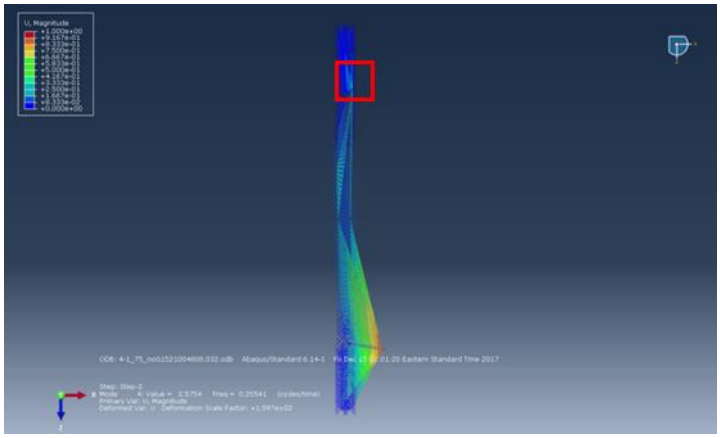

(b)

Fig. 5.13. The 4th mode shape of (a) reference case, (b) subcase 4-1-75.

Figures 5.12(a) and (b) show the 2nd vibration mode for the reference case, where no corrosion was applied to the cables, and the subcase 3-1-75, for which the corroded cables were distributed on one deck only, therefore, deflections of both decks could not register the same amount as the reference case. The deflection of the north deck was 0.98 m, while that of the south deck was 0.92m. The corroded cables with less effective cross-section areas reduced the restrains of the middle of the north deck, and thus it induced more deformation than the south deck side, which was not affected by the corroded cables. Figures 5.13(a) and (b) illustrate the comparison of the 4th vibration mode shape, which is related to the bending movement of the towers, between the reference case and the subcase 4-1-75, for which all the corroded cables lie on the east

side of both decks. It can be noticed that the out-of-plane movements of both towers were very different. Due to the same reason, the affected cables cannot fully restrain the tower, thus different displacements of the two towers were registered as 1.0 m for the west side tower and 0.21 m for the east side tower; this also indicated that the coupled response of the cables and towers was weakened because of cable corrosion.

5.1.5. Summary and discussion

In summary, the natural frequencies of the Stonecutters Bridge model were affected by the level of corrosion in the stay cables, the distance between two groups of corroded cables and the mid-span of the deck, and the distribution of the corroded cables. However, the vibration mode shapes remain similar regarding the coupled movements of cable, decks and towers. Only small difference can be observed in certain mode shapes, due to diminished deck restraint by the corroded cables, for major cases 3 and 4.

Unlike the static responses of the bridge, where the deflection of the bridge gradually increased with the increase of corrosion level, the natural frequencies do not follow the same trend for all the modes, when the corrosion is applied. It can be noted that the frequencies associated to the 2^{nd} and 6^{th} vibration modes, which are respectively first order of vertical and torsional vibration of the decks, experienced the highest decrease for 25% and for 50% corrosion levels in subcases 1-1, 2-1, 3-1 and 4-1, showing a large influence in the frequencies of symmetric vertical and torsional vibration. As for the cases with symmetric distribution with regard to the middle line (subcases 1-1 and 3-1), the 75% corrosion level did not result in a significant decrease of the vertical and torsional frequencies, but increased frequency of the 3^{rd} mode which is the second order of vertical vibration of the decks. For the subcases 2-1 and 4-1 which have asymmetric distribution with regard to the middle line, the 75% corrosion level reduced the frequencies of the 2^{nd} and 6^{th} modes, but also increased the frequency of the 3^{rd} mode. It can be noted that the frequencies of the 3^{rd} and 6^{th} modes, which are respectively the vertical deformation and torsional vibration, became close to each other

due to the critical corrosion condition, producing a dangerous trend for the deck to have a coupled motion of vertical and torsion.

Regarding the distance of the corroded cables placement from the mid-span, with the same 75% corrosion level, a similar frequency change for the 2nd and 6th modes can be noted. In the major cases 1 and 3, which have symmetric distribution with regard to the middle line, the subcases 1, for which the corroded cables are around the mid-span, resulted in an increase in the frequency for the 3rd mode. The subcase 2, for which the corroded cables are located from the 3rd cable from the middle point, resulted in significant decrease ratios in the 2nd, 3rd and 6th modes compared to the subcases 1 and 2, showing that the frequencies of the deck in the symmetric vertical and torsional vibrations are significantly affected. In the major cases 2 and 4, which have asymmetric distribution with regard to the middle line, both subcases 1 and 2 resulted in decreased frequencies in the 2nd and 6th modes; the subcase 3 has limited influence on the increase ratio of the frequency. Considering the different distribution of corroded cables for the same corrosion level and subcase, the similar decrease in natural frequencies can be observed for the 2nd and 6th modes. When in the same subcase 1, all major cases with symmetric and asymmetric distribution have a similar change. The major cases 2 and 4 resulted in significant decrease ratios in the frequency of the 2nd and 6th modes. The frequency of the 3rd mode was increased in all the major cases, especially for major cases 1 and 3. The convergence of frequencies between the 3rd and 6th modes for all the major cases in the subcase 1 was likely to occur, thus if the these two modes approach the same frequency, the bridge might become unstable under the effect of the dynamic wind load. In the subcase 2, the different corrosion distributions have a similar effect in every mode. The four major cases all resulted in a large decrease in the frequency relative change ratio in the 2nd, 3rd and 6th modes, especially for the major case 1, which resulted in the largest frequency change ratio decrease. The major case 1 was affected more in vertical and torsional frequencies than the other major cases. However, in the subcase 3, all the major cases have a similar change, which is a limited increase in the

frequency change ratio for all the modes. Therefore, as the corroded cables are located further from the mid-span, the different distributions have less effect on changing the natural frequencies. The detailed frequencies ratios are summarized in Tables B1 to B3 in Appendix B.

5.2. Response to wind load

The three components of wind load were calculated according to Eq. (3.2) described in Chapter 3. The lift and drag loads and the torsional moments calculated for a mean wind speed of 20.75 m/s are applied on the mass centers of each segment of both decks of the Stonecutters Bridge model. The wind loads were applied on the decks as shown in Figure 5.14. The 500-seconds interval of the random wind speed data was used to simulate the real wind loading conditions in Hong Kong. Figures 5.15(a) to (c) plot the three wind load components during the 500-s period. The wind load analysis was performed by observing the deck's deflection for the subcase 2 of the 1st and 2nd major cases (cases 1-2 and 2-2) and subcase 1 of the 3rd and 4th major cases (cases 3-1 and 4-1), because the largest deflections in the middle can be observed in the subcases 1 or 2 compared to the other subcases under the same major case The response was determined for 25% corrosion damage in the stay cables, which represents a more realistic structural damage scenario. Moreover, the response to wind load, under the critical condition of 75% corrosion level, was also considered and compared to the 25% damage response. The response at some key locations, which are the middle of the bridge, the top of both towers and the cables from different locations, was extracted from the modal analysis under the wind loading scenario.

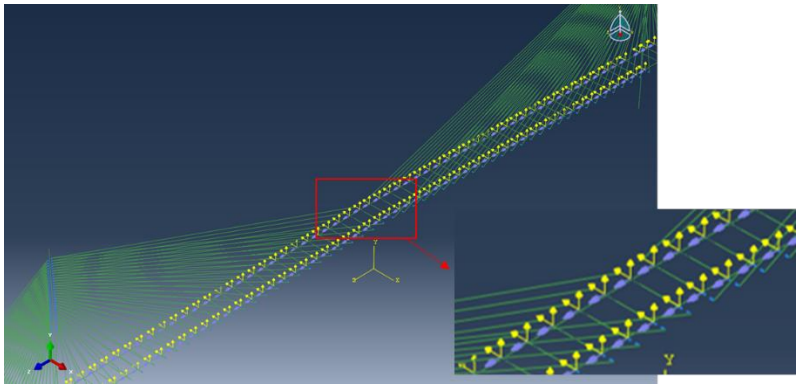

Fig. 5.14. Wind loads on bridge decks

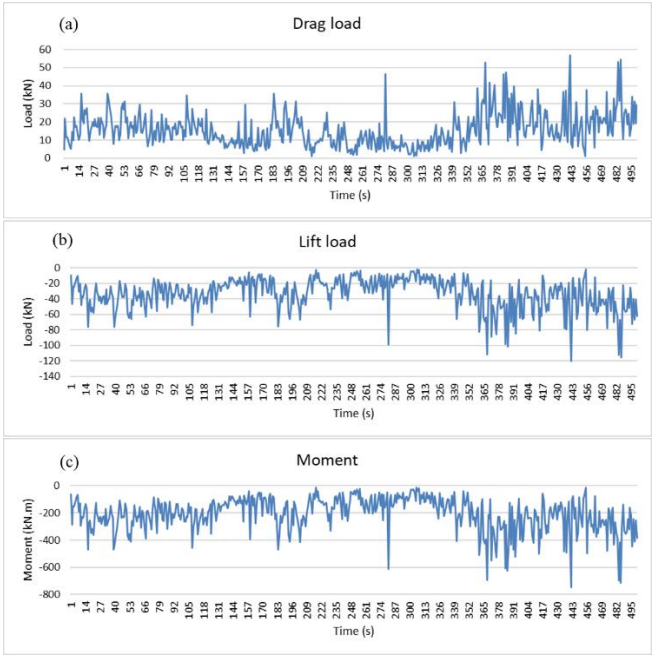

Fig. 5.15. Wind load components: (a) drag load; (b) lift load; (c) moment

5.2.1. Displacement of decks and towers

5.2.1.1. Parametric study of case 1-2

For the subcase 1-2, the horizontal displacement time history of the mid-span of both decks and of the top of the towers, during the 500 seconds of applied wind load, is presented in Figure 5.16. Due to the symmetric configuration of the bridge with regard to the longitudinal line, both decks and towers have the same displacement for the reference case and for the subcase 1-2.

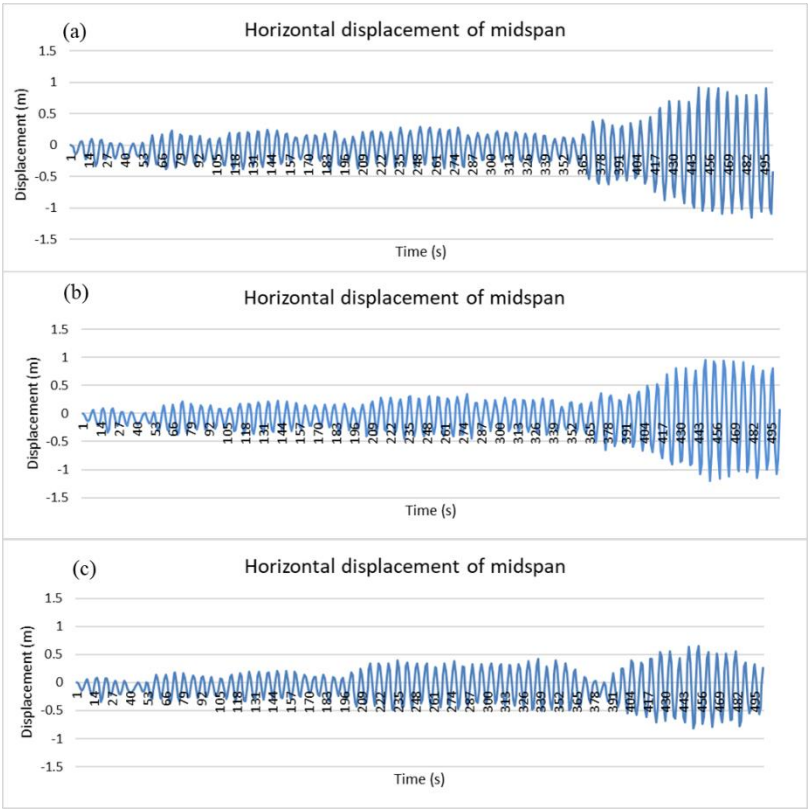

Fig. 5.16. Horizontal displacement of mid-span for case 1-2: (a) reference case; (b) subcase 1-2-25; (c) subcase 1-2-75

It can be seen in Figures 5.16(a) to (c) that the deck did not have large horizontal vibration during the first 350 seconds, after which the horizontal vibration began to increase for the last 150 seconds of the applied load. The maximum horizontal displacements for the reference case, subcase 1-2-25 and subcase 1-2-75 are 1.15 m, 1.20 m and 0.81 m, respectively. It can be concluded that the horizontal vibration of the bridge increased due to slight corrosion (25%) of the affected cables; however, the more severe corrosion of 75% damage did not increase the maximum horizontal displacement.

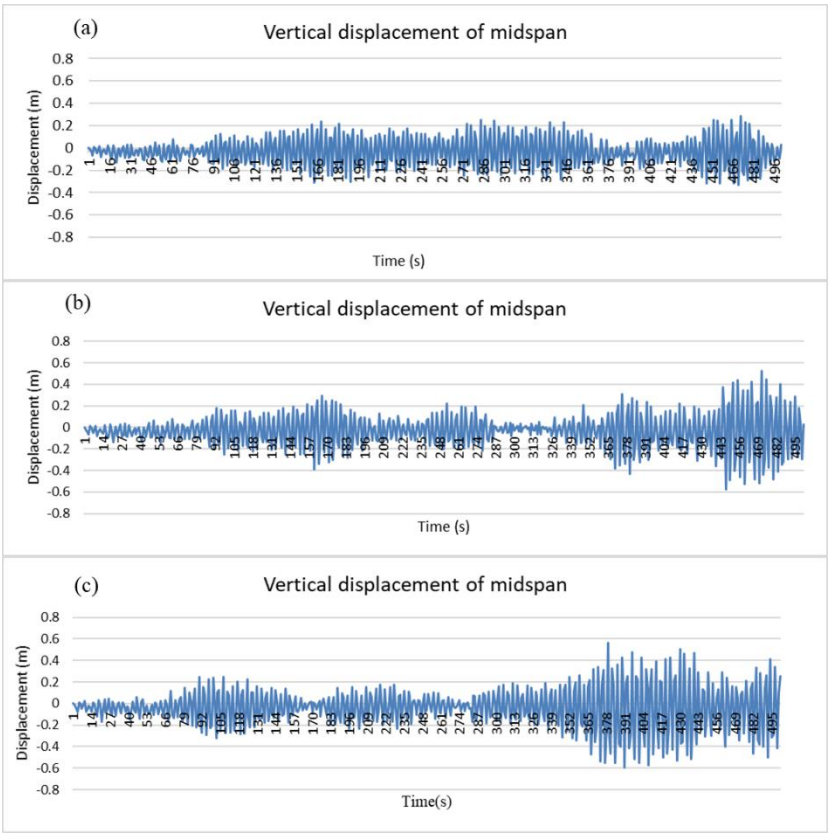

Fig. 5.17. Vertical displacement of mid-span for case 1-2: (a) reference case; (b) subcase 1-2-25; (c) subcase 1-2-75

The time history of the vertical displacement of the midpoint of the deck, which is identical to the south deck vertical displacement due to the symmetric arrangement of the corroded cables, is illustrated in Figures 5.17(a) to (c). The subcases 1-2-25 and 1-2-75 have the similar time intervals in which the large and small amplitudes occur alternatively in the 500-s period, when compared to the reference case. The largest amplitude of the vertical displacement was noticed for the case with 75% corrosion damage, with a value of 0.59 m, whereas the maximum amplitude for the reference case with no corrosion applied and with 25% corrosion were 0.33 m and 0.57 m, respectively. Also, it can be noticed that the largest vertical displacement amplitude occurred during the last 50 s for the subcase 1-2-25, at around 380 s of the applied wind load for the subcase 1-2-75 and along several time intervals for the reference, no-corrosion case. Therefore, the severe corrosion case of 75% determines larger vertical response than the slight corrosion case of 25%. The worst corrosion also brought forward the time

when the maximum deflection occurred.

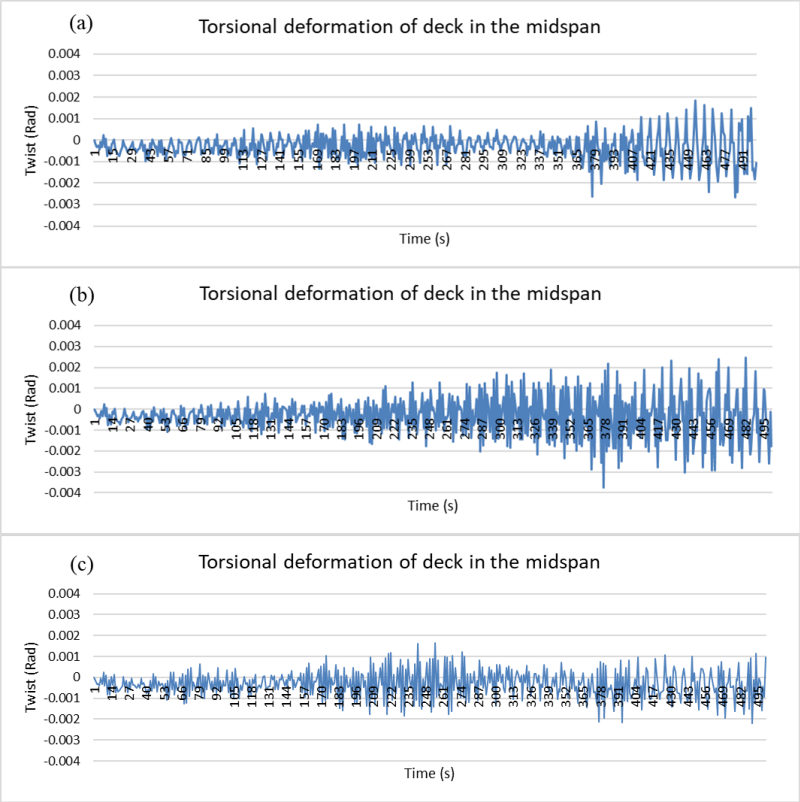

Fig. 5.18. Torsional deformation of mid-span for case 1-2: (a) reference case; (b) subcase 1-2-25; (c) subcase 1-2-75

The torsional vibration of the bridge deck can induce structural instability, especially when it couples with the vertical or horizontal vibrations. The time history of the torsional motion of the deck's mid-span for the case 1-2 is shown in Figures 5.18(a) to (c). When investigating the torsional deformation of the midpoint of the north deck, it was noticed that low values of deformation were recorded for all the cases, with 0.0027 rad for the reference case, 0.0037 rad for subcase 1-2-25 and 0.0017 rad for subcase 1-2-75. Increasing amplitude can be observed from the start for the subcase 1-2-25 and the non-corrosion case.

The horizontal displacement of the top of the tower, for the subcase 1-2 with different levels of cable corrosion is presented in Figures 5.19(a) to (c). The reference case and the subcase 1-2-25 have similar trends with the displacement amplitudes, both starting to increase in the last 150 seconds of applied load and reaching the maximum value of 0.07 m and 0.1 m, respectively. The horizontal displacement of the top of the

tower was small initially, for the subcase 1-2-75; however, the amplitude gradually increased reaching values of up to 0.12 m. It is interesting to notice that when the deck has larger horizontal and torsional responses for the subcase 1-2-25, the subcase 1-2-75 can result in higher amplitude of vertical deck deflection and lower horizontal displacement of the tower.

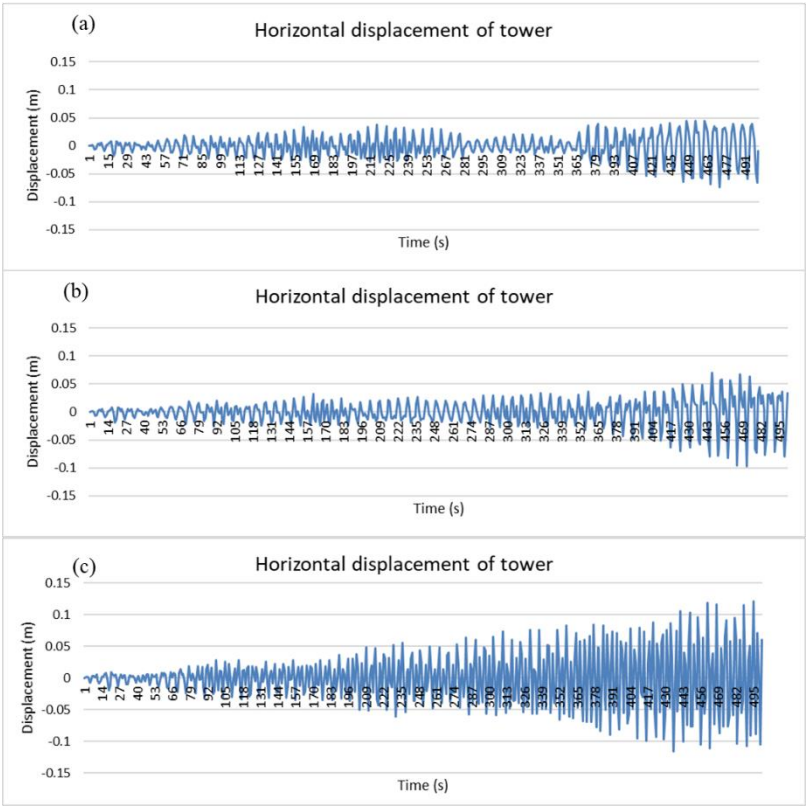

Fig. 5.19. Horizontal displacement of tower top for case 1-2: (a) reference case; (b) subcase 1-2-25; (c) subcase 1-2-75

5.2.1.2. Parametric study of case 2-2

Figures 5.20 to 5.23 present the responses of the middle of the decks and the top of the towers under the action of wind load when the distribution of corroded cables is considered at different locations on the north and south decks, as described for the cable corrosion case 2-2.

Figures 5.20(a) to (c) compare the horizontal deflection obtained at the mid-span of the north deck for the reference case and subcases 2-2-25 and 2-2-75. Both corrosion cases 2-2-25 and 2-2-75 have the same trend as the reference case, for which the

horizontal displacement amplitude starts to increase in the last 150 seconds of the applied wind load. The highest amplitude of 1.2 m was noticed for the subcase 2-2-25, whereas 0.90 m was observed for the subcase 2-2-75 and 1.15 m for the reference case. For subcase 2-2, the 25% corrosion damage in the stay cables induces a similar horizontal vibration of the deck to that of the reference case; however, the 75% corrosion level can mitigate the deck vibration along this direction.

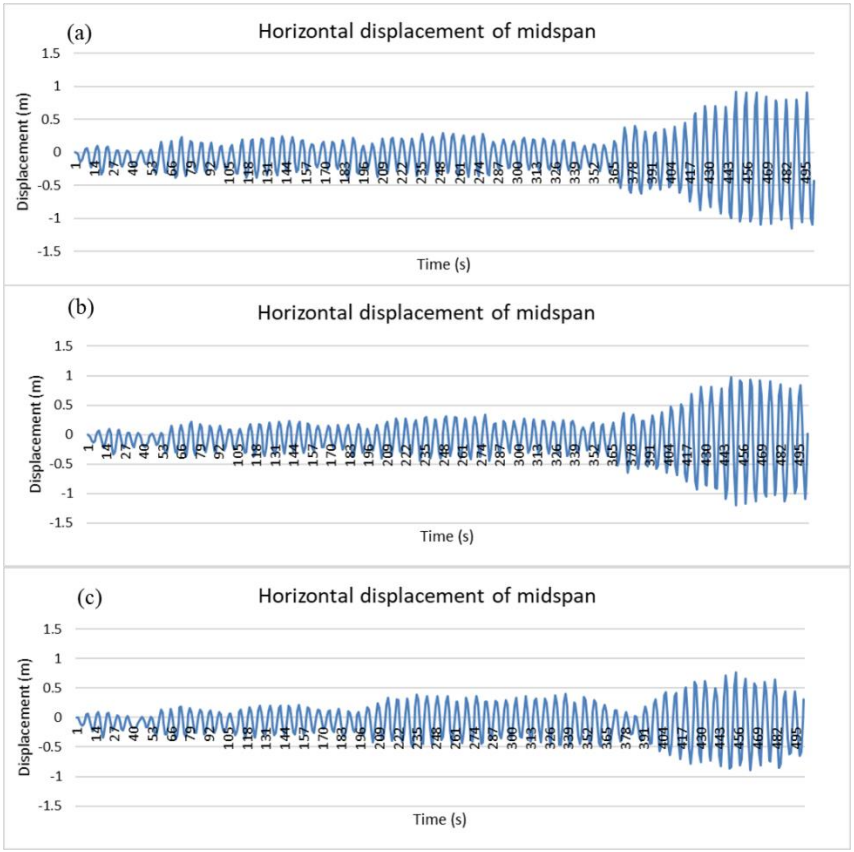

Fig. 5.20. Horizontal displacement of mid-span for case 2-2: (a) reference case; (b) subcase 2-2-25; (c) subcase 2-2-75

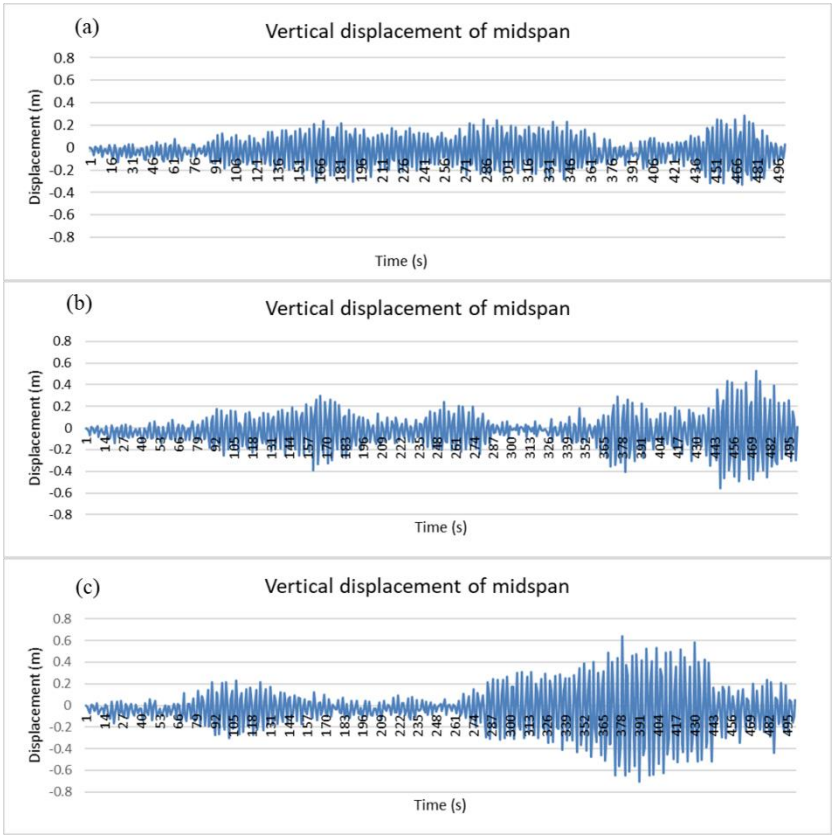

Fig. 5.21. Vertical displacement of mid-span for case 2-2: (a) reference case; (b) subcase 2-2-25; (c) subcase 2-2-75

The vertical displacement at the mid-span for subcases 2-2-25 and 2-2-75 are compared to the reference case in Figures 5.21(a) to (c). Both cases where stay cables are damaged by corrosion (2-2-25 and 2-2-75) have a different vertical displacement time history from the reference case. The subcase 2-2-25 has some segments of identical periods, in which the large and small amplitudes occur alternatively over the 500-s interval; however, the vertical vibration for the reference case seems to have consistent amplitudes for most of the time during the 500-s interval. Thus, a second frequency could be identified in the vertical vibrations of the subcases 2-2-25 and 2-2-75. As for the subcase 2-2-75, the response increases gradually at nearly the 250th s of the applied load, and then it decays from the 450th s. The maximum displacements for the reference case, subcase 2-2-25 and subcase 2-2-75 are 0.33 m at the last 50 s, 0.55 m at the last 50 s and 0.71 m at around 380 s, respectively. Therefore, the higher the corrosion level in the stay cables, the higher is the vertical deflection response of the deck. Also, for

the highest corrosion level, the time at which the maximum vertical deflection occurred was earlier.

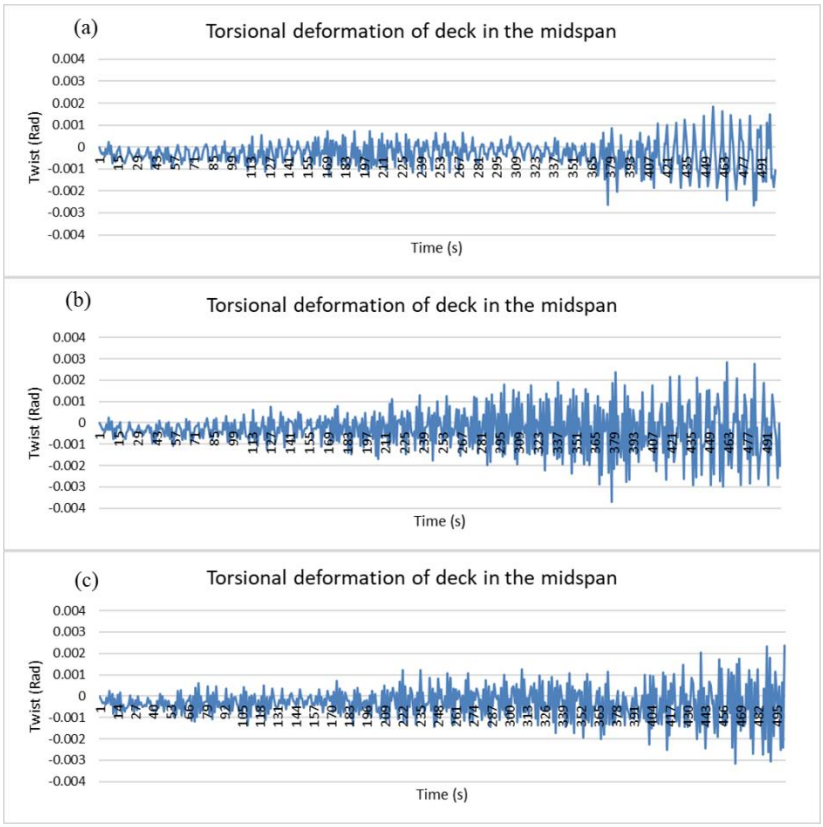

Fig. 5.22. Torsional deformation of mid-span for case 2-2: (a) reference case; (b) subcase 2-2-25; (c) subcase 2-2-75

The torsional responses of the midpoint of the deck, illustrated in Figures 5.22(a) to (c), show that the vibration amplitudes gradually increase with time for the reference case and for both corrosion cases with 25% and 75% damage, respectively. The maximum torsional deformation for the three cases is 0.0027 rad, 0.0037 rad and 0.0032 rad for the reference case, subcase 2-2-25 and subcase 2-2-75, respectively. The lower amplitude of the torsional vibration registered for subcase 2-2-75 indicates that the higher corrosion level in the cables did not increase the wind effect on the torsional and horizontal response for subcase 2-2; the vertical vibration though was much more amplified under the effect of wind loading for subcase 2-2-75.

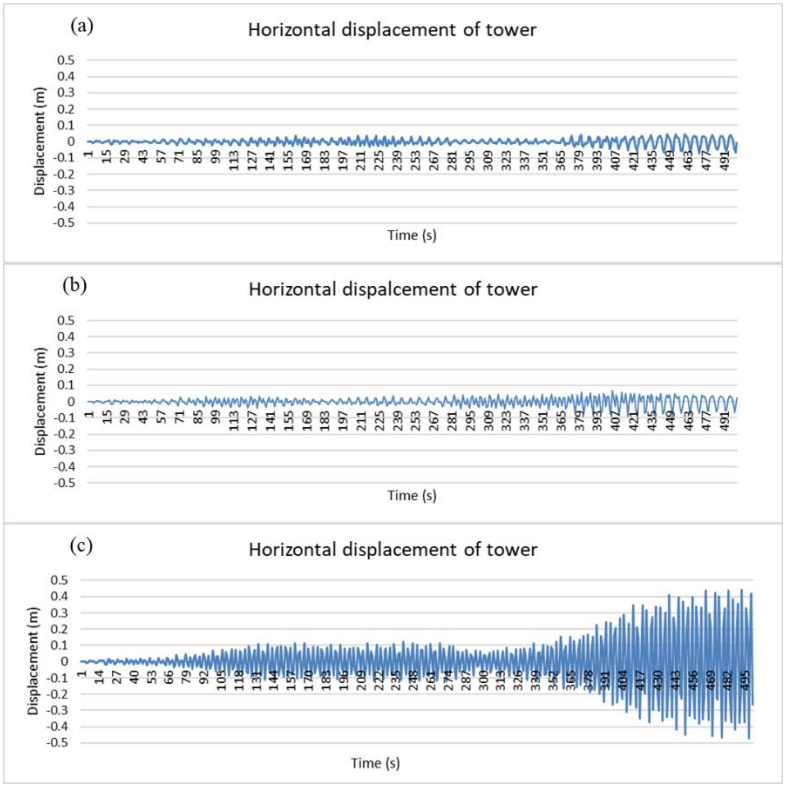

Fig. 5.23. Horizontal displacement of tower top for case 2-2: (a) reference case; (b) subcase 2-2-25; (c) subcase 2-2-75

The cables connect the tower structure with the main span of the deck, thus any alteration of the cable characteristics, coupled with the vibration of the deck, would also affect the dynamic response of the tower. Figures 5.23(a) to (c) present the time history of the horizontal displacement of the top of the tower for subcase 2-2. When investigating the horizontal displacement at the top of the tower, which occurs in the out-of-plane direction with respect to the bridge structure, it was noted that the response for the corrosion subcase 2-2-25 had a similar trend as the response for the reference case; however, for the subcase 2-2-75, the tower top started to amplify its vibration for the last 200 s of applied load. Moreover, the maximum horizontal displacement of 0.47 m for the subcase 2-2-75 was much higher than the 0.07 m for the reference case and 0.09 m for the subcase 2-2-25. Therefore, the horizontal response of the top of the tower is highly affected by the 75% corrosion level of the cables for the subcase 2-2 which has an asymmetric distribution of damaged cables.

5.2.1.3. Parametric study of case 3-1

The time-dependent response of the mid-point of the deck and of the tower top, for different corrosion levels and same wind loading, is compared in Figures 5.24 to 5.28 for the subcase 3-1, when the corroded cables are arranged on the north deck close to the mid-span.

Figures 5.24(a) to (c) illustrate the time history of the horizontal displacement of the deck mid-span for subcase 3-1. It can be noticed from Figures 5.24(b) and (c) that the deck's horizontal vibration does not change significantly from the first 350 s and increase for the last 150 s when the corroded cables were arranged as per the layout of case 3-1. The maximum displacements for each of the three cases were 1.15 m, 1.21 m and 0.89 m for the reference case, subcases 3-1-25 and 3-1-75, respectively. Similar to the subcases 1-2-75 and 2-2-75, the higher corrosion case of 75% did not result in amplifying the horizontal response of the deck under the wind load effect with respect to the subcase 3-1-25.

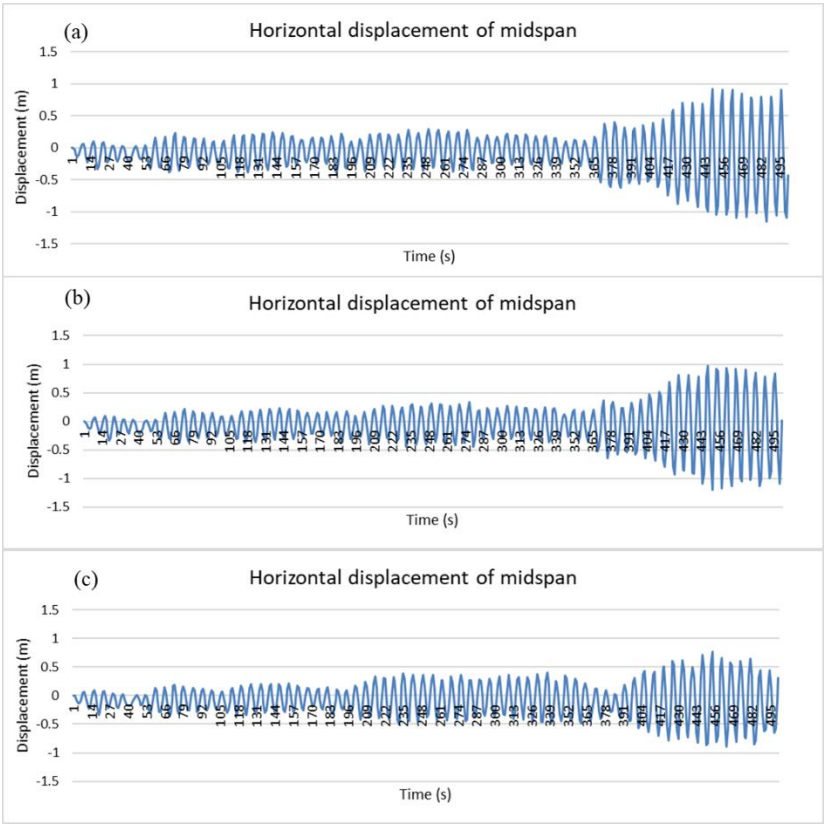

Fig. 5.24. Horizontal displacement of mid-span for case 3-1: (a) reference case; (b) subcase 3-1-25; (c) subcase 3-1-75

When analyzing the vertical deflection induced by the dynamic wind load, as shown in Figures 5.25(a) and (b) and 5.26(a) to (c), the arrangement of corroded cables for subcase 3-1 induced different magnitude of displacements at mid-span for the north and south decks, as it can be seen in Figures 5.25(a) and (b). Both decks registered similar patterns of vertical vibrations; however, the amplitudes were different. For the north deck, on which the corroded cables are located, the amplitude of vertical motion is larger with a maximum amplitude of 0.74 m, whereas for the south deck, it is 0.65 m. The different deflections on both decks were noted due to the reduced restraint caused by corroded cables on the north deck.

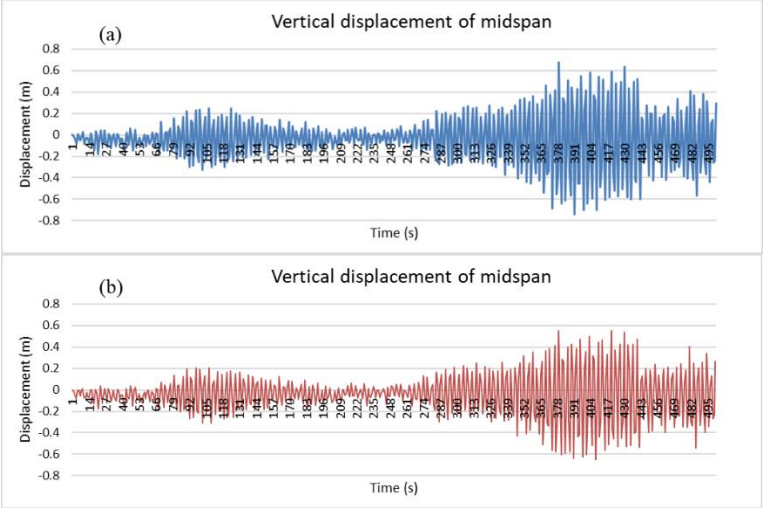

Fig. 5.25. Vertical displacement for both decks for subcase 3-1-75: (a) North deck; (b) South deck

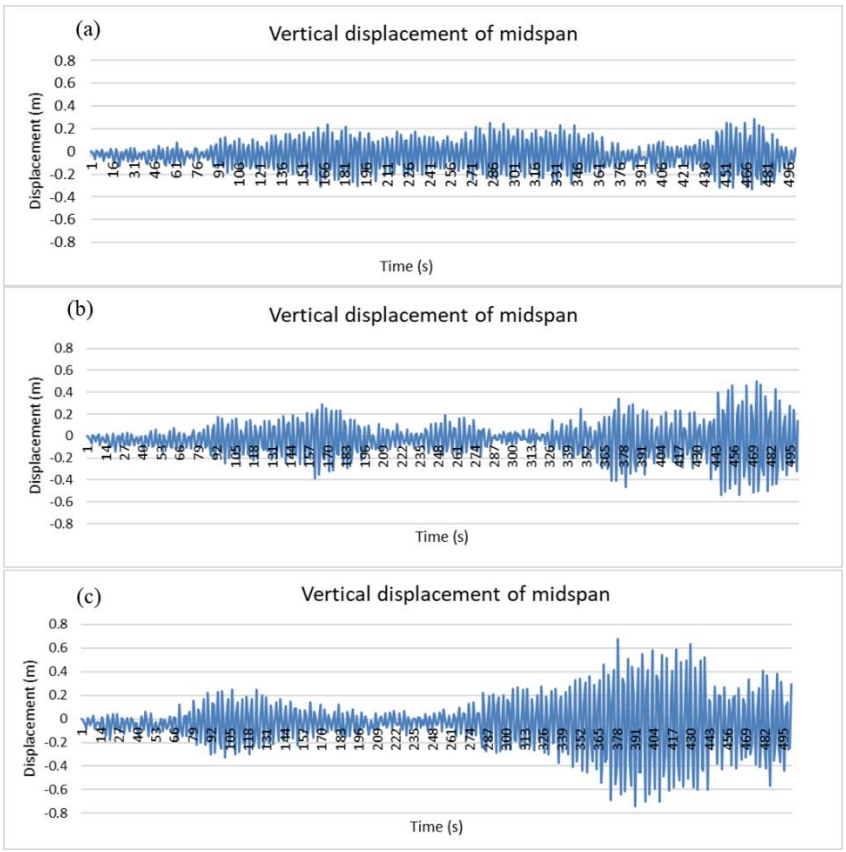

Fig. 5.26. Vertical displacement of mid-span for case 3-1: (a) reference case; (b) subcase 3-1-25; (c) subcase 3-1-75

Figures 5.26(a) to (c) compare the time histories of the vertical deflection at mid-span for the reference case and subcases 3-1-25 and 3-1-75. Both cases where stay cables are damaged by corrosion (3-1-25 and 3-1-75) have a different vertical displacement time history from the reference case. The vertical displacement of subcase 3-1-25 has some periodic vibrations during the 500 s interval, whereas subcase 3-1-75 starts amplifying at the 250 s, then decreasing at around the 450 s. The maximum deflection on the north deck is 0.33 m at the last 50 s, 0.58 m at the last 50 s and 0.74 m at around 380 s for the reference case, subcase 3-1-25 and subcase 3-1-75, respectively.

The torsional deformation of the deck mid-span is shown in Figures 5.27(a) to (c) for the reference case and subcases 3-1-25 and 3-1-75. When corrosion damage in the stay cables reaches 25%, subcase 3-1-25, the amplitude of the torsional deformation is higher than the reference case right from the beginning, which is similar to the reference

case. The higher amplitudes for case 3-1-75 start at around 200 s. The largest amplitudes for the three cases are 0.0027 rad, 0.0037 rad and 0.0039 rad, respectively. For subcase 3-1, the higher the corrosion level in the stay cables, the higher the twisting of the deck. Both decks registered the same pattern of response for the torsional vibration.

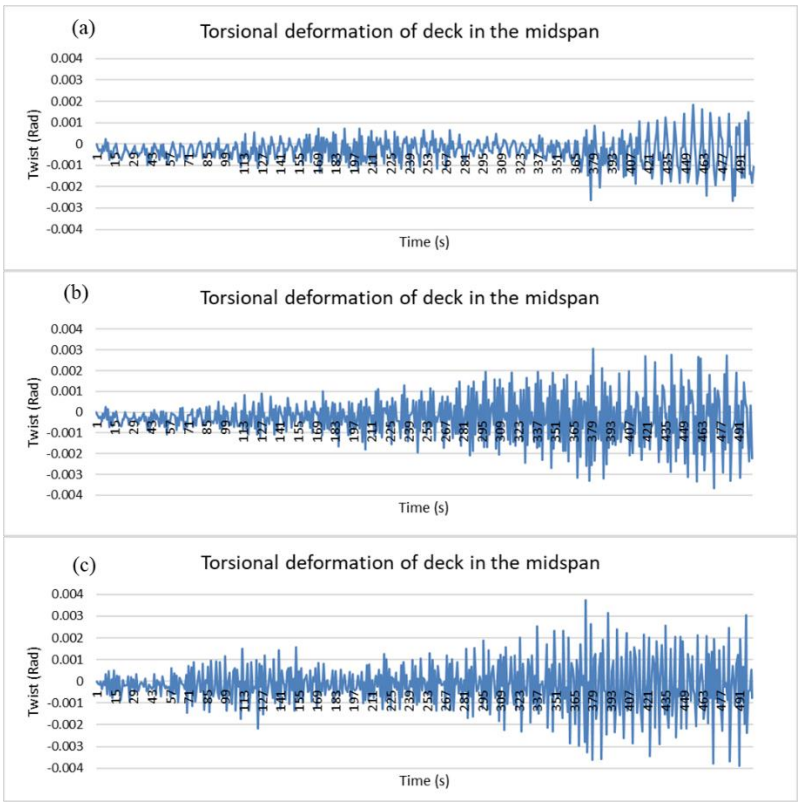

Fig. 5.27. Torsional deformation of mid-span for case 3-1: (a) reference case; (b) subcase 3-1-25; (c) subcase 3-1-75

Figures 5.28(a) to (c) illustrate the time histories of the top tower horizontal displacement for the reference case and for the subcases 3-1-25 and 3-1-75. The tower top has similar movement along the 500 s of the applied load, for all three cases, in which the amplitude gradually increases from the beginning of the applied wind load. The larger out-of-plane movement can be observed for both corrosion cases of subcase 3-1 during the last 150 s of applied load. However, the displacements for the three cases are within 0.1 m. The maximum displacement for the reference case, subcases 3-1-25 and 3-1-75 are 0.07 m, 0.1 m and 0.09 m, respectively. The close amplitude for the subcase 3-1 with 75% corrosion than that of 25% corrosion indicates that corrosion

level have less effect on increasing the tower's deflection for the subcase 3-1.

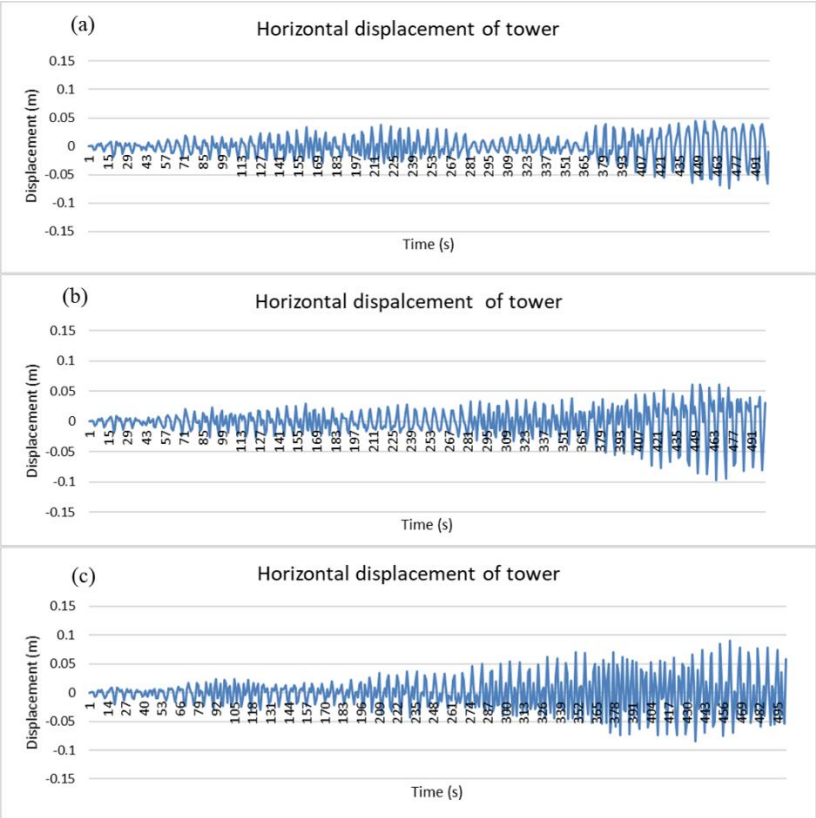

Fig. 5.28. Horizontal displacement of tower top for case 3-1: (a) reference case; (b) subcase 3-1-25; (c) subcase 3-1-75

5.2.1.4. Parametric study of case 4-1

Figures 5.29(a) to (c) show the comparison of the horizontal response of the midpoint of the deck for the reference case and for the subcases 4-1-25 and 4-1-75. Subcase 4-1 represents the scenario in which the stay cables are damaged only on the east side of the deck from the mid-span. Like the other cases, the deck vibrated steady for the first 350 s and registered a higher amplitude for the last 150 s of applied wind loading. The maximum responses for the three cases are 1.15 m, 1.2 m and 0.83 m, respectively. Subcase 4-1-25 governs the response, whereas a 75% damage in the stay cables, subcase 4-1-75, mitigates the amplitude in this direction.

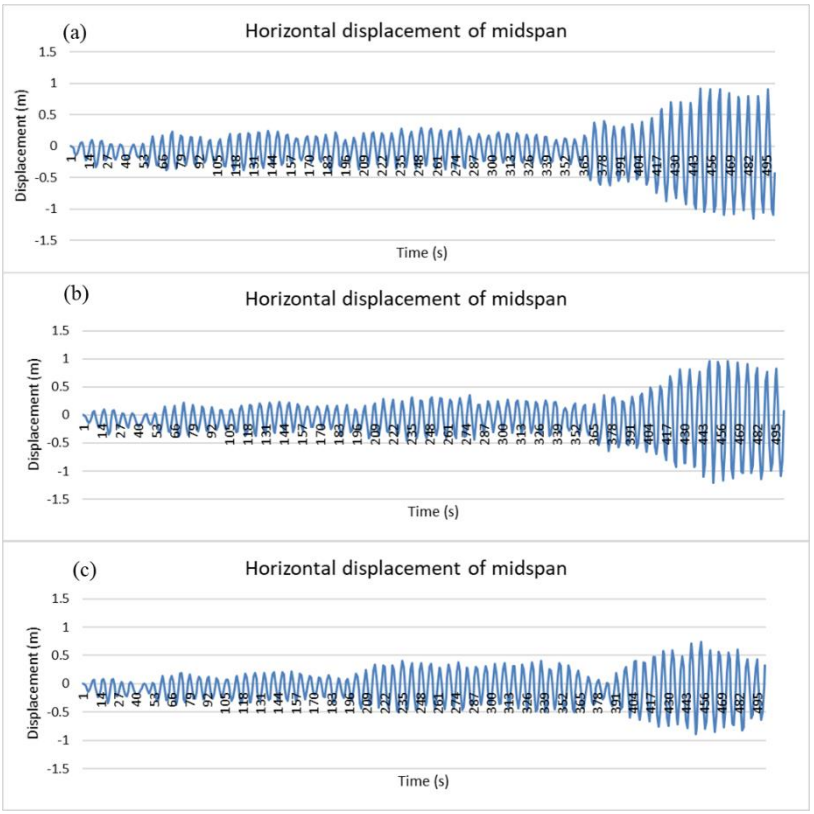

Fig. 5.29. Horizontal displacement of mid-span for case 4-1: (a) reference case; (b) subcase 4-1-25; (c) subcase 4-1-75

Figures 5.30(a) to (c) present the time history of the deck mid-span vertical deflection for the references case and for the subcases 4-1-25 and 4-1-75. Figure 5.30 (b) shows the results for the subcase 4-1-25, which presents similar periodic vibrations during the first 500 s as the previous subcases with 25% damage level (subcases 1-2-25, 2-2-25 and 3-1-25). The largest amplitude for subcase 4-1-75 is 0.66 m at around 380 s, which is larger than that of 0.54 m at the last 50 s for case 4-1-25 and 0.33 m at the last 50 s for the reference case. Therefore, the vertical vibration amplitude increased with the corrosion level of the damaged of the stay cables in subcase 4-1.

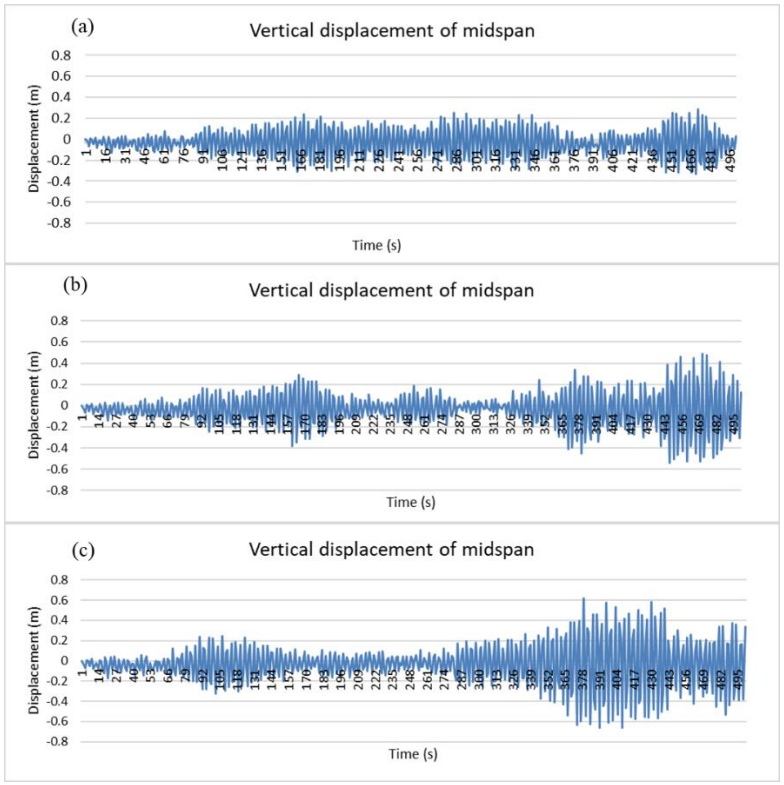

Fig. 5.30. Vertical displacement of mid-span for subcase 4-1: (a) reference case; (b) subcase 4-1-25; (c) subcase 4-1-75

Figures 5.31(a) to (c) illustrate the torsional response changes for the reference case (no corrosion damage) and for 25% and 75% corrosion damage levels (subcases 4-1-25 and 4-1-75). Both decks have the same vertical response for the subcases 4-1 with 25% and 75% damage levels. When comparing these to the reference case, it was noticed that the deck's torsional response increased gradually for the subcase 4-1-25. However, the torsional vibration seems to have no specific pattern for the subcase 4-1-75, in which the twisting amplitudes remain consistent during last 200 s of applied load. When comparing the maximum amplitudes, it can be concluded that the torsional response is not significant, as the amplitudes for the subcase 4-1-25 increases to 0.0038 rad, while the amplitudes for the reference case and the corrosion subcase 4-1-75 are 0.0027 rad and 0.0022 rad, respectively.

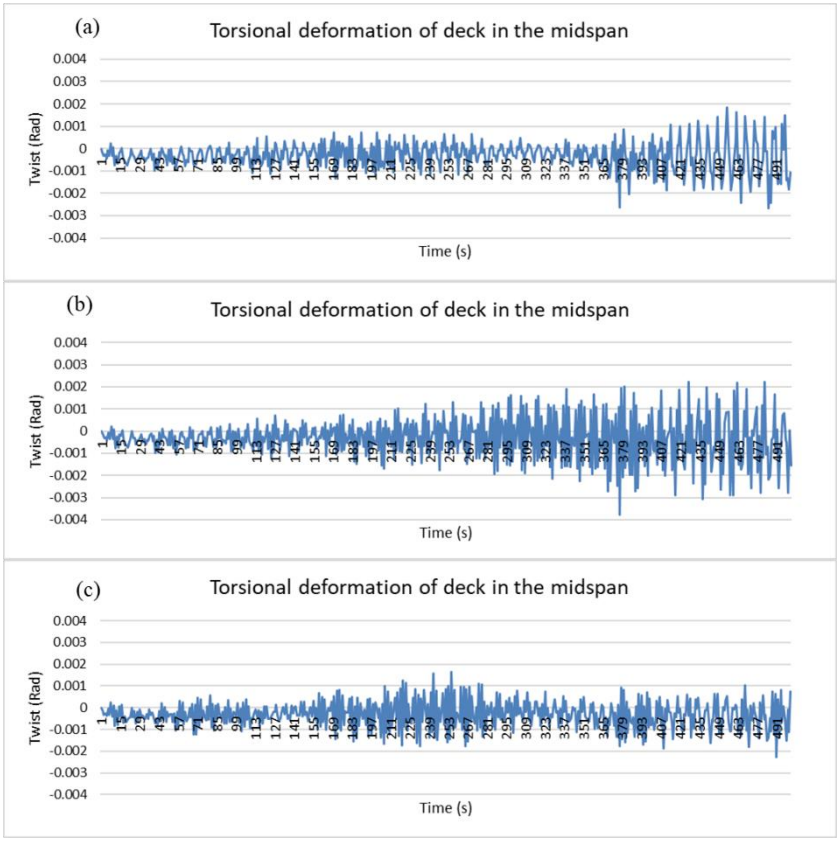

Fig. 5.31. Torsional deformation of mid-span for case 4-1: (a) reference case; (b) subcase 4-1-25; (c) subcase 4-1-75

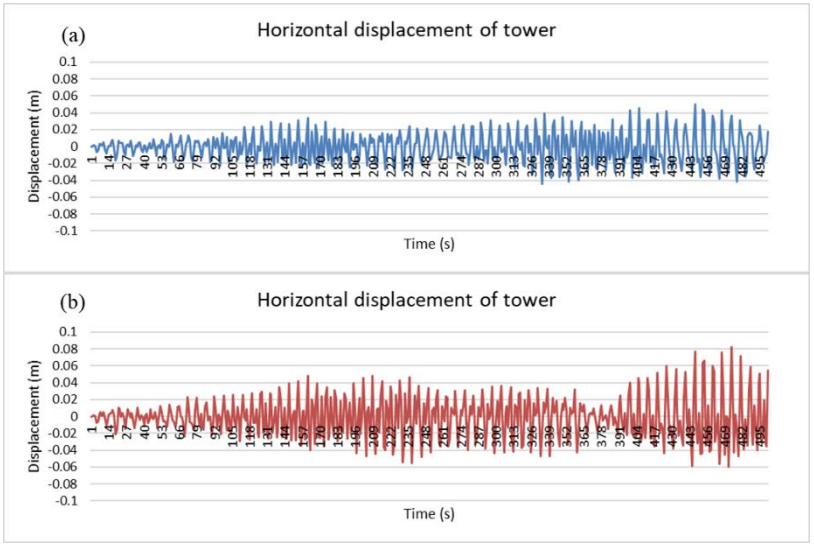

Fig. 5.32. Horizontal displacement of different tower tops for subcase 4-1-75: (a) East tower; (b) West tower

Due to the arrangement of the corroded cables in subcase 4-1, when all the affected cables are located on the east side of the deck, both towers respond with an out-of-phase

horizontal displacement time history with respect to each other (as shown in Figures 5.32(a) and (b)), which determines an asymmetric motion. The maximum horizontal amplitude of the east tower was 0.05 m, lower than that of 0.08 m registered for the west tower.

The effect of 25% and 75% corrosion levels in the affected cables on the horizontal displacement of the east and west towers are respectively compared in Figures 5.33(a) to (c) and 5.34(a) to (c), respectively. For the east tower (Figures 5.33(a) to (c)), the horizontal displacement for the subcase 4-1-25 is similar to that of the reference case, which has a steady vibration at the beginning of the applied wind loading and gradually increases in the last 150 s of applied load. On the contrary, there is no regular pattern for the tower horizontal displacement for the subcase 4-1-75. The maximum displacement of the top east tower is 0.06 m for subcase 4-1-25, which is higher than the 0.05 m for the subcase 4-1-75. For the west tower (Figure 5.34(a) to (c)), however, it was noticed that the amplitudes of the horizontal displacement at the top of the west tower for the two corrosion cases (4-1-25 and 4-1-75) had a similar pattern to the reference case, in which the amplitudes increased suddenly during the last 150 s of applied load. The maximum displacement of the west tower top is 0.08 m for subcase 4-1-75, which is higher than 0.07 m for the subcase 4-1-25.

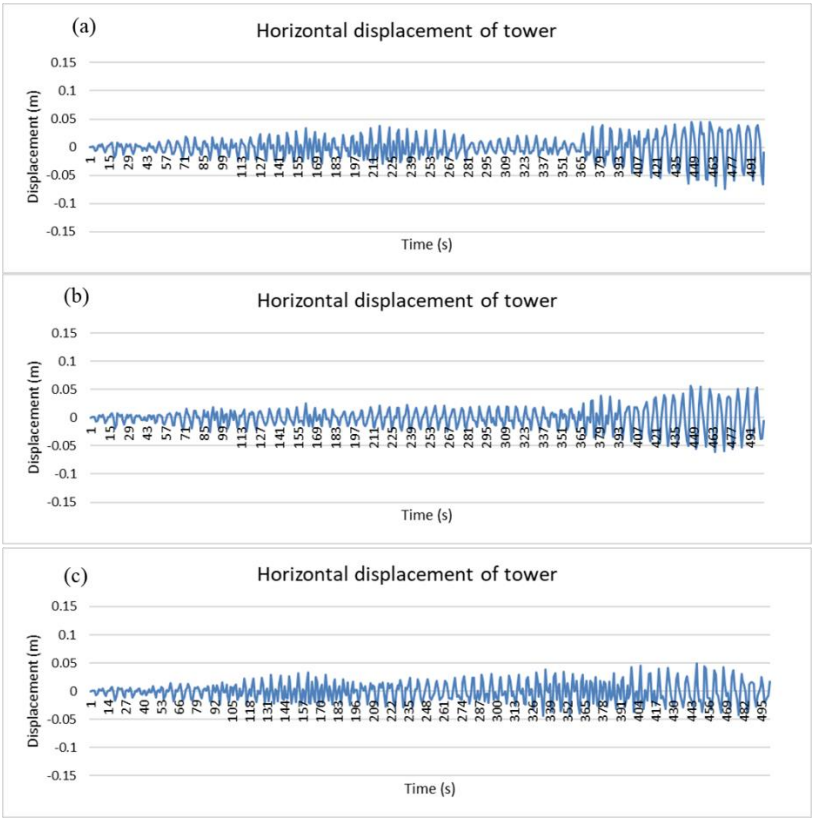

Fig. 5.33. Horizontal displacement of east tower top for case 4-1: (a) reference case; (b) subcase 4-1-25; (c) subcase 4-1-75

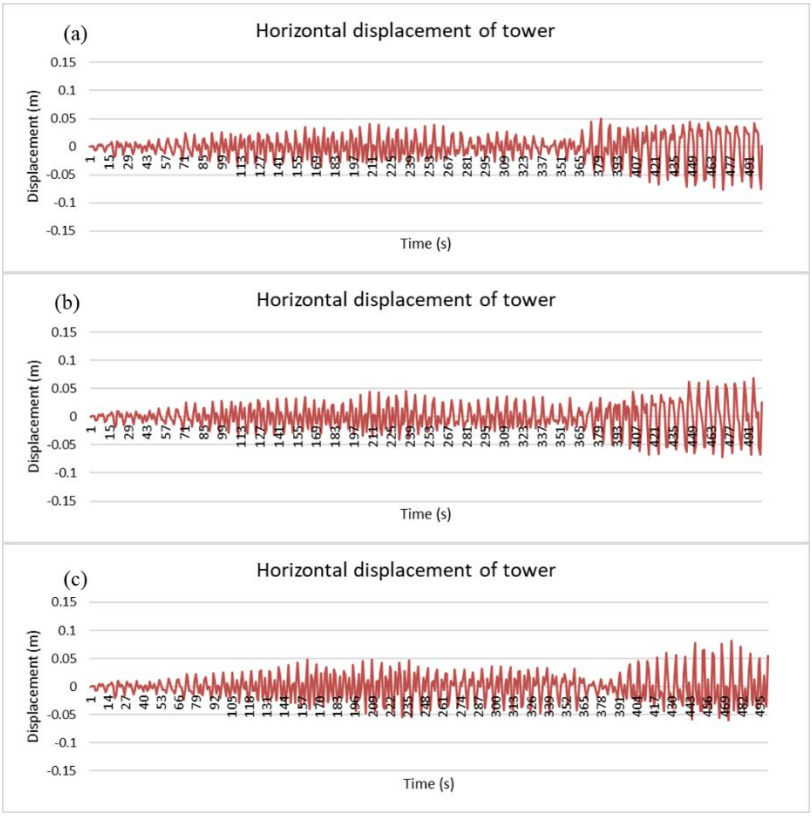

Fig. 5.34. Horizontal displacement of west tower top for case 4-1: (a) reference case; (b) subcase 4-1-25; (c) subcase 4-1-75

5.2.1.5. Summary and discussion

In general, most of the corrosion cases investigated induce similar responses on both decks and towers, except for the vertical response of the decks in subcase 3-1 and the horizontal deflection of the tower tops in subcase 4-1. The different magnitudes of vibration amplitudes occurred because of the asymmetric distribution of corroded cables. The horizontal and vertical deflections of the midpoint of the decks have similar patterns for the four cases investigated at the same corrosion condition during the 500 s of applied load. Therefore, the distribution of the corroded cables has less effect on changing the dynamic response at the middle of deck. For the cases with low corrosion level, the torsional deformation of the deck and also the horizontal deformation of the tower top had similar responses, regardless of the different distributions of the corroded cables along the deck. Once corroded, the cables provide less support to the deck, the distribution of these corroded cables changed the two of vibration modes, when 75% corrosion was applied.

Table 5.1 summarizes the maximum and average displacements for the midpoint of the deck and tower. From Table 5.1, the average horizontal deformations for all cases is the same. The maximum vertical displacement increases as the corrosion level increases for the four subcases. The torsional deformation of the deck's middle point is small during the 500 s of applied load. The average torsional deformations remain the same for every case. The maximum torsional deformation for the subcases with 25% corrosion is higher than for the reference case and the subcases with 75% corrosion, except for the subcase 3-1 with an unbalanced distribution of corroded cables. It can be concluded that the vertical vibration has a dominant effect on the bridge deck response, for critical cable's corrosion. The towers experienced an out-of-plane movement due to the drag by the cables connected to the decks. The average horizontal deformations do not change for every case. The horizontal displacement of the tower top for the all the subcases with 25% corrosion damage is similar to the reference case, while the subcases 1-2 and 2-2 with 75% corrosion condition increase the response during the 500-s

interval, especially for the subcase 2-2 for which the maximum displacement reached 0.47 m. For certain asymmetric distributions, the highest corrosion level has more effect on the tower's dynamic response. Subcase 3-1, for which the distribution of all corroded cables is on one deck, mitigated the most the cable corrosion effect on the tower's vibration. The different vibration patterns during the 500 s interval were noted for the two towers for the subcase 4-1, for which the west tower deflected more than the east tower due to the asymmetric distribution of corroded cables.

Table 5.1. Deformation of decks and towers

	North deck						East tower	
Case No.	U1 (m)	Average	U2 (m)	Average	UR3 (Rad)	Average	U1 of tower (m)	Average
Reference	1.15	-0.08	0.33	-0.04	0.0027	0.00	0.07	0.00
1-2-25	1.20	-0.08	0.57	-0.04	0.0037	0.00	0.07	0.00
1-2-75	0.82	-0.08	0.59	-0.04	0.0017	0.00	0.12	0.00
2-2-25	1.20	-0.08	0.55	-0.04	0.0037	0.00	0.09	0.00
2-2-75	0.90	-0.08	0.71	-0.04	0.0032	0.00	0.47	0.00
3-1-25	1.21	-0.08	0.58	-0.04	0.0037	0.00	0.10	0.00
3-1-75	0.89	-0.08	0.74	-0.04	0.0039	0.00	0.09	0.00
4-1-25	1.20	-0.08	0.54	-0.04	0.0038	0.00	0.06	0.00
4-1-75	0.83	-0.08	0.66	-0.04	0.0023	0.00	0.05	0.00

	South deck						West tower	
Case No.	U1 (m)	Average	U2 (m)	Average	UR3 (Rad)	Average	U1 of tower (m)	Average
Reference	1.15	-0.08	0.33	-0.04	0.0027	0.00	0.07	0.00
1-2-25	1.20	-0.08	0.57	-0.04	0.0037	0.00	0.07	0.00
1-2-75	0.82	-0.08	0.59	-0.04	0.0017	0.00	0.12	0.00
2-2-25	1.20	-0.08	0.55	-0.04	0.0037	0.00	0.09	0.00
2-2-75	0.90	-0.08	0.71	-0.04	0.0032	0.00	0.47	0.00
3-1-25	1.21	-0.08	0.54	-0.04	0.0037	0.00	0.10	0.00
3-1-75	0.89	-0.08	0.65	-0.04	0.0039	0.00	0.09	0.00
4-1-25	1.20	-0.08	0.54	-0.04	0.0038	0.00	0.07	0.00
4-1-75	0.83	-0.08	0.66	-0.04	0.0023	0.00	0.08	0.00

5.2.2. Frequency analysis

The Fast Fourier transform (FFT) is used to transfer the time domain signals into frequency domain signals and to determine the magnitude of its frequency. The power spectrum density (PSD) can be used to connect the power and the frequency obtained from a frequency domain distribution, by transforming the auto-correlation function of the time-history signal. The peak values represent the largest power and its corresponding frequency. In PSD, the frequency with peak power density represents the most critical frequency with the distinct response. The peak values of vertical,

horizontal and torsional deformation can help to identify the coupled movement between two or three of them at the same frequency. The resonance of the structure could happen if the peak frequency of the response is the same or close to the natural frequency of the structure and therefore would enhance the amplitude of vibration. In the aerodynamic analysis of the bridge, the frequency analysis can help to locate the frequency and corresponding simultaneous vibration of the deck at the different planes induced by the corrosion condition.

5.2.2.1. PSD results

For the corrosion cases, both decks have a similar vibration response, therefore the PSD results are the same for both decks. The results for the north deck are presented here, and those for the south deck, which have the same response, can be found in the Appendix B.

Figures 5.35(a) to (c) show the PSD of the horizontal, vertical and torsional displacements of the mid-point of the deck for the reference case. Figure 5.35(a) shows that the high spectral peaks are 0.146 Hz and 0.446 Hz for the horizontal deformation. The peak frequencies of 0.302 Hz and 0.388 Hz for the vertical deformation can be retrieved from Figure 5.35(b). As for the torsional deformation in Figure 5.35(c), the largest responses for torsional movement happened at frequencies of 0.146 Hz, 0.292 Hz and 0.446 Hz. The horizontal and torsional motions are coupled at the frequency of 0.146 Hz and 0.446 Hz.

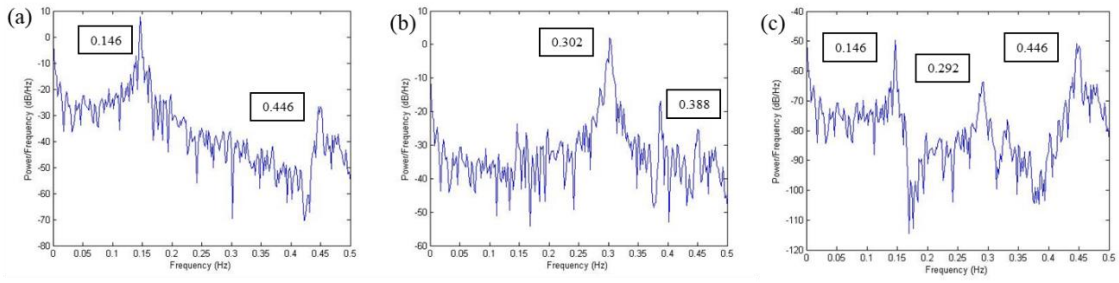

Fig. 5.35. PSD results of mid-span for reference case: (a) horizontal deformation; (b) vertical deformation; (c) torsional deformation

Figures 5.36(a) to (c) and 5.37(a) to (c) illustrate the comparison of the PSD for the vertical, horizontal and torsional deflections of the mid-point of the deck, considering the subcase 1-2 with 25 % and 75% corrosion levels, respectively. In terms of subcase 1-2-25, the peaks represented in the power spectrum correspond to the frequencies of 0.146 Hz and 0.45 Hz for horizontal deformation, 0.302 Hz, 0.388 Hz and 0.45 Hz for the vertical deformation, and 0.146 Hz, 0.294 Hz and 0.45 Hz for the torsional deformation. The coupled motions of horizontal and torsion happened at the frequency of 0.146 Hz, while there is coupling between vertical and torsion occurring at 0.294/0.302 Hz, and between the three directions occurring at a larger frequency of 0.45 Hz. For the subcase 1-2 with worse corrosion condition, 75% corrosion level, the horizontal deformation is significant at the frequencies of 0.148 Hz and 0.456 Hz, the vertical deformation has the peak frequencies of 0.298 Hz, 0.392 Hz and 0.456 Hz, and torsional deformation has peak frequencies of 0.148 Hz, 0.298 Hz and 0.456 Hz. The coupled motions of horizontal and torsion, vertical and torsion, and the three directions for the subcase 1-2-75 occur at the frequencies of 0.148 Hz, 0.298 Hz and 0.456 Hz, respectively.

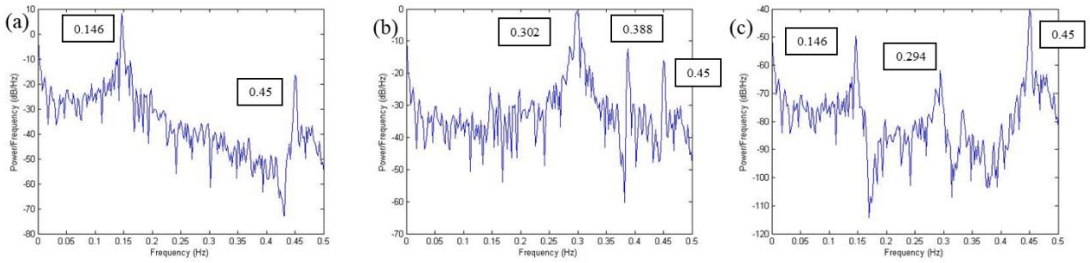

Fig. 5.36. PSD results of mid-span for subcase 1-2-25: (a) horizontal deformation; (b) vertical deformation; (c) torsional deformation

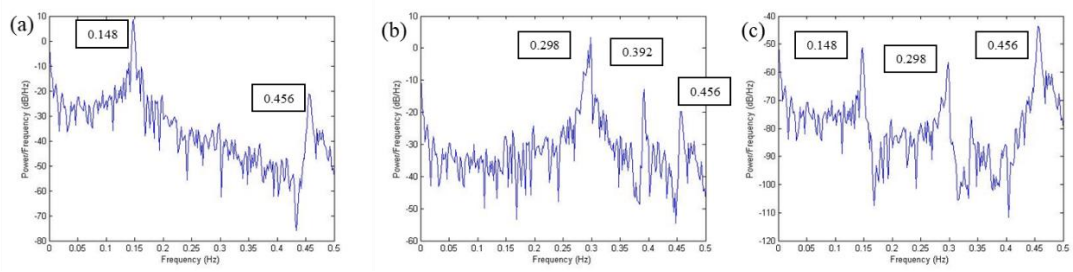

Fig. 5.37. PSD results of mid-span for subcase 1-2-75: (a) horizontal displacement; (b) vertical displacement; (c) torsional deformation

The PSD of the horizontal, vertical and torsional responses of the mid-point of the deck for subcases 2-2-25 and 2-2-75 are compared in Figures 5.38(a) to (c) and 5.39(a) to (c). For subcase 2-2-25, the frequency peaks of 0.146 Hz and 0.45 Hz, 0.298 Hz are for the horizontal vibration, 0.388 Hz and 0.45 Hz for the vertical deformation, and 0.146 Hz, 0.294 Hz and 0.45 Hz for the torsional deformation. The coupled motions of horizontal and torsional vibrations occur at 0.146 Hz, of the vertical and torsional vibration occur at 0.294/0.298 Hz, and of the three deformation modes at 0.45 Hz. For the subcase 2-2-75 (Figure 5.39), the dominant frequencies are 0.148 Hz and 0.458 Hz for the horizontal deformation, 0.294 Hz, 0.392 Hz and 0.458 Hz for the vertical deformation, and 0.148 Hz, 0.298 Hz and 0.458 Hz for the torsional deformation. Therefore, the horizontal and torsional motions are coupled at a frequency of 0.148 Hz, and the coupled motions of vertical and torsional at 0.294/0.298 Hz, while the coupled motions of the three movements occur at a larger frequency of 0.458 Hz.

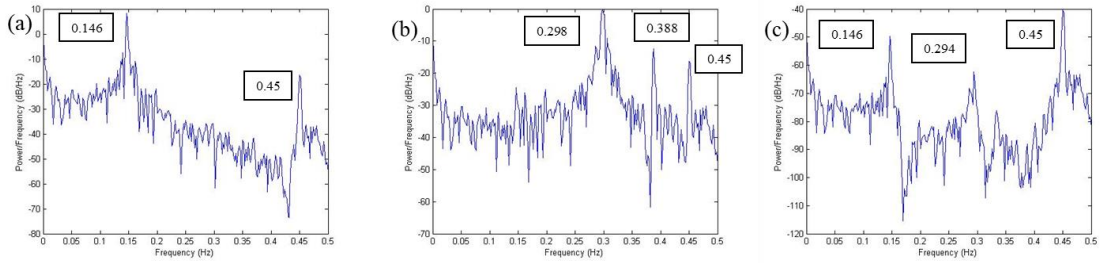

Fig. 5.38. PSD results of mid-span for subcase 2-2-25: (a) horizontal deformation; (b) vertical deformation; (c) torsional deformation

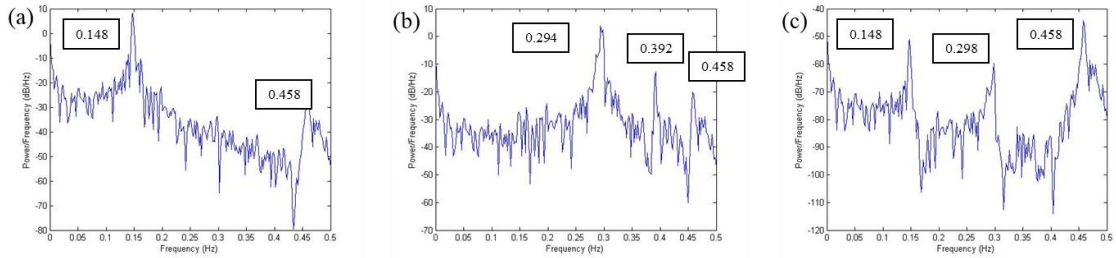

Fig. 5.39. PSD results of mid-span for subcase 2-2-75: (a) horizontal deformation; (b) vertical deformation; (c) torsional deformation

Figures 5.40(a) to (c) and 5.41(a) to (c) present the PDS of the response for the vertical, horizontal and torsional deflections of the mid-span for subcases 3-1-25 and 3-1-75, respectively. As observed in Figures 5.40(a) to (c), there are two peak frequencies at 0.146 Hz and 0.45 Hz for the horizontal deformation, three peaks at 0.302 Hz, 0.388 Hz and 0.45 Hz for the vertical deformation and three peaks at 0.146 Hz, 0.298 Hz and 0.45 Hz for the torsional deformation. There is coupling between the horizontal and torsional motions at a frequency of 0.146 Hz, between vertical and torsional motions at a frequency of 0.298/0.302 Hz, and between the three movements at a frequency of 0.45 Hz. When the subcase 3-1 with 75% corrosion is considered, as illustrated in Figure 5.41, three peaks are observed in the three vibration modes, which are 0.148 Hz, 0.392 Hz and 0.462 Hz for the horizontal deformation, 0.294 Hz, 0.392 Hz and 0.462 Hz for the vertical deformation, and 0.148 Hz, 0.294 Hz and 0.462 Hz for the torsional deformation. There is coupling between horizontal and torsional motions at a frequency of 0.148 Hz, and between horizontal and vertical motions at a frequency of 0.392 Hz. The three movements are coupled at a frequency of 0.462 Hz.

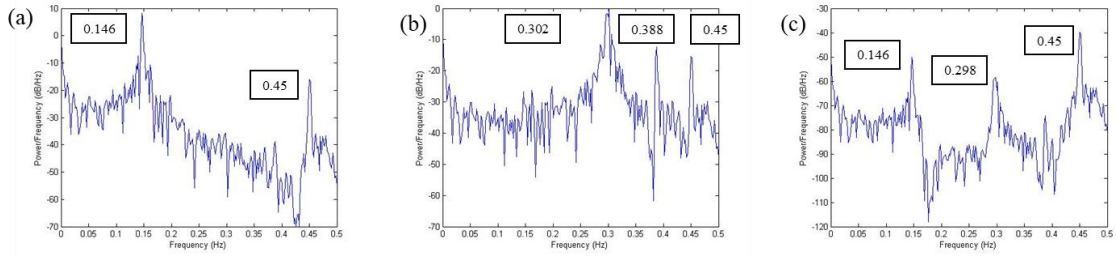

Fig. 5.40. PSD results of mid-span for subcase 3-1-25: (a) horizontal deformation; (b) vertical deformation; (c) torsional deformation

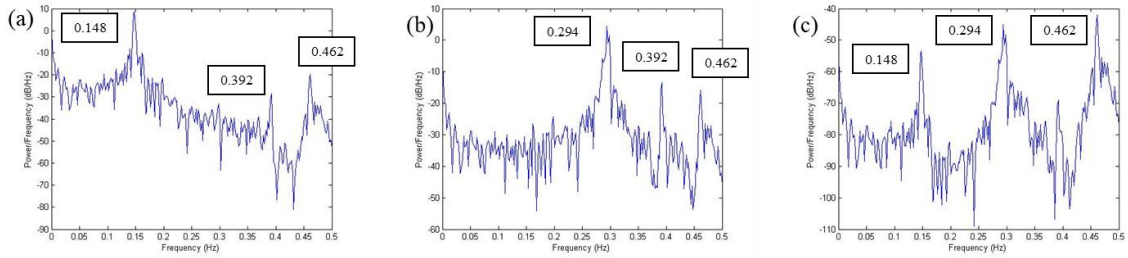

Fig. 5.41. PSD results of mid-span for subcase 3-1-75: (a) horizontal deformation; (b) vertical deformation; (c) torsional deformation

The PSD for the subcase 4-1 with two different corrosion levels is illustrated in Figures 5.42(a) to (c) and 5.43(a) to (c). For subcase 4-1-25 (Figure 5.42), the peaks represented in the power spectrum correspond to frequencies of 0.146 Hz and 0.45 Hz for the horizontal deformation, 0.302 Hz, 0.388 Hz and 0.45 Hz for the vertical deformation, and 0.146 Hz, 0.29 Hz and 0.45 Hz for the torsional deformation. The horizontal and torsional movements are coupled at a frequency of 0.146 Hz, while the vertical and torsional motions are coupled at 0.29/0.302 Hz and the three directions at a larger frequency of 0.45 Hz. For the subcase 4-1-75 (Figure 5.43), the horizontal deformation is significant at frequencies of 0.148 Hz and 0.456 Hz, the vertical deformation has peak frequencies of 0.294 Hz, 0.392 Hz and 0.456 Hz, and the torsional deformation has peak frequencies at 0.148 Hz, 0.292 Hz and 0.456 Hz. There is coupling between horizontal and torsional motions, between vertical and torsional motions, and between the three directions for the subcase 4-1-75 at frequencies of 0.148 Hz, 0.292/0.294 Hz and 0.456 Hz, respectively.

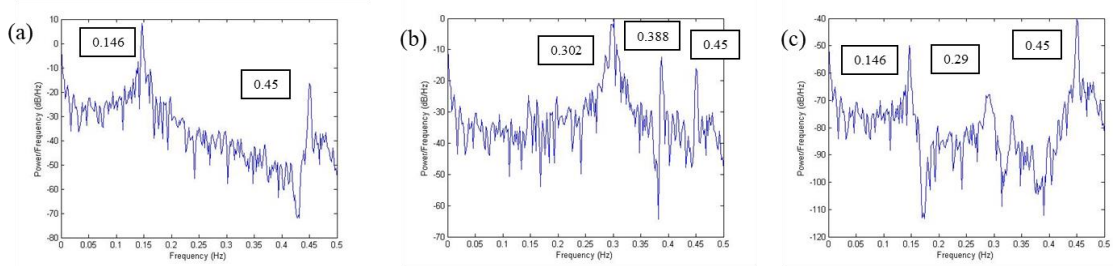

Fig. 5.42. PSD results of mid-span for subcase 4-1-25: (a) horizontal deformation; (b) vertical deformation; (c) torsional deformation

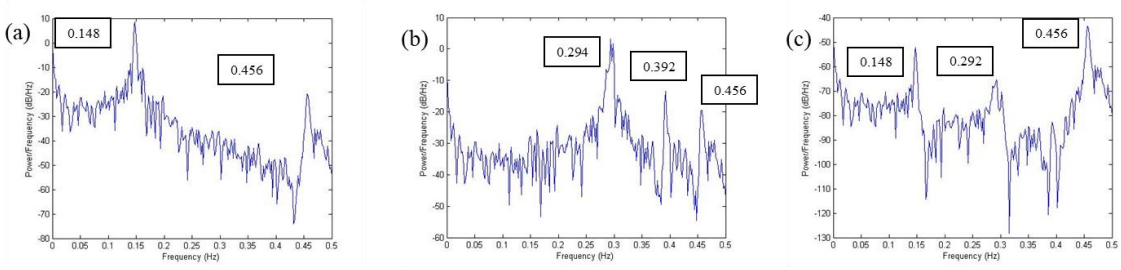

Fig. 5.43. PSD results of mid-span for subcase 4-1-75: (a) horizontal deformation; (b) vertical deformation; (c) torsional deformation

5.2.2.2. Summary and discussion

The frequency domain diagrams for the responses of the middle point of the deck are illustrated through the method of power spectrum density, presenting the significant responses and their corresponding frequencies for subcases 1-2, 2-2, 3-1 and 4-1 under different corrosion levels. The coupled motions could occur at different frequencies.

Applying the recorded wind load, the coupled movement can be observed for the reference case, which are horizontal and torsional at frequencies of 0.146 Hz and 0.446 Hz. When the corroded cables are distributed, one more peak frequency appears in the vertical deformation for all the cases due to less restraint provided by the cables. Furthermore, when the distribution of corroded cables corresponding to subcase 3-1 with 75% corrosion damage, one more peak frequency can be observed in the horizontal deformation at 0.392 Hz. For all the cases, peak frequencies in all three directions for the cases with 25% corrosion are close to that for the reference case; however, there is a slight increase in the peak frequencies when the corrosion condition becomes worse. The distribution of corroded cables has less influence on creating more peak frequencies.

The corrosion condition also induces coupled motions of the three directions at the largest peak frequency for each case when compared to the reference case, while the bridge is exposed to real wind conditions. Moreover, the three coupled motions, which are horizontal and torsional, vertical and torsional, and the three-direction responses, can be observed for both subcases with 25% and 75% corrosion levels, except for the

subcase 3-1-75. Four coupled motions, which contain the horizontal and torsional, vertical and torsional, horizontal and vertical, and the three-direction responses, are observed for the case with all the highly-corroded cables on one deck, such as subcase 3-1-75. The increasing corrosion level lead to an increasing frequency of the coupling of the horizontal and torsional motions, and the three-directional responses compared to the reference case. The coupled movement at the same frequency can compromise the structure and damage the bridge components, finally leading to the failure of bridge. The cable corrosion reduces the capacity to sustain the deck and increases the coupled movements for the deck when subjected to the wind load.

The peak frequencies from the responses, presented in Table 5.2, are compared to the natural frequencies listed in Table 5.3, indicating that one of the peak frequencies, 0.146 Hz or 0.148 Hz, of the horizontal motion for each case is close to the fundamental frequency of 0.145 Hz/0.146 Hz, corresponding to the mode shape of the first order of horizontal vibration of the deck. It is also observed from the comparison that one of the peak frequencies of vertical motion (0.388 Hz or 0.392 Hz) is close to the natural frequency associated to the 8^{th} mode, which represents the third-order vertical motion of the deck for all the cases. For the torsional deformation, the subcase 1-2-75 registered a frequency of 0.298 Hz, which is close to the frequency of 0.292 Hz associated to the 6^{th} mode, which corresponds to the 1^{st}-order torsional motion of deck. However, the rest of the cases do not have the same frequency as the natural frequency for the torsional motion. Therefore, the 1^{st} and 8^{th} modes, which are respectively horizontal and vertical motion, are easily excited for the bridge when exposed to the real wind load, and the corrosion level and the corrosion distribution have less effect on the excited modes.

Table 5.2. Summary of peak frequencies in every direction

Deck's movement	Frequency (Hz)				
	Reference	1-2-25	1-2-75	2-2-25	2-2-75
Horizontal	0.146/0.446	0.146/0.45	0.148/0.456	0.146/0.45	0.148/0.458
Vertical	0.302/0.388	0.302/0.388/ 0.45	0.298/0.392/ 0.456	0.298/0.388/ 0.45	0.294/0.392/ 0.458
Twist	0.146/0.292/ 0.446	0.146/0.294/ 0.45	0.148/0.298/ 0.456	0.146/0.294/ 0.45	0.148/0.298/ 0.458

Deck's movement	Reference	3-1-25	3-1-75	4-1-25	4-1-75
Horizontal	0.146/0.446	0.146/0.45	0.148/0.392/ 0.462	0.146/0.45	0.148/0.456
Vertical	0.302/0.388	0.294/0.392/ 0.462	0.294/0.392/ 0.462	0.302/0.388/ 0.45	0.294/0.392/ 0.456
Twist	0.146/0.292/ 0.446	0.146/0.298/ 0.45	0.148/0.294/ 0.462	0.146/0.290/ 0.45	0.148/0.292/ 0.456

Table 5.3. Natural frequencies and corresponding mode shapes

Frequency summary						
Mode no	reference	1-2-25	1-2-75	2-2-25	2-2-75	Mode shape
1	0.145	0.145	0.146	0.145	0.146	S-H-deck
2	0.172	0.167	0.153	0.170	0.164	S-V-deck
3	0.192	0.191	0.187	0.191	0.190	A-V-deck
4	0.253	0.254	0.255	0.254	0.256	S-H-tower
5	0.256	0.257	0.259	0.257	0.259	A-H-tower
6	0.324	0.314	0.292	0.320	0.310	S-T-deck
7	0.358	0.358	0.357	0.359	0.359	A-H-deck
8	0.387	0.386	0.382	0.387	0.385	S-V-deck
9	0.424	0.422	0.419	0.423	0.423	A-T-deck
10	0.581	0.581	0.581	0.582	0.583	A-T-V-deck
Mode no	reference	3-1-25	3-1-75	4-1-25	4-1-75	Mode shape
1	0.145	0.145	0.146	0.145	0.146	S-H-deck
2	0.172	0.167	0.173	0.167	0.164	S-V-deck
3	0.192	0.191	0.199	0.191	0.195	A-V-deck
4	0.253	0.254	0.257	0.254	0.255	S-H-tower
5	0.256	0.257	0.260	0.258	0.263	A-H-tower
6	0.324	0.315	0.323	0.315	0.310	S-T-deck
7	0.358	0.358	0.358	0.358	0.358	A-H-deck
8	0.387	0.386	0.388	0.386	0.386	S-V-deck
9	0.424	0.423	0.434	0.423	0.429	A-T-deck
10	0.581	0.582	0.588	0.582	0.586	A-T-V-deck
S : symmetry, A : asymmetry, H : horizontal, V : vertical, T : torsion						

Chapter 6 - Conclusions and future work

6.1. Conclusions

This thesis has investigated the effect of corroded stay cables on the structural behaviour of cable-stayed bridges through finite element modelling of the problem. A finite element model of the Stonecutters Cable-stayed Bridge was used to investigate the static response caused by dead load and the dynamic response induced by wind load, when a series of its stay cables were subjected to three different levels of corrosion, losing 25%, 50% and 75% of the cross-section. Several damage scenarios were considered in the simulations: four distributions of a group of 8 corroded cables (symmetric and asymmetric distributions) and different locations along the decks from the mid-span.

Through the static analysis, the maximum deflection of the decks' mid-span and cable stresses were verified initially by following the serviceability limit criteria specified in the Canadian Highway Bridge Design Code (CSA-S6-14), proving that the results were within the allowable deflection limits. The structural response investigation of the bridge with corroded cables, under static load, led to the following conclusions:

- An increasing corrosion level in the stay cables, regardless of the distribution of cables and location along the deck, results in a larger deck's deflection due to less support from the damaged cables.
- The location of the 8 corroded cables along the deck showed different changes in the mid-span deflection, for the four major cases. The 1st to 4th cables from the midpoint are more important in supporting the deck, because all these damaged cables on one side (subcase 4-1-75) or one deck (subcase 3-1-75) resulted in the largest deflection.
- When considering an asymmetric distribution of the corroded cables, the deflection of the deck for the corroded side is larger than non-corroded one, thus resulting in different locations of the maximum deflection along the deck.

- In terms of cables stress changes, under the static load applied to the deck, the corroded cables cannot support the deck as usual. As a result, the damaged and adjacent cables were all affected by an increase in the stress level with increasing level of corrosion damage.
- Furthermore, due to the reduced cross-section area and the increased load in the damaged cables closest to the mid-span, a rapid increase of internal stress is observed. The case with damaged cables located on one side of both decks resulted in the largest stress relative change percentage among

When the impact of the corroded stay cables on the dynamic response of the bridge was investigated, the first 30 natural frequencies were compared in terms of relative change percentage for different corroded cable distributions and locations along the deck. The following conclusions can be drawn from the results:

- The corresponding mode shapes are similar for different corrosion conditions, except for the towers' motion of the 4^{th} vibration mode for subcase 4-1 and the decks' motion of the 2^{nd} vibration mode for subcase 3-1, both due to asymmetrical distribution of corroded stay cables.
- The frequency changes in the 2^{nd}, 3^{rd} and 6^{th} modes for the cases with symmetric distribution are different from that with asymmetric distribution. The low corrosion level (25% and 50%) reduced deck's frequencies in symmetric vertical and torsional vibration. For a corrosion level of 75%-section reduction, the deck's frequencies in asymmetric vibration was increased. For the cases with asymmetric distribution with regard to center line, the 75% corrosion level also registered a similar decrease in the 2^{nd} and 6^{th} modes compared to the cases with symmetric distribution. The subcase 2 decreased the natural frequencies in the 2^{nd}, 3^{rd} and 6^{th} modes for all symmetric and asymmetric cases, whereas the subcase 1 increased the frequency of the 3^{rd} mode for symmetric cases, and decreased frequencies of the 2^{nd} and 6^{th} modes for asymmetric cases.
- As the corroded cables were located further from the mid-span, the distribution

of corroded cables has less influence on changing the natural frequencies.

To simulate the bridge's behavior under real wind conditions, the wind load resulting from a record of 500 s of actual wind data was applied on the twin decks. The 500 s time history response showed the vertical, horizontal and torsional motions of the middle point of the deck and the horizontal motion of the tower top. From the dynamic analysis under wind load, the following conclusions are drawn:

- The distribution of corroded cables with low corrosion level has less influence on changing the dynamic response in which the mid-span vibrates in vertical and horizontal directions and for torsional vibration.
- The cases with all corroded cables on one deck and one side of the deck influence the vertical deformation of both decks and also the horizontal vibration of both towers, respectively.
- The vertical vibration dominates the deck's response when the corrosion condition becomes critical.
- The increased corrosion level also reduces the restraint to the tower and increases the maximum amplification of horizontal vibration, especially for the subcase 2-2.

The frequency analysis can highlight the different frequencies in the time history signal, and the PSD method can help identify the larger response with the corresponding frequency. The same or close frequency of different vibration could result in a coupled motion of the deck, which could endanger the stability of the bridge. Based on this analysis, the following observations were concluded:

- There is one more peak frequency in the vertical movement for the cases with corroded cables compared to the reference case.
- The cases with corrosion-damaged cables resulted in more coupling motions of the deck, especially the subcase 3-1 with 75% corrosion level. The frequency of coupled motions increased as the corrosion level became worse.
- When comparing the peak frequencies of each motion with the natural

frequencies, the fundamental frequency and that one associated with the 8th vibration mode, which respectively correspond to symmetric horizontal and symmetric vertical vibrations of the deck, were found easily to be excited in all the non-corroded and corroded cases. When cables were subjected to a 75%-corrosion level, the 6th mode, in addition to the 1st and 8th modes, was also easily excited for subcase 1-2.

The results show different changes in dynamic response for a long-span cable-stayed bridge compared to the medium-span cable-stayed bridge discussed by Zhang (2015). The effect induced by the corroded cables on the static response of the deck is in good agreement with the results reported by Zhang (2015); however, the variance of natural frequencies on each mode is different because the bridge models were different. Zhang (2015) investigated a medium-span cable-stayed bridge, thus the results are not directly comparable to the bridge structure in this study, showing the uniqueness of the long-span bridge behavior. It also provides a supplement to the responses of a cable-stayed bridge with multiple damaged cables. This study explores a numerical method that could complement existing non-destructive technology (e.g., in-situ sensors) to diagnose the distribution and corrosion condition of stay cables by comparing with information of cable stresses, deck deflection, and deck's vibration gathered from the sensors installed on the cables and decks.

6.2. Research limitations

In the work presented in this thesis, several limitations of the model were identified. The estimated time for the corroded cables when they reached the designed corrosion level was solved under the simplification method of applying uniform on the cable corrosion cross-section, which does not represent real conditions as it ignors the protection layer. The corrosion on the cable was simulated along the entire length of the cable because the truss element cannot simulate corrosion on one section. Also, the wind load was calculated by queasy-steady equations based on the mean wind load, and

the effect of the wind angle of attack was ignored as a simplification. Further investigation is needed to simulate real wind load conditions given by recorded wind data.

6.3. Future work

In this study, the finite element model of the Stonecutters Cable-stayed Bridge was developed based on the geometric shape and material properties from published papers, but some detailed parts for the cable-stayed bridge are not introduced in the literature, and some modelling methods maybe not accurate enough to model the structure, since this super-long cable-stayed bridge is different from the standard cable-stayed bridges. The model is not able to be calibrated for the static response due to a lack of enough monitoring data of the bridge's behavior. In the future, the model can be developed more accurately to reflect the real structure, if more research and technical information on the Stonecutters Bridge becomes available.

In the dynamic analysis, the deck is assumed to be the main component to withstand the wind load, and the three components of the wind load are only applied on both decks to study their responses. However, the wind load effects of cables and towers, which are also subjected to wind, are considered as minor and are ignored for simplification. Therefore, the wind load equations for the cables and towers need to be applied in a future study as well.

This study only focuses on the static and dynamic responses of the cable-stayed bridge with corroded cables under gravity and wind loads. If cable corrosion can be detected through responses while the bridge is still open, the effect of traffic load on the bridge needs to be investigated as well as a future study.

References

ABAQUS Inc. (2012). *ABAQUS/Standard user's manual Version 6.11*. Hibbitt, Karlsson & Sorensen.

Andrade, C., Alonso, C., and Molina, F. J. (1993). "Cover cracking as a function of bar corrosion: Part I-Experimental test." *Materials and Structures*, 26(8), 453–464.

Bao, X. (2014). "Cable's Seismic Vulnerability in Cable-stayed Bridges under Corrosive Service Environment." Dalian University of Technology. (In Chinese)

Barton, S. C., Vermaas, G. W., West, A. C., and Betti, R. (2000). "Accelerated Corrosion and Embrittlement of High-strength Bridge Wire." *Journal of Material in Civil Engineering*, 12, 33–38.

Betti, R., Khazem, D., Carlos, M., Gostautas, R., and Virmani, Y. P. (2014). *Corrosion Monitoring Research for City of New York Bridges*.

Billah, K. Y., and Scanlan, R. H. (1991a). "Resonance, Tacoma Narrows bridge failure, and undergraduate physics textbooks." *American Journal of Physics*, 59(2), 118–124.

Billah, K. Y., and Scanlan, R. H. (1991b). "Resonance, Tacoma Narrows bridge failure, and undergraduate physics textbooks." *American Journal of Physics*, AAPT, 59(2), 118–124.

Caetano, E. (2016). *Cables*. *Innovative Bridge Design Handbook*.

Chen, W., and Yang, J. (2014). "Inspection and Assessment of Stay Cables in Cable Stayed Bridges." 954–960.

Chen, X., Matsumoto, M., and Kareem, A. (2000). "Aerodynamic Coupling Effects on Flutter and Buffeting of Bridges." *Journal of Engineering Mechanics*, 126(9), 891–898.

Chen, Z. (2005). *Bridge Wind Engineering*. China Communications Press.

Cheng, S. H., and Lau, D. T. (2002). "Modeling of cable vibration effects of cable-

stayed bridges." *Earthquake Engineering and Engineering Vibration*, 1(1), 74–85.

Coca, F. J. O., Tello, M. U. L., Gaona-Tiburcio, C., Romero, J. A., Martínez-Villafañe, A., Maldonado, E. B., and Almeraya-Calderón, F. (2011). "Corrosion fatigue of road bridges: A review." *International Journal of Electrochemical Science*, 6(8), 3438–3451.

Craig, R. R., and Kurdila, A. J. (2006). *Fundamentals of structural dynamics*. John Wiley & Sons.

Das, R., Pandey, A. D., Soumya, Mahesh, M. J., Saini, P., and Anvesh, S. (2016). "Progressive Collapse of a Cable Stayed Bridge." *Procedia Engineering*, The Author(s), 144, 132–139.

Diana, G., Fiammenghi, G., Belloli, M., and Rocchi, D. (2013). "Wind tunnel tests and numerical approach for long span bridges: The Messina bridge." *Journal of Wind Engineering and Industrial Aerodynamics*, Elsevier, 122, 38–49.

Elachachi, S. M., Breysse, D., Yotte, S., and Cremona, C. (2006). "A probabilistic multi-scale time dependent model for corroded structural suspension cables." *Probabilistic Engineering Mechanics*, 21(3), 235–245.

Ernst, H. . J. (1965). "Der E-modul von Seilen unter Berücksichtigung des Durchhanges." *Der Bauingenieur*, 40, 52–55.

Ewins, D. J. (2003). "Modal testing: theory, practice and application (mechanical engineering research studies: engineering dynamics series)." Wiley.

Falbe-hansen, K., Hauge, L., and Kite, S. (2004). "Stonecutters Bridge - Detailed Design." *IABSE Symposium Report*, International Association for Bridge and Structural Engineering, 19--24.

Falbe-hansen, K., HAUGE, L., and KITE, S. (2017). "Stonecutters Bridge - Detailed Design." (January 2004).

Farquhar, D. J. (2008). *Cable Stayed Bridges*. *ICE manual of bridge engineering*, Thomas Telford.

Feng, F. (2015). “Flutter Analysis of Stonecutters Cable-stayed Bridge using Finite Element Model.” University of Ottawa.

Francis, J., Bakht, B., Richard, G., Tharmabala, T. ., and Yea, H. (2006). *A National Standard of Canada Canadian Highway Bridge*. (M. Braiter, ed.), Canadian Standards Association.

Gimsing, N. J., and Georgakis, C. T. (2011). *Cable supported bridges: Concept and design*. John Wiley & Sons.

Guo, Y. (2014). “Cable Corrosion Analysis and Damage Monitoring.” 1302–1305.

Hauge, L., and Andersun, H. (2011). “Longer.” *35th Annual Symposium of IABSE/52nd Annual Symposium of IASS/6th International Conference on Space Structures, London*, 20–23.

Heerah, A. R. P. (2009). “Field Investigation of Fundamental Frequency of brodges using ambient vibration measurements.” McGill University.

Hua, X. G., Ni, Y. Q., Chen, Z. Q., and Ko, J. M. (2009). “Structural Damage Detection of Cable-Stayed Bridges Using Changes in Cable Forces and Model Updating.” 135(September), 1093–1106.

Hui, M. C. H. (2013). “Full-bridge aeroelastic model wind tunnel tests for the Stonecutters Bridge.” *HKIE Transactions Hong Kong Institution of Engineers*, 20(2), 109–123.

Hui, M. C. H., Ding, Q. S., and Xu, Y. L. (2006). “Flutter analysis of Stonecutters Bridge.” *Wind and Structures*, Vol. 9(No. 2), 125–146.

Kaji, A., and Grady, R. O. (2010). “An introduction to Stonecutters bridge , Hong Kong : Erection of the steel segments , hydraulic buffers and lateral bearings.” 978–984.

Kaji, A., Hirai, T., Grady, R. O., and Sham, R. (2010). “An introduction to Stonecutters bridge , Hong Kong : Erection of the steel segments , hydraulic buffers and lateral bearings.” *IABSE-JSCE Joint Conference on Advances in Bridge Engineering-II*, 182–190.

Kao, C. S., and Kou, C. H. (2010). “The influence of broken cables on the structural behavior of long-span cable-stayed bridges.” *Journal of Marine Science and Technology*, 18(3), 395–404.

Kao, C. S., Kou, C. H., and Xie, X. (2006). “Static instability analysis of long-span cable-stayed bridges with carbon fiber composite cable under wind load.” *Tamkang Journal of Science and Engineering*, 9(2), 89–95.

Karanci, E. (2017). “Modeling Corrosion in Suspension Bridge Main Cables.” Columbia University.

Kite, S., Yeung, N., and Kwok, S. (2007). “Stonecutters bridge - Detailed design and construction of superstructure.” *Bridge Design, Construction and Maintenance - Proceedings of the two-day International Conference organised by the Institution of Civil Engineers, ICE*, 11–20.

Kivi, E. (2009). “Structural Behavior of Cable- Stayed Suspension Bridge Structure.” Tallinn University of Technology.

Klinesmith, D. E., McCuen, R. H., and Albrecht, P. (2007). “Effect of Environmental Conditions on Corrosion Rates.” *Journal of Materials in Civil Engineering*, 19(2), 121–129.

Larsen, A., and Larose, G. L. (2015). “Dynamic wind effects on suspension and cable-stayed bridges.” *Journal of Sound and Vibration*, Elsevier, 334(1), 2–28.

Larsen, A., Yeung, N., and Carter, M. (2012). “Stonecutters Bridge, Hong Kong: wind tunnel tests and studies.” *Proceedings of the Institution of Civil Engineers-Bridge Engineering*, 91–104.

Li, D., Ou, J., Lan, C., and Li, H. (2012). “Monitoring and failure analysis of corroded bridge cables under fatigue loading using acoustic emission sensors.” *Sensors*, 12(4), 3901–3915.

Li, X., Zhou, J., Liu, Q., Kong, L., and Zhou, J. (2007). “Effect of tension on corrosion behavior of galvanized steel wire for cable-stayed bridge [J].” *Electrochemistry*, 3, 297–301.

Liang, X. (2008). “Corrosion Behavior and Service Life Evaluation Study on Cable of Cable-Stayed Bridge.” Chongqing Jiaotong University. (In Chinese)

Lonetti, P., Pascuzzo, A., and Sarubbo, R. (2011). “Dynamic Behavior of Cable Supported Bridges Affected by Corrosion Mechanisms under Moving Loads.” *Europe, Comsol Conference*, 87030.

Lu, W., and He, Z. (2016). “Vulnerability and Robustness of Corroded Large-Span Cable-Stayed Bridges under Marine Environment.” *Journal of Performance of Constructed Facilities*, 30(1), 04014204.

Mehranfar, S. (2014). “Finite Element Modelling and On-Site Measurements for Roof Mounted Photovoltaic Solar Panels under High Wind Load.”

Meier, U. (2012). “Carbon Fiber Reinforced Polymer Cables: Why? Why Not? What If?” *Arabian Journal for Science and Engineering*, 37(2), 399–411.

Morcillo, M., Chico, B., Díaz, I., Cano, H., and de la Fuente, D. (2013). “Atmospheric corrosion data of weathering steels. A review.” *Corrosion Science*, Elsevier Ltd, 77, 6–24.

Nakamura, S. I., Suzumura, K., and Tarui, T. (2004). “Mechanical Properties and Remaining Strength of Corroded Bridge Wires.” *Structural Engineering International: Journal of the International Association for Bridge and Structural Engineering (IABSE)*, 14(1), 50–54.

Newland, D. E. (2012). *An introduction to random vibrations, spectral & wavelet analysis*. Courier Corporation.

Olamigoke, O. (2017). “Structural Response of Cable-Stayed Bridges to Cable Loss.”

Pipinato, A., Pellegrino, C., Fregno, G., and Modena, C. (2012). “Influence of fatigue on cable arrangement in cable-stayed bridges.” *International Journal of Steel Structures*, 12(1), 107–123.

Pollock, E. (2018). “Italy’s Morandi Bridge collapse-what do we know.” *engineering.com*, <https://www.engineering.com/BIM/ArticleID/17517/Italys-Morandi-Bridge-CollapseWhat-Do-We-Know.aspx>.

Rui, D., and Yang, G. Y. (2012). “Accurate equivalent static wind loads of lang-span bridges based on the displacement responses.” 765–773.

Sabri, A. (2012). “Finite element modelling of the stonecutters cable-stayed bridge.” *M.Eng report of University of Ottawa*, (April), 144–234e.

Salter, S. H. (2006). “Flushing Tape to Stop Corrosion of Suspension Bridge Cables.”

Sarcos-Portillo, A., Navarro-Cerpa, A., and Garcia-Legl, H. (2003). “Inspection and Process of Tension of Cables of General Rafael Urdaneta Bridge.” *Journal of Bridge Engineering*, 8(4), 223–228.

Scanlan, R. H. (1996). “Aerodynamics of cable-supported bridges.” *Journal of Constructional Steel Research*, Elsevier, 39(1), 51–68.

Stahl, F. L., and Gagnon, C. P. (1996). *Cable corrosion in bridges and other structures: Causes and solutions*. New York: ASCE Press.

Tabatabai, H. (2005). *Inspection and Maintenance of Bridge Stay Cable Systems - A Synthesis of Highway Practice*.

Thu, A. N., and Khaing, S. Y. (2014). “Structural Behaviors of Long-Span Cable-Stayed Bridge With A-Shaped Tower Due to Three Wind Speeds.” *International Journal of Engineering Research and*, 3(10), 405–411.

Trauth, M. H., Gebbers, R., Marwan, N., and Sillmann, E. (2006). *MATLAB recipes for earth sciences*. Springer.

Vickneswaran, S. V., and Eyre, J. (2013). “Deck stiffness selection in the design of long span cable stayed bridges.”

Vikas, A. C., Prashanth, M. H., Gogoi, I., and Channappa, T. M. (2013). “Effect of Cable Degradation on Dynamic Behavior of Cable Stayed Bridges.” *Journal of Civil Engineering Research*, 3(1), 35–45.

Virola, J., and Ing-FEANI, E. (2011). “The Russky Island Bridge--world-record cable-stayed bridge in Russia.” *Tierakennusmestari TIRA*, 2, 64–65.

Xie, F. X., Chen, L., Ji, B. H., and Hu, X. Y. (2015). “Electrochemical Test Research on Corrosion Resistance of Cable Wires with Different Protection Layers.”

Applied Mechanics and Materials, 713–715, 2689–2694.

Xu, J., and Chen, W. (2006). "Detection and Analysis of the Cable Deteriorations of Shimen Bridge." 81–84. (In Chinese)

Xu, J., and Chen, W. (2013). "Behavior of wires in parallel wire stayed cable under general corrosion effects." *Journal of Constructional Steel Research*, Elsevier Ltd, 85, 40–47.

Yang, L. (2013). "Mechanical Behavior of Cable Damage and Their Influence on the Structure for a Cable-Stayed bridge." Beijing University of Civil Engineering and Architecture.(In Chinese)

Zhang, Y. (2015). "A Study on the Influence of Cable Damage on the Structure Performance of the Cable-stayed Bridge." Chongqing Jiaotong University. (In Chinese)

Zhu, Q. (2014). "Frequency-domain buffeting analysis of a long-span twin-box-deck bridge with distributed buffeting loads." The Hong Kong Polytechnic University.

Appendix A

Table A1. Pretension values and equivalent E in each stay cable

Cable No.				Tension Force on Cable (N)	$E_{eq\ (N/m^2)}$
ES1	EN1	WN1	WS1	51246621	1.99E+11
ES2	EN2	WN2	WS2	50939142	1.99E+11
ES3	EN3	WN3	WS3	49869420	1.99E+11
ES4	EN4	WN4	WS4	48921901	1.99E+11
ES5	EN5	WN5	WS5	42878000	1.99E+11
ES6	EN6	WN6	WS6	41806050	1.99E+11
ES7	EN7	WN7	WS7	40802704	1.99E+11
ES8	EN8	WN8	WS8	39660229	1.99E+11
ES9	EN9	WN9	WS9	35474549	1.99E+11
ES10	EN10	WN10	WS10	34410313	1.99E+11
ES11	EN11	WN11	WS11	33274772	1.99E+11
ES12	EN12	WN12	WS12	31943781	1.99E+11
ES13	EN13	WN13	WS13	28975688	1.99E+11
ES14	EN14	WN14	WS14	27816660	1.99E+11
ES15	EN15	WN15	WS15	26592727	1.99E+11
ES16	EN16	WN16	WS16	25396054	1.99E+11
ES17	EN17	WN17	WS17	21366738	1.99E+11
ES18	EN18	WN18	WS18	20234300	1.99E+11
ES19	EN19	WN19	WS19	19020242	1.99E+11
ES20	EN20	WN20	WS20	17860008	1.99E+11
ES21	EN21	WN21	WS21	13607611	1.99E+11
ES22	EN22	WN22	WS22	12655078	1.99E+11
ES23	EN23	WN23	WS23	11769223	1.99E+11
ES24	EN24	WN24	WS24	10933608	1.99E+11
ES25	EN25	WN25	WS25	6239141	2.00E+11
ES26	EN26	WN26	WS26	5864793	2.00E+11
ES27	EN27	WN27	WS27	5512905	2.00E+11
ES28	EN28	WN28	WS28	5264824	2.00E+11
ES29	EN29	WN29	WS29	5264824	2.00E+11
ES30	EN30	WN30	WS30	5512905	2.00E+11
ES31	EN31	WN31	WS31	5864793	2.00E+11
ES32	EN32	WN32	WS32	6239141	2.00E+11
ES33	EN33	WN33	WS33	10933608	2.00E+11
ES34	EN34	WN34	WS34	11769223	2.00E+11
ES35	EN35	WN35	WS35	12655078	2.00E+11
ES36	EN36	WN36	WS36	13607611	2.00E+11
ES37	EN37	WN37	WS37	17860008	2.00E+11
ES38	EN38	WN38	WS38	19020242	2.00E+11
ES39	EN39	WN39	WS39	20234300	2.00E+11
ES40	EN40	WN40	WS40	21366738	2.00E+11
ES41	EN41	WN41	WS41	25396054	2.00E+11
ES42	EN42	WN42	WS42	26592727	2.00E+11
ES43	EN43	WN43	WS43	27816660	2.00E+11
ES44	EN44	WN44	WS44	28975688	2.00E+11
ES45	EN45	WN45	WS45	31943781	2.00E+11
ES46	EN46	WN46	WS46	33274772	2.00E+11
ES47	EN47	WN47	WS47	34410313	2.00E+11
ES48	EN48	WN48	WS48	35474549	2.00E+11
ES49	EN49	WN49	WS49	39660229	2.00E+11
ES50	EN50	WN50	WS50	40802704	2.00E+11
ES51	EN51	WN51	WS51	41806050	2.00E+11
ES52	EN52	WN52	WS52	42878000	2.00E+11

ES53	EN53	WN53	WS53	48921901	2.00E+11
ES54	EN54	WN54	WS54	49869420	2.00E+11
ES55	EN55	WN55	WS55	50939142	2.00E+11
ES56	EN56	WN56	WS56	51246621	2.00E+11

Appendix B

Table B1. Frequency variance of each case with 25% corrosion level cables

Mode no.	1-1	1-2	1-3	2-1	2-2	2-3	3-1	3-2	3-3	4-1	4-2	4-3
1	0.26%	0.25%	0.28%	0.21%	0.23%	0.25%	0.21%	0.26%	0.25%	0.25%	0.26%	0.25%
2	-2.12%	-3.07%	0.19%	-2.69%	-1.40%	0.22%	-2.90%	-1.43%	0.22%	-2.80%	-1.44%	0.22%
3	-0.04%	-0.69%	0.11%	-0.35%	-0.27%	0.14%	-0.36%	-0.28%	0.14%	-0.33%	-0.26%	0.15%
4	0.44%	0.33%	0.34%	0.38%	0.34%	0.31%	0.38%	0.34%	0.31%	0.16%	0.20%	0.22%
5	0.48%	0.41%	0.33%	0.44%	0.37%	0.30%	0.45%	0.37%	0.30%	0.68%	0.52%	0.39%
6	-2.33%	-2.97%	0.40%	-2.82%	-1.30%	0.40%	-2.85%	-1.30%	0.40%	-2.74%	-1.28%	0.40%
7	-0.16%	-0.13%	0.10%	0.01%	0.07%	0.13%	-0.15%	-0.01%	0.13%	-0.12%	0.00%	0.13%
8	-0.36%	-0.35%	0.13%	-0.52%	-0.17%	0.09%	-0.32%	-0.09%	0.10%	-0.39%	-0.10%	0.10%
9	-0.04%	-0.34%	0.18%	-0.19%	-0.08%	0.24%	-0.20%	-0.08%	0.24%	-0.18%	-0.08%	0.24%
10	0.12%	0.04%	0.17%	0.08%	0.12%	0.16%	0.08%	0.11%	0.15%	0.08%	0.11%	0.15%
11	0.14%	0.07%	0.16%	0.11%	0.10%	0.11%	0.10%	0.11%	0.14%	0.10%	0.11%	0.14%
12	-0.16%	-0.31%	0.30%	-0.30%	-0.01%	0.22%	-0.32%	-0.03%	0.20%	-0.24%	-0.01%	0.20%
13	-0.17%	-0.40%	0.05%	-0.30%	-0.16%	0.10%	-0.24%	-0.14%	0.10%	-0.47%	-0.18%	0.06%
14	-0.24%	-0.36%	0.06%	-0.29%	-0.12%	0.11%	-0.31%	-0.13%	0.11%	-0.15%	-0.10%	0.16%
15	-0.01%	0.02%	0.15%	0.09%	0.13%	0.16%	0.00%	0.09%	0.17%	0.00%	0.09%	0.17%
16	0.03%	-0.02%	0.07%	-0.06%	0.00%	0.09%	0.00%	0.03%	0.09%	0.00%	0.03%	0.09%
17	0.04%	0.08%	0.43%	0.05%	0.25%	0.44%	0.06%	0.25%	0.44%	0.06%	0.26%	0.45%
18	0.33%	0.20%	0.10%	0.26%	0.15%	0.07%	0.26%	0.15%	0.07%	0.25%	0.14%	0.07%
19	0.25%	0.14%	0.16%	0.19%	0.14%	0.14%	0.20%	0.15%	0.14%	0.22%	0.16%	0.14%
20	0.25%	0.13%	0.06%	0.20%	0.11%	0.06%	0.19%	0.10%	0.07%	0.19%	0.10%	0.07%
21	0.21%	0.14%	0.12%	0.07%	0.06%	0.11%	0.17%	0.13%	0.12%	0.18%	0.13%	0.12%
22	0.31%	0.14%	0.10%	0.31%	0.19%	0.11%	0.21%	0.11%	0.10%	0.22%	0.11%	0.10%
23	0.06%	0.11%	0.23%	0.03%	0.16%	0.19%	0.08%	0.18%	0.18%	0.08%	0.18%	0.18%
24	-0.31%	-0.30%	0.24%	-0.31%	0.02%	0.27%	-0.32%	0.02%	0.27%	-0.55%	0.01%	0.21%
25	-0.62%	-0.60%	0.25%	-0.51%	-0.09%	0.27%	-0.59%	-0.14%	0.27%	-0.44%	-0.14%	0.33%
26	0.06%	0.30%	0.49%	0.17%	0.37%	0.33%	0.18%	0.40%	0.34%	0.19%	0.40%	0.33%
27	0.04%	0.01%	0.10%	-0.01%	0.06%	0.16%	0.03%	0.06%	0.14%	0.01%	0.06%	0.15%
28	0.21%	0.07%	0.08%	0.15%	0.08%	0.15%	0.14%	0.08%	0.14%	0.15%	0.08%	0.15%
29	-0.26%	-0.36%	0.22%	-0.31%	-0.08%	0.20%	-0.31%	-0.08%	0.21%	-0.27%	-0.07%	0.21%
30	0.45%	0.07%	0.13%	0.24%	0.10%	0.30%	0.26%	0.10%	0.28%	0.25%	0.10%	0.29%

Table B2. Frequency variance of each case with 50% corrosion level cables

Mode no.	1-1	1-2	1-3	2-1	2-2	2-3	3-1	3-2	3-3	4-1	4-2	4-3
1	0.48%	0.47%	0.55%	0.35%	0.46%	0.50%	0.54%	0.48%	0.50%	0.46%	0.52%	0.50%
2	-4.71%	-6.75%	0.41%	-6.06%	-3.00%	0.45%	-1.45%	-3.22%	0.44%	-6.36%	-3.22%	0.44%
3	-0.07%	-1.47%	0.22%	-0.79%	-0.60%	0.28%	1.36%	-0.60%	0.29%	-0.55%	-0.51%	0.30%
4	0.85%	0.60%	0.68%	0.69%	0.67%	0.63%	0.91%	0.67%	0.63%	0.64%	0.23%	0.35%
5	0.97%	0.83%	0.66%	0.89%	0.75%	0.61%	0.93%	0.75%	0.61%	1.62%	1.20%	0.90%
6	-4.89%	-6.22%	0.81%	-6.30%	-2.76%	0.81%	-1.66%	-2.77%	0.81%	-5.88%	-2.69%	0.79%
7	-0.33%	-0.28%	0.21%	-0.01%	0.13%	0.26%	-0.11%	-0.03%	0.25%	-0.20%	0.01%	0.26%
8	-0.81%	-0.77%	0.28%	-1.15%	-0.37%	0.18%	-0.01%	-0.19%	0.20%	-0.88%	-0.25%	0.19%
9	-0.08%	-0.68%	0.36%	-0.39%	-0.17%	0.48%	0.96%	-0.18%	0.48%	-0.35%	-0.15%	0.50%
10	0.23%	0.06%	0.33%	0.14%	0.23%	0.33%	0.70%	0.21%	0.30%	0.14%	0.20%	0.30%
11	0.29%	0.13%	0.32%	0.23%	0.19%	0.23%	0.45%	0.22%	0.29%	0.21%	0.22%	0.29%
12	-0.33%	-0.63%	0.61%	-0.80%	-0.06%	0.44%	0.45%	-0.10%	0.41%	-0.50%	-0.02%	0.40%
13	-0.38%	-0.85%	0.14%	-0.64%	-0.33%	0.20%	0.17%	-0.26%	0.20%	-1.24%	-0.46%	0.09%
14	-0.52%	-0.75%	0.16%	-0.53%	-0.23%	0.22%	0.07%	-0.27%	0.22%	1.80%	-0.13%	0.34%
15	-0.02%	0.03%	0.30%	0.17%	0.25%	0.32%	0.27%	0.17%	0.33%	0.06%	0.17%	0.34%
16	0.04%	-0.04%	0.14%	-0.13%	0.00%	0.19%	0.21%	0.06%	0.17%	0.03%	0.05%	0.17%
17	0.08%	0.15%	0.85%	0.09%	0.50%	0.88%	0.97%	0.50%	0.89%	0.11%	0.52%	0.91%
18	0.67%	0.40%	0.20%	0.53%	0.30%	0.15%	0.55%	0.30%	0.14%	0.47%	0.28%	0.14%
19	0.52%	0.29%	0.33%	0.38%	0.29%	0.29%	0.52%	0.30%	0.29%	0.51%	0.34%	0.30%
20	0.48%	0.26%	0.12%	0.41%	0.21%	0.12%	0.56%	0.19%	0.13%	0.37%	0.19%	0.13%
21	0.40%	0.27%	0.24%	0.11%	0.11%	0.21%	0.42%	0.26%	0.25%	0.34%	0.26%	0.24%
22	0.65%	0.27%	0.20%	0.60%	0.39%	0.24%	1.05%	0.23%	0.20%	0.44%	0.23%	0.19%
23	0.10%	0.14%	0.47%	-0.04%	0.28%	0.38%	0.33%	0.35%	0.38%	-0.13%	0.35%	0.37%
24	-0.74%	-0.68%	0.57%	-0.66%	0.03%	0.54%	0.00%	0.01%	0.54%	-1.37%	-0.01%	0.36%
25	-1.30%	-1.15%	0.58%	-1.01%	-0.19%	0.53%	-0.32%	-0.26%	0.54%	0.42%	-0.28%	0.75%
26	0.12%	0.59%	0.99%	0.37%	0.73%	0.64%	0.87%	0.80%	0.70%	0.37%	0.82%	0.68%
27	0.11%	0.04%	0.22%	-0.01%	0.16%	0.34%	0.40%	0.13%	0.29%	0.06%	0.12%	0.31%
28	0.38%	0.13%	0.17%	0.29%	0.17%	0.30%	0.38%	0.17%	0.30%	0.31%	0.16%	0.30%
29	-0.41%	-0.68%	0.44%	-0.54%	-0.14%	0.41%	-0.02%	-0.14%	0.42%	-0.38%	-0.11%	0.43%
30	0.93%	0.13%	0.27%	0.50%	0.21%	0.61%	0.87%	0.20%	0.56%	0.52%	0.20%	0.61%

Table B3. Frequency variance of each case with 75% corrosion level cables

Mode no.	1-1	1-2	1-3	2-1	2-2	2-3	3-1	3-2	3-3	4-1	4-2	4-3
1	0.92%	0.66%	0.84%	0.75%	0.65%	0.76%	0.83%	0.64%	0.76%	0.81%	0.77%	0.76%
2	1.06%	−11.22%	0.64%	−4.61%	−4.82%	0.67%	0.39%	−5.45%	0.66%	−4.60%	−5.40%	0.64%
3	3.10%	−2.37%	0.33%	1.05%	−1.02%	0.42%	3.82%	−0.96%	0.43%	1.43%	−0.73%	0.46%
4	1.61%	0.71%	1.03%	1.24%	0.98%	0.95%	1.46%	0.99%	0.95%	0.78%	0.19%	0.41%
5	1.51%	1.25%	1.00%	1.37%	1.12%	0.92%	1.42%	1.13%	0.92%	2.58%	1.95%	1.47%
6	0.23%	−9.73%	1.22%	−5.01%	−4.41%	1.22%	−0.25%	−4.43%	1.22%	−4.18%	−4.25%	1.19%
7	−0.20%	−0.45%	0.31%	0.04%	0.18%	0.39%	−0.11%	−0.06%	0.39%	−0.15%	0.03%	0.39%
8	−0.42%	−1.27%	0.43%	−0.92%	−0.59%	0.28%	0.18%	−0.29%	0.31%	−0.41%	−0.43%	0.29%
9	1.59%	−1.03%	0.54%	0.77%	−0.27%	0.73%	2.50%	−0.28%	0.72%	1.16%	−0.22%	0.76%
10	0.81%	0.04%	0.50%	0.78%	0.34%	0.49%	1.14%	0.31%	0.45%	0.89%	0.29%	0.45%
11	0.80%	0.19%	0.48%	0.50%	0.29%	0.35%	1.13%	0.33%	0.44%	0.88%	0.32%	0.45%
12	0.88%	−0.95%	0.92%	−0.04%	−0.17%	0.67%	0.98%	−0.23%	0.63%	0.58%	−0.03%	0.60%
13	0.66%	−1.35%	0.22%	−0.22%	−0.52%	0.30%	0.79%	−0.35%	0.31%	−0.31%	−0.81%	0.11%
14	0.55%	−1.19%	0.27%	−0.11%	−0.32%	0.33%	0.52%	−0.42%	0.33%	1.88%	−0.14%	0.53%
15	0.10%	0.03%	0.45%	0.45%	0.37%	0.49%	0.34%	0.25%	0.50%	0.31%	0.25%	0.50%
16	0.19%	−0.06%	0.22%	0.07%	0.00%	0.28%	0.65%	0.09%	0.26%	0.61%	0.09%	0.27%
17	0.87%	0.23%	1.28%	0.97%	0.75%	1.32%	1.82%	0.76%	1.35%	1.30%	0.79%	1.39%
18	1.03%	0.61%	0.30%	0.82%	0.45%	0.22%	0.83%	0.46%	0.22%	0.72%	0.41%	0.21%
19	0.96%	0.44%	0.50%	0.70%	0.44%	0.45%	0.92%	0.45%	0.44%	1.00%	0.53%	0.47%
20	0.82%	0.39%	0.18%	0.76%	0.32%	0.18%	0.80%	0.29%	0.20%	0.77%	0.29%	0.20%
21	0.75%	0.39%	0.34%	0.20%	0.16%	0.32%	1.25%	0.38%	0.36%	1.22%	0.38%	0.36%
22	1.14%	0.40%	0.33%	1.63%	0.57%	0.37%	1.35%	0.34%	0.31%	1.35%	0.35%	0.30%
23	0.34%	0.01%	0.71%	0.24%	0.39%	0.57%	0.52%	0.50%	0.57%	0.40%	0.50%	0.54%
24	0.31%	−1.15%	0.90%	−0.35%	0.02%	0.82%	0.25%	−0.03%	0.82%	−1.20%	−0.12%	0.45%
25	−0.14%	−1.57%	0.91%	−0.78%	−0.26%	0.80%	−0.10%	−0.38%	0.82%	0.47%	−0.38%	1.23%
26	0.60%	0.89%	1.51%	1.09%	1.07%	0.96%	1.81%	1.22%	1.09%	1.65%	1.25%	1.05%
27	0.21%	0.08%	0.34%	0.31%	0.31%	0.55%	0.55%	0.20%	0.45%	0.50%	0.19%	0.46%
28	0.74%	0.17%	0.26%	0.58%	0.25%	0.45%	0.57%	0.26%	0.45%	0.59%	0.24%	0.46%
29	0.42%	−0.94%	0.66%	−0.34%	−0.20%	0.62%	0.30%	−0.19%	0.64%	−0.03%	−0.13%	0.65%
30	1.48%	0.21%	0.41%	1.06%	0.32%	0.92%	1.60%	0.30%	0.83%	1.48%	0.30%	0.94%

Table B4. Maximum deflection and corresponding location for different corrosion levels

	South		North	
Case number	Maximum deflection (m)	location (m)	Maximum deflection (m)	location (m)
Reference	-0.712	0	-0.712	0
1-1-25	-0.714	0.00	-0.714	0.00
1-1-50	-0.718	0.00	-0.718	0.00
1-1-75	-0.727	0.00	-0.727	0.00
2-1-25	-0.716	0.70	-0.716	-0.70
2-1-50	-0.724	2.30	-0.724	-2.30
2-1-75	-0.737	3.91	-0.737	-3.91
3-1-25	-0.707	0.00	-0.726	0.00
3-1-50	-0.704	0.00	-0.749	0.00
3-1-75	-0.704	0.00	-0.784	0.00
4-1-25	-0.717	1.10	-0.717	1.10
4-1-50	-0.728	3.11	-0.728	3.11
4-1-75	-0.748	3.51	-0.748	3.51

m-n-a : *m* means the major case, *n* means the subcase, *a* means the percentage of corrosion

Location: positive means on west side, negtive means on east side

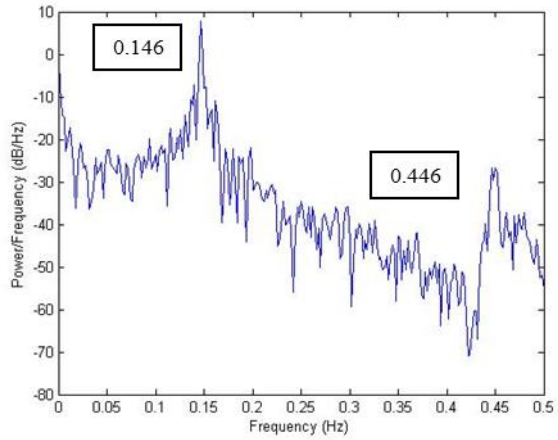

Fig. B1. PSD of horizontal deformation of south deck for reference case

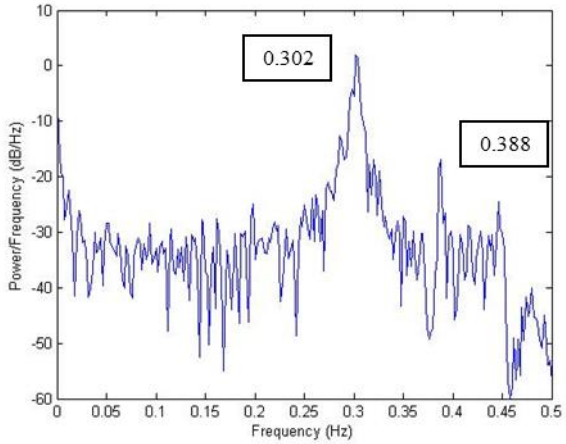

Fig. B2. PSD of vertical deformation of south deck for reference case

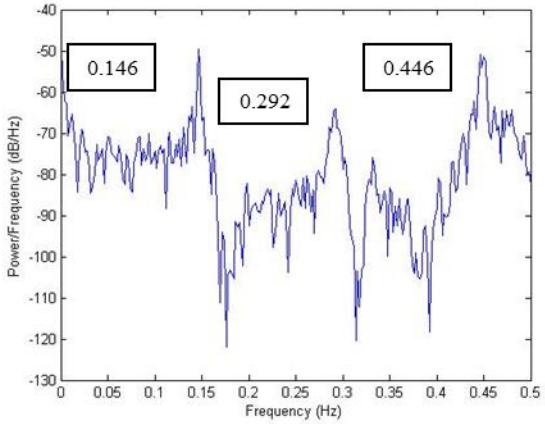

Fig. B3. PSD of torsional deformation of south deck for reference case

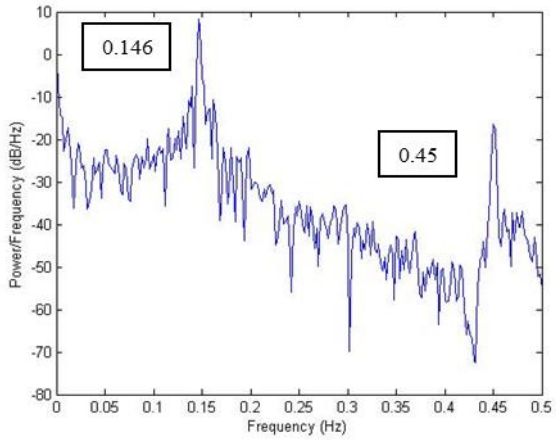

Fig. B4. PSD of horizontal deformation of south deck for subcase 1-2-25

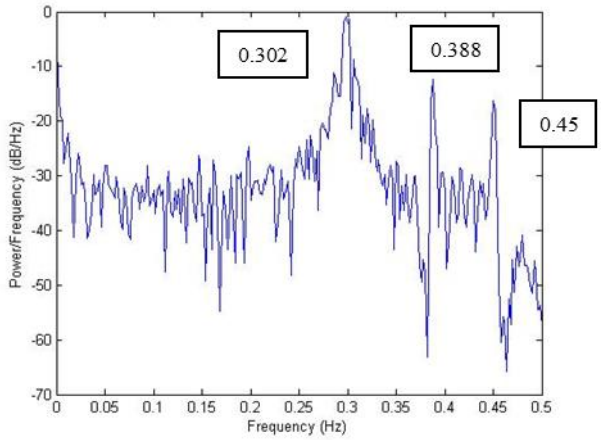

Fig. B5. PSD of vertical deformation of south deck for subcase 1-2-25

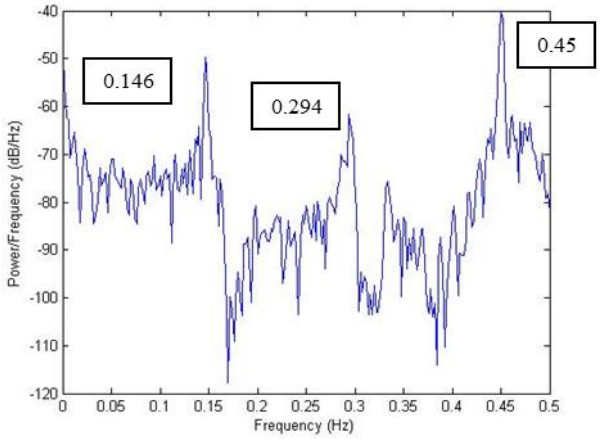

Fig. B6. PSD of torsional deformation of south deck for subcase 1-2-25

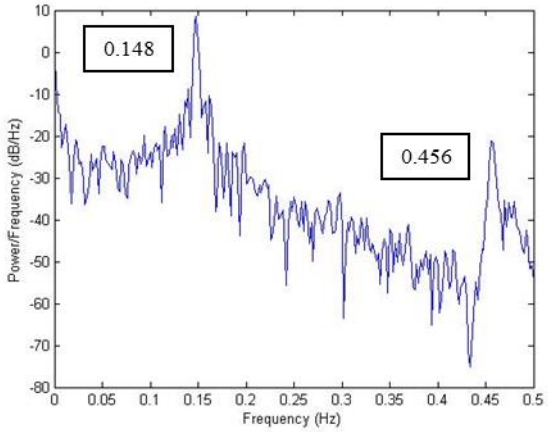

Fig. B7. PSD of horizontal deformation of south deck for subcase 1-2-75

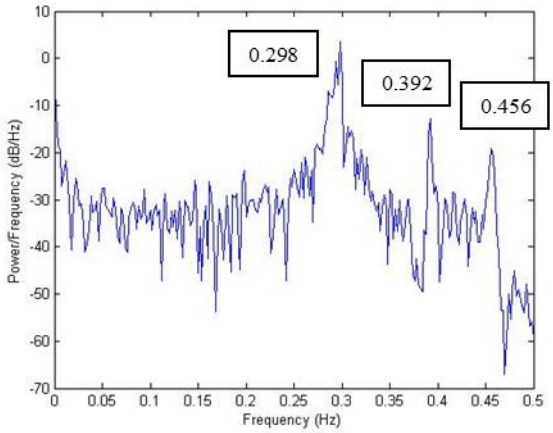

Fig. B8. PSD of vertical deformation of south deck for subcase 1-2-75

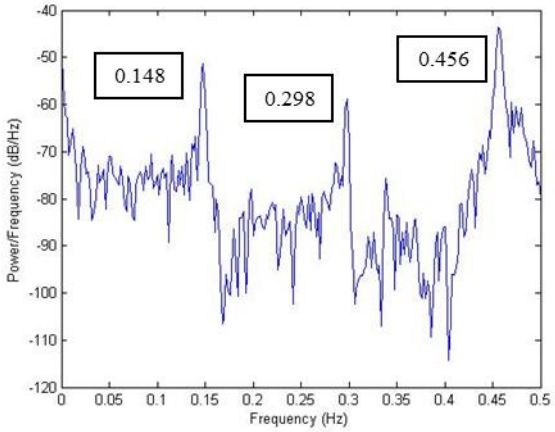

Fig. B9. PSD of torsional deformation of south deck for subcase 1-2-75

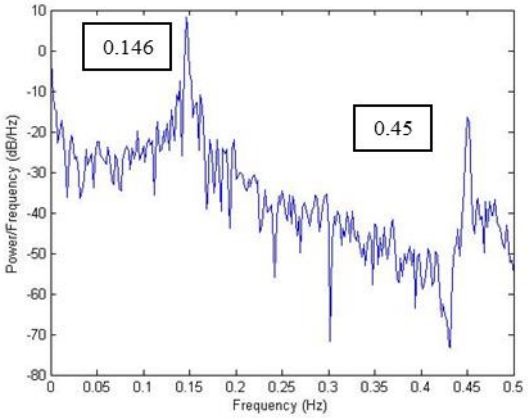

Fig. B10. PSD of horizontal deformation of south deck for subcase 2-2-25

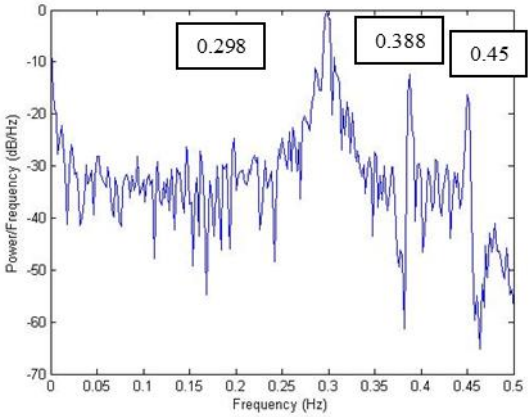

Fig. B11. PSD of vertical deformation of south deck for subcase 2-2-25

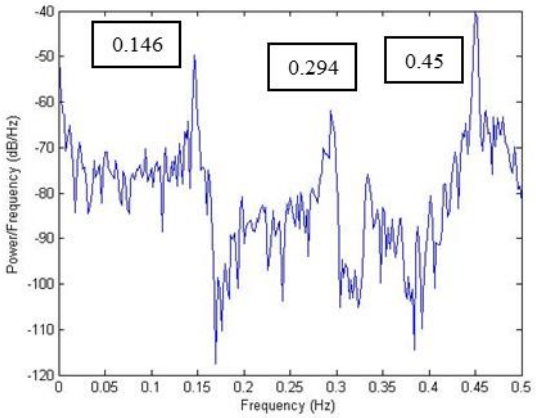

Fig. B12. PSD of torsional deformation of south deck for subcase 2-2-25

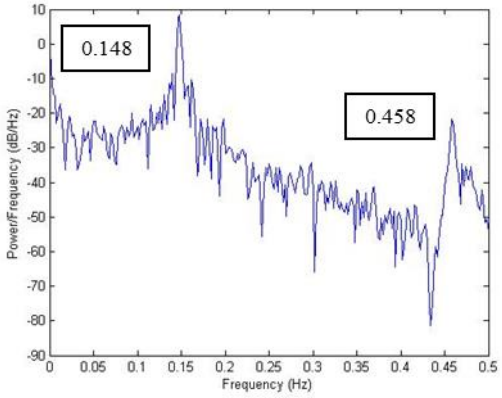

Fig. B13. PSD of horizontal deformation of south deck for subcase 2-2-75

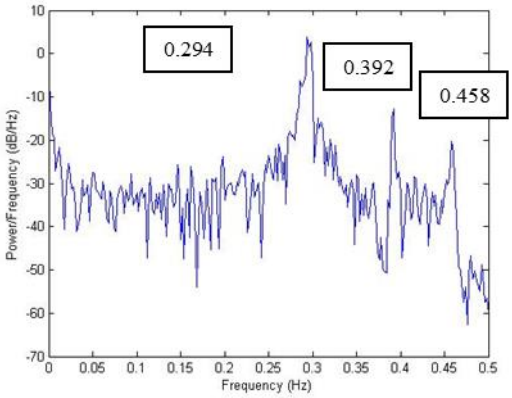

Fig. B14. PSD of vertical deformation of south deck for subcase 2-2-75

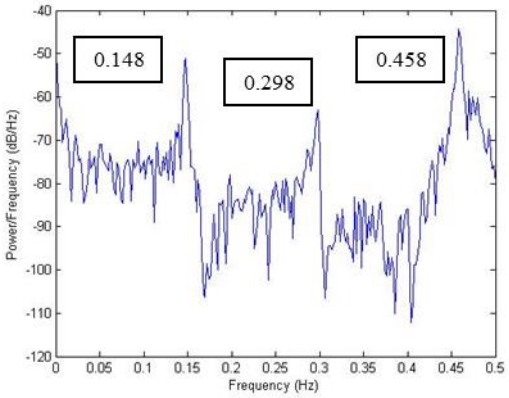

Fig. B15. PSD of torsional deformation of south deck for subcase 2-2-75

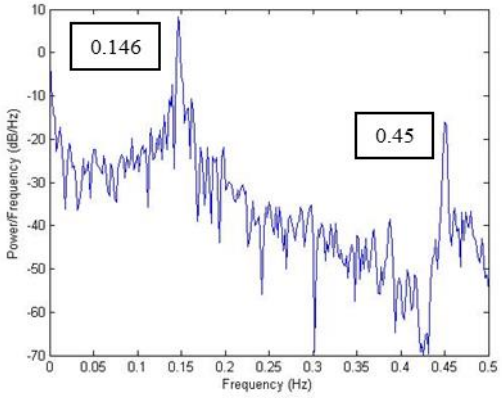

Fig. B16. PSD of horizontal deformation of south deck for subcase 3-1-25

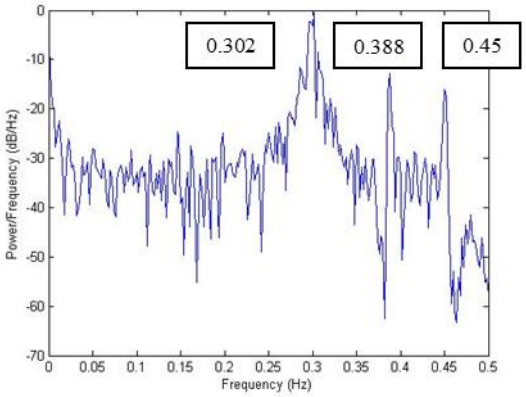

Fig. B17. PSD of vertical deformation of south deck for subcase 3-1-25

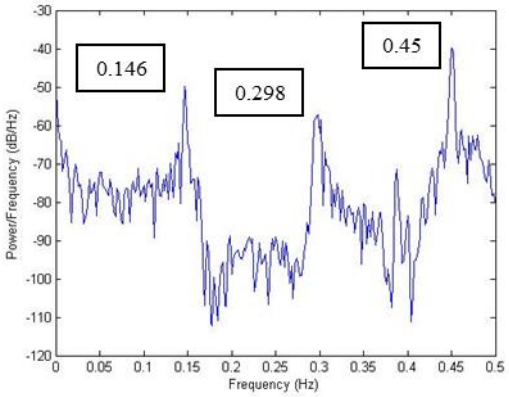

Fig. B18. PSD of torsional deformation of south deck for subcase 3-1-25

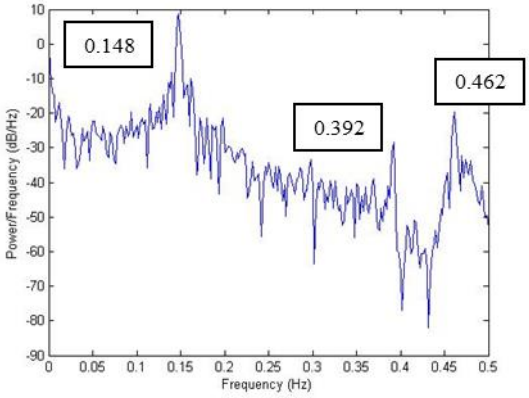

Fig. B19. PSD of horizontal deformation of south deck for subcase 3-1-75

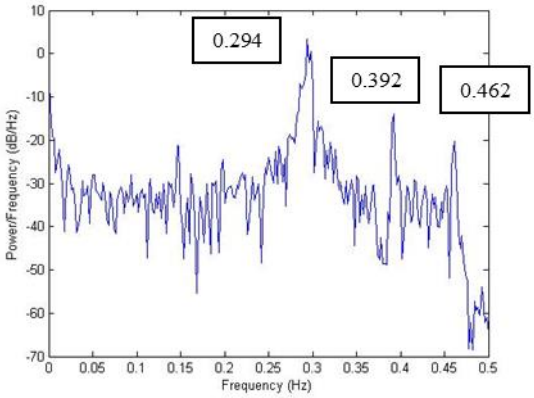

Fig. B20. PSD of vertical deformation of south deck for subcase 3-1-75

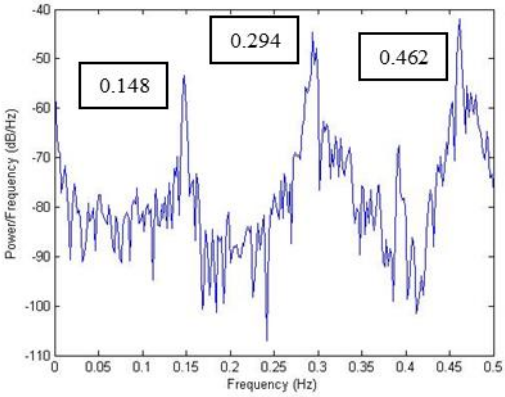

Fig. B21. PSD of torsional deformation of south deck for subcase 3-1-75

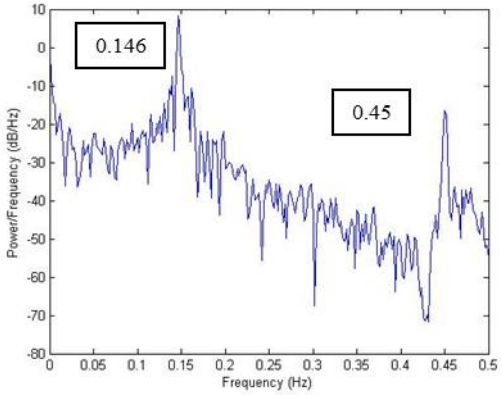

Fig. B22. PSD of horizontal deformation of south deck for subcase 4-1-25

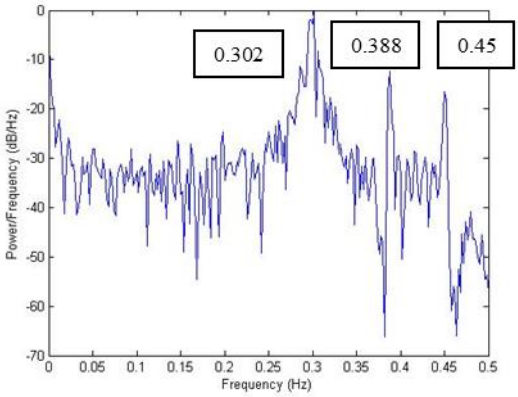

Fig. B23. PSD of vertical deformation of south deck for subcase 4-1-25

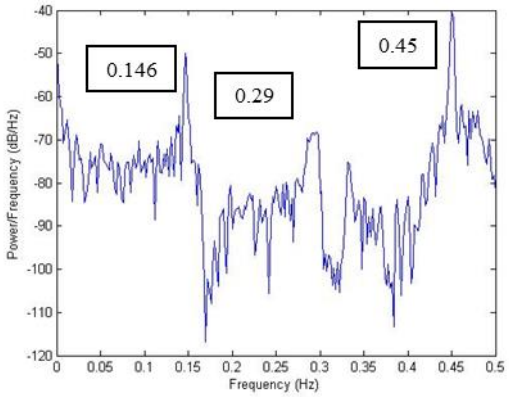

Fig. B24. PSD of torsional deformation of south deck for subcase 4-1-25

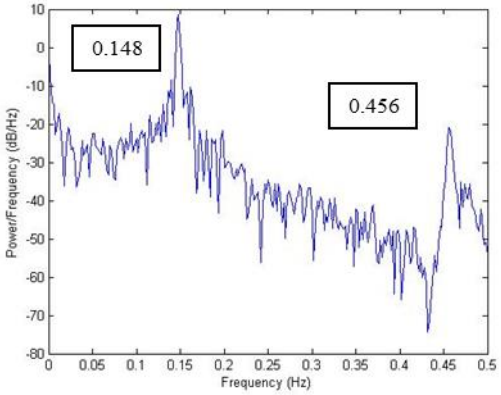

Fig. B25. PSD of horizontal deformation of south deck for subcase 4-1-75

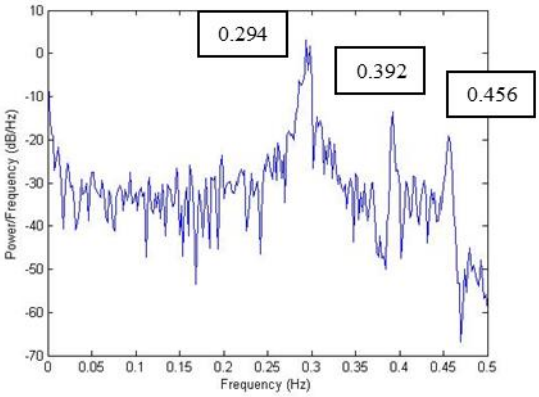

Fig. B26. PSD of vertical deformation of south deck for subcase 4-1-75

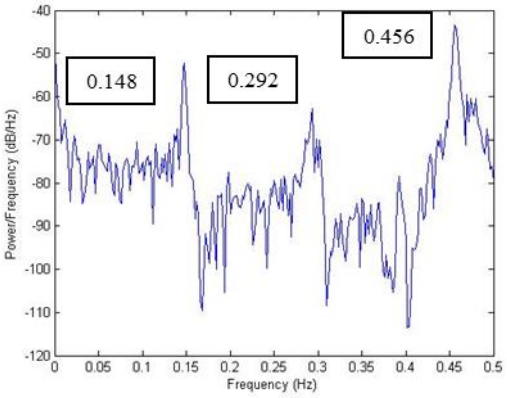

Fig. B27. PSD of torsional deformation of south deck for subcase 4-1-75

Appendix C

```
%PSD
x=xlsread('xxx.xlsx');
Nfft=500;
Fs=1;
n=0:Nfft-1;
t=n/Fs; window=hanning(Nfft);
noverlap=0;
dflag='none';
[Pxx,Pxxc,f]=psd(x,Nfft,Fs,window,noverlap,0);
figure(1)
plot(f,10*log10(Pxx));
xlabel('Frequency (Hz)');ylabel('Power/Frequency (dB/Hz)');
```

Appendix D

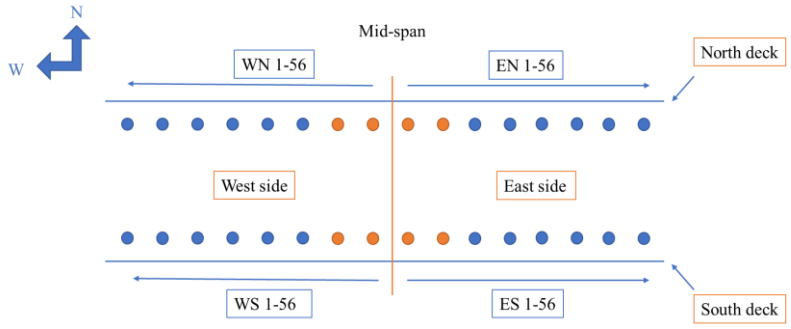

Fig. D1. Subcase 1-1

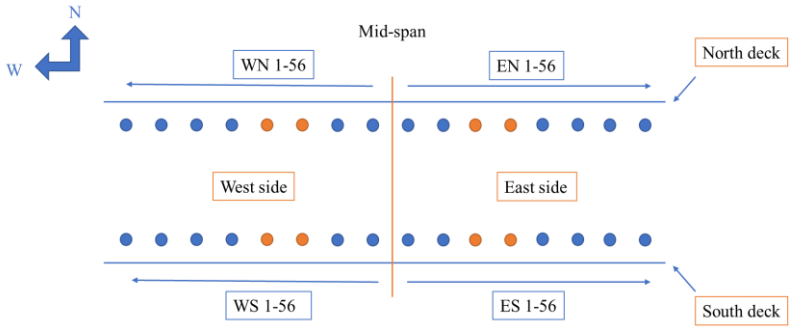

Fig. D2. Subcase 1-2

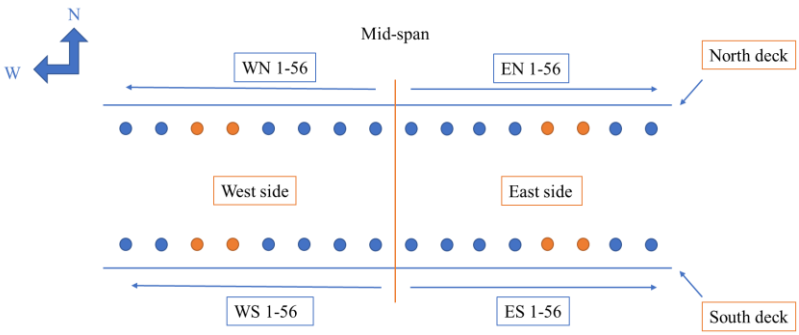

Fig. D3. Subcase 1-3

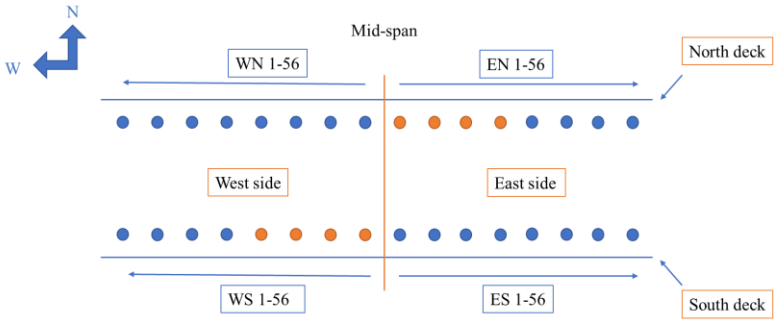

Fig. D4. Subcase 2-1

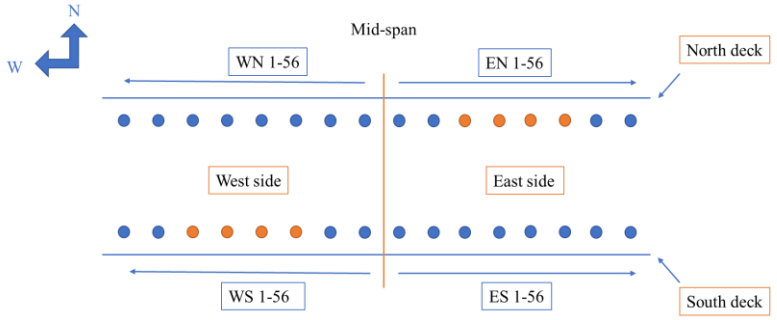

Fig. D5. Subcase 2-2

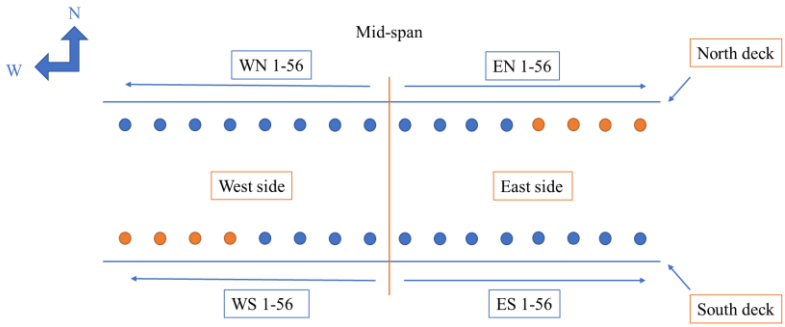

Fig. D6. Subcase 2-3

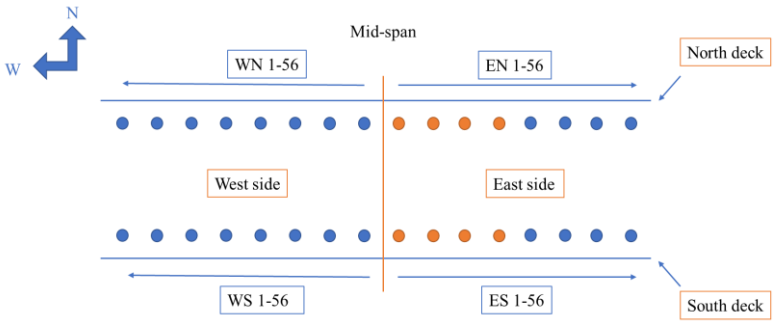

Fig. D7. Subcase 4-1

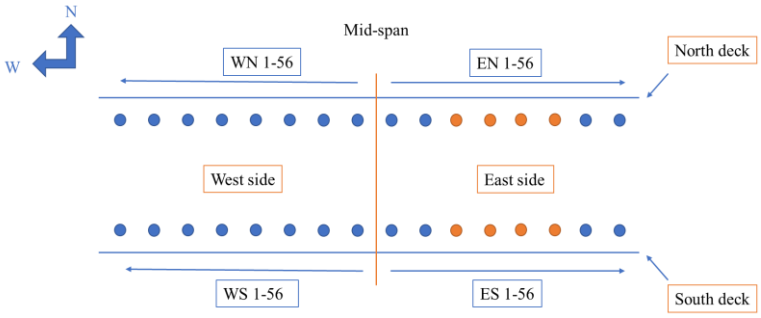

Fig. D8. Subcase 4-2

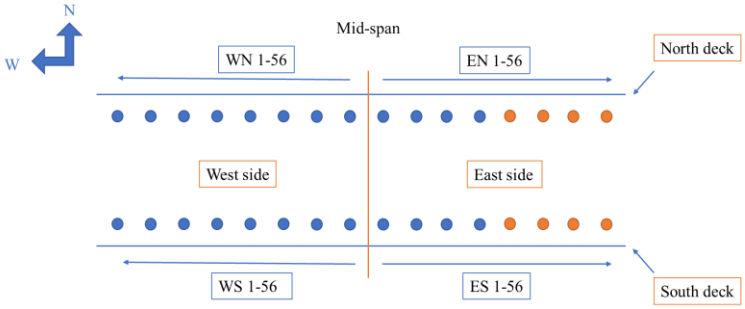

Fig. D9. Subcase 4-3

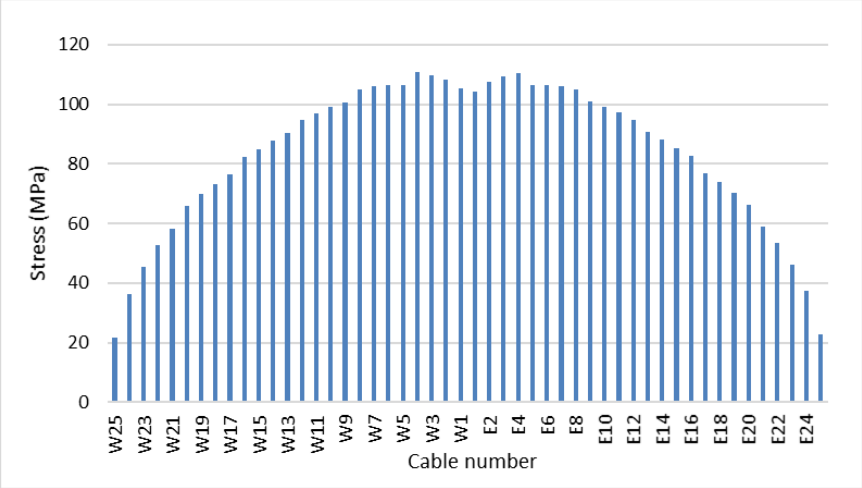

Fig. D10. Cable stress in SLS case